

From Condensed Matter to Higgs Physics – Solving Functional Renormalization Group Equations Globally in Field Space

Dissertation

zur Erlangung des akademischen Grades
doctor rerum naturalium (Dr. rer. nat.)

vorgelegt dem Rat der Physikalisch-Astronomischen Fakultät der
Friedrich-Schiller-Universität Jena

von M. Sc. Julia Borchardt
geboren am 19.02.1990 in Jena

Gutachter

1. Prof. Dr. Holger Gies (Friedrich-Schiller-Universität Jena)
2. Priv-Doz. Dr. Michael Scherer (Ruprecht-Karls-Universität Heidelberg)
3. Prof. Dr. Alfio Bonanno (INAF, Osservatorio Astrofisico di Catania)

Datum der Disputation: 07.02.2017

Abstract

By means of the functional renormalization group (FRG), systems can be described in a nonperturbative way. The derived flow equations are solved via pseudo-spectral methods. As they allow to resolve the full field dependence of the effective potential and provide highly accurate results, these numerical methods are very powerful but have hardly been used in the FRG context. We show their benefits using several examples. Moreover, we apply the pseudo-spectral methods to explore the phase diagram of a bosonic model with two coupled order parameters and to clarify the nature of a possible metastability of the Higgs-Yukawa potential.

In the phase diagram of systems with two competing order parameters, fixed points govern multicritical behavior. Such systems are often discussed in the context of condensed matter. Considering the phase diagram of the bosonic model between two and three dimensions, we discover additional fixed points besides the well-known ones from studies in three dimensions. Interestingly, our findings suggest that in certain regions of the phase diagram, two universality classes coexist. To our knowledge, this is the first bosonic model where coexisting (multi-)criticalities are found.

Also, the absence of nontrivial fixed points can have a physical meaning, such as in the electroweak sector of the standard model which suffers from the triviality problem. The electroweak transition giving rise to the Higgs mechanism is dominated by the Gaussian fixed point. Due to the low Higgs mass, perturbative calculations suggest a metastable potential. However, the existence of the lower Higgs-mass bound eventually is interrelated with the maximal ultraviolet extension of the standard model. A relaxation of the lower bound would mean that the standard model may be still valid to even higher scales. Within a simple Higgs-Yukawa model, we discuss the origin of metastabilities and mechanisms, which relax the Higgs-mass bound, including higher field operators.

Zusammenfassung

Mithilfe der funktionalen Renormierungsgruppe (FRG), können Systeme nicht-störungstheoretisch beschrieben werden. Die daraus abgeleiteten Flussgleichungen werden mittels pseudo-spektraler Methoden gelöst. Da die volle Feldabhängigkeit des Potentials aufgelöst und eine hohe Genauigkeit der Resultate erreicht werden kann, sind diese Methoden sehr interessant, jedoch bisher wenig genutzt im FRG Kontext. Wir zeigen ihre Vorteile an einer Reihe von Beispielen. Darüber hinaus, wenden wir pseudo-spektrale Methoden an, um das Phasendiagramm des $O(N) \oplus O(M)$ Modells zu erforschen und die Existenz einer Metastabilität des Higgs-Yukawa Potentials zu klären.

Im Phasendiagramm von Systemen mit zwei Ordnungsparametern beherrschen Fixpunkte multikritisches Verhalten. Solche Systeme werden oft im Kontext von Festkörpern diskutiert. Wir studieren das Phasendiagramm des $O(N) \oplus O(M)$ Modells zwischen zwei und drei Dimensionen und finden weitere Fixpunkte neben den bekannten Fixpunkten aus Untersuchungen in drei Dimensionen. Interessanterweise legen unsere Resultate nahe, dass in bestimmten Bereichen des Phasendiagramms zwei Universalitätsklassen koexistieren. Uns ist kein anderes bosonisches Modell bekannt, in dem koexistierende (multi-)kritische Phänomene gefunden wurden.

Die Abwesenheit von nicht-trivialen Fixpunkten kann auch eine physikalische Bedeutung haben, wie zum Beispiel im elektroschwachen Sektor des Standardmodells, welches das Trivialitätsproblem aufweist. Der elektroschwache Übergang mit dem Higgs-Mechanismus ist dominiert durch den Gaußschen Fixpunkt. Wegen der geringen Higgsmasse sagen Störungsrechnungen ein metastabiles Potential voraus. Die Existenz der unteren Higgsmassenschranke ist jedoch verknüpft mit der maximalen Ultraviolettscala, bis zu der das Standardmodell nur gültig sein kann. Eine Aufweichung der unteren Higgsmassenschranke würde bedeuten, dass das Standardmodell auch auf höheren Skalen gültig sein könnte. In einem einfachen Higgs-Yukawa Modell diskutieren wir den Ursprung von Metastabilitäten und Mechanismen, welche die Higgsmassenschranke unter Einbeziehung von höherwertigen Feldoperatoren aufweichen.

Contents

1. Introduction	3
2. Flows in quantum field theory and critical behavior	8
2.1. The effective action	8
2.2. The functional renormalization group	9
2.3. Truncations and critical behavior	11
2.4. Introduction to the models	16
3. Pseudo-spectral methods	21
3.1. Pseudo-spectral expansions	21
3.2. Convergence properties	23
3.3. Implementation	24
4. Solving functional fixed-point equations via pseudo-spectral methods	28
4.1. Fixed-point equations of \mathbb{Z}_2 symmetric models with one order parameter	29
4.1.1. The Ising model near criticality	29
4.1.2. A simple Yukawa model model in $d = 3$	34
4.2. Universal behavior of coupled order parameters below three dimensions	39
4.2.1. Systems of competing orders	40
4.2.2. Fixed-point content	42
4.2.3. Breakdown of local expansions	46
4.2.4. Interplay of fixed points and phase structure in $d \leq 3$	47
4.2.5. Summary: Stability trading between $d = 3$ and $d = 2$	53
4.2.6. Testing the quantitative reliability of our results	55
4.3. Conclusions	56
5. Solving functional flow equations via pseudo-spectral methods	59
5.1. Flows of the $O(N)$ model	60
5.1.1. Flows for large N in $d = 3$: A comparison	60
5.1.2. Flows for $N = 1, 4$ in $d = 3$	62
5.1.3. Flow between two critical regimes for $N = 1$	64
5.2. Quantum Mechanics with a bounded potential	65
5.2.1. Models	66

5.2.2.	Exact results	67
5.2.3.	WKB approximation	67
5.2.4.	One-loop approximation	68
5.2.5.	Flow of the effective potential	69
5.2.6.	Large N approximation	72
5.3.	Flows of the Higgs potential in a Yukawa model	75
5.3.1.	Higgs-Yukawa model with discrete symmetry	76
5.3.2.	Perturbative effective single-scale potential	77
5.3.3.	Mean-field effective potential and stability	79
5.3.4.	Nonperturbative flow of the scalar potential	85
5.3.5.	Convexity of the effective potential	89
5.3.6.	Quantum phase diagram of the Higgs-Yukawa model	92
5.4.	Conclusions	95
6.	Conclusions	97
A.	Threshold functions	I
B.	Expansions via rational Chebyshev functions	III
C.	Rotated solutions with two order parameters	V
D.	One-loop effective action in quantum mechanics	VIII
E.	Computation of the single-scale potential	IX
F.	Computation of the scale dependent fermion determinant	XI

1. Introduction

Our world consists of various structures on different length scales. For a long time, only a small window of scales was accessible for mankind. In the last centuries, we spent a lot of effort to overcome these boundaries.

Nowadays, we know that we are comparatively tiny creatures living on the planet Earth, which is a little component of the solar system that is placed in a larger Galaxy in an even larger Universe. Gravity is an important force on these length scales. Whereas Newton's theory can successfully explain the gravitational force on a wide range of scales, general relativity provides an even more precise description which particularly applies for "extreme" cases, such as high densities or at speeds comparable to the speed of light. There is, however, a huge number of effects not yet understood, for instance dark energy or dark matter.

On the opposite side of the length measurement, a coherent picture of the fundamental building blocks of our world is also still incomplete. Bacteria live on small length scales that we mostly are not able to resolve by eye. Nevertheless, just like us, they are also composed of atoms which are between three to six orders of magnitude smaller. On these length scales, quantum fluctuations become more and more important. In our everyday life, which can be described classically pretty well, quantum effects are, however, far away from intuition.

These examples indicate that the physically relevant degrees of freedom of a theory naturally change as a function of the length or energy scale. An appropriate description of the scale dependence of theories is provided by the renormalization group (RG). According to the Wilsonian idea, quantum fluctuations are taken into account scale by scale, starting at large energy scales and ending up at small energy scales. This procedure is described as a flow from microscopic to macroscopic scales of a given theory.

Grazing the space of all possible theories, we may find scale invariant theories which look similar on all scales. These theories arise as *fixed points* of the RG flow. Of course, fixed points are of high physical relevance, as they give rise to universal properties of flows in their vicinity. Moreover, critical phenomena are connected to these scale invariant points. It clearly seems puzzling at first sight that the critical behavior of two very different microscopic systems is the same. The RG, however, yields an explanation going back to Wilson's work [1–3] for which he was awarded the Nobel Prize in 1982. Critical phenomena and fixed points indicate the existence of phase transitions. The phases are characterized by the preservation or spontaneous breaking of the theory's symmetry. Commonly, an order parameter can be defined which measures the degree of order of the phases. In some cases, different kinds of

symmetry breaking occur with different residual symmetries leading to a rich structure of the phase diagram. The behavior of the order parameter at the transition allows to distinguish between different types of phase transitions. Usually, phase transitions of second order are connected with critical, universal behavior. However, some degree of universality can also be found in bosonic models for weak first order phase transitions [4]. The confinement-deconfinement phase in quantum chromodynamics (QCD) [5–7], condensed matter systems such as anisotropic antiferromagnets in an external magnetic field [8, 9], high- T_c superconductors [10, 11] and graphene [12, 13] are only a few examples of a huge number of systems exhibiting critical behavior. In particle physics, the dynamical breaking of the electroweak symmetry, which gives rise to the nonvanishing vacuum expectation value of the Higgs field [14, 15], attracted a lot of attention in the last decades.

In the first part of this work, we are interested in multicritical behavior such as arising in systems with two competing order parameters. These systems have been explored theoretically in great detail, in particular in three dimensions, [16–25]. Furthermore, they are heavily discussed in the context of anisotropic antiferromagnets [26–33] which exhibit transitions from the paramagnetic phase to the spin-flop or antiferromagnetic phase as a function of the temperature and the magnetic field. Another interesting application is given by high- T_c superconductors [34–36] showing an antiferromagnetic and d -wave superconducting order. Certain aspects of Dirac materials, e.g., graphene, also fall into the class of multicritical systems [37, 38]. Recently, multicritical field theories have also drawn attention as toy models for fundamental quantum field theories [25].

The $O(N) \oplus O(M)$ model plays an important role for condensed matter physics as it serves as a perfect playground for investigating multicritical systems. As they are experimentally realizable, systems with phase diagrams with two transition lines of second order, which meet at a *multicritical point*, have been in the focus of the literature. Besides the usual three phases – two corresponding to the breaking of the separate symmetries and one symmetric phase – there may exist an additional so-called “mixed” phase close to the multicritical point. Which kind of phase structure is realized, can be answered by the properties of that point, which is either *bicritical* or *tetracritical*. Multicritical points show up as scale invariant points in theory space.

The $O(N) \oplus O(M)$ model has already been in the focus of various studies employing, e.g., the $\varepsilon = 4 - d$ expansion [16, 19, 39, 40], Monte Carlo simulations [11, 33, 41], two-loop perturbative RG methods [21, 42, 43] and the exact RG [22–25, 44]. However, the results from these studies do not necessarily give rise to a clear picture or partly do not agree with experimental investigations [9, 26, 27], e.g., for the case of the anisotropic antiferromagnet. Therefore, a lot of open questions remain such as a detailed understanding of the phase diagram between two and three dimensions. As a function of N and M , different fixed points determine the phase structure of the multicritical system. This gives rise to interrelations between these points in dependence on N and M . It is an interesting question how the inter-

play between the multicritical points works as a function of the dimension. Furthermore, in two dimensions, the two coupled Ising models ($O(1)$ models) provide a fascinating case: One possible candidate for the multicritical point yields tetracritical behavior and a decoupling of both field sectors. It can be derived from the analytic Onsager solution of the single-field model. Another candidate features a symmetry enhancement to an $O(2)$ symmetry which would suggest Berezinskii-Kosterlitz-Thouless (BKT) type physics that is a phase transition of “infinite” order. The phases of such a topological phase transition correspond to binding and unbinding vortex-antivortex pairs. For “theoretical discoveries of topological phase transitions and topological phases of matter”,¹ Thouless, Haldane and Kosterlitz were recently awarded the Nobel Prize that shows the significance of identifying BKT physics in systems. Which kind of physical behavior is realized in the $O(N) \oplus O(M)$ model as a function of the dimension shall be discussed in detail in this work for the first time.

A wide range of systems does not exhibit a nontrivial fixed point. In particular, the absence of such a fixed point promotes the *triviality* problem which is an open problem of the standard model. The electroweak phase transition in particle physics is therefore connected with the *Gaussian* fixed point. So far, colliders probe a regime where Nature is close to that fixed point and perturbative approaches successfully describe the electroweak collider data. The spontaneous symmetry breaking within the electroweak sector, the Higgs mechanism, is crucial to explain the generation of the mass for the massive gauge bosons [14, 15, 45–47] and the fermions [48–50] in the standard model of particle physics. The discovery of the therein predicted Higgs boson at the LHC [51, 52] finally completed the search for the building blocks of the standard model.

The Higgs mass is in principle a free but not an arbitrary parameter. With some “natural” assumptions, upper and lower bounds on the Higgs mass can be computed. In order to fix the renormalization condition in the infrared (IR) to the measured value of the Higgs mass, perturbative calculations yield a metastable Higgs potential, i.e., a second vacuum besides the electroweak Higgs vacuum. This becomes already visible as an instability in a simple Higgs-Yukawa model which mimics the electroweak sector of the standard model.

In the present work, we address the origin of the arising in-/metastability in the simple Higgs-Yukawa model and consider a more general class of microscopic actions in order to study mechanisms relaxing the conventional lower Higgs-mass bound. For that purpose, we assume that the standard model is an effective theory valid up to the ultraviolet (UV) cutoff scale. Beyond that scale, new degrees of freedom, e.g., gravitational ones, are supposed to become important. These degrees should be incorporated in a more fundamental theory. From this viewpoint, there is no unique choice for a suitable microscopic action. In particular, the UV action should be provided by the underlying theory which is, however, unknown. The mass bounds are connected with the maximal UV extension of the standard model up to which the measured Higgs mass lies within the range between the two bounds. Thus, the

¹www.nobelprize.org/nobel_prizes/physics/laureates/2016/

Higgs-mass bounds are directly related to the range of validity of the standard model.

We consider the extension of the class of perturbatively renormalizable actions by higher dimensional operators which requires a careful analysis. Due to their RG irrelevance, they do not exert a significant effect on the IR physics. On the other hand, they may render the Higgs potential stable in the UV [53]. This has been confirmed by lattice simulations in the range of scales accessible to current lattice sizes [54–57]. Resolving the Higgs potential as a function of the Higgs field, we pursue the question as to whether there is nevertheless a possibility, that a metastability can arise. We pick up the discussion of [53, 58, 59] and clarify the situation in this work.

Both studies within the $O(N) \oplus O(M)$ model and the Higgs-Yukawa model are unified in a technical way. We employ the functional renormalization group (FRG) combined with a pseudo-spectral expansion of the effective average potentials. The FRG has been proven to be a powerful tool in a quite more general context such as in applications to scalar field theories [60–69], fermionic systems [58, 70–75], critical phenomena [76–82], gauge theories [83–90] and quantum gravity [91–105]. In many cases, physical phenomena are dominated by strong correlations, or the description of a theory is governed by couplings that run from small to large values during the flow. A prominent example is given by QCD, which is asymptotically free at high energy scales and strongly coupled at low energy scales. Also the UV completion of gravity in terms of asymptotic safety [91, 106, 107] demands the inclusion of strong correlations. Hence, to cover all aspects of our study, a nonperturbative approach such as the FRG is indispensable. From a technical perspective, the generic outcome of FRG computations is a coupled system of nonlinear (integro-)differential equations of complex structure. Commonly, the full equations cannot be solved analytically and one has to consider the system within some truncation, retaining only a manageable number of operators. Even then, the equations are rarely analytically solvable, e.g., in a mean-field approximation. However, if one seeks a solution without a mean-field approximation or an expansion in powers of the field for instance, numerical methods appear indispensable. In the present work, we employ a pseudo-spectral expansion in Chebyshev polynomials.

In a general physical context, pseudo-spectral methods have become an often used numerical method [108–115]. First applications to FRG problems can be found in [116–121]. Let us point out that full potential flows were already solved in the past employing finite element or finite difference methods [4, 122–136]. Here, we show that pseudo-spectral methods are a versatile tool which deserves even more attention especially referring to FRG problems. Pseudo-spectral methods allow for global solutions to functional fixed-point equations which we compute in the first part and (global) functional flows in theory space which are considered in the second part of this work.

This work is organized as follows: In Chap. 2, we provide a short review of the FRG in terms of the effective average action and of critical behavior, in particular close to continuous phase transitions. As we study various models, some of them treating as a benchmark for our

numerical method, we introduce them once in the last section of this chapter. In Chap. 3, we summarize the most important properties of pseudo-spectral methods and sketch how they are applied in the particular cases. At the beginning of the next two chapters, the benefits of this numerical method are demonstrated including also special cases where they yield superior results while other commonly used methods are unfeasible. In Chap. 4, the $O(N)$ model between two and three dimensions and a simple Yukawa model in three dimensions are in the focus of our tests. As we provide global solutions for the fixed-point potentials also for cases where polynomial truncations cannot be trusted, we gain a deeper insight into both systems. In the second part of this chapter, an extensive study of the phase diagram of the $O(N) \oplus O(M)$ model for various dimensions follows which yields new results, in particular below three dimensions. The following chapter deals with functional flows. We demonstrate the power of pseudo-spectral methods with the example of the $O(N)$ model, which can be solved analytically within the large N limit. We study the approach to convexity and flows between different universality classes. Within quantum mechanics, we consider the flow of bounded potentials from above and below which gives rise to new technical challenges. Such potentials are prominent in models for Higgs inflation and dark energy. In the last part of this chapter, we conduct an extensive study of the Higgs-Yukawa model, shedding light on the fate of the metastability of the Higgs potential, the influence of nonperturbatively renormalizable operators on the perturbative lower Higgs-mass bound, and the phase diagram as a function of the microscopic couplings. New insights concerning the effect of convexity on estimates of the tunnel rate are found. Finally, we conclude in Chap. 6.

The compilation of this thesis is solely due to the author. However, parts of this work have been developed in several collaborations with members of the Theoretical Physical Institute in Jena and the Imperial College in London. The results on the global fixed-point solutions in Chap. 4 were achieved in collaboration with B. Knorr and can be also found in [137, 138]. The study of the $O(N) \oplus O(M)$ model was done with A. Eichhorn and published in [139]. The results of the first two sections of Chap. 5 have been elaborated with B. Knorr and reported in [140]. The last section where flows within a simple Higgs-Yukawa model are considered originates from the collaboration with H. Gies and R. Sondenheimer and was published in [141].

2. Flows in quantum field theory and critical behavior

The effective action provides an efficient way of describing a quantum field theory in terms of the path integral. In the following section, we exemplify its construction for a theory with single scalar field. For the computation of the effective action, a nonlinear, functional, integro-differential equation has to be solved for which different approaches exist. In the present work, we employ the FRG method providing an exact differential flow equation. For this purpose, we introduce the effective average action depending on a momentum scale k . We give first insights applying it to the Ising model with a single scalar field. For more details we refer the reader to [62, 74, 76, 84, 85, 122]. After pointing out the relevance of scale independent solutions, we discuss their relation to critical phenomena. In the second part of this chapter, we give an introduction to the models which play a role in this work.

2.1. The effective action

Let us consider a quantum field theory of one real scalar field φ in d dimensional spacetime with Euclidean signature. All information of this quantum field theory is stored in terms of correlation functions which can be derived from the generating functional,

$$Z[J] \equiv e^{W[J]} := \int_{\Lambda} \mathcal{D}\varphi e^{-S[\varphi] + \int J\varphi}, \quad (2.1)$$

by differentiating with respect to J and setting $J = 0$ afterwards. In the integral, all field configurations are weighted by the classical, microscopic action $S[\varphi]$ (which is also called bare action) and the source term $\int J\varphi$. The UV momentum modes are cut off at the scale Λ for a proper regularization.

An efficient way of storing quantum information is provided by the effective action, which is obtained by the Legendre transform of the Schwinger functional $W[J]$,

$$\Gamma[\phi] := \sup_J (J\phi - W[J]). \quad (2.2)$$

In presence of the source J , the expectation value of the field φ is given by the classical field $\phi(x) = \frac{\delta W[J]}{\delta J(x)} = \langle \varphi(x) \rangle_J$. The source acts as an inhomogeneity in the quantum equation of

motion,

$$J = \frac{\delta\Gamma[\phi]}{\delta\phi}. \quad (2.3)$$

From the definition (2.2), it can be seen that Γ is a convex functional of ϕ .

For the effective action, we obtain a nonlinear, first order, functional, integro-differential equation

$$e^{-\Gamma[\phi]} = \int_{\Lambda} \mathcal{D}\varphi \exp\left(-S[\varphi + \phi] + \int \frac{\delta\Gamma[\phi]}{\delta\phi} \varphi\right). \quad (2.4)$$

Note that these considerations can be easily extended to other kinds of fields such as vector or fermionic fields.

There are different ways of solving Eq. (2.4), e.g., given by Dyson-Schwinger equations, see [142] for a detailed review. However, from a practical viewpoint, it is more convenient to employ the FRG in our cases, in particular for critical phenomena.

2.2. The functional renormalization group

The FRG is a versatile nonperturbative approach for solving Eq. (2.4). We restart with a slightly modified definition of the generating functional

$$Z_k[J] \equiv e^{W_k[J]} := \int_{\Lambda} \mathcal{D}\varphi e^{-S[\varphi] - \Delta S_k[\varphi] + \int J\varphi}, \quad (2.5)$$

where the regulator term

$$\Delta S_k[\varphi] = \frac{1}{2} \int \frac{d^d p}{(2\pi)^d} \varphi(-p) R_k(p) \varphi(p) \quad (2.6)$$

acts as an additional mass term which suppresses low momentum modes $p^2 < k^2$. Thus, the scale k denotes an IR momentum scale. By contrast, high momentum modes $k^2 < p^2 < \Lambda^2$ are integrated out according to the Wilsonian idea of momentum-shell-wise integration of quantum fluctuations. This is implemented by requiring the following conditions for the regulator function

$$\lim_{p^2/k^2 \rightarrow 0} R_k(p) > 0, \quad (2.7)$$

$$\lim_{k^2/p^2 \rightarrow 0} R_k(p) = 0, \quad (2.8)$$

$$\lim_{k \rightarrow \Lambda \rightarrow \infty} R_k(p) \rightarrow \infty. \quad (2.9)$$

The condition (2.8) guarantees that $Z_{k \rightarrow 0} = Z$. For $k \rightarrow \Lambda \rightarrow \infty$, no fluctuations are integrated out and we recover the classical action.

We define the effective average action as

$$\Gamma_k[\phi] = \sup_J (J\phi - W_k[J]) - \Delta S_k[\phi]. \quad (2.10)$$

Also on this level, the properties of the regulator function imply $\Gamma_{k \rightarrow 0} = \Gamma$ and $\Gamma_\Lambda \rightarrow S + \text{const.}$ The quantum equation of motion becomes

$$J(x) = \frac{\delta \Gamma_k[\phi]}{\delta \phi(x)} + \int \frac{d^d p}{(2\pi)^d} e^{ipx} R_k(p) \phi(p). \quad (2.11)$$

In contrast to the source, the field $\phi = \frac{\delta W_k[J]}{\delta J(x)} = \langle \varphi(x) \rangle_J$ is assumed to be independent from the scale k . From Eq. (2.11), one can infer that $\Gamma_k^{(2)}[\phi] + R_k$ corresponds to the inverse of the connected propagator. Here, we have used the shorthand notation

$$\Gamma_k^{(n)}[\phi] = \frac{\delta^n \Gamma_k[\phi]}{\delta \phi \dots \delta \phi}. \quad (2.12)$$

The *flow* of the effective average action from one scale k to another is described by a functional differential equation, the Wetterich equation [143],

$$\partial_t \Gamma_k[\phi] = \frac{1}{2} \text{STr} \left[\left(\Gamma_k^{(2)}[\phi] + R_k \right)^{-1} \partial_t R_k \right], \quad (2.13)$$

where $t = \ln(k/\Lambda)$. The super trace acts as an ordinary trace for bosonic fields, but provides a minus sign for the fermions. Although Eq. (2.13) is of one loop structure, it is exact due to the presence of the full propagator. IR physics does not depend on the specific choice of the regulator, i.e., all IR observables are regularization scheme independent. However, this property is not necessarily maintained if a truncation scheme is employed which neglects classes of operators. Therefore, the necessity for the choice of an optimized regulator arises that guarantees a fast convergence of the physical observables. An optimization criterion is provided in [144–146] which encloses a natural minimum sensitivity condition. For practical purposes, this condition is usually used to optimize a specific physical observable. The solutions then also depend on the considered class of regulator functions. We mostly use the linear optimized regulator [145] in this work, which is

$$R_{\phi,k}(p) = Z_{\phi,k} p^2 r_{\phi,k}(p^2) \quad \text{with} \quad r_{\phi,k}^{\text{opt}} = \left(\frac{k^2}{p^2} - 1 \right) \Theta(k^2 - p^2) \quad (2.14)$$

for bosons, and

$$R_{\psi,k}(p) = -Z_{\psi,k} \not{p} r_{\psi,k}(p^2) \quad \text{with} \quad r_{\psi,k}^{\text{opt}} = \left(\sqrt{\frac{k^2}{p^2}} - 1 \right) \Theta(k^2 - p^2) \quad (2.15)$$

for fermions, where we have introduced the bosonic and fermionic wave function renormalizations $Z_{\phi,k}$ and $Z_{\psi,k}$, cf. below. For more details about an adapted choice of the regulator, see also [44, 85].

The flow equation (2.13) also contains perturbation theory. If we insert the loop expansion $\Gamma_k^{1\text{-loop}} = S + \hbar\Gamma_k^1 + \mathcal{O}(\hbar^2)$ into Eq. (2.13), we obtain the one-loop effective action for $k \rightarrow 0$,

$$\Gamma_{\text{eff}}^{1\text{-loop}} = S + \frac{1}{2}\hbar \text{STr} \ln S^{(2)} + \text{const} = S + \frac{1}{2}\hbar \ln \text{Sdet} S^{(2)} + \text{const}. \quad (2.16)$$

Note that the trace/determinant still requires an appropriate regularization. In the case of the Higgs potential in Sec. 5.3.3, this formula corresponds to the mean-field effective action if only fermionic fluctuations are taken into account.

2.3. Truncations and critical behavior

In most cases of interest, Eq. (2.13) cannot be solved exactly. A possible ansatz has already been given by the loop expansion. However, perturbation theory fails if the system is strongly coupled and loop terms of higher order become important. Thus, we solve Eq. (2.13) within nonperturbative approximation schemes which can be summarized under the method of truncations. Within the vertex expansion,

$$\Gamma_k[\bar{\phi}] = \sum_{n=0} \frac{1}{n!} \int d^d x_1 \dots d^d x_n \Gamma_k^{(n)}(x_1, \dots, x_n) \bar{\phi}(x_1) \dots \bar{\phi}(x_n), \quad (2.17)$$

the full momentum dependence is collected in the vertices $\Gamma_k^{(n)}(x_1, \dots, x_n)$, whereas only a finite order of the power in the field is taken into account. From now on, the dimensionful, unrenormalized field is denoted by $\bar{\phi}$. Assuming that $\bar{\phi}$ stands for a bosonic field and d approaches 2, the canonical dimension for all vertices is $[\Gamma_k^{(n)}(x_1, \dots, x_n)] = 2$. A power-counting hierarchy of the terms breaks down such that the vertex truncation scheme is not suitable in this limit. Another scheme, which allows for arbitrary field dependence and we usually use in this work, is the derivative expansion. For a theory with a single scalar field $\bar{\phi}$, a starting point for a systematic expansion is given by

$$\Gamma_k[\bar{\phi}] = \int d^d x \left[\frac{1}{2} Z_{\phi,k} (\partial_\mu \bar{\phi})^2 + U_k(\bar{\phi}) \right], \quad (2.18)$$

where we have introduced the bosonic, effective potential U_k next to the wave function renormalization $Z_{\phi,k}$. Note that this example corresponds to the local potential approximation. We distinguish between $Z_{\phi,k} \equiv 1$ (LPA) and scale-dependent wave function renormalization (LPA') which is a compromise between LPA and the next-to-leading order in the derivative expansion (NLO). Within NLO, the full field dependence of all operators up to $\mathcal{O}(\partial^2)$, i.e., a field dependent $Z_{\phi,k}$, is taken into account. Employing next-to-next-to-leading order, higher

derivatives of the field are included. Also, if we have a scalar field with more than a single component, the structure of the momentum dependent part becomes more complex because there are two different modes entering the game, the Goldstone modes next to the radial mode.

Let us make some general remarks on the model (2.18) that is called Ising or O(1) model. The potential U_k is a function of $\bar{\rho} = \bar{\phi}^2/2$ rather than of $\bar{\phi}$. Thus, the model exhibits a \mathbb{Z}_2 symmetry in the field $\bar{\phi} \rightarrow -\bar{\phi}$. Taking the Ising model as an example, we compute the flow of the potential within the derivative expansion to leading order. It is given by projecting the right-hand-side of Eq. (2.13) onto constant fields [60],

$$\partial_t U_k = \frac{1}{2} \int \frac{d^d p}{(2\pi)^d} \frac{\partial_t R_k(p)}{Z_{\phi,k} p^2 + R_k(p) + U'_k(\bar{\rho}) + 2\bar{\rho} U''_k(\bar{\rho})}, \quad (2.19)$$

where the prime stands for the derivative with respect to the field invariant $\bar{\rho}$. For the dimensionless potential $u = k^{-d} U_k$ as a function of the dimensionless renormalized field $\rho = k^{2-d} \bar{\rho}_R = k^{2-d} \bar{\phi}_R^2/2 = Z_{\phi,k} k^{2-d} \bar{\phi}^2/2$, we obtain

$$\partial_t u = -du + (d-2 + \eta_\phi) \rho u' + \frac{1}{2} k^{-d} \int \frac{d^d p}{(2\pi)^d} \frac{\partial_t R_k(p)}{Z_{\phi,k} p^2 + R_k(p) + (u' + 2\rho u'') k^2}, \quad (2.20)$$

with the bosonic anomalous dimension

$$\eta_\phi = -\frac{\partial_t Z_{\phi,k}}{Z_{\phi,k}}. \quad (2.21)$$

Within LPA', the flow of $Z_{\phi,k}$ is typically evaluated at the minimum of the potential which approaches the vacuum expectation value (VEV) for $k \rightarrow 0$. For brevity, we refer to this running minimum also as VEV even for finite k . Although the potential u is still k -dependent, the subscript k at dimensionless quantities is suppressed for the sake of a compact notation. The first part of Eq. (2.20) corresponds to the canonical and anomalous scaling of u , the second part provides the quantum fluctuations. A common ansatz for solving Eq. (2.20) is given by a Taylor expansion,

$$u(\rho) = \sum_{n=0}^{N_p} \frac{\lambda_n}{n!} (\rho - \kappa)^n, \quad (2.22)$$

where κ as the expansion point is usually the flowing minimum of the potential. The flow of the potential (2.20) translates into the flow of the couplings $\beta_{\lambda_n} = \partial_t \lambda_n$ and the VEV $\beta_\kappa = \partial_t \kappa$. The beta functions can be derived by inserting Eq. (2.22) into Eq. (2.20) and projecting onto these couplings and the VEV. Although in many practical cases, Taylor expansions provide satisfying results, the reliability of the derived quantities is hard to control when the convergence radius shrinks or higher order field operators become important which is the case particularly for low dimensions $d \rightarrow 2$. Additionally, global statements cannot be made. Therefore, we will follow another ansatz, which is explained in the next chapter and

more advanced in the sense that the potential is not expanded at only one point but at a special grid employing a set of orthogonal basis functions.

Fluctuations can drive the system (2.18) into different regimes, the symmetric or the spontaneously broken regime. Depending on the IR behavior, we distinguish between the two corresponding phases. In the symmetric phase, the VEV vanishes whereas it is nontrivial in the spontaneously broken phase. There, the \mathbb{Z}_2 symmetry is broken close to the VEV. Thus, it serves as an order parameter whose value provides a clear criterion to distinguish both phases. In case of a field with N components with a nonvanishing VEV, we observe a massive radial mode and a number of massless Goldstone modes that corresponds to the $N - 1$ broken symmetry generators. The occurrence of Goldstone bosons [147–149] appears quite generally in the context of spontaneously broken continuous global symmetries.

The two phases are separated by a phase transition exhibiting critical behavior. Systems close to criticality are controlled by fixed points – scale invariant solutions of Eq. (2.13), e.g., solutions of the flow equation (2.20) setting the left-hand-side to zero. The flow close to the fixed points is governed by universal behavior which only depends on the long range degrees of freedom, symmetry and dimensionality of the model. That becomes visible in the suppression of irrelevant eigendirections in the vicinity of the fixed points, whereas relevant directions grow. These eigendirections δu and the corresponding critical exponents θ can be derived from the perturbed, linearized flow equation

$$-\theta \delta u = \sum_{n=0} \left. \frac{\partial(\partial_t u)}{\partial u^{(n)}} \right|_{u=u_*} \delta u^{(n)}. \quad (2.23)$$

Using Eq. (2.22), Eq. (2.23) reads in terms of the couplings λ_n

$$-\theta \delta \lambda_i = \sum_{n=0}^{N_p} \frac{\partial(\partial_t \lambda_i)}{\partial \lambda_n} \delta \lambda_n. \quad (2.24)$$

As the flow scales like $e^{-\theta t}$ in the direction δu , a positive sign of θ is assigned to a relevant and a negative sign to an irrelevant direction. In experiments, relevant directions have to be tuned in order to observe critical behavior. A fixed point is said to be stable, if only one parameter has to be tuned, i.e., there is only one $\theta > 0$.² The corresponding phase transition is of second order and is characterized by a continuous change of the order parameter. Otherwise, for unstable fixed points, the presence of additional relevant directions generally entails the discontinuous change of the order parameter between the phases which is a phase transition of first order.

The behavior of the Ising model close to criticality can be understood in terms of the

²We ignore the trivial exponent which is related to the zero point energy (“cosmological constant”) of the potential, cf. discussion below.

critical behavior of ferromagnets. Let us assume the following microscopic action at $k = \Lambda$,

$$u = \lambda_{2,\Lambda}(\rho - \kappa_\Lambda)^2. \quad (2.25)$$

The deviation from the phase transition given by $\delta\kappa_\Lambda$ can be interpreted as the deviation from the critical temperature $|\delta\kappa_\Lambda| \propto |T_c - T|$. Equation (2.3) gives a relation between the magnetic field, denoted by J , the temperature and the field $\bar{\phi}$ which corresponds to the magnetization of the ferromagnetic system. Close to the second order phase transition, $\delta\kappa_\Lambda$ and $\bar{\phi}$ completely describe the system at $k = 0$. Taking a proper rescaling into account, we find that the universal scaling function [4, 150, 151],

$$f(x) = \frac{\partial_{\bar{\phi}} U_{k=0}}{\bar{\phi}^\delta}, \quad x = \frac{-\delta\kappa_\Lambda}{\bar{\phi}^{1/\beta}}, \quad (2.26)$$

with the critical exponents δ and β , only depends on the Widom scaling variable x [152]. With these prerequisites, the scaling of thermodynamic quantities and relations between the corresponding critical exponents can be determined, see also [60, 153–155]. Close to the phase transition of second order, $\delta u_1 \approx \delta\kappa_\Lambda \neq 0$, we observe an exponential decay of the two-point correlation function

$$G(x; \delta u_1, \dots) \propto e^{-|x|/\xi}, \quad (2.27)$$

with the inverse decay rate ξ , which is the correlation length of the system. At the phase transition, fluctuations occur on any scale and ξ tends to infinity. The correlation function decays as a power law

$$G(x; \delta u_1 = 0, \dots) \propto \frac{1}{|x|^{d-2+\eta_\phi}}, \quad (2.28)$$

with the anomalous dimension introduced above. The divergence of ξ is described by the critical exponent ν ,

$$\xi = \bar{m}_R^{-1} \propto |\delta\kappa_\Lambda|^{-\nu} \quad \text{with} \quad \nu = \frac{1}{\theta_1}, \quad (2.29)$$

where $\theta_1 > 0$ is the largest critical exponent derived from Eq. (2.23). The correlation length is linked to the renormalized mass of the theory $\bar{m}_R = \bar{m}_{k=0}/Z_{\phi,k=0}$. Equivalently, the unrenormalized mass $\bar{m}_{k=0}^2$ which corresponds to the inverse susceptibility χ , obeys a simple scaling behavior,

$$\chi = \bar{m}^{-2} \propto |\delta\kappa_\Lambda|^{-\gamma}, \quad (2.30)$$

with γ fulfilling the scaling relation $\gamma = \nu(2 - \eta_\phi)$. The external source vanishes at the minimum of the potential which corresponds to the situation of a vanishing magnetic field. For the unrenormalized VEV $\bar{\phi}_0$, it can then be shown that

$$\langle \varphi(x) \rangle_{J=0} = \bar{\phi}_0 \propto \delta\kappa_\Lambda^\beta. \quad (2.31)$$

The critical exponent β satisfies $\beta = \nu(d - 2 + \eta_\phi)/2$. Similarly, we can study the system at the critical temperature, $\delta\kappa_\Lambda = 0$, but at nonvanishing source and find

$$\langle\varphi(x)\rangle_J \propto |J|^{1/\delta} \text{sgn } J, \quad (2.32)$$

with the scaling relation $\delta = (d + 2 - \eta_\phi)/(d - 2 + \eta_\phi)$.

In case of an additional relevant parameter a third scale is introduced in our system that exhibits a phase transition of first order then. For instance, this new scale is the jump of the order parameter at the transition. Note that also the correlation length jumps. In [4], it was stated that also in the case of a bosonic system close to a weak first order phase transition, a universal scaling function can be found which depends on two instead of only one scaling variables.

Besides continuous and discontinuous phase transitions, there is another special kind of phase transition in two dimensional systems, the BKT phase transition. In terms of the O(2) nonlinear σ -model, the two topological phases are related to the unbinding and binding of vortices [156, 157]. Vortices correspond to singular points of circulating field configurations. For low temperatures, true long-range order is avoided by thermal fluctuations. Nevertheless, the two phases can be identified from the behavior of the correlation length. Whereas the correlation length is finite in the high temperature phase, it diverges for low temperatures. There, the correlation function G decays as a power law with increasing distance, similar to Eq. (2.28), but the critical exponent η_ϕ continuously depends on the temperature now. Instead of isolated fixed points, the β functions vanish on a line of fixed points. In terms of the FRG, the O(2) linear σ -model in $d = 2$ provides an effective description for the behavior at a BKT phase transition without introducing vortices [82, 158–160]. In fact, there is a close correspondence between the linear and the nonlinear σ -model as both phase transitions lie in the same universality class [158]. Experimentally, the BKT phase transition was observed, e.g., in liquid-helium films [161, 162] and atomic gases [163–166].

We close this review with a short comment on systems with two order parameters which play a role in Sec. 4.2. The two order parameters can receive finite values independently from each other corresponding to different phases. In comparison with the Ising model, the phase diagram is more complex due to several phase transition lines which can be of first or second order. We are interested in the case where these lines meet at a multicritical fixed point. The details of the phase diagram depend on the properties of the bosonic fixed-point potential. Stable fixed points now have two relevant directions because of the two order parameters. Similar to systems with one order parameter, each fixed point provides a universality class with universal critical exponents.

2.4. Introduction to the models

In this work, we mainly consider two classes of models: the purely bosonic $O(N)$ model and a simple Yukawa model including fermionic degrees of freedom. Note that the Yukawa model can be understood as arising from partial bosonization of the Gross-Neveu model with only fermionic fields. Because of their comparatively simple structure, both models have great importance in understanding general aspects of quantum physical systems, which, however, are by no means simple in their nature. Their role in the investigation of technical as well as physical aspects is undeniable. For instance, both models give rise to nontrivial fixed points below $d = 4$, and they reveal a complex structure of multicritical fixed points for $d \rightarrow 2$ [69, 167, 168]. In the context of one order parameter, “multicritical fixed points” are not to be confused with multicritical points arising in models with two order parameters. Their significant relevance for physical systems range from electroweak physics over QCD to condensed matter systems. Scalar field theories for example may serve as toy models to investigate the properties of phase transitions occurring in these systems [169]. The electrons close to the K -point in graphene can be effectively described by massless Dirac fermions in $d = 3$, see, e.g., [170–172]. For $d \rightarrow 4$, the Yukawa model as a simplified quark-meson model allows for the investigation of the chiral phase transition, cf. [168]. Furthermore, in $d = 4$, it can be seen as a reduction of the standard model to the most important degrees of freedom regarding Higgs-top interactions [53, 141, 173, 174]. In Sec. 5.3, we employ this model to particularly study the lower mass bound of the Higgs boson. Finally, the Yukawa model serves as a toy model for exploring asymptotic safety in $d = 3$ [73].

In Sec. 4.2, we consider a system of two competing order parameters, characterized by an $O(N)$ and $O(M)$ symmetry. As a function of two external parameters, the separate symmetries may be broken spontaneously. A multicritical fixed point determines the phase diagram of the $O(N) \oplus O(M)$ model. Examples for systems described by two order parameters are anisotropic antiferromagnets in an external magnetic field, with $N = 1$, $M = 2$ [8, 9, 26–31], models of high- T_c superconductors [10, 11, 34–36], as well as graphene [13, 37, 38].

Let us start with the $O(N)$ model with an arbitrary number of components of the bosonic field $\bar{\phi}$. For $N = 1$, which corresponds to the Ising model, a short discussion of the effective action and its flow has been given above. More generally, the ansatz of the effective average action within LPA' reads

$$\Gamma_k[\bar{\phi}] = \int d^d x \left\{ \frac{1}{2} Z_{\phi,k} (\partial_\mu \bar{\phi}^a) (\partial_\mu \bar{\phi}^a) + U_k \left(\frac{\bar{\phi}^a \bar{\phi}^a}{2} \right) \right\}, \quad (2.33)$$

where the sum over $a = 1, \dots, N$ is understood implicitly. Due to the symmetry, the flow of the potential and the wave function renormalization can be written in terms of the field invariant $\bar{\rho} = \bar{\phi}^a \bar{\phi}^a / 2$. If $\bar{\phi}$ acquires a nonvanishing VEV, the $O(N)$ symmetry is broken to an $O(N - 1)$ symmetry, where the field consists of one radial and $N - 1$ Goldstone modes.

In principle, most of the information of interest for us is contained in the first derivative of the potential u' with respect to the field invariant. Thus, we investigate the flow of u' in most cases. The potential can be obtained by an integration then. In $d > 1$, the integration constant corresponds to the cosmological constant which, however, does not play a role in this work. By contrast, it has a meaningful interpretation in quantum mechanics ($d = 1$) as it yields the ground state energy of the system, cf. Sec. 5.2. In this case, we compute it from the flow of u' at the VEV. Here, we give the flow equation for the potential, which reads, [60],

$$\partial_t u = -du + (d - 2 + \eta_\phi)\rho u' + 2v_d l_0^{(B)d}(u' + 2\rho u''; \eta_\phi) + 2v_d(N - 1)l_0^{(B)d}(u'; \eta_\phi), \quad (2.34)$$

or for the first derivative

$$\begin{aligned} \partial_t u' = & (-2 + \eta_\phi)u' + (d - 2 + \eta_\phi)\rho u'' - 2v_d(3u'' + 2\rho u''')l_1^{(B)d}(u' + 2\rho u''; \eta_\phi) \\ & - 2v_d(N - 1)u''l_1^{(B)d}(u'; \eta_\phi). \end{aligned} \quad (2.35)$$

The anomalous dimension,

$$\eta_\phi = \frac{16v_d}{d} \kappa u''^2 m_2^{(B)d}(u' + 2\kappa u''; \eta_\phi), \quad (2.36)$$

is evaluated at the VEV, $\rho = \kappa$. Here, we have introduced $v_d^{-1} := 2^{d+1}\pi^{d/2}\Gamma(d/2)$ and the threshold functions $l_n^{(B)d}$ and $m_2^{(B)d}$ which contain all information about the regulator, see App. A for their definition. Note that the equation for the anomalous dimension gives rise to some confusion for $N = 1$. Although Eq. (2.36) corresponds to the Goldstone anomalous dimension, in comparison with the anomalous dimension of the radial mode, it provides superior results. In this work, we especially focus on the $N = 1, 4$ and large N case. In the limit $N \rightarrow \infty$, only the Goldstone contributions (leading order in N) and the dimensional scaling terms survive. The flow of the wave function renormalization vanishes. In this limit, an analytical implicit solution can be computed by the method of characteristics [175]. Additionally, there exists an exact solution for $N = 1$ in $d = 1$ [176] as well as $d = 2$ [177].

We can add fermionic degrees of freedom to the $O(N)$ model. Generally, the fermionic field ψ consist of N_f flavors whereas we now take only one bosonic field into account. The Yukawa model with the effective average action

$$\Gamma_k[\bar{\psi}, \psi, \bar{\phi}] = \int d^d x \left\{ \bar{\psi}(Z_{\psi,k} i \not{\partial} + i \bar{h}_k \bar{\phi}) \psi + \frac{1}{2} Z_{\phi,k} (\partial_\mu \bar{\phi})^2 + U \left(\frac{\bar{\phi}^2}{2} \right) \right\}. \quad (2.37)$$

features a discrete chiral symmetry

$$\psi \mapsto i\gamma_5 \psi, \quad \bar{\psi} \mapsto i\bar{\psi}\gamma_5, \quad \bar{\phi} \mapsto -\bar{\phi}. \quad (2.38)$$

The 4×4 matrix γ_5 anticommutes with the Dirac matrices of the $d_\gamma = 4$ representation of the Dirac algebra,

$$\{\gamma_\mu, \gamma_\nu\} = 2\delta_{\mu\nu}\mathbb{1}_4, \quad (2.39)$$

and furthermore fulfills $\gamma_5^2 = 1$. As this representation is reducible in $d = 3$, we can find an additional matrix entailing additional continuous symmetries [73]. These shall not be of interest here.

The flow of the scalar potential and its first derivative in this Yukawa model are given by, [53],

$$\partial_t u = -du + (d - 2 + \eta_\phi)\rho u' + 2v_d \left[l_0^{(\text{B})d} (u' + 2\rho u''; \eta_\phi) - d_\gamma N_f l_0^{(\text{F})d} (2\rho h^2; \eta_\psi) \right], \quad (2.40)$$

or

$$\begin{aligned} \partial_t u' = & (-2 + \eta)u' + (d - 2 + \eta)\rho u'' - 2v_d(3u'' + 2\rho u''')l_1^{(\text{B})d}(u' + 2\rho u''; \eta_\phi) \\ & + 4v_d d_\gamma N_f h^2 l_1^{(\text{F})d}(2\rho h^2; \eta_\phi), \end{aligned} \quad (2.41)$$

respectively. As for the $O(N)$ model, we solve Eq. (2.41) for practical reasons. The Yukawa coupling provides the interaction between the fermions and the bosons and is assumed to be field independent, see [168, 178] for field dependent studies. The flow equation for the dimensionless renormalized Yukawa coupling, $h^2 = Z_{\phi,k}^{-1} Z_{\psi,k}^{-2} k^{d-4} \bar{h}^2$, reads

$$\begin{aligned} \partial_t h^2 = & [\eta_\phi + 2\eta_\psi + d - 4] h^2 + 8v_d h^4 \left[l_{1,1}^{(\text{FB})d} (2h^2 \kappa, u' + 2\kappa u''; \eta_\psi, \eta_\phi) \right. \\ & - (6\kappa u'' + 4\kappa^2 u''') l_{1,2}^{(\text{FB})d} (2h^2 \kappa, u' + 2\kappa u''; \eta_\psi, \eta_\phi) \\ & \left. - 4h^2 \kappa l_{2,1}^{(\text{FB})d} (2h^2 \kappa, u' + 2\kappa u''; \eta_\psi, \eta_\phi) \right] \end{aligned} \quad (2.42)$$

and is evaluated at the potential's running minimum. The bosonic and fermionic anomalous dimensions are

$$\begin{aligned} \eta_\phi = & \frac{8v_d}{d} \left[\kappa [3u'' + 2\kappa u''']^2 m_4^{(\text{B})d} (u' + 2\kappa u''; \eta_\phi) \right. \\ & \left. + d_\gamma h^2 N_f \left[m_4^{(\text{F})d} (2h^2 \kappa; \eta_\psi) - 2h^2 \kappa m_2^{(\text{F})d} (2h^2 \kappa; \eta_\psi) \right] \right], \end{aligned} \quad (2.43)$$

$$\eta_\psi = \frac{8v_d}{d} h^2 m_{1,2}^{(\text{FB})d} (2h^2 \kappa, u' + 2\kappa u''; \eta_\psi, \eta_\phi), \quad (2.44)$$

which are again computed at the minimum. In contrast to the $O(N)$ model, we use the anomalous dimension of the radial mode here, which is actually the correct one for $N = 1$. In Sec. 4.1, we solve the fixed point equation as a function of the parameter N_f . We are also interested in the large N_f limit for which the system has an analytical solution [73]. Employing a proper rescaling, only the fermionic fluctuations contribute to the flow. The

evolution of h^2 even reduces to its dimensional scaling, whereas the fermionic anomalous dimension vanishes.

Let us now consider the combination of an $O(N)$ with an $O(M)$ model which has two competing order parameters and exhibits an $O(N) \oplus O(M)$ symmetry. The vector valued fields $\bar{\phi}^a$ ($a = 1, \dots, N$) and $\bar{\chi}^b$ ($b = 1, \dots, M$) parametrize the $O(N)$ and $O(M)$ symmetry, respectively. If $\bar{\phi}$ acquires a nonvanishing VEV, the $O(N)$ symmetry is broken spontaneously to an $O(N - 1)$ symmetry, and accordingly for $\bar{\chi}$. The corresponding invariants read

$$\bar{\rho}_\phi = \frac{\bar{\phi}^a \bar{\phi}^a}{2} \quad \text{and} \quad \bar{\rho}_\chi = \frac{\bar{\chi}^b \bar{\chi}^b}{2}. \quad (2.45)$$

The potential of the effective average action,

$$\Gamma_k[\bar{\phi}, \bar{\chi}] = \int d^d x \left\{ \frac{Z_{\phi,k}}{2} \partial_\mu \bar{\phi}^a \partial_\mu \bar{\phi}^a + \frac{Z_{\chi,k}}{2} \partial_\mu \bar{\chi}^b \partial_\mu \bar{\chi}^b + U_k \left(\frac{\bar{\phi}^a \bar{\phi}^a}{2}, \frac{\bar{\chi}^b \bar{\chi}^b}{2} \right) \right\}, \quad (2.46)$$

depends on both these invariants. The dimensionless renormalized fields are given by $\rho_\phi = Z_{\phi,k} \bar{\rho}_\phi k^{2-d}$, $\rho_\chi = Z_{\chi,k} \bar{\rho}_\chi k^{2-d}$. Derivatives of the potential are denoted by the shorthand

$$\frac{\delta^{n_1}}{\delta \rho_\phi^{n_1}} \frac{\delta^{n_2}}{\delta \rho_\chi^{n_2}} u(\rho_\phi, \rho_\chi) = u^{(n_1, n_2)}(\rho_\phi, \rho_\chi). \quad (2.47)$$

In the case of two order parameters, it is convenient to consider the potential u rather than derivatives of it, since we would have to consider the derivative in both field directions. The flow of the potential yields, [22],

$$\begin{aligned} \partial_t u = & -du + (d - 2 + \eta_\phi) \rho_\phi u^{(1,0)} + (d - 2 + \eta_\chi) \rho_\chi u^{(0,1)} \\ & + 2v_d \left[l_{R,0}^{(B)d}(\omega_\phi, \omega_\chi, \omega_{\phi\chi}; \eta_\phi, \eta_\chi) + (N - 1) l_0^{(B)d}(u^{(1,0)}; \eta_\phi) \right. \\ & \left. + (M - 1) l_0^{(B)d}(u^{(0,1)}; \eta_\chi) \right]. \end{aligned} \quad (2.48)$$

The arguments of the threshold function $l_{R,0}^{(B)d}$ read

$$\omega_\phi = u^{(1,0)} + 2\rho_\phi u^{(2,0)}, \quad (2.49)$$

$$\omega_\chi = u^{(0,1)} + 2\rho_\chi u^{(0,2)}, \quad (2.50)$$

$$\omega_{\phi\chi} = 4\rho_\phi \rho_\chi (u^{(1,1)})^2. \quad (2.51)$$

The flow of the wave function renormalizations is given by the corresponding anomalous

dimensions, [179],

$$\eta_\phi = \frac{16v_d}{d} \left[(u^{(2,0)})^2 \kappa_\phi (1 + u^{(0,1)} + 2u^{(0,2)} \kappa_\chi)^2 - 4u^{(2,0)} (u^{(1,1)})^2 \kappa_\chi \kappa_\phi (1 + u^{(0,1)} + 2u^{(0,2)} \kappa_\chi) \right. \\ \left. + (u^{(1,1)})^2 \kappa_\chi (1 + 2u^{(1,0)} + (u^{(1,0)})^2 + 4(u^{(1,1)})^2 \kappa_\chi \kappa_\phi) \right] \times \quad (2.52)$$

$$\times \left[(1 + u^{(1,0)})(1 + u^{(0,1)} + 2u^{(0,2)} \kappa_\chi)(1 + u^{(1,0)} + 2u^{(2,0)} \kappa_\phi) - 4(u^{(1,1)})^2 \kappa_\phi \kappa_\chi \right]^{-2}, \\ \eta_\chi = \eta_\phi \{ \phi \leftrightarrow \chi, u^{(i,j)} \leftrightarrow u^{(j,i)} \}, \quad (2.53)$$

where $(\kappa_\phi, \kappa_\chi)$ is the position of the nontrivial minimum in both field directions.

3. Pseudo-spectral methods

This chapter gives an overview over the properties of pseudo-spectral expansions, their convergence and how these methods are applied to flow equations. In the first section, we compare pseudo-spectral expansions to other numerical methods and elucidate their advantages. Afterwards, the different kinds of convergence are introduced and shortly discussed. Finally, we describe the implementation of pseudo-spectral methods for solving systems of nonlinear differential equations. For a detailed presentation of this topic, we refer the reader to [108, 180–182].

3.1. Pseudo-spectral expansions

Let us consider a smooth function $f : [a, b] \rightarrow \mathbb{R}$. This function could be, e.g., the unknown solution of a differential equation with the nonlinear differential operator \mathcal{L}

$$\mathcal{L}f(x) = 0, \quad (3.1)$$

which shall be solved numerically at a set of grid points $\{x_n\}_{n=0}^{N_p}$. Therefore, we search for approximations of $f(x_n)$ and its derivatives. There are several approximation schemes, such as finite elements, finite differences and (pseudo-)spectral methods. For the latter, $f(x)$ is expanded as

$$f(x) \approx \sum_{n=0}^{N_p} a_n \Omega_n(x), \quad (3.2)$$

where $\{\Omega_n(x)\}_{n=0}^{N_p}$ is a set of orthogonal basis functions and N_p the interpolation order of the expansion which in comparison with finite elements or finite difference methods, is usually high. In contrast to these methods, the basis functions $\Omega_n(x)$ are nonzero on the whole interval $[a, b]$ except at some points. For finite elements or differences, only locally nonvanishing functions or sequences of overlapping polynomials of fixed degree are employed, respectively.

In order to solve Eq. (3.1), the residual function $R(x; a_0, \dots, a_{N_p}) = \mathcal{L}f(x)$ must be minimized in dependence on the coefficients. We use the collocation method where $R = 0$ is required at $\{x_n\}_{n=0}^{N_p}$ which are called collocation points. The Galerkin method provides an alternative criterion

$$r_n = (R, \Omega_n) = 0, \quad n = 0, 1, \dots, N_p, \quad (3.3)$$

where the bilinear operator (\cdot, \cdot) is the inner product with respect to the weight $w(x)$ of the orthogonality condition of the $\{\Omega_n(x)\}_{n=0}^{N_p}$. Under the assumption that the collocation points are carefully chosen, cf. discussion below, both methods are identical if Gaussian quadrature is employed for evaluating the inner products. Note that the number of the grid points is equal to the number of the coefficients. The function values $f(x_n)$ depend on the a_n via a linear map and vice versa and can, therefore, be used instead of the coefficients. The connection between the interpolation order of the expansion and the number of coefficients has a remarkable benefit: if N_p is increased, the approximation error is lowered not only due to the increasing order but also due to the decreasing distance between the grid points, $\epsilon \sim \mathcal{O}[(1/N_p)^{N_p}]$. This entails that we already obtain comparatively high accuracy for comparatively small N_p . In this sense, spectral methods are memory-minimizing in contrast to finite elements or differences. Of course, there is also a price to pay: As the basis functions $\Omega_n(x)$ do not vanish on the whole interval, the matrices, e.g., differential matrices we have to deal with, are usually dense. Therefore, it may be advantageous to use a hybrid of spectral methods and finite elements which is called *spectral elements*. We come back to this in the last section.

Employing Eq. (3.2), we ask for a suitable choice of basis functions $\Omega_n(x)$. If the domain of $f(x)$ is $[0, \infty)$, the Hermite or Laguerre polynomials appear to be natural choices because they are also defined on an unbounded interval [183–186]. However, increasing the interpolation order changes the asymptotic behavior. For the problems usually encountered, the asymptotic behavior is fixed and thus the convergence properties of Hermite and Laguerre polynomials are difficult to control. In this work, we employ Chebyshev polynomials of the first kind defined on $[-1, 1]$,

$$T_n(\cos(x)) = \cos(nx), \quad n \in \mathbb{N}_0 \quad (3.4)$$

which satisfy the orthogonality condition

$$\int_{-1}^1 T_n(x)T_m(x) \frac{dx}{\sqrt{1-x^2}} = \begin{cases} 0, & n \neq m \\ \pi, & n = m = 0 \\ \pi/2, & n = m \neq 0, \end{cases} \quad (3.5)$$

with $w(x) = \sqrt{1-x^2}^{-1}$. Legendre polynomials which are defined on a bounded interval as well, are also considered as a possible set of basis functions [187, 188]. However, Chebyshev polynomials generally show slightly better convergence properties [189]. Note that they are closely related to the Fourier basis functions which actually differ only by a transformation in the argument. Therefore, Chebyshev series inherit many properties from Fourier series, such as convergence properties. Nevertheless, no conditions of periodicity are imposed on $f(x)$.

For the choice of grid points, there are four different types [190], the *Lobatto* grid,

$$x_n = -\cos\left(\frac{\pi n}{N_p}\right), \quad n = 0, 1, \dots, N_p, \quad (3.6)$$

the *Gauss* grid,

$$x_n = -\cos\left(\frac{\pi\left(n + \frac{1}{2}\right)}{N_p + 1}\right), \quad n = 0, 1, \dots, N_p, \quad (3.7)$$

and right-sided or left-sided *Radau* grid,

$$x_n = \cos\left(\frac{2\pi(N_p - n)}{2N_p + 1}\right), \quad \text{or} \quad x_n = -\cos\left(\frac{2\pi n}{2N_p + 1}\right), \quad n = 0, 1, \dots, N_p. \quad (3.8)$$

The points correspond to the nodes or extrema of Chebyshev polynomials. Due to their nonequidistant distribution – there are more points at the end of the interval than in the middle – the Runge phenomenon is avoided. More generally, choosing these grid points is the key to obtain an optimal interpolation of the function $f(x)$.

3.2. Convergence properties

By Darboux's principle, the rate and domain of convergence of Eq. (3.2) in the complex plane is controlled by the location and strength of the singularities of $f(x)$. This includes poles, fractional powers, logarithms, branch cuts and discontinuities. For Taylor series for instance, the shape of the convergence domain is a disc around the expansion point. Although $f(x)$ might have singularities exclusively on the imaginary axis, the range of convergence on the real axis is equal to their distance from the expansion point. By contrast, the convergence domain of a Chebyshev series is the interior of an ellipse with foci ± 1 . This guarantees convergence on $[-1, 1]$ regardless of the position of the singularities unless they are not exactly in the interval $[-1, 1]$.

To determine the order of convergence, we introduce the algebraic index which is the largest real number $q > 0$ satisfying

$$\lim_{n \rightarrow \infty} |a_n| n^q < \infty. \quad (3.9)$$

If q is finite, the convergence is called to be algebraic and the absolute value of the coefficients decays asymptotically as $\sim \mathcal{O}(1/n^q)$. For an unbounded q , it decreases faster than any power of n which is called exponential convergence $\sim \mathcal{O}(e^{-sn^r})$ with positive real numbers s, r .

The rate of exponential convergence is defined as

$$\lim_{n \rightarrow \infty} \frac{|\ln(|a_n|)|}{n} = \begin{cases} \infty, & \text{supergeometric} \\ \text{const}, & \text{geometric} \\ 0, & \text{subgeometric.} \end{cases} \quad (3.10)$$

If the coefficients oscillate, the rate of convergence is determined by the envelope of the spectral coefficients. We point out that convergence can only be read off from the asymptotic behavior of the coefficients. However in practical applications, it may be spoiled by a “roundoff plateau” due to the limited machine precision.

For the accuracy of an approximation, three different types of errors are important to control: The truncation error originates from the negligence of the coefficients $n > N_p$. The discretization error is the deviation of the truncated series from the expansion of the exact solution up to order N_p . Finally, the interpolation error comes from the approximation of a function to agree with the exact one at only a finite number of collocation points. As the exact solution is usually not known, the last two errors can be hardly estimated. Therefore, the assumption of equal errors is commonly applied that states that all errors are of the same order of magnitude and, thus, the truncation error can be taken as a representative for the overall error. For practical purposes, the last coefficient provides a rough estimate for the truncation error,

$$\left| f(x) - \sum_{n=0}^{N_p} a_n T_n(x) \right| \leq \sum_{n=N_p+1}^{\infty} |a_n| = \sum_{n=N_p+1}^{\infty} (e^{-s})^n = \frac{(e^{-s})^{N_p+1}}{1 - e^{-s}} \sim \mathcal{O}(|a_{N_p}|), \quad (3.11)$$

in case of geometrically exponential convergence, and

$$\left| f(x) - \sum_{n=0}^{N_p} a_n T_n(x) \right| \leq \sum_{n=N_p+1}^{\infty} |a_n| = \sum_{n=N_p+1}^{\infty} \frac{1}{n^q} \sim \frac{1}{(q-1)N_p^{q-1}} \sim \mathcal{O}(N_p |a_{N_p}|), \quad (3.12)$$

for algebraic convergence.

3.3. Implementation

In this work, we have to deal with ordinary differential equations (ODEs), such as fixed-point equations in Sec. 4.1 and partial differential equations (PDEs), i.e., fixed-point equations with more than one field invariant, see Sec. 4.2, and functional flows in Chap. 5. In case of more than one variable, e.g., $f = f(x, y)$, we expand the function as a tensor product,

$$f(x, y) = \sum_{i=0}^{N_p^x} a_i(y) T_i(x) = \sum_{i=0}^{N_p^x} \sum_{j=0}^{N_p^y} a_{ij} T_i(x) T_j(y). \quad (3.13)$$

Besides the field direction x , the second variable is either the RG scale or a second field invariant. Of course, the arguments x and y do not necessarily correspond to the physical variables of our problems. In what follows, we assume that there exists a linear, invertible map between the domain of definition of the physical variables and the arguments of the Chebyshev functions.

A fast way of evaluating the sum of Chebyshev polynomials is given by the Clenshaw algorithm [191],

$$\begin{aligned} b_{N_p+2} &= b_{N_p+1} = 0, \\ b_i &= a_i + 2xb_{i+1} - b_{i+2}, \\ f(x) &= a_0 + xb_1 - b_2. \end{aligned} \tag{3.14}$$

The derivative of f can again be expanded in a sum of Chebyshev polynomials of degree $N_p - 1$ with coefficients

$$\begin{aligned} a'_{N_p-1} &= 2N_p a_{N_p}, \\ a'_{N_p-2} &= 2(N_p - 1)a_{N_p-1}, \\ a'_i &= 2(i + 1)a_{i+1} + a'_{i+2} \\ a'_0 &= a_1 + \frac{1}{2}a'_2. \end{aligned} \tag{3.15}$$

Due to the recursive nature of these high-performance algorithms, they are numerically stable.

Regarding the differential equation (3.1), we now know how to discretize the system and how to compute derivatives. To obtain a solution, we evaluate the system (3.1) at the grid points and require $R(x_i; a_0, \dots, a_{N_p}) = 0$ at every point as a function of the coefficients $\{a_i\}_{n=0}^{N_p}$. This leaves us with an algebraic equation which we solve by a stabilized Newton-Raphson iteration where the Jacobian,

$$J_{ij} = \frac{\partial \mathcal{L}f(x_i)}{\partial a_j}, \tag{3.16}$$

must be inverted. This matrix is usually dense and, depending on the size, iterative solvers have to be used. In order to obtain a Jacobian which is more sparse, it may be convenient to use the spectral elements method. There, the domain of f is divided into subdomains on which f is expanded in Chebyshev series separately. Note that the number of subdomains cannot be arbitrarily large. For each expansion on a subdomain, less coefficients are taken into account, otherwise the efficiency would not increase. Hence, the more subdomains are used the less coefficients each expansion contains. However, for the number of coefficients falling below a certain limit, the convergence of the expansions is spoiled. We emphasize that the number of subdomains which we use is chosen due to practical convenience. Furthermore,

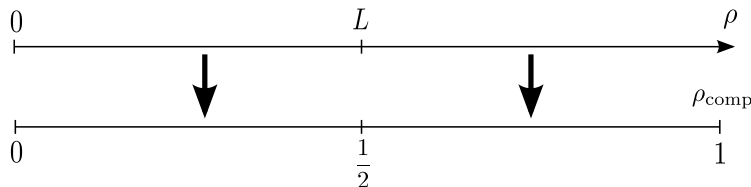


Fig. 3.1.: The role of the parameter L in the field compactification (3.17).

using multiple domains has another advantage going beyond considerations of speed and efficiency. Assuming f is only piecewise analytical, we can improve the convergence of the coefficients if the border of two domains is as close as possible to the singular point. At the boundaries of the patches, we impose matching conditions for the function and its derivatives. In particular, for a differential equation of order q , $q - 1$ derivatives and the function itself have to be matched. For each matching condition, we employ additional coefficients which actually conflicts the one-to-one mapping between grid points and coefficients assumed in the previous sections. At the collocation points, we exclusively require the fulfillment of the differential equation (3.1). Another less problematic possibility is to demand the matching conditions on grid points instead of the fulfillment of the equation. However, we emphasize that we did not encounter a worse convergence or stability problems arising from this. In this sense, we usually employ the Gauss- or Radau grid. As these types of collocation points do not include any or only one boundary, a potential overdetermination by imposing too many conditions at one point does not occur.

In this work, the function f is the effective average potential u or its derivative which depends on one or two field invariants and the RG scale k . The operator \mathcal{L} corresponds to a differential operator such as given in Eq. (2.20). In addition, we may have to deal with RG time dependent but field independent quantities, e.g., anomalous dimensions or the Yukawa coupling in a fermionic system, cf. Sec. 2.4. We emphasize that this method is also adapted for systems of differential equations. In some cases, we are interested in the global behavior of the potential in field space. For this purpose, we use the compactification

$$u_{\text{comp}}^{(\prime)} = \frac{u^{(\prime)}}{\rho^\alpha} \quad \text{and} \quad \rho_{\text{comp}} = \frac{\rho}{\rho + L} \quad (3.17)$$

for the potential or its derivative $u^{(\prime)}$ with the asymptotic behavior $\propto \rho^\alpha$ and for the field, respectively, with the free parameter $L > 0$. We employ the compactification of the derivative of the potential u'_{comp} only in Sec. 4.1 for the outermost subdomain. We emphasize that the compactification is well defined in this case. The compactification in the field can be applied only to the outer subdomain, cf. Sec. 4.1, or all subdomains, cf. Sec. 5.2. Figure 3.1 shows how L influences the map of the field range $[0, \infty)$ onto $[0, 1]$. For the discussion of particular choices, see Sec. 4.1. More details about compactifications using pseudo-spectral methods can be found in App. B and in [192–195].

In case of functional flows, where the potential is a function of one field invariant and

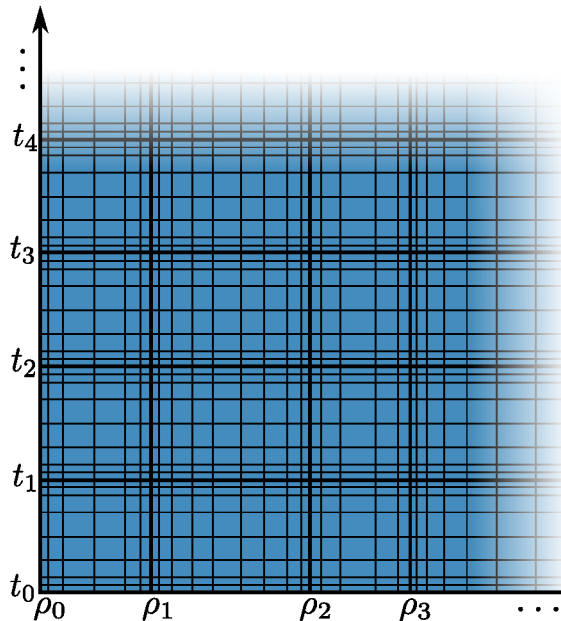


Fig. 3.2.: Sketch of the decomposition of the whole domain into subdomains. The t_i and ρ_i denote the boundaries of the subdomains in t and ρ direction, respectively. For each subdomain, an own expansion of u' is used. The thin grid lines depict the Chebyshev grid for each subdomain.

the RG time, not the potential itself but its first derivative u' is evolved [123, 196]. This flow is more stable as it is not affected by the fast growing cosmological constant. For the time direction, an “ordinary” ODE solver, such as Runge-Kutta, could actually be used. They efficiently evolve forward in time, but for problems close to singular points, e.g., if convexity mechanisms occur (cf. Sec. 5.1), implicit methods have to be employed which are more involved and slower. We apply pseudo-spectral methods also in time direction, in order to achieve high accuracy and to control the error which can best be done in this way. In Sec. 5.3, we see that this is especially important for fine-tuning problems and flows over many orders of magnitude to obtain reliable results. To increase the efficiency, we divide the RG time interval into small patches which is illustrated in Fig. 3.2. The PDE is solved simultaneously on all subdomains in field direction of a specific slice $t \in [t_i, t_{i+1}]$. Imposing the initial condition on the first slice and continuity on the following slices leads to an initial value problem on every time patch.

All numerical results presented in this work are obtained with a C++ code, using the libraries BOOST [197], Eigen [198] and Blitz [199] and the data types `long double` and `float128`, the latter giving twice as many digits as the conventional double data type.

4. Solving functional fixed-point equations via pseudo-spectral methods

In the first chapter, we have argued that scale invariant solutions are of physical relevance in many aspects, such as critical phenomena. There is a number of well-established methods to solve fixed-point equations. Employing Taylor expansions, for instance, yields local solutions with a finite convergence radius. As we see in this chapter, the convergence of Taylor expansions may be spoiled in some cases and, therefore, the results become unreliable. To obtain fixed-point potentials on a larger domain, the shooting method can be used. A parameter of the potential is tuned such that the integration of the potential remains stable over a large field range. However, this method is very intricate for systems with a number of additional couplings, e.g., Yukawa couplings, and anomalous dimensions, or with more than one order parameter.

The first part of this chapter demonstrates the power of pseudo-spectral methods by constructing global solutions of FRG equations in field space to high accuracy with a comparatively small amount of effort. Our approach is benchmarked using the critical behavior of the Ising model, providing results for the global fixed-point potential as well as leading critical exponents and their respective global eigenfunctions in $d = 3$. We also compare to the analytical solution of a three-dimensional simple Yukawa model for large flavor numbers. Where local expansions break down, we nevertheless provide new results for multicritical scaling solutions of the Ising model in $d \leq 3$ and the Yukawa model for small flavor numbers due to the superior convergence properties of pseudo-spectral methods.

In the second part of this chapter, we explore universal critical behavior in models with two competing order parameters, and an $O(N) \oplus O(M)$ symmetry for dimensions $2 < d \leq 3$. There is a complex interplay between different universality classes. For the first time of our knowledge, coexisting stable fixed points are found and discussed in a bosonic model. Also in the two field case, pseudo-spectral methods are an efficient tool to give reliable results. As far as we know, there is no comparable method for solving the FRG fixed-point equations which also works well for the low dimensional case.

This chapter follows the line of argument of [137, 138] in the first part and [139] in the second part.

4.1. Fixed-point equations of \mathbb{Z}_2 symmetric models with one order parameter

For the following examples, a few technical remarks are in order: We decompose the space of the field invariant ρ into two subdomains $[0, \rho_1]$ and $[\rho_1, \infty)$, where the matching point ρ_1 is chosen appropriately, see below. In the first subdomain, the derivative of the fixed-point potential itself is interpolated, whereas we use the compactification (3.17) in the second subdomain to capture its global behavior. In order to map the field values $[\rho_1, \infty)$ onto $[0, 1]$, ρ has to be shifted by ρ_1 in the field compactification. The distribution of the grid points over the second subdomain is affected by the choice of the parameter L . The order of the asymptotic behavior denoted by α in Eq. (3.17) can be easily derived from the dimensional scaling terms of the fixed-point equations.

4.1.1. The Ising model near criticality

This section is devoted to a detailed study of various properties of the Ising model with the effective average action (2.33). Here, we solve the fixed-point equation (2.35) for the first derivative of the potential, setting $N = 1$ and the left-hand-side to zero. The potential can be easily derived from it by integration. The anomalous dimension, if taken into account, is given by Eq. (2.36).

Wilson-Fisher fixed point in LPA and LPA'

In the following, we compare the Wilson-Fisher solution in LPA ($\eta_\phi = 0$), and in LPA', where we include the anomalous dimension. As numerical parameters, $\rho_1 = 3/10$ and $L = 1$ were chosen, and we used `float128`. From Eq. (2.35), one infers the leading asymptotic behavior $u'_\infty(\rho) \propto \rho^{(2-\eta_\phi)/(d-2+\eta_\phi)}$ as the quantum fluctuations contribute only to subleading order.

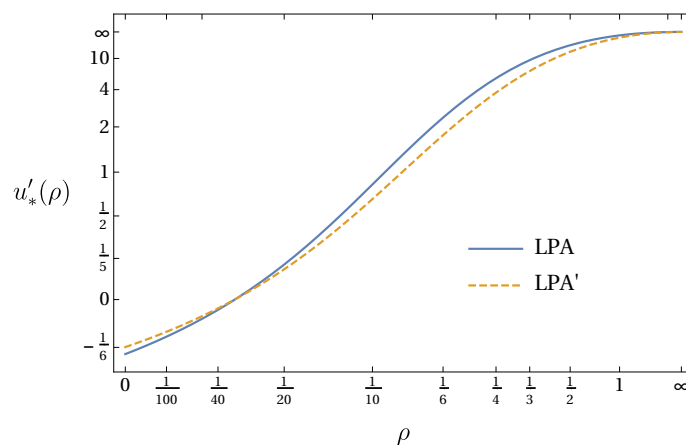


Fig. 4.1.: Derivative of the fixed-point potential at the Wilson-Fisher fixed point in LPA and LPA'.

Figure 4.1 displays the derivative of the effective potential. One can see that the inclusion of the anomalous dimension has a quantitative influence for intermediate values of ρ . For the VEV, we get

$$\begin{aligned}\kappa^{\text{LPA}} &= 0.030647942408697774953, \\ \kappa^{\text{LPA}'} &= 0.030592776234779436405.\end{aligned}\tag{4.1}$$

In LPA', we find the anomalous dimension to be

$$\eta_\phi = 0.044272337370315035214.\tag{4.2}$$

It may seem ridiculous to present that many figures, but they illustrate the power of pseudo-spectral methods. Our viewpoint is to solve a truncated problem (numerically) exactly, and any numbers given here are to be understood as the solution to the truncated problem.

We find that our values match very well with earlier results, e.g., given in [24, 61, 63, 67], and [123] where fixed-point quantities were calculated via full potential flows. In particular, we can reproduce all digits of the high precision results given in [64], where an LPA truncation was used. In comparison to results obtained from high-temperature expansions and Monte-Carlo simulations ($\eta_\phi = 0.036$) [200], our value has a systematic error which is to be expected in the LPA' truncation. Within the FRG, an accuracy competitive with other methods has been reached using the BMW approximation technique [66, 81].

Figure 4.2 shows the coefficients of the expansions of $u'(\rho)$ and $u'(\rho)/\rho^{\frac{2-\eta_\phi}{1+\eta_\phi}}$. In LPA, one perfectly sees exponential convergence in both domains. On the other hand, as soon as we include the anomalous dimension, we only find asymptotically algebraic convergence

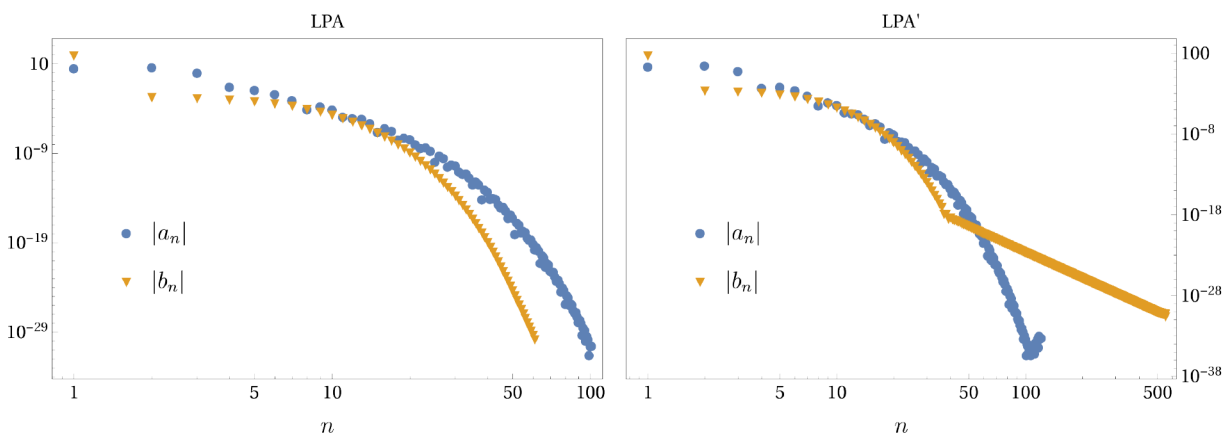


Fig. 4.2.: Decay of the Chebyshev coefficients in the first subdomain a_n and second subdomain b_n of the derivative of the Wilson-Fisher fixed-point potential, LPA on the left and LPA' on the right. Notice the algebraic decay in LPA' in the second region, which needs a factor of 10 as many coefficients as in the case of exponential convergence in LPA to achieve the same order of accuracy.

in the second domain. This behavior is indeed expected by the asymptotic behavior of the potential, as it rises with a fractional power. Furthermore, one can also see that this problem is irrelevant for all practical purposes, as the algebraic convergence only sets in at about 10^{-18} , up to that point one still observes exponential convergence. This emphasizes the fact that any statement about convergence is really an asymptotic one, and one cannot predict where this behavior sets in. As a final comment on this, note also the number of coefficients needed to gain a certain accuracy: In case of exponential convergence, one needs very few coefficients to get an adequate result, but as soon as there are singularities of any kind, one needs a large number of coefficients to further increase the accuracy as can be seen in Fig. 4.2.

Let us now expand the LPA solution into a Taylor series (2.22) with vanishing expansion point $\kappa = 0$ as well as a Laurent series around $\rho = \infty$. As a further test for the method, we compare whether the relations between the coefficients λ_n , obtained by plugging in such an ansatz into the fixed point equation, are satisfied. One obtains the well-known relations (see, e.g., [80])

$$\begin{aligned}\lambda_2 &= -4\pi^2\lambda_1(1 + \lambda_1)^2, \\ \lambda_3 &= \frac{24}{5}\pi^4\lambda_1(1 + \lambda_1)^3(1 + 13\lambda_1), \\ \lambda_4 &= -\frac{1728}{7}\pi^6\lambda_1^2(1 + \lambda_1)^4(1 + 7\lambda_1), \\ \lambda_5 &= \frac{768}{7}\pi^8\lambda_1^2(1 + \lambda_1)^5(2 + \lambda_1(121 + 623\lambda_1)), \text{ etc.}\end{aligned}\tag{4.3}$$

Inserting our solution, one finds that the absolute error in these coefficients are ($< 10^{-30}, 2 \times 10^{-23}, 2 \times 10^{-19}, 7 \times 10^{-16}$). For the expansion around infinity, one obtains

$$u'_*(\rho) = A\rho^2 - \frac{1}{75A\pi^2\rho^3} + \mathcal{O}(\rho^{-5}).\tag{4.4}$$

Expanding our solution, the coefficients of $\rho^1, \rho^0, \rho^{-1}, \rho^{-2}$ (which should vanish in the exact solution) are ($-4 \times 10^{-27}, 3 \times 10^{-24}, -8 \times 10^{-22}, 10^{-19}$), and the relation between the leading and the first sub-leading coefficient is fulfilled to an absolute accuracy of 10^{-17} . For completeness, let us give the values of λ_1 and A both in LPA and LPA':

$$\begin{aligned}\lambda_1^{\text{LPA}} &= -0.18606424947031443565, \\ \lambda_1^{\text{LPA}'} &= -0.16574071049155738982, \\ A^{\text{LPA}} &= 84.182303273336100651, \\ A^{\text{LPA}'} &= 50.323366981670544177.\end{aligned}\tag{4.5}$$

These results match with [80] and [201] where local expansions and the shooting method were employed. This underlines that we can trust the global solution and that we can relate

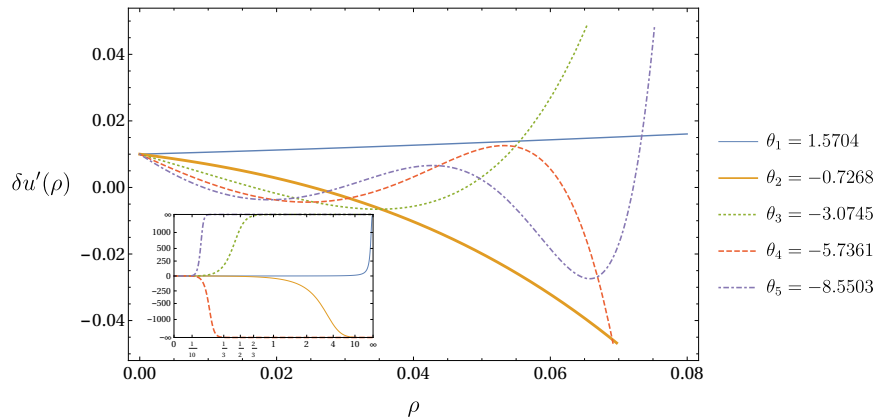


Fig. 4.3.: Eigenperturbations of the Wilson-Fisher fixed point, normalized to 0.01 at $\rho = 0$.

to earlier results.

Let us now turn our attention to the critical exponents of the Wilson-Fisher fixed point. They are defined by Eq. (2.23). Again, a global approach to the solution of the perturbed equation is used. Figure 4.3 shows the eigenfunctions corresponding to the five highest eigenvalues, where the anomalous dimension has been taken into account. As for the fixed-point solution itself, any precision can be achieved in the eigenfunctions and critical exponents. The critical exponents match with earlier results, e.g., given in [24, 61]. Let us emphasize again that the largest error arises from the systematic errors of the derivative expansion to order LPA/LPA'. If we compare with Monte-Carlo results [200], we find a deviation of about 1% for the first and 14% for the second critical exponent. Especially the error of the second critical exponent is to be expected from the low order of the derivative expansion used, see [63]. For this reason, from now on we only give a few relevant digits, bearing in mind that within a given truncation, we in principle could calculate as many digits as needed.

Multi-critical fixed points for $2 < d < 3$

It is worthwhile to have a closer look at fractional dimensions $2 < d < 3$. The fixed-point structure is getting richer for decreasing dimension. Therefore, it is interesting to investigate the interpolation between the two fixed points in $d = 3$, the Gaussian and the Wilson-Fisher fixed point, and the infinite number of fixed points in $d = 2$. In [202], for $N = 1$ and $d = 2$, and in [69, 167], as a function of d and N , the existence and properties of multicritical fixed points are investigated. In this context, *multicritical* means that the corresponding fixed points have more than one relevant direction, i.e., they are unstable compared with the stable Wilson-Fisher fixed point, and are therefore supposed to exhibit a phase transition of first order. Any of these fixed points represents a new universality class next to the Wilson-Fisher universality class. Two dimensions is an intriguing case due to the Mermin-Wagner-Hohenberg theorem [203–206]. It states that continuous symmetries cannot be broken within a continuous phase transition in $d = 2$. An RG proof of this theorem can

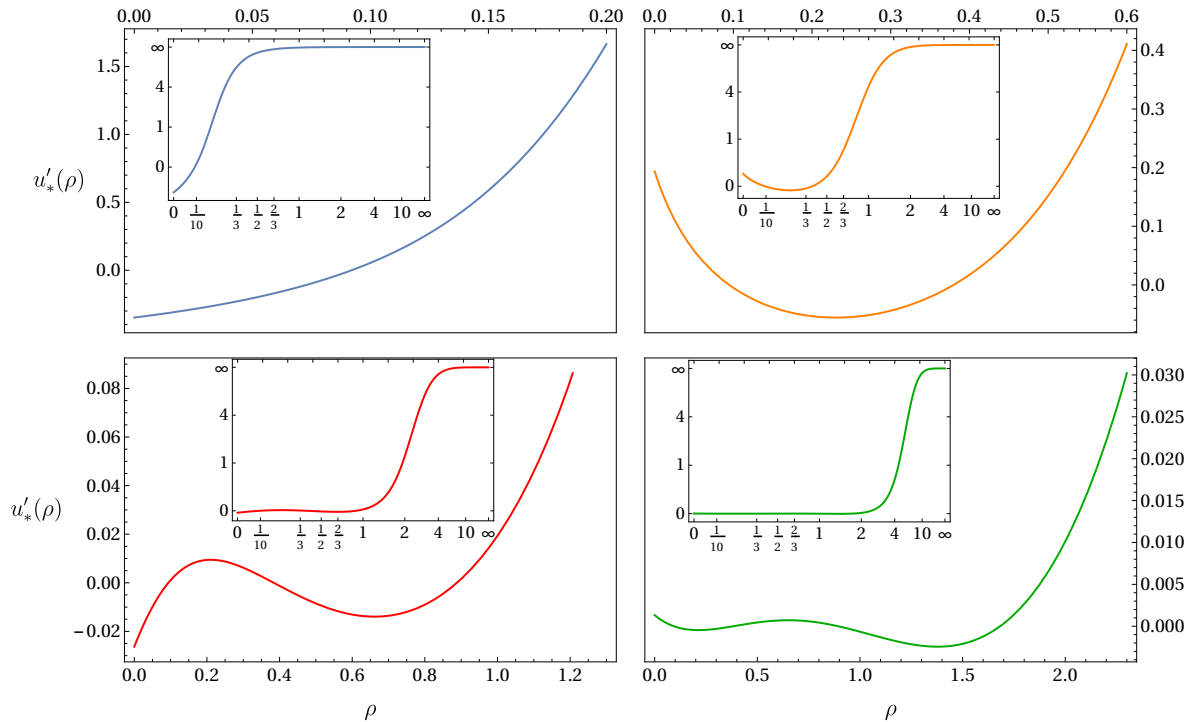


Fig. 4.4.: First derivative of multicritical fixed-point potentials in $d = 2.4$ exhibiting two minima regarded as function of the dimensionless renormalized scalar field ϕ (blue, Wilson-Fisher potential), three minima (yellow), four minima (red), five minima (green). The small insets depict the global behavior of the solutions.

be found, e.g., in [67, 69]. We emphasize that $N = 2$ is a special case giving rise to a BKT phase transition.

As has been done in [67], we restrict ourselves to $N = 1$. We emphasize that the following investigations can straightforwardly be applied to arbitrary numbers N if the set of fixed-point solutions is still discrete. In [67], a sequence of critical dimensions $d_{c,i} = 2i/(i-1)$ where the next multicritical fixed-point potential $u_i(\rho)$ emerges was stated. These are those dimensions where new operators $\sim \rho^i$ become relevant for $d < d_{c,i}$. The emergence of new solutions can be motivated as follows: If one of the critical exponents is zero, the solution of the fixed-point equation is degenerate. Here, the degenerate solution is the Gaussian fixed point for whose critical exponents dimensional power counting can be applied. Lowering d , the degenerate solution separates into two distinct solutions, the Gaussian fixed point and a new multicritical fixed point. Concentrating in the following on $d = 2.4$ as an example, we find three more multicritical fixed points $\text{FP}_{i \in \{3,4,5\}}$ besides the Wilson-Fisher (FP_2) and the Gaussian (FP_1) fixed point. The index $i \geq 2$ counts the minima of the corresponding fixed-point potential regarded as a function of the dimensionless renormalized scalar field ϕ . Our results around $d = 2.4$ confirm the predicted value $d_{c,6} = \frac{12}{5}$.

For our calculations, we have employed Eq. (2.35) within the LPA' truncation. The anomalous dimension, Eq. (2.36), is again evaluated at the global minimum of the potential

WF-FP			multicritical FP _{<i>i</i>=4}		
η_ϕ	relev. exp.	irrelev. exp.	η_ϕ	relev. exp.	irrelev. exp.
0.1390	1.1883	-1.0977	0.001753	1.9968	-0.3035
		-3.1108		1.4607	-1.3957
		-5.6147		0.6632	
multicritical FP _{<i>i</i>=3}			multicritical FP _{<i>i</i>=5}		
η_ϕ	relev. exp.	irrelev. exp.	η_ϕ	relev. exp.	irrelev. exp.
0.01598	1.9636	-0.5467	8.2715×10^{-5}	1.9999	-0.1555
	0.8507	-2.0694		1.5972	-0.9284
		-3.8156		1.1235	
				0.5329	

Tab. 4.1.: Anomalous dimensions and highest critical exponents of all scaling solutions in $d = 2.4$ besides the Gaussian fixed point.

which is in the following cases the outermost minimum. In Fig. 4.4, the first derivative of the multicritical fixed-point potentials is shown. As the values of the anomalous dimension of the multicritical fixed points $\text{FP}_{i \geq 3}$ are small compared to the one of the Wilson-Fisher fixed point, the convergence of their coefficients is exponential within the used precision of `float128`. Therefore, the deviation from the exact solution can be estimated to be below 10^{-30} . In Tab. 4.1, the anomalous dimensions and the largest critical exponents calculated by pseudo-spectral methods are given. The highest relevant critical exponent for the fixed points $i \geq 3$ is close to the mean-field value 2 which they attain at the corresponding critical dimension. The other relevant exponents are smaller. Our results are in good agreement with [67, 69, 167]. Additionally, the results for the Wilson-Fisher fixed point in $d = 2.4$ can be related to earlier works [207–209], where the ε -expansion and lattice simulations were applied.

The sequence of critical dimensions predicts that a new fixed-point potential with six minima (regarded as function of the dimensionless scalar field) emerges exactly at $d = 2.4$. Similar to the Wilson-Fisher fixed point that probably does not exist in $d = 4$ but exists in all dimensions $2 < d < 4$, we find this fixed point for all dimensions $2 < d < 2.4$. In fact, we are able to determine a global solution for $d = 2.399$ where the nonasymptotic behavior is realized on very small scales $|u'_*(\rho \leq \kappa)| \sim 10^{-6}$ and $\eta_\phi = 2.3446 \times 10^{-10}$.

4.1.2. A simple Yukawa model model in $d = 3$

We extend our studies to the simple Yukawa model in $d = 3$ with the fermionic field ψ containing N_f flavors. The effective average action is given by Eq. (2.37). As a function of the parameter N_f , the Gross-Neveu fixed-point potential is in the symmetric regime for large N_f and in the symmetry broken regime for small N_f . We use the flow equations (2.41)-(2.44).

Large N_f analysis

The large N_f approximation is a good test case for our numerical method because an explicit analytical solution for the fixed-point potential can be found [73]. Interestingly, the scalar anomalous dimension does not vanish in contrast to the one of the Wilson-Fisher fixed point for increasing N_f . Even the fixed-point potential looks very different. The fixed-point equations in the large N_f limit are given by, [73],

$$0 = (-2 + \eta_\phi)u' + (d - 2 + \eta_\phi)\rho u'' + 4v_d d_\gamma h^2 l_1^{(F)d}(2\rho h^2; \eta_\phi), \quad (4.6)$$

$$0 = (\eta_\phi + 2\eta_\psi + d - 4)h^2, \quad (4.7)$$

$$\eta_\phi = \frac{8v_d}{d} d_\gamma h^2 \left[m_4^{(F)d}(2h^2\kappa; \eta_\psi) - 2h^2\kappa m_2^{(F)d}(2h^2\kappa; \eta_\psi) \right], \quad (4.8)$$

$$\eta_\psi = 0. \quad (4.9)$$

Note that an appropriate rescaling has been taken into account. In this approximation, we encounter a first order system. For solutions with a nontrivial Yukawa coupling, the bosonic anomalous dimension can be read off from Eqs. (4.7) and (4.9) to be $\eta_\phi = 1$ exactly. We can reproduce this result to all digits of `float128` which gives an accuracy of about 10^{-32} . The exact fixed-point value of the Yukawa coupling reads

$$h_*^2 = \left(\frac{d}{d_\gamma v_d} \right) \frac{(d-4)(d-2)}{(8-6d)}, \quad (4.10)$$

and can be confirmed up to 10^{-32} as well. The fixed-point potential is given by the Gaussian hypergeometric function,

$$u_*(\rho) = - \frac{4(8-6d+d^2)}{3d-4} \rho \times {}_2F_1 \left(\frac{1}{1-d}, 1; \frac{2-d}{1-d}; \frac{d}{d_\gamma v_d} \frac{8-6d+d^2}{3d-4} \rho \right). \quad (4.11)$$

The absolute difference between the analytical solution and our numerical one can be estimated to be smaller than 3×10^{-17} for large ρ . For finite ρ , it is even smaller. This is due to the Gaussian grid which only has points at finite ρ . Thus, the asymptotic prefactor is only tuned regarding finite field values and, therefore, has a larger error of about 3×10^{-17} . For this calculation we have used $\rho_1 = 3/10$ and $L = 2$. The decay of the coefficients can be seen in Fig. 4.5. The Chebyshev expansion in the first domain shows exponential convergence. By contrast, the expansion in the second domain decreases exponentially at first, but only up to a certain number of coefficients. The actual convergence rate is algebraic. This is to be expected due to the asymptotic behavior $\propto \sqrt{\rho}$. The downwards bending of the last coefficients shows a truncation effect which is not a numerical effect. If we calculate the spectral coefficients from the analytical solution, we obtain a good agreement with the numerically

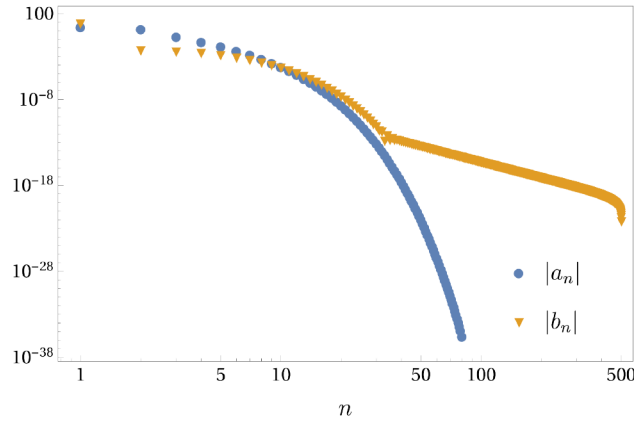


Fig. 4.5.: Decay of Chebyshev coefficients of the first derivative of the Gross-Neveu fixed-point potential in the first subdomain a_n and second subdomain b_n .

calculated ones. Ignoring the last coefficients affected by the truncation, we read off $\sim 10^{-19}$ for the lowest coefficient. The rule of thumb for the truncation error (3.12) is in very good agreement with the maximal deviation of about 3×10^{-17} from the exact solution.

Let us have a closer look at the choice of the two parameters ρ_1 and L . They have quite some influence on the convergence behavior of the coefficients. We observe that if the matching point ρ_1 is chosen to be smaller, then the decrease of the Chebyshev coefficients in the first domain is exponential as well, but faster. This also holds for the coefficients in the second domain if the matching point is increased. However, the algebraic convergence sets in earlier. Lowering ρ_1 , the algebraic convergence sets in later. It is remarkable that the gain of accuracy is inappreciable when taking a large number of coefficients into account because the algebraically decaying coefficients do not depend significantly on the choice of ρ_1 . This is different for the parameter L . Figure 4.6 shows that one can gain orders of magnitude of accuracy if L is increased for large enough number of coefficients. As before, the decrease of the first coefficients is more slowly, but the algebraic convergence sets in later. The algebraically decaying coefficients now depend on the parameter. This short analysis already makes clear that the choice of optimized parameters can strongly depend on the

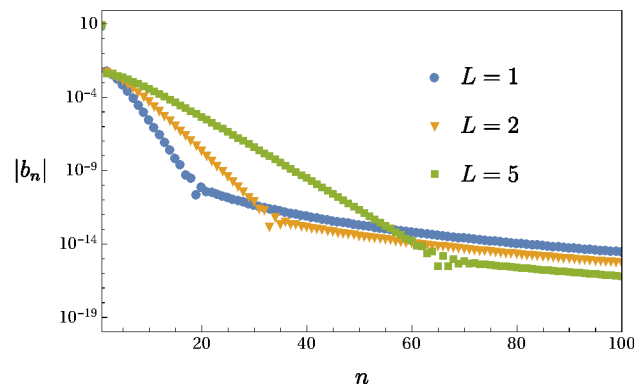


Fig. 4.6.: Decay of Chebyshev coefficients in the second subdomain in dependence on L .

maximal number of coefficients that one takes into account. These observations from one specific example may give an indication for other calculations as well.

Finite N_f analysis

For finite N_f , the fixed-point potential gives rise to an interesting behavior. In [73], it is shown that the fixed-point potential lies in the symmetric regime for all $N_f \geq 2$. For that reason, the potential was expanded polynomially around vanishing field value. A study of the convergence radius indicates the reliability of these results. Unfortunately, the convergence is less clear for smaller N_f such that another approach is required. For small N_f , the fixed-point potential moves from the symmetric regime to the spontaneously symmetry-broken regime. In [210], a fixed-point potential for $N_f = \frac{1}{2}$ (corresponding to one Dirac fermion in the irreducible representation) was found in the symmetry-broken regime. In [73], it was assumed that the non-Gaussian Gross-Neveu fixed point interpolates between the large N_f fixed point and the Wilson-Fisher fixed point in the $N_f \rightarrow 0$ limit.

To uncover the details of the transition for small N_f , we compute the fixed-point potential as a function of N_f . The asymptotic behavior of the potential can be read off from Eq. (2.41), $u'(\rho) \propto \rho^{\frac{2-\eta_\phi}{d-2+\eta_\phi}}$. Next to the the global solution, we compute the relevant critical exponent

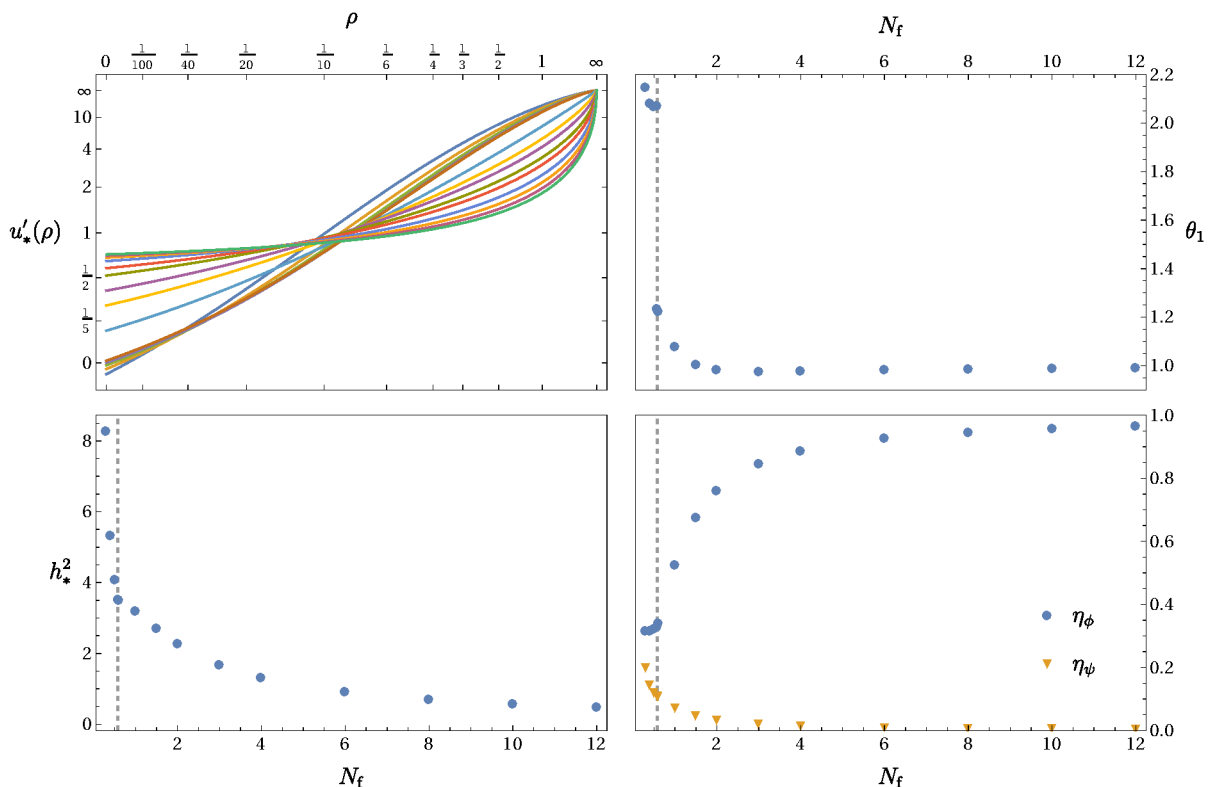


Fig. 4.7.: Fixed-point potential (upper left panel), relevant exponent (upper right panel), Yukawa-coupling (lower left panel) and anomalous dimensions (lower right panel) for $0.3 \leq N_f \leq 12$. For increasing flavor number, $u'_*(0)$ increases as well. The dashed line depicts the flavor number N_t of the transition.

in $d = 3$ for N_f lying between 0.3 and 12, see Fig. 4.7. We obtain a very good agreement with the polynomial approximation employed in [73] for $N_f \geq 2$. Even the relevant exponent matches in the first four relevant digits. It is worth mentioning that this good agreement is only obtained by taking high orders in the polynomial truncation into account [73], especially for small N_f . Our results for $N_f \geq 2$ are also compatible with other methods such as $1/N_f$ expansions [211, 212], and Monte-Carlo simulations [213, 214]. In fact, systematic truncation errors appear to be smaller for the Yukawa model in comparison with the Ising model. The overall consensus among the nonperturbative methods is very satisfactory.

Let us now concentrate on the small N_f regime. The transition from the symmetric to the symmetry-broken regime can be determined to be at $N_t \approx 0.5766$. As a new result, we observe that the Gross-Neveu fixed point does not approach the Wilson-Fisher fixed point for small N_f . This can be seen from the behavior of the Yukawa coupling and the anomalous dimensions on the one hand and the relevant exponent on the other hand. In particular, the behavior of h_* suggests that the Gross-Neveu fixed point moves to infinity in theory space for $N \rightarrow 0$.

It is instructive to compare our results for $N_f = 1/2$ with those of [210] where also a full potential flow has been studied (note that our convention of $N_f = 1/2$ corresponds to $N_f = 1$ in [210]; for aspects of criticality see [77]). In [210], the fluctuation terms $\propto \kappa u'' h^4$, $\propto \kappa^2 u''' h^4$ and $\propto \kappa h^6$ have been missed in the derivation of the flow equation of the Yukawa coupling, see the discussion in [118]. If we artificially switch off these terms, the vacuum expectation value and the critical exponent of our calculations are in good agreement with those of [210]. On the contrary, including these terms, even the first relevant digit changes. For $N_f = 1/2$, we obtain $\nu = 1/\theta_1 = 0.4836$, $\eta_\phi = 0.3227$ and $\eta_\psi = 0.1204$. In conclusion, it is remarkable that our approach is able to find a global solution in a regime where a polynomial truncation is not reliable.

4.2. Universal behavior of coupled order parameters below three dimensions

Let us now consider the combination of an $O(N)$ with an $O(M)$ model exhibiting an $O(N) \oplus O(M)$ symmetry with two competing order parameters. It is already known that the phase diagram of a system with an $O(N) \oplus O(M)$ symmetry features multicritical points³ [39, 215, 216]. We are interested in the following case: As a function of two external parameters, the $O(N)$ and $O(M)$ symmetry are separately broken to an $O(N - 1)$ or $O(M - 1)$ symmetry across second-order phase transition lines which meet at such a point. The universality class of that point is encoded in a stable fixed point featuring two relevant directions [40]. For a bicritical fixed point, there are three phases adjacent to it - the two broken phases and a phase of unbroken symmetry. If it is a tetracritical point, an additional mixed phase with two spontaneously broken symmetries exists.

It is an intriguing question what is the dominating critical behavior for $d = 2$ and $N = M = 1$. On the one hand, it could be determined by the decoupled fixed point, a combination of the Onsager solutions of the simple Ising model. On the other hand, multicritical models also feature fixed points exhibiting an enhanced $O(N + M)$ symmetry. This would suggest BKT type physics as d approaches 2. Besides, the model also features a biconical fixed point which provides another candidate for a stable fixed point in $d = 2$ for $N = M = 1$. Finally, additional fixed points may exist below $d = 3$, which could become relevant for the physics of two coupled Ising models in $d = 2$.

In what follows, we are interested in the phase diagram, that shows which of the various $O(N) \oplus O(M)$ fixed points is the stable one as a function of $N = M$ and d . In particular, we investigate how the stability is traded between the multicritical points. We discover that several simultaneously stable fixed points underlie different possibilities for the universal critical behavior of the system. We find that besides the long-range degrees of freedom, symmetries and the dimensionality of the system, additional information is required to determine which of the possible universality classes is realized in the IR.

According to Eq. (3.13), we use an expansion in the two field invariants ρ_ϕ and ρ_χ . If global issues are not particularly concerned, an expansion of the effective potential on a finite domain is sufficient. Of course, that domain must be large enough to capture all the physics relevant for the system. Doing so, we do not observe any significant influence of the choice of the maximal field values. We mostly choose the whole domain to be $[0, 1] \times [0, 1]$ in ρ_ϕ and ρ_χ and use a decomposition into 3×3 subdomains increasing the speed of the computation. The innermost domain is chosen such that the VEV lies in it. The outer ones are already dominated by the asymptotic behavior of the potential.

³Note that *multicritical* has a different meaning in this context than in Sec. 4.1 where it was used for unstable fixed points.

4.2.1. Systems of competing orders

The degrees of freedom of the $O(N) \oplus O(M)$ model are given by two fields ϕ^a , $a = 1, \dots, N$ and χ^b , $b = 1, \dots, M$ which may assume a nonvanishing VEV separately. In $d = 3$, universal critical behavior can be studied within the ε -expansion around $d = 4$ dimensions, however, this becomes challenging already for the $O(N)$ model in $d = 2$, see, e.g., [217], as well as for two coupled order parameters [32]. Thus, we employ the FRG for which it has been shown in [22–25] and in the previous section as well as [64, 65, 67, 167, 202, 218, 219] to give reliable results for the physics of coupled order parameters in $d = 3$ and for $O(N)$ models below $d = 3$, respectively.

Equation (2.46) yields an ansatz for the effective average action. The flow of the potential and the wave function renormalizations is given by Eqs. (2.48) and (2.52), (2.53). For tetracritical fixed points, the nontrivial minimum lies at nonvanishing expectation values for both order parameter fields, $(\kappa_\phi, \kappa_\chi)$. In this case, the anomalous dimensions are projected onto the nontrivial $(\kappa_\phi, \kappa_\chi)$. By contrast, for bicritical fixed points with the minima lying on the axes, we evaluate η_ϕ at $(\kappa_\phi, 0)$ and η_χ at $(0, \kappa_\chi)$. In $d = 3$, the local expansion of the potential,

$$u(\rho_\phi, \rho_\chi) = \sum_{i,j} \frac{\lambda_{i,j}}{i!j!} (\rho_\phi - \kappa_\phi)^i (\rho_\chi - \kappa_\chi)^j, \quad (4.12)$$

is a suitable approximation. For the symmetry broken regime, it is advantageous to choose the expansion points $\kappa_{\phi/\chi}$ as the nontrivial minima. However, for lower d , the expansion breaks down as it is to be expected from the dimensional power counting and shown explicitly in Sec. 4.2.3. Therefore, we consider the full potential as a general function of the two fields. According to Eq. (2.23), a linearized equation for small perturbations around the fixed point can be derived from the fixed-point equation (2.48) with vanishing left-hand side. As done with the potential, we expand the eigenperturbations on a finite domain inferring the critical exponents from the solution of the analog of Eq. (2.23).

An important property of the fixed point is encoded in the field dependent parameter Δ , which is related to the determinant of the matrix consisting of the second derivatives of the potential, [22]. The general definition is given by

$$\Delta = u^{(2,0)}u^{(0,2)} - (u^{(1,1)})^2. \quad (4.13)$$

If we choose a nontrivial expansion point for the effective potential, as in Eq. (4.12), the evaluation of Δ reduces to

$$\Delta = \lambda_{2,0}\lambda_{0,2} - \lambda_{1,1}^2. \quad (4.14)$$

If the first derivatives of u vanish at the expansion point, the expansion point corresponds to a saddle point for $\Delta \leq 0$, whereas it corresponds to a minimum for $\Delta > 0$. Thus, for $\Delta > 0$, the fixed point is tetracritical, as a mean-field analysis relates it to a multicritical point which

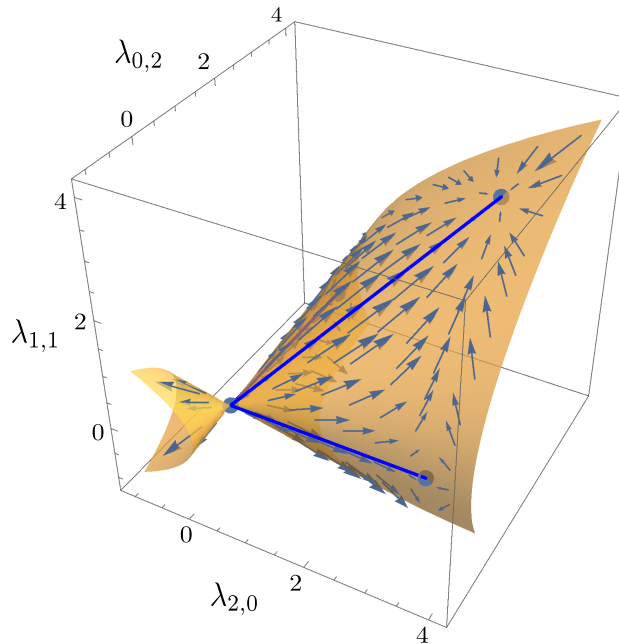


Fig. 4.8.: We show the three-dimensional theory space spanned by the quartic couplings. The orange surface is defined by $\Delta = 0$, and blue arrows show the RG flow towards the IR. Blue dots denote different fixed points that lie in this surface.

is bordered by a mixed phase [216]. On the other hand, for $\Delta \leq 0$, there is no mixed phase, which corresponds to a bicritical fixed-point. As the sign of Δ for the fixed-point solutions we consider does not depend on whether it is evaluated at the extremum/saddle point or the origin in field space, we typically extract Δ at the origin in field space.

If $\Delta = 0$ at every point in field space, the symmetry is enhanced to an $O(N+M)$ symmetry. An enhanced $O(N+M)$ symmetry requires that the potential has a flat direction everywhere in field space, i.e., the Hessian must have vanishing determinant. Hence, the RG flow cannot cross the hypersurface defined by $\Delta = 0$ as a *global* criterion. That hypersurface also contains several separatrices between fixed points, cf. Fig. 4.8. Note that this does not necessarily imply that $\Delta = 0$, if it is imposed only locally in field space, is preserved during the flow. Within a local expansion up to fourth order in the fields, one can show that the flow of Δ is proportional to Δ , using scale dependent redefinitions of the field. These correspond to deforming “elliptical” potentials such that the symmetry enhancement is obvious. We assume in the following that the sign of Δ evaluated at the extremum/saddle point $\kappa_\phi = \kappa_\chi \neq 0$ of the potential does not change under the flow, if that flow is in the universality class of an IR fixed point. In particular, it might be possible that additional separatrices outside the global surface $\Delta = 0$ connect the fixed points in Fig. 4.8, if they have appropriate attractive directions perpendicular to that surface. These separatrices would serve to separate the theory space. To comprehensively uncover the structure of the theory space and its separate regions, global flows have to be considered that do not rely on a choice of expansion point.

4.2.2. Fixed-point content

This section provides an overview over the fixed-point content of the model for dimensions $2 < d \leq 3$. We are interested in the stable fixed point, which features not more than two relevant directions. These correspond to parameters that require tuning in a given experimental situation, in order to observe the universal scaling behavior associated to the fixed-point solution. Typically, there is one tunable parameter for each of the order parameters, e.g., the temperature and the magnetic field for an anisotropic antiferromagnet.

Gaussian fixed point

The trivial scaling solution is the Gaussian fixed point (GFP). The critical exponents can be deduced from dimensional scaling, which implies, that in $d = 3$, there are five relevant directions and even more for lower d . Hence, it will not play a role for the description of realistic systems at criticality.

Decoupled fixed points

The $O(N) \oplus O(M)$ model decouples into an $O(N)$ and $O(M)$ model, if the mixed couplings vanish, $\lambda_{n,m} = 0$ for $n > 0$ and $m > 0$. The fixed-point potentials separate into two unrelated scaling solutions of the single-field models. In particular, the decoupled fixed point (DFP) is the combination of the $O(N)$ and $O(M)$ Wilson-Fisher scaling solutions. As $\Delta > 0$, the fixed point corresponds to tetracritical behavior, cf. Fig. 4.9. In addition to one relevant direction from each Wilson-Fisher solution, the vanishing mixed couplings $\lambda_{n,m}$ are associated to nontrivial critical exponents. Hence, the fixed point can be stable, i.e., features two relevant directions, depending on the values of those exponents. The third critical exponent is related to the inverse Wilson-Fisher correlation length critical exponents, $\theta_{1/2} = \frac{1}{\nu_{1/2}}$, by Aharony's scaling relation [10, 16–18],

$$\theta_3 = \theta_1 + \theta_2 - d. \quad (4.15)$$

The scaling relation is satisfied to any order in the ε -expansion [19] and thus expected to be exact. Within LPA, it is fulfilled whereas LPA' gives rise to an ambiguity, see [24]: The scaling relation is only satisfied if the anomalous dimensions are held fixed in the computation of the critical exponents. However, the critical exponents dominating the flow close to the fixed point correspond to the one where variations of the anomalous dimensions are taken into account. In particular, the first two relevant critical exponents change whereas θ_3 does not depend on variations of the anomalous dimension. This ambiguity might be resolved in a further extension of the truncation beyond LPA'. In order to obtain results consistent with those of the other fixed points, we compute the critical exponents by employing Eq. (2.23) and taking the variations of the anomalous dimensions into account within the usual LPA' scheme if not stated differently.

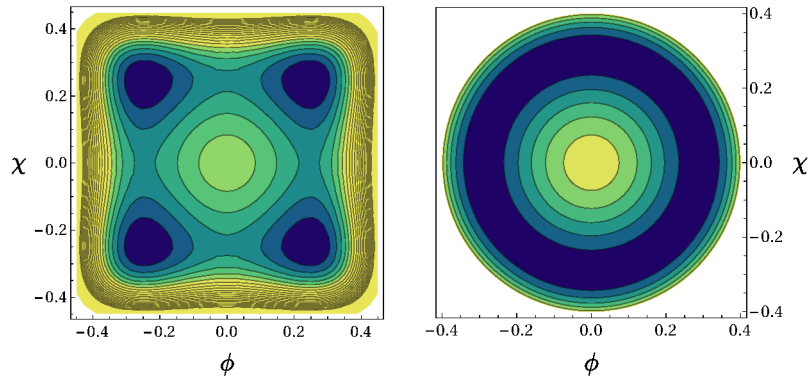


Fig. 4.9.: Fixed-point potential at the DFP (left panel) and IFP (right panel) within LPA in $d = 3$ and $N = M = 1$. From blue to yellow, the potential grows. The decoupled fixed point is clearly tetracritical, i.e., $\Delta > 0$, as the minima lie between the axes. The isotropic fixed point features a symmetry enhancement to an $O(2)$ rotational symmetry.

Another special subclass contains the semi-Gaussian fixed points, which are a combination of a Gaussian and a non-Gaussian fixed point, e.g., the Wilson-Fisher fixed point (DGFP). The separatrices between those fixed points and the GFP lie in the hypersurface $\Delta = 0$, cf. Fig. 4.8. Furthermore, one or two of the sectors may assume a *multicritical* fixed-point solution in the meaning of Sec. 4.1. However, all these fixed points do not play a role for the description of realistic systems as they inherit more than one relevant direction from at least one of the two sectors. Also, for the stability trading mechanisms, they are not of interest.

Fixed points with symmetry enhancement

There is another class of solutions with the special property that all couplings $\lambda_{n,m} = \lambda_{c,0} = \lambda_{0,c}$ with $n + m = c$ independent from the expansion point. Hence, $\Delta = 0$ at every point. The fixed-point potential does not depend on ρ_ϕ and ρ_χ separately, but on $\rho_\phi + \rho_\chi$ which corresponds to an enhancement of the $O(N) \oplus O(M)$ symmetry to an $O(N + M)$ symmetry. For our investigations, the most interesting fixed point in this class features the coordinates of the single-field $O(N + M)$ Wilson-Fisher fixed point which is called the isotropic fixed point (IFP), cf. Fig. 4.9. Figure 4.8 shows that a separatrix leads from the Gaussian fixed point to the IFP in the surface $\Delta = 0$.

As for the class of the decoupled fixed points, we also find solutions corresponding to single-field *multicritical* fixed points for $d < 3$ which were discussed in Sec. 4.1. Due to the number of relevant directions, we do not consider them in what follows.

Biconical fixed point

There is one scaling solution for which both sectors are coupled nontrivially, i.e., $\lambda_{i,j} \neq 0$, without continuous symmetry enhancement. Consequently, for the existence of the biconical fixed point (BFP), the nonvanishing interaction of the two sectors is essential. This mechanism occurs more generally in models of several coupled sectors [23, 25], as well as for

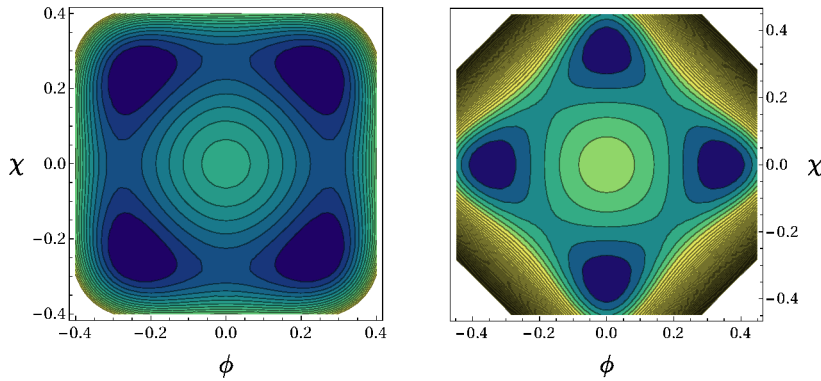


Fig. 4.10.: Fixed-point potential at the BFP in $d = 3$ and $N = M = 1.2$ (left panel) within LPA. From blue to yellow, the potential grows. The fixed point features global minima between the axes, i.e., $\Delta > 0$ and corresponds to tetracritical behavior. For $N = M = 1$ (right panel) the minima lie on the axes, and accordingly $\Delta < 0$.

coupled gauge theories [220]. The BFP can either be bicritical $\Delta < 0$ or tetracritical $\Delta > 0$ which is realized for different values of $N = M$, cf. Fig. 4.10. As it is discussed in more detail below, the change of its nature is connected to the collision with the IFP.

Bicritical fixed points

For $N = M$, the fixed-point equation gives rise to an exchange symmetry under $\phi \leftrightarrow \chi$. We find solutions exhibiting this symmetry, the DFP for example, as well as solutions which do not, e.g., the DGFPs.⁴ If we specialize $N = M = 1$, additional solutions can be deduced from the fixed-point solutions preserving that symmetry. A solution $u_*(\phi, \chi)$ to the fixed-point equation in ϕ, χ , also solves the fixed-point equation in ϕ', χ' , where

$$\phi = \frac{1}{\sqrt{2}}(\phi' + \chi'), \quad \chi = \frac{1}{\sqrt{2}}(-\phi' + \chi'), \quad (4.16)$$

see App. C for details. The transformation (4.16) corresponds to a $\pi/4$ rotation in field space. Consequently, the IFP is left unchanged under the rotation (4.16). For the BFP and DFP, however, this transformation turns a tetracritical fixed point into a bicritical one and vice versa resulting in two distinct solutions.

Using the ε -expansion around $d = 4$, the application of the transformation (4.16) can be easily illustrated. Within first order, $\mathcal{O}(\varepsilon)$, the beta functions of the quartic couplings read [21, 39],

$$\beta_{\lambda_{2,0}} = -\varepsilon\lambda_{2,0} + (64 + 8N)\lambda_{2,0}^2 + 8M\lambda_{1,1}^2, \quad (4.17)$$

$$\beta_{\lambda_{0,2}} = -\varepsilon\lambda_{0,2} + (64 + 8M)\lambda_{0,2}^2 + 8N\lambda_{1,1}^2, \quad (4.18)$$

$$\beta_{\lambda_{1,1}} = -\varepsilon\lambda_{1,1} + 32\lambda_{1,1}^2 + (16 + 8N)\lambda_{2,0}\lambda_{1,1} + (16 + 8M)\lambda_{0,2}\lambda_{1,1}. \quad (4.19)$$

⁴Such solutions emerge in pairs which transform into each other under $\phi \leftrightarrow \chi$. Therefore, the complete spectrum of solutions is invariant under the exchange symmetry.

Note that we have adopted a convenient redefinition of the couplings, corresponding to a potential of the form

$$u_*^\epsilon(\phi, \chi) = \lambda_{2,0}\phi^4 + 2\lambda_{1,1}\phi^2\chi^2 + \lambda_{0,2}\chi^4, \quad (4.20)$$

where we have specialized to the case $N = M = 1$. We now implement the rotation (4.16), which leaves us with

$$u_*^\epsilon = \frac{\phi'^4 + \chi'^4}{4}(\lambda_{2,0} + \lambda_{0,2} + 2\lambda_{1,1}) + (\phi'^3\chi' + \phi'\chi'^3)(\lambda_{2,0} - \lambda_{0,2}) + \frac{\phi'^2\chi'^2}{2}(3(\lambda_{2,0} + \lambda_{0,2}) - 2\lambda_{1,1}). \quad (4.21)$$

For this to be a viable fixed-point potential, we demand

$$0 = \lambda_{2,0} - \lambda_{0,2}, \quad \lambda'_{2,0} = \frac{\lambda_{2,0}}{2} + \frac{\lambda_{1,1}}{2}, \quad \lambda'_{1,1} = \frac{3}{2}\lambda_{2,0} - \frac{\lambda_{1,1}}{2}, \quad (4.22)$$

where the first requirement corresponds to the exchange symmetry $\phi \leftrightarrow \chi$. Let us take the DFP in $d = 3$ as a representative which fulfills this requirement. Its coordinates are $\lambda_{2,0} = \lambda_{0,2} = \frac{1}{72}$ and $\lambda_{1,1} = 0$. Upon the rotation (4.16), this gives a bicritical fixed-point potential with coordinates $\lambda_{2,0} = \lambda_{0,2} = \frac{1}{144}$ and $\lambda_{1,1} = \frac{1}{48}$. This fixed point was already considered in [22], see also [221–223], and called symmetric fixed point (SFP). We refer to it as the rotated decoupled fixed point (RDFP). In $d = 3$, the BFP equals the rotated DFP at $N = 1$, which is also visible by comparing the left panel in Fig. 4.9 and the right panel in Fig. 4.10. Below $d = 3$, that degeneracy is lifted, and the BFP exists independently of the RDFP at $N = 1$. Accordingly, the BFP implies the existence of another scaling solution, which we call the rotated biconical fixed point (RBFP).

From these considerations, one can infer that the eigenvalue spectra of $u_*(\rho_\phi, \rho_\chi)$ and its rotated counterpart are related to each other. The equation for the eigenperturbations inherits the $\pi/4$ symmetry from Eq. (2.48) as it is linear in δu . Similar to the requirement

	θ_1	θ_2	θ_3	θ_4	θ_5	θ_6
$d = 2.8$						
DFP	1.408	1.408	0.0165	-0.753	-0.753	-2.145
RDFP	2	1.408	0.0165	0	-0.753	-2
BFP	1.498	1.329	-0.0098	-0.734	-0.759	-2.126
RBFP	1.944	1.329	-0.0098	-0.154	-0.759	-2.077
$d = 2.7$						
DFP	1.334	1.334	-0.033	-0.800	-0.800	-2.166
RDFP	2	1.334	0	-0.033	-0.800	-2

Tab. 4.2.: We show the five largest critical exponents of the DFP and BFP and the rotated counterparts in LPA for $N = M = 1$. The dimension $d = 2.8$ is chosen as a representative. For the RDFP we additionally give the values for $d = 2.7$ to clarify that $2, 0, -2, \dots$ are always present in the spectrum at $N = 1$, independent of the dimension.

	$\eta_{\phi,\chi}$	θ_1	θ_2	θ_3	θ_4	θ_5	θ_6
$d = 2.7$							
DFP	0.0841	1.398	1.398	0.0232	-0.916	-0.916	-2.051
RDFP	0.0480	1.952	1.371	0.0015	-0.102	-0.864	-1.952
BFP	0.0789	1.522	1.296	-0.0108	-0.877	-0.915	-2.035
RBFP	0.0491	1.945	1.362	-0.0014	-0.123	-0.866	-1.963
$d = 2.5$							
DFP	0.119	1.264	1.264	-0.0549	-1.038	-1.038	-2.048
RDFP	0.0694	1.931	1.221	-0.104	-0.134	-0.973	-1.931

Tab. 4.3.: Anomalous dimensions and first critical exponents of the DFP and BFP and the rotated counterparts in LPA' for $N = M = 1$, where the symmetry (4.16) is slightly broken. The dimensions $d = 2.7$ is chosen as a representative. For the DFP we additionally give the values for $d = 2.5$ to show that we do not obtain d -independent critical exponents anymore.

above, only those eigenperturbations δu that preserve the $\phi \leftrightarrow \chi$ symmetry are also eigenperturbations of the rotated solution \tilde{u}_* , cf. Tab. 4.2. A clear explanation of this requirement can be found in App. C. From Tab. 4.2 it can be seen that the instability of the DFP implies instability of the RDFP. By contrast, if the DFP is stable, the RDFP features an additional marginal direction, as we obtain $\theta_i = 2, 0, -2, \dots$ as additional critical exponents,⁵ independent of d , at least within LPA.

Finally, we emphasize that the $\pi/4$ symmetry is only exact in LPA. Table 4.3 shows that the anomalous dimensions are not invariant under the transformation (4.16). In fact, the difference between the anomalous dimensions of u_* and its rotated counterpart may be large. Thus, the $\pi/4$ rotational symmetry is broken in LPA'. Note that this could change in a more extensive truncation, where a field dependent wave function renormalization is taken into account. However, that does not affect the existence of the rotated fixed-point solutions. Moreover, those critical exponents that are exactly equal for the solution u_* and its rotation in LPA, are still close to each other in LPA', cf. Tab. 4.2 and Tab. 4.3. Thus, rotating the (D/B)FP at $N = M = 1$ by $\pi/4$ in field space results in a potential that is not exactly equal but close to the R(D/B)FP.

4.2.3. Breakdown of local expansions

We explicitly show the necessity of solving for the fixed-point potential nonlocally, in particular for d towards 2. For that purpose, we review the convergence properties of LPA' in a local expansion. We focus on the DFP as a representative example, cf. Tab. 4.4. Whereas in $d = 3$, the difference between LPA' 12 and LPA' 16 (see Tab. 4.4 for explanation) is at the level of 0.3 %, it is of order 2% in $d = 2.9$, 17 % in $d = 2.8$. For satisfying convergence, higher orders in the polynomial expansion have to be taken into account. However, in particular for

⁵Note that $\theta_3 = 0$ presumably implies the existence of another fixed point with which the RDFP collides at that point. In this work, we do not search for such a fixed-point solution.

the coupled fixed points as the BFP, it is much more challenging to reach comparably high orders because they do not follow from single-field fixed-point solutions. Thus, they require the simultaneous solution of a much larger set of fixed-point equations for all the couplings.

d	$\theta_3(n=4)$	$\theta_3(n=8)$	$\theta_3(n=12)$	$\theta_3(n=16)$	$\theta_3(n=\infty)$
3	0.8026	0.1274	0.1412	0.1408	0.1407
2.9	0.9919	0.1317	0.1298	0.1327	0.1321
2.8	1.1976	0.1644	0.1033	0.1208	0.1175

Tab. 4.4.: We give the third largest critical exponent θ_3 at the DFP for $N = M = 1$ in d dimensions in LPA' n using the scaling relation (4.15). $n = 4$ includes all couplings up to four powers in the fields (i.e., two powers in the invariants ρ_ϕ, ρ_χ) and correspondingly for higher n . Results from the solution computed via pseudo-spectral methods ($n = \infty$) are given for comparison.

4.2.4. Interplay of fixed points and phase structure in $d \leq 3$

Fixed points trade their stability in collisions in the space of couplings that occur at particular values of N and M , see, e.g., [23], where one critical exponent vanishes. These are distinct from fixed-point annihilations in which the two fixed points collide and then disappear into the complex plane. In a stability trading collision, both fixed points continue to exist after the collision, and simply “pass through” each other on the real line. As stability trading must involve fixed-point collisions, a fixed point can only become (un)stable, if it approaches another fixed point. At the collision point, the fixed-point action of both fixed points is the same. Therefore, collisions between specific classes of fixed points cannot occur. In particular, tetracritical ($\Delta > 0$) and bicritical ($\Delta < 0$) fixed points cannot collide with each other due to the different location of the minima of the potential. Both types of fixed points can however collide with the IFP since the IFP interpolates between both types. In that collision, they pass through the surface $\Delta = 0$ and thereby change their nature from bi- to tetracritical and vice versa. Note that it is not a contradiction that the RG flow for a given theory, at fixed N and M cannot pass through the symmetry enhanced surface $\Delta = 0$, while the location of fixed points under variations of N and M , i.e., for different theories, can, of course, pass through that surface. With the choice of the evaluation point of the anomalous dimensions, some of the critical exponents jump as soon as the collision partner of the IFP changes its nature. However, as the anomalous dimensions themselves and the third critical exponent change continuously, that discontinuity is not relevant in the following.

In what follows, we concentrate on the case $N = M$. Moreover, we focus on fixed points with an explicit $\phi \leftrightarrow \chi$ exchange symmetry and do not explore possible fixed points which do not share that symmetry.

Review of stability trading in $d = 3$

The case of $d = 3$ has been explored extensively [11, 16, 19, 21, 39–43, 200], also with FRG methods [22, 24, 44], where stability trading was discussed in detail in [23]. Here, we briefly review the mechanism, and benchmark the pseudo-spectral method by comparing our LPA' results to previous results.

The DFP is stable at large N , and loses its stability in a collision with the tetracritical BFP at $N = N_{\text{crit,DFP}} = 1.38$, cf. Fig. 4.11 (left panel). This lies at a slightly higher value than that obtained by perturbative methods, cf. [21]. Towards smaller N , the BFP approaches the IFP, as its mixed couplings $\lambda_{i,j}$, $i, j \neq 0$, grow. It collides with the IFP at $N = N_{\text{crit,IFP}} = 1.15$. Again, this estimate is slightly above that obtained in [21], and agrees – as it should – with the FRG result in [24] that employed the shooting method. “Tunneling” through the IFP, cf. Fig. 4.11 (right panel), the BFP becomes bicritical, as its mixed couplings continue to grow. At $N = 1$, the BFP is a bicritical fixed point, with the minima of the potential lying along the axes in field space. Rotating this fixed point by $\pi/4$ in field space reproduces the DFP at $N = 1$. In fact, as discussed above, this exact symmetry is only true in LPA. However, also within LPA', the rotation of the BFP by $\pi/4$ in field space features a vanishing mixed coupling $\lambda_{1,1} = 0$ at $N = 1$, which is the defining property of the DFP. Thus, we conclude that the BFP and RDFP are degenerate in $d = 3$. In particular, they remain degenerate away from $N = 1$, i.e., the existence of the BFP can be viewed as arising from the existence of the single-field Wilson-Fisher fixed point, combined with the rotational symmetry of the fixed-point equation.

This picture of stability trading and the degeneracy of the RDFP and the BFP persist down to $d \approx 2.8$, where additional fixed points appear.

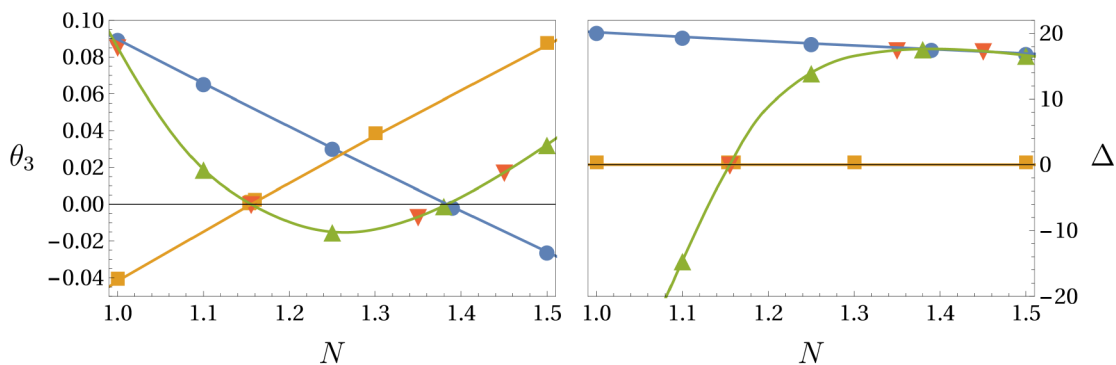


Fig. 4.11.: The third critical exponent (left panel) and Δ (right panel) of the DFP (blue dots), IFP (orange squares), BFP (green triangles/red inverted triangles) as a function of N for $d = 3$. The IFP divides the bicritical region ($\Delta < 0$) from the tetracritical region ($\Delta > 0$). The BFP collides with the DFP at $N = N_{\text{crit,DFP}} = 1.38$ and with the IFP at $N = N_{\text{crit,IFP}} = 1.15$.

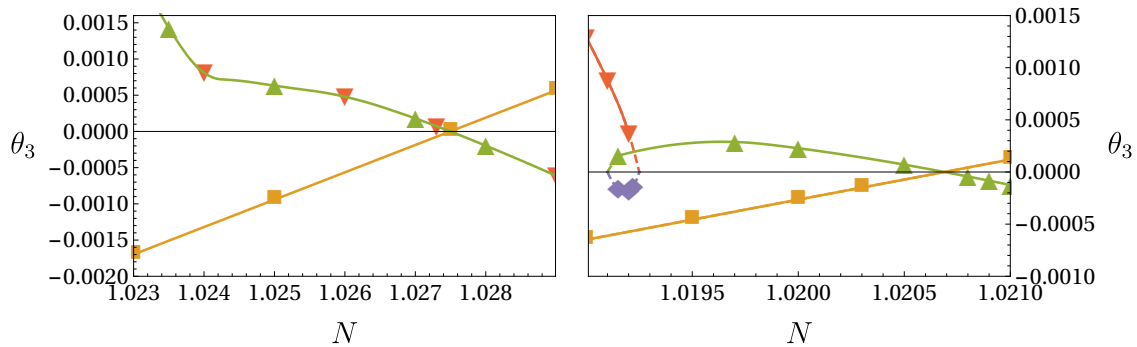


Fig. 4.12.: We show the third critical exponent of the IFP (orange squares) and the BFP/RDFP (green/red inverted triangles) in $d = 2.88$ within LPA (left panel) and $d = 2.87$ (right panel), where two additional bicritical fixed points (red inverted triangles and purple diamonds) exist. The second bicritical fixed point, indicated by red inverted triangles corresponds to the rotation of the DFP at $N = 1$. In $d = 2.88$, the BFP and RDFP are still degenerate.

Appearance of new fixed points for $d < 3$

A pair of new fixed points appears below $d = 3$. Its influence can already be detected in the left panel of Fig. 4.12: There, the third critical exponent of the BFP/RDFP exhibits a slight kink near $N \approx 1.024 < N_{\text{crit,IFP}}$. That kink is due to a pair of fixed points that still lies within the complex plane at that value of d , but already starts to approach the BFP. At a slightly lower value of d , that pair emerges from the complex plane at $N = N_{\text{em}}$, cf. right panel of Fig. 4.12. As soon as these new bicritical fixed points appear, the degeneracy between the BFP and the RDFP is lifted. As $N_{\text{crit,IFP}} > N_{\text{em}}$, the BFP is bicritical in that region as well, allowing it to collide with one of the new fixed points. At that collision point, they move off into the complex plane. Thus, one of the newly appearing fixed points has a rather short “lifespan”, emerging from the complex plane at $N_{\text{em}} = 1.01925$, and disappearing at $N_{\text{ann}} = 1.0191$ (in LPA). It serves as the annihilation partner of the BFP. In that process, the second new bicritical fixed point is left behind and continues to exist for lower N . At $N = 1$, it can be rotated by $\pi/4$ in the space of fields, where it maps onto the DFP. Continuing to lower d , the new fixed points play a more important role, as they take part in stability trading mechanisms.

Separation of stability trading mechanisms in $d \approx 2.7$

At $N_{\text{crit,DFP}}$, the tetracritical BFP trades stability with the DFP for all $d \leq 3$. However, it ceases to trade stability with the IFP, which instead finds a new trading partner. Hence, the stability trading of IFP and DFP becomes disconnected, i.e., the stability is no longer transmitted between the two by a single fixed point, cf. Fig. 4.13. Instead, the trading partner of the IFP never approaches the DFP.

Towards lower d , $N_{\text{crit,IFP}}$ decreases. The major change in the stability trading mechanism occurs when $N_{\text{crit,IFP}} \lesssim 1$, where the IFP finds a new trading partner. The dynamics

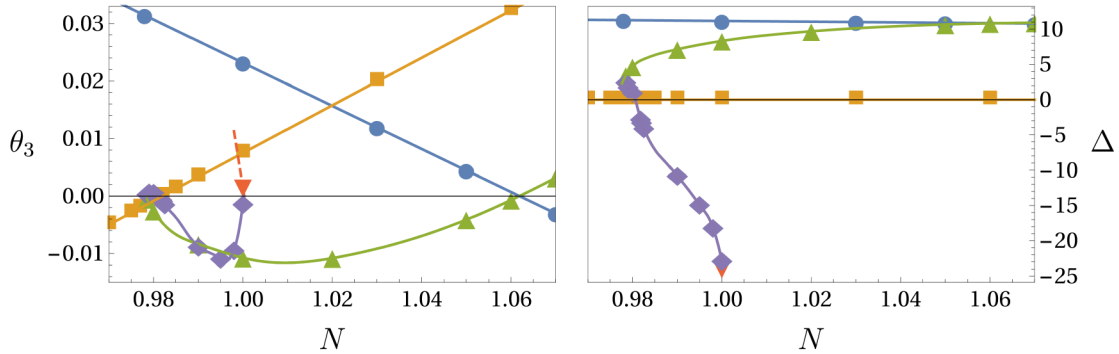


Fig. 4.13.: The third critical exponent (left panel) and Δ (right panel) of the DFP (blue dots), IFP (orange squares), BFP (green triangles), RBFP (purple diamonds) and RDFP (red inverted triangles) as a function of N for $d = 2.7$. The IFP divides the bicritical region ($\Delta < 0$) from the tetracritical region ($\Delta > 0$). The stability trading occurs between IFP and RBFP at $N = N_{\text{crit,IFP}} = 0.98$, as well as BFP and DFP at $N = N_{\text{crit,DFP}} = 1.06$.

underlying this change of stability trading is clearly visible by comparing Figs. 4.14 and 4.13 (right panel): When the new bicritical fixed point first appears, it annihilates with the BFP at N_{ann} at a point in the space of couplings, where $\Delta < 0$, cf. Fig. 4.14. Towards lower d , we observe that $\Delta(N_{\text{ann}})$ increases, i.e., the annihilation of the BFP occurs at larger values of Δ . Thus the annihilation point of the BFP starts to move closer to its collision point with the IFP. Finally, $\Delta(N_{\text{ann}}) > 0$, and therefore the BFP remains tetracritical over its entire lifespan, cf. Fig. 4.13 (right panel). As soon as $\Delta > 0$ at N_{ann} , the collision partner of the IFP must change. Hence, the new bicritical fixed point collides with the IFP, trades stability, thereby becoming tetracritical, and can then annihilate the BFP at N_{ann} , where $\Delta > 0$. For $N = 1$, these two annihilation partners can actually be related by an (approximate) $\pi/4$ rotation in field space, i.e., the new collision partner of the IFP is the RBFP.

Note that within LPA', additional fixed points appear for tiny ranges of N , close to the collision point with the IFP. These are not present within LPA. We thus tentatively discard them as truncation artifacts, and discuss the mechanisms that we observe within LPA, even

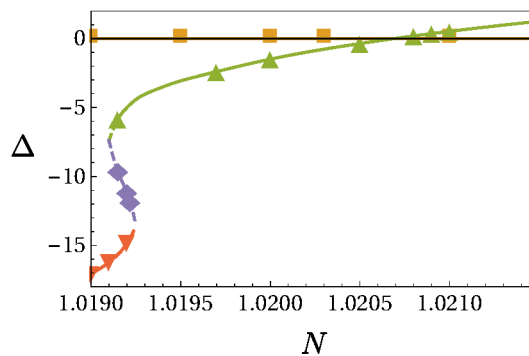


Fig. 4.14.: We plot Δ in $d = 2.87$ (within LPA) as a function of N for the IFP (orange squares), the BFP (green triangles), the RDFP (red inverted triangles) and the RBFP (purple diamonds). The IFP divides the bicritical region ($\Delta < 0$) from the tetracritical region ($\Delta > 0$). The BFP is still the collision partner of the IFP.

when referring to numerical values for N_{crit} etc. from LPA'.

Coexisting stable fixed points

In $d = 2.7$, we first observe the new property of coexisting stable fixed points. Usually, one might expect that the critical behavior in bosonic systems only depends on the long-range degrees of freedom, the symmetries and the dimensionality. Here, there are two fixed points that are simultaneously stable for $0.98 < N = M \lesssim 1$, and underly possible continuous phase transitions. These two are the BFP, and the newly generated bicritical fixed point, the RBFP, cf. Fig. 4.13.

These two imply very distinct phase diagrams in the vicinity of the multicritical point. The tetracritical BFP implies the existence of a fourth, mixed phase, however, the other fixed point is bicritical, preventing the formation of a mixed phase. To decide which of the two stable fixed points is dominant for low-energy physics, we conjecture that the sign of Δ at the extremum/saddle point is all the additional information that is required in this case. We assume that microscopic models with $\Delta > 0$ most likely flow towards the BFP, and exhibit tetracritical behavior. Microscopic models with $\Delta < 0$ conversely flow towards the RBFP and exhibit bicritical behavior. It would be interesting to understand whether Δ corresponds to a microscopic parameter in realistic models, or whether it can be related to a macroscopic parameter, just as the mass-like couplings in these models which can be related to the temperature or magnetic field.

A related property, namely that universality classes can depend on the presence of unbroken ‘‘spectator symmetries’’ has been discussed in [12]. In fermionic systems, coexisting stable fixed points are a common phenomenon, see, e.g., [72, 220, 224, 225]. In these cases, there is a unique fixed point with zero relevant directions, but there exist several fixed points with one relevant direction. To our best knowledge, ours is the first example of coexisting stable fixed points in bosonic systems.

Stability trading in $d = 2.5$

The only change between $d \approx 2.7$ and $d \lesssim 2.5$ lies in the properties of the IFP’s collision partner. At $N = 1$, the collision partner of the IFP is always bicritical, cf. Fig. 4.15 (right panel), and can thus be related to one of the two tetracritical fixed points, the DFP or the BFP, by an (approximate) $\pi/4$ rotation in field space. In $d \approx 2.7$, that relation is with the BFP, i.e., the collision partner of the IFP is the RBFP. Towards $d \approx 2.5$, $N_{\text{crit,DFP}}$ approaches 1, the BFP and the DFP become more similar to each other at $N = 1$. Accordingly, so do their rotated counterparts, the RBFP and the RDFP. For $d = 2.63$ (within LPA'), $N_{\text{crit,DFP}} = 1$, and the DFP and BFP lie on top of each other at $N = 1$. At that point, the rotated counterparts must be degenerate as well. Actually, this happens slightly before $N_{\text{crit,DFP}} = 1$ at $d \approx 2.69$ in LPA', since the rotation in field space is not exact. Thus, at

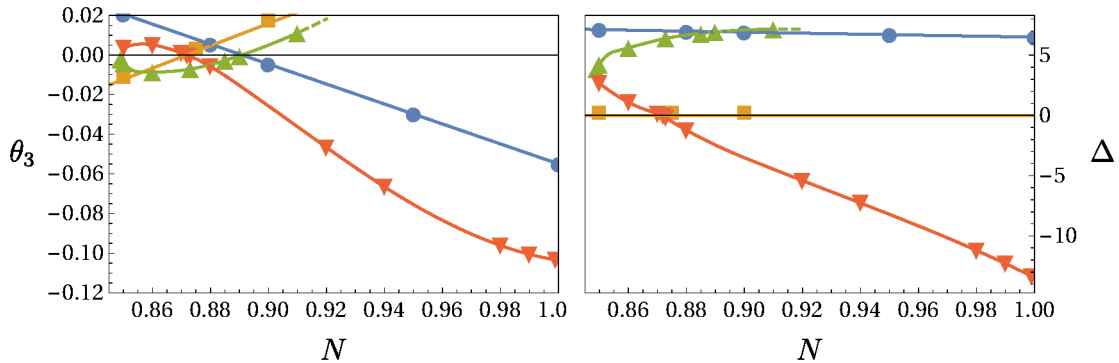


Fig. 4.15.: The third critical exponent (left panel) and Δ (right panel) of the DFP (blue dots), IFP (orange squares), BFP (green triangles) and RDFP (red inverted triangles) as a function of N for $d = 2.5$. The IFP divides the bicritical region ($\Delta < 0$) from the tetracritical region ($\Delta > 0$). The BFP collides with the DFP at $N = N_{\text{crit,DFP}} = 0.89$. The IFP collides with the RDFP at $N = N_{\text{crit,IFP}} = 0.87$.

lower d , the bicritical stability trading partner of the IFP is the RDFP, cf. Fig. 4.16.

There is a significant region in which more than one fixed point is stable, cf. Fig. 4.15 (left panel). In particular, there are ranges of N for which the DFP is simultaneously stable with the RDFP. Moreover, the IFP is simultaneously stable with the BFP. Again, there is never more than one stable fixed point in each of the three separate regions of the theory space, $\Delta > 0$, $\Delta = 0$ and $\Delta < 0$ (imposed as global conditions). In the case of the IFP being stable, more information is required than only the sign of Δ to determine which of the possible universality classes dominates low energy physics since the hypersurface $\Delta = 0$ may be attractive also for theories starting at $\Delta \geq 0$. The coexistence of two stable fixed points, that we have first observed in $d \approx 2.7$, continues to the case $d = 2.5$. In particular, it now includes the region $N = M = 1$, at least in our approximation.

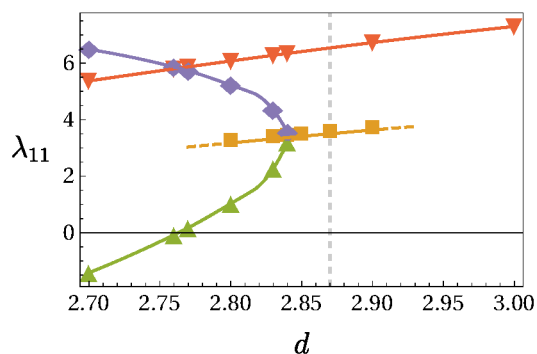


Fig. 4.16.: The coupling $\lambda_{1,1}$ of the IFP (orange squares), BFP (green triangles), RBFP (purple diamonds) and RDFP (red inverted triangles) as a function of d for $N = 1$ (within LPA). The gray dashed line shows the point at which the two new bicritical fixed points emerge. The plot summarizes the main changes in the stability trading: As $N_{\text{ann}} = N_{\text{crit,IFP}} = 1$, the stability trading partner of the IFP changes from the BFP to the RBFP. When the RBFP and the RDFP become degenerate, the IFP again changes the stability trading partner from the RBFP to the RDFP.

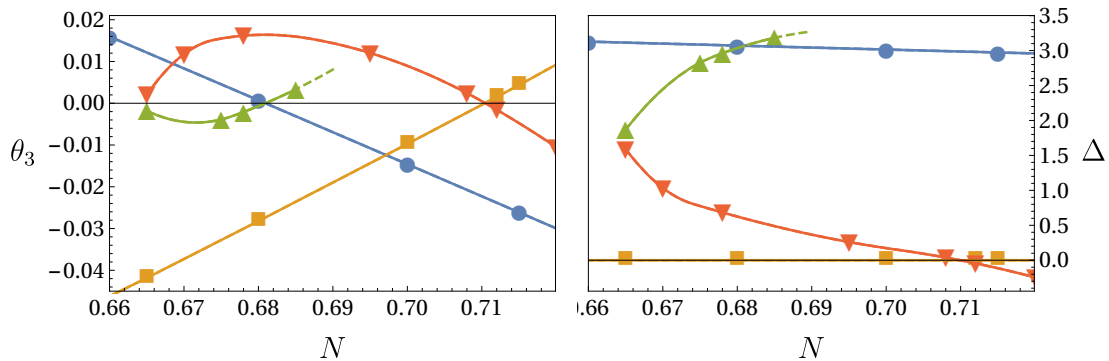


Fig. 4.17.: The third critical exponent (left panel) and Δ (right panel) of the DFP (blue dots), IFP (orange squares), BFP (green triangles), and RDFP (red inverted triangles) as a function of N for $d = 2.2$. The IFP divides the bicritical region ($\Delta < 0$) from the tetracritical region ($\Delta > 0$). The BFP collides with the DFP at $N = N_{\text{crit,DFP}} = 0.68$. The IFP collides with the RDFP at $N = N_{\text{crit,IFP}} = 0.71$.

Stability trading towards $d = 2$: Overlapping stability regions of the DFP and the IFP

Towards lower d , $N_{\text{crit,IFP}}$ and $N_{\text{crit,DFP}}$ approach each other. Finally, both stability regions touch and then start to overlap. Note that the DFP and the IFP can never be degenerate. Whereas the IFP still lies in the plane of enhanced symmetry $\Delta = 0$, the DFP must stay tetracritical $\Delta > 0$. Thus, collisions between them are excluded. This also holds for the case, where both scaling solutions change stability at the same value of N . Viewed in the space of couplings, the two stability trading fixed-point collisions occur at rather different positions, similar to the case shown in Fig. 4.17 (right panel), even if they accidentally occur at the same value of N .

The collision partners of the IFP and DFP are the RDFP and BFP, respectively. Figure 4.17 (left panel) depicts the situation where both the stability regions of the DFP and IFP overlap, $N_{\text{crit,DFP}} < N_{\text{crit,IFP}} < 1$ at $d = 2.2$, which is another instance of two coexisting stable fixed points. Note that our estimates for $N_{\text{crit,I/DFP}}$ are not yet quantitatively exact, cf. Sec. 4.2.6.

4.2.5. Summary: Stability trading between $d = 3$ and $d = 2$

We summarize the mechanisms of stability trading. There are two kinds of fixed-point potentials, tetracritical fixed points, as the DFP, and bicritical fixed points. The bicritical IFP is a special fixed-point solution with $\Delta = 0$ everywhere in field space. The DFP can collide only with another tetracritical fixed point whereas the IFP can trade stability with either tetra- or bicritical fixed points, changing their nature ($\Delta \gtrless 0$) within the process. At $N = M = 1$, the DFP and BFP imply the existence of two further fixed points, the RDFP and RBFP. These fixed-point potentials are bicritical and related to the DFP and BFP, respectively, by an (approximate) $\pi/4$ rotation in field space.

Figure 4.18 summarizes the stability regions of the IFP, DFP and BFP in LPA and LPA'.

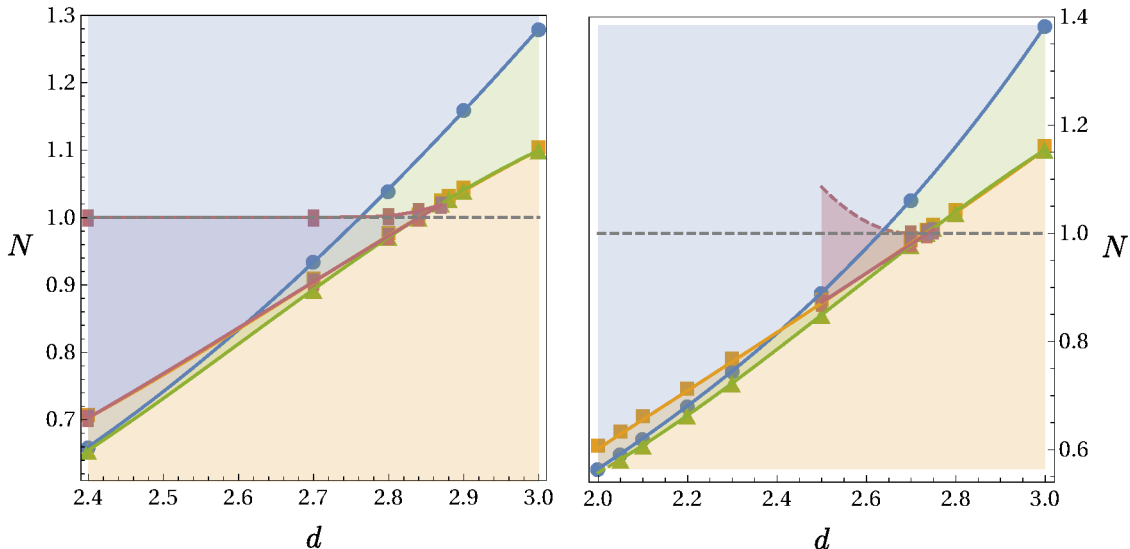


Fig. 4.18.: Stability regions of the DFP (blue circles), IFP (orange squares), BFP (green triangles) and the R(B/D)FP (mauve rectangles) as a function of N and the dimension. The DFP is stable in the blue region (between blue line and large N), the IFP in the light-orange region (between orange line and small N), the BFP in the light green region (between green and blue line) and the R(B/D)FP in the mauve region (between the mauve lines). The left panel is for LPA, the right one for LPA'. In LPA', we can only give an estimate for the upper stability bound of the R(B/D)FP (dashed mauve line). In fact, it extends to $d = 2$, which is not depicted here. The lower bound continues on the orange line.

In $d = 3$, the stability between the IFP which is stable for low N and the DFP being stable for large N is traded by the BFP. For $N < N_{\text{crit,IFP}}$, the BFP is bicritical and coincides with the RDFP. Within the collision with the IFP, it becomes stable and tetracritical and can, therefore, trade stability with the DFP. As long as $N_{\text{crit,IFP}} > 1$, the stabilization of the IFP and the destabilization of the BFP occur simultaneously. For $d < 3$ close to $N_{\text{crit,IFP}} = 1$, the degeneracy of the BFP and RDFP is lifted as a pair of bicritical fixed points emerges from the complex plane. One of these new fixed points is partly stable. We obtain regions of simultaneously stable fixed points. The stability region of the new, stable, bicritical fixed point is depicted as well in Fig. 4.18 (appearance of mauve region). Note that this bicritical fixed point is called RBFP at first, and later RDFP, as it corresponds to a rotation of the BFP, or DFP at $N = 1$, respectively. For $d \lesssim 2.7$, the IFP trades stability with the new, stable, bicritical fixed point instead of the BFP, thus the two lines separate. The stability loss of the IFP, and the stability gain of the DFP occur in collisions with two different fixed points. This enables that the stability region of the DFP and IFP overlap for lower d .

Interestingly, there is always only one stable fixed point in each of the separate regions of the theory space $\Delta < 0$, $\Delta = 0$ and $\Delta > 0$. This tweaks the usual expectation that the universality class of the stable fixed point is determined solely by the dimensionality, symmetries and long-range degrees of freedom in bosonic models. We conjecture that the sign of Δ in the microscopic potential decides about which universality class is realized.

4.2.6. Testing the quantitative reliability of our results

LPA and LPA', combined with a Taylor expansion, give rather good results in $d = 3$, [22], in comparison to high orders of the loop expansion [19, 21], at a very manageable computational complexity. As we have seen in Sec. 4.2.3, the Taylor expansion breaks down towards $d = 2$ and we, therefore, resort to nonlocal methods. Moreover, momentum-dependence is becoming more important, indicated, e.g., by the growth of the anomalous dimension. Thus, we expect that our estimates for $N_{\text{crit,IFP}}$ and $N_{\text{crit,DFP}}$ are not fully accurate in the limit $d \rightarrow 2$.

Comparing LPA and LPA' in Fig. 4.18, the stability boundaries are shifted to lower values of d in LPA'. The point where the DFP and IFP stability lines intersect lies at a different value of d , but at a similar value of N . Taking these observations into account, it is an interesting question, how far the stability lines are shifted to lower dimensions when the order of the derivative expansion is increased.

To judge the quantitative reliability of our results, we use the Onsager solution for the Ising model in $d = 2$. We can combine the scaling relation (4.15) for the DFP with the Onsager solution in $d = 2$ [177],

$$\nu_{\text{Onsager}} = 1, \quad (4.23)$$

to obtain

$$\theta_3(d = 2) = 1 + 1 - 2 = 0. \quad (4.24)$$

Thus, the DFP is on the verge of stability for the $O(1) \oplus O(1)$ model in $d = 2$. Note that for clarifying if the third eigenperturbation is marginally relevant or irrelevant, higher orders beyond the linear one have to be taken into account in the eigenvalue problem (2.23). As $\theta_3 > 0$ for the DFP in $d = 3$, and $\theta_3 = 0$ in $d = 2$, a monotonic dependence on d would suggest that $\theta_3 > 0$ for $2 < d < 3$. In our approximation, θ_3 changes sign at d_{crit} above $d = 2$, cf. Fig. 4.19. As we improve the approximation from LPA to LPA' and employ the scaling

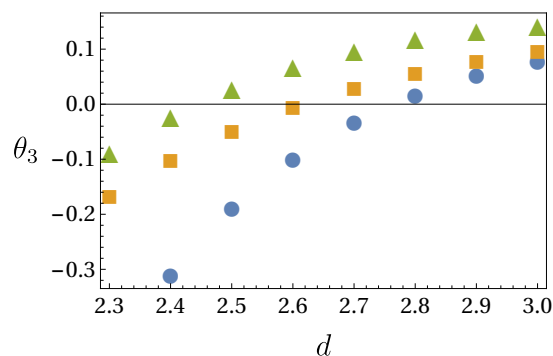


Fig. 4.19.: The third largest critical exponent of the DFP for $N = M = 1$ as a function of d is depicted. The symbols (colors) indicate different truncations: The blue dots correspond to LPA, the orange squares to LPA' and the green triangles to LPA' but employing the scaling relation (4.15).

relation, d_{crit} decreases, as expected. We find $d_{\text{crit}} \approx 2.45$ using the scaling relation and $\theta_3 \approx 0.5$ (approximately with and without the scaling relation) at $d = 2$, implying that our results are not yet quantitatively precise. Extended truncations with momentum-dependent interactions are expected to improve these results.

For the overlapping stability region of the IFP and DFP at $d = 2$, there are several possible scenarios: The overlapping region persists and is shifted to $N \approx 1$. In this case, the system of two coupled Ising models in two dimensions might either exhibit a tetracritical phase diagram with a mixed phase, or a multicritical point associated to a BKT type phase transition. In the case that the $\pi/4$ rotational symmetry holds at $N = 1$ in extended derivative expansions, the stability trading mechanisms are linked to the position of $N_{\text{crit,DFP}}$ and $N_{\text{crit,IFP}}$ with respect to $N = 1$. As $N_{\text{crit,DFP}} = 1$ at $d = 2$ is predicted by the Onsager solution, it is rather unlikely that the overlapping stability region of the IFP and DFP still exists in this case. If the overall picture of the coexistence of several stable fixed points persists, the RDFP or the RBFP potentially provide further candidates for stable fixed points, in particular in the case of the broken rotational symmetry.

4.3. Conclusions

In this chapter, we have shown the application of pseudo-spectral methods to fixed-point equations with one and two order parameters. For systems with a single order parameter, we have employed a compactification for resolving the whole field space. The existence of global fixed-point solutions is an important question, since the nonlinear differential equations encountered in FRG studies can have many stable, but local solutions. If only local information is accessible, they are hardly distinguishable from global ones. For instance, the physical criterion of polynomial boundedness is difficult to impose locally [226]. The pseudo-spectral method presented here offers a comparatively easy access to global considerations. Even if the fully global potential is not of interest, cf. Sec. 4.2, the pseudo-spectral expansion is still superior to local expansions which, for example, is visible for $d \rightarrow 2$ where arbitrarily high orders of polynomial couplings become important.

We have first considered the well known Ising model in three dimensions in both LPA and LPA'. There are numerous works on expansions for small and large fields and results gained via the shooting method which give a good notion of the global behavior of the Wilson-Fisher fixed point. We reported on the difference between LPA and LPA' truncations taking the global behavior of the potential into account. Although the anomalous dimension is very small, the asymptotic behavior, especially with regard to the prefactor, changes significantly. Besides the fixed-point potential itself, we calculated the eigenfunctions globally and determined the critical exponents. For all quantities we obtained good agreement with already known results calculated with other methods. As far as numerical accuracy is concerned, our method outperforms previous results by many orders of magnitude, while being very stable,

fast and lightweight.

Subsequently, we extended our study to fractional dimensions, taking $d = 2.4$ as a representative. We considered all multicritical fixed-point potentials (with more than one relevant direction) predicted in [67] and could moreover determine their global behavior. Especially in these cases, the structure with more than one local minimum cannot be captured within a single local expansion. We were able to see the next higher critical fixed point emerging at $d < 2.4$ which demonstrates that our numerical method is highly accurate and stable. All physical quantities, the anomalous dimension and critical exponents, again match with earlier results.

In the simple Yukawa model, fermionic and bosonic degrees of freedom respect a discrete chiral symmetry. In Sec. 5.3, we study flows of the Higgs potential in $d = 4$ where the Yukawa model is taken as a suitable reduction of the standard model for that purpose. Here, we considered $d = 3$ where it gives rise to the nontrivial Gross-Neveu fixed point. The large N_f limit provides an explicit analytical solution with which we obtained a conclusive agreement. For finite N_f , our results agree very well with other data, including $1/N_f$ -expansions and lattice methods. We determined the transition flavor number $N_t \approx 0.5766$ where the fixed-point potential goes over from the symmetric to the symmetry broken regime. The small N_f limit is not easily accessible by use of common local expansions which provides another instance for demonstrating the power of our method. We found that the fixed point Yukawa coupling grows large for $N_f \rightarrow 0$. This suggests that the Gross-Neveu fixed point does not merge with the Wilson-Fisher fixed point in the limit $N_f \rightarrow 0$, contrary to what has been anticipated in [73]. Additionally, we saw that all fluctuation terms in the Yukawa fixed-point equation which occur in the symmetry broken regime have a significant influence on physical quantities, such as critical exponents. Compared to [210] where some fluctuation terms were missed, we determine the deviation to be up to 30%.

Finally, we investigated the stability trading between the fixed points of the $O(N) \oplus O(M)$ model. As both d and $N = M$ can be treated as continuous parameters in the FRG, we explored $2 < d \leq 3$ and $N = M$ in the vicinity of $N = M \approx 1$. The system is dominated by an interplay of several fixed points, which trade stability and thus physical relevance for the critical behavior of different systems at fixed-point collisions. We observed regions of simultaneously stable fixed-point solutions. However, in each of the separate regions of the theory space, defined by the sign of Δ at the minimum or saddle point, we have only found one stable fixed point. We conjectured that this provides a criterion to decide which of the universality classes is realized in the IR. To test this conjecture, studies of RG trajectories are necessary. For the case of one order parameter, we come to that in the next chapter. For two order parameters, however, this is technically more involved and is thus left for future work.

For the low dimensional case, $d = 2$, the comparison to the Onsager solution shows that the order of derivative expansion has to be increased in order to get quantitatively precise

results.⁶ Therefore, we are not yet able to give a clear answer, which of the fixed points dominates the critical behavior at $N = M = 1$. The comparison between LPA and LPA' indicates that the mechanisms that we observed for stability trading, might only be shifted to lower d . It is an interesting question if the overlapping stability regions, in particular those of the DFP and IFP, persist. Besides the DFP and IFP, further candidates for the dominating universality class in $d = 2$ and at $N = M = 1$ might be provided by the RDFP or RBFP. Our conjecture could be tested employing, e.g., lattice simulations.

Another interesting region of the phase diagram is around $N = 1$ and $M = 2$ corresponding to anisotropic antiferromagnets. The nature of the multicritical point, explored in [32, 33], see also references therein, can be further clarified, and connected to experimental results in quasi-two-dimensional systems [227–233].

We already mentioned the existence of multicritical solutions in the sense of Sec. 4.1 in the decoupled and symmetry enhanced sector. We anticipate that there are new fixed points, such as generalizations of the BFP, which are unique to two field models. Thus, stability-trading mechanisms as the ones that we have discussed here, could also be relevant for each of the multicritical sectors. It would be interesting to explore this conjecture further.

⁶We emphasize, that once the flow equations of the NLO system are calculated, solving them is straightforwardly doable with our method.

5. Solving functional flow equations via pseudo-spectral methods

Plenty of information can already be retrieved from the fixed-point structure of the theory as we have seen in the previous chapter. On the other hand, it turned out that for a clear discussion of, e.g., the phase diagram of the $O(N) \oplus O(M)$ model, functional flows need to be considered. Also phase transitions of first order, systems far away from criticality, or the fate of metastabilities of the Higgs potential are suitable examples which require the solution of full functional flows. As discussed for fixed-point equations, Taylor expansions cannot resolve nonlocal behavior. Moreover, it may give a wrong indication for the flow towards the IR if the convergence radius shrinks.

In this chapter, we solve functional flows with the help of pseudo-spectral methods in order to capture also nonlocal information. In the first section, we again benchmark the method considering the $O(N)$ model in the large N limit and for finite N in $d = 3$. The occurrence of convexity poses one of the most challenging problems to the convergence of pseudo-spectral methods. We discuss how close the singularity can be approached. We finally consider flows between two (multicritical) fixed points, the tricritical one and the Wilson-Fisher one in $d = 2.4$, cf. Sec. 4.1. We find a separatrix connecting the multicritical fixed point and the Wilson-Fisher fixed point.

Whereas these potentials grow arbitrarily large for increasing field, we additionally consider bounded potentials in quantum mechanics. The energies of the first eigenstates can be deduced from the flow and compared to the exact values obtained from the solution of the Schrödinger equation. From a technical view point, the flow has interesting properties. These investigations can be taken as a notion of a nonperturbative flow of potentials which are reminiscent to those employed in Higgs inflation models.

In the last part of this chapter, we consider a simple Higgs-Yukawa model which features the most important degrees of freedom relevant for the investigation of Higgs-mass bounds and vacuum stability. Employing the FRG, we particularly discuss the lower mass bound, also in presence of higher field operators in the microscopic action which are perturbatively nonrenormalizable, and a potential metastable phase. These results are compared to those of polynomial expansions and mean-field calculations.

We use the expansion (3.13) of the potential as a function of the field invariant ρ and the RG scale k . We consider flows on a finite field range $[0, \rho_{\max}]$, typically starting from a

UV cutoff Λ and integrating down to an effective scale k_{IR} . Generally, k_{IR} is chosen to be small enough such that the characteristic scales of the theory do not depend significantly on the remaining momentum scales $k < k_{\text{IR}}$. These low momentum modes mainly affect the nonconvex regions of the potential, but do not modify the outer part. The dependence of the potential, in particular the inner region, on k_{IR} may be interpreted as a scheme dependence describing the effect of different coarse graining procedures, cf. [61]. For quantum mechanics, no UV regularization is needed and Λ can be sent to infinity.

To ensure the absence of boundary effects, the potential should actually be considered on the global domain $[0, \infty)$ as it is done for the bounded potentials in Sec. 5.2. Resolving the dynamics on that infinite interval is numerically challenging but possible via pseudo-spectral techniques. For a finite interval, ρ_{max} could be understood to be a parameter of a truncation scheme the potential may depend on.⁷ However, if the potential is unbounded from above for large field values, it is practically sufficient to choose the value of ρ_{max} such that the physically relevant field range is resolved without observing a significant scheme dependence. The fluctuations are damped for large values of the potential.

The time interval is divided into patches with approximately 10 coefficients which are joined by imposing continuity conditions. The field domain is decomposed into subdomains which not only increases the efficiency of the algorithm but also the resolution, i.e., in regions where the potential gives rise to singular structures.

The content of this chapter follows the line of argument of [140] and [141].

5.1. Flows of the $O(N)$ model

We take the same ansatz for the effective average action, Eq. (2.33), as in Sec. 4.1.1. We use the flow equation for the first derivative of the potential (2.35). The scalar anomalous dimension obeys Eq. (2.36). In the first part of this section, we set $\eta_\phi \equiv 0$ ($Z_{\phi,k} \equiv 1$) which becomes exact in the large N limit. In the second part, we take the scale dependence of the wave function renormalization into account.

5.1.1. Flows for large N in $d = 3$: A comparison

In the large N limit, the flow is analytically solvable by the method of characteristics [175]. This offers the opportunity to easily demonstrate the accuracy of pseudo-spectral flows. For that purpose, we choose trajectories in the symmetry broken phase close to criticality to show stability of the numerical method over 5 orders of magnitude ($t \in [0, -12.4]$). We use

⁷Note that this is more or less a technical viewpoint. Practically, the influence of boundary effects decides if this problem is well-defined.

Eqs. (2.35) and (2.36) in the limit $N \rightarrow \infty$ [175],

$$\begin{aligned}\partial_t u' &= (-2 + \eta_\phi)u' + (d - 2 + \eta_\phi)\rho u'' - 2v_d u'' l_1^{(B)d}(u'; \eta_\phi), \\ \eta_\phi &= 0,\end{aligned}\tag{5.1}$$

where an appropriate rescaling has been taken into account. We switch to dimensional quantities as soon as the VEV starts scaling exponentially in t . We expand the first derivative of the potential on $[0, 0.2]$ for the dimensionless and on $[0, 0.2k_S]$ for the dimensional flow, where k_S is the scale of switching between both regimes. With this choice, the maximal field value is 10 – 20 times larger than the VEV which is large enough to avoid boundary effects.

The initial condition reads

$$U'_\Lambda(\bar{\rho}) = -0.008443603515625 + 0.5\bar{\rho}\tag{5.2}$$

at $t = 0$ or $k = \Lambda$, where Λ is the UV cutoff. All dimensional quantities are to be understood in units of Λ , which we set to 1. For switching to the dimensional version of the flow (5.1), we choose $t_S = \ln(k_S/\Lambda) = -10.1$. Furthermore, the temporal subdomains and the number of coefficients in time direction are taken to achieve exponential convergence down to machine precision. In order to compare the analytical potential [175] with the numerically computed one, we employ the maximum norm of their difference as error criterion.

In Fig. 5.1, the absolute deviation between the numerical and the analytical flow in dependence of the number of the coefficients in field direction N_p can be seen. The flow was compared at two scales: $t = -10$ ($k = 4.5 \cdot 10^{-5}$), before switching to dimensional quantities, and $k = 4 \cdot 10^{-6}$ ($t = -12.4$), after switching to dimensional quantities, where we have stopped the integration. We also depict the relative error of the dimensional VEV $\bar{\kappa}$ at this

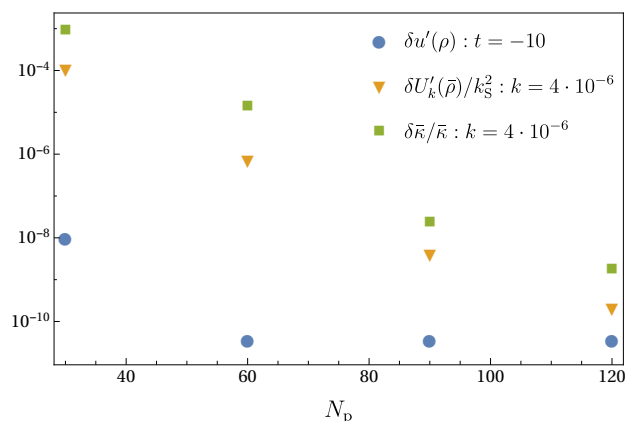


Fig. 5.1.: Absolute and relative error ($\delta u'(\rho)$, $\delta U'_k(\bar{\rho})$ and $\delta \bar{\kappa}/\bar{\kappa}$) of the first derivative of the potential and the VEV, respectively, as a function of the number of coefficients N_p in field direction. The errors $\delta U'_k(\bar{\rho})$ and $\delta \bar{\kappa}/\bar{\kappa}$ decrease. For the error of $u'(\rho)$ at $t = -10$, one can see a plateau which is due to the condition of the differential equation. This indicates that the solution is accurate to almost machine precision.

scale. The more coefficients are taken into account, the higher the accuracy, which can be seen by the decrease of $\delta U'(\bar{\rho})$ and $\delta \bar{\kappa}/\bar{\kappa}$ in particular. For the error $\delta u'(\rho)$ at $t = -10$, we see a plateau for $N_p \gtrsim 60$. This can be explained by the condition of the differential equation. To illustrate this, we compare two analytically computed solutions, one with the initial condition (5.2), and the other with a small deviation from it. To obtain an error of about $\sim 10^{-11}$ at $t = -10$, one can allow for a deviation of 10^{-18} for the constant term, and 10^{-16} for the linear term, which is about the order of magnitude that we can resolve with `long double`. This example indicates how accurately the time integration has to be done for staying close to the original trajectory. On the other hand, it shows that we have integrated out the flow close to machine precision over many orders of magnitude for $N_p \gtrsim 60$. This fact is supported by the exponential convergence till $\sim 10^{-18}$ of the coefficients.

For the IR flow, the decrease of the error is slower, but still tends to the lower bound $\sim 10^{-11}$ for a large number of coefficients. The error is now dominated by the truncation error of the expansion of the potential in field direction since convexity starts to set in. From the asymptotic decrease of the last coefficients for $N_p \gtrsim 60$, we obtain a measure for the truncation error which agrees very well with the errors depicted in Fig. 5.1. It is based on an estimate for the sum over the neglected coefficients. In order to achieve machine precision, more coefficients are needed.

We conclude that the pseudo-spectral flow is highly efficient in a large part of theory space, and we generically observe exponential convergence for an increasing number of Chebyshev coefficients. Therefore, we concentrate in the following on the most challenging part of theory space involving the built-up of nonanalyticities, whose first adumbration we just started to discuss.

5.1.2. Flows for $N = 1, 4$ in $d = 3$

In the spontaneously symmetry broken phase, the effective potential is nonconvex in the field for all intermediate scales $k > 0$. On the other hand, by definition of the effective action as a Legendre transform of the Schwinger functional (2.2), the effective action and particularly its potential has to be convex at $k = 0$, see e.g., [122, 234], even in LPA. Technically, convexity of the effective potential is generated by singularities in the bosonic propagators, in particular in the radial mode as we see at the end of Sec. 5.2, entering the threshold functions. In Eq. (2.34), the bosonic threshold function $l_0^{(B)d}$ corresponding to the regularized radial propagator is proportional to

$$l_0^{(B)d} \sim \frac{1}{1 + u' + 2\rho u''}, \quad (5.3)$$

which exhibits a singularity at $u' + 2\rho u'' \rightarrow -1$, or $u' \rightarrow -1$ for small ρ or small absolute value of u'' . The flow avoids this singularity by renormalizing the negative curvature of the

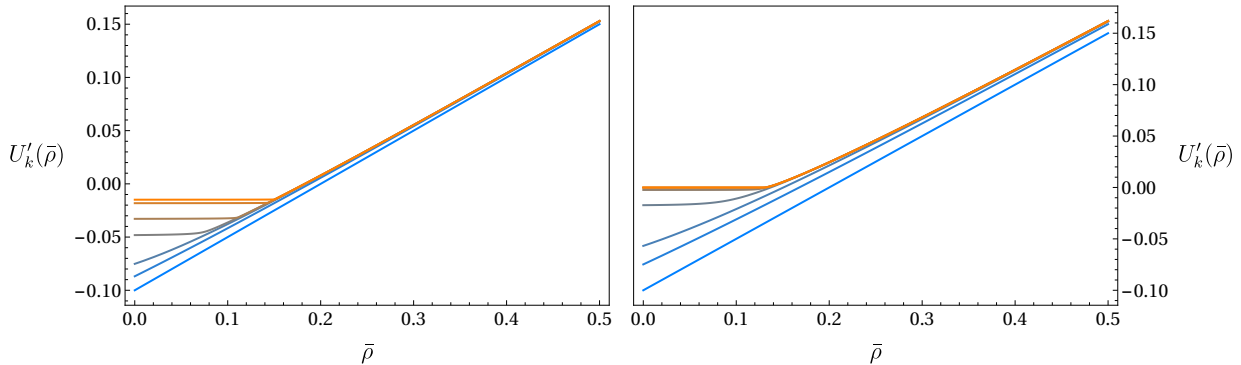


Fig. 5.2.: Evolution of $U'_k(\bar{\rho})$ from blue (bottom) to orange (top) for $N = 1$ (left panel; $t = 0, -0.5, -1, -1.5, -1.7, -2, -2.1$) and $N = 4$ (right panel; $t = 0, -0.5, -1, -2, -3, -4, -5, -13$). Convexity is seen in the flattening of $U'_k(\bar{\rho})$ for small fields $\bar{\rho} < \bar{\kappa}$. Whereas $U''_k(\bar{\rho})$ is still continuous for $N = 4$, in the single-scalar case a jump occurs.

potential in the inner region $0 \geq \partial^2 U_k(\bar{\phi}) / \partial \bar{\phi}^2 \sim k^2(u' + 2\rho u'') \gtrsim -k^2 \rightarrow 0$ with $k \rightarrow 0$. This establishes convexity for $k \rightarrow 0$. While the outer region ($\bar{\rho} > \bar{\kappa}$) already is convex, the inner region ($\bar{\rho} < \bar{\kappa}$) becomes flat during the IR flow. Since the radial mass does not vanish for $N = 1$, the curvature jumps at the VEV at $k = 0$. By contrast for $N > 1$, the influence of Goldstone bosons partly suppresses this nonanalyticity.

We picked out two particular values for N , namely $N = 1$ and $N = 4$. The following calculations are done with the dimensional version of Eq. (2.35) since we choose the initial condition to be far from criticality, $U'_\Lambda(\bar{\rho}) = -0.1 + 0.5\bar{\rho}$ at $k = \Lambda$, where a fast growth of the dimensionless couplings already sets in close to Λ . It is convenient to use the logarithmic time scale t instead of k . After a few orders of magnitude dimensional scaling can be observed.

Figure 5.2 depicts the evolution of $U'_k(\bar{\rho})$ for $N = 1$ and $N = 4$, from large to small scales. The approach to convexity is clearly visible. The built-up of the corresponding nonanalyticity can be monitored over a range of scales, especially for $N = 4$. As $U'_k(\bar{\rho})$ for $N = 1$ has an edge at $\bar{\kappa}$ at $k = 0$ where $U''_k(\bar{\kappa})$ jumps, the flow is numerically much harder to track and finally breaks down earlier. The reason is as follows: Exponential convergence of the coefficients is only guaranteed if the function is analytical as discussed in Sec. 3.2. For $k = \Lambda$, the convergence of the coefficients in field direction is very fast. Plateaus that build up for higher order coefficients are on the level of the machine precision. However, for low scales k , the requirement for exponential convergence is not fulfilled anymore. Thus, we observe a slower convergence of the coefficients till it breaks down. Although this problem cannot be avoided completely, there are two possibilities for improvement. On the one hand, one can simply take more coefficients. This will not cure the problem completely since the convergence becomes too slow and finally, an unacceptably large number of coefficients is needed. On the other hand, one can choose the domains in such a way that the nonanalyticity lies close to the boundary of two neighboring domains. For that reason, we have used 24 or 16 domains for $N = 1$ or $N = 4$, respectively. The high accuracy of pseudo-spectral

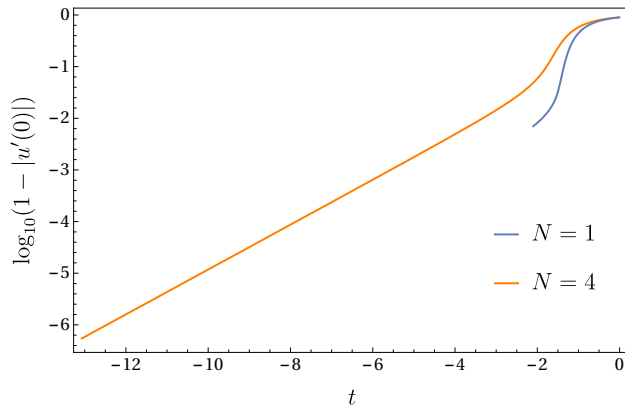


Fig. 5.3.: $u'(0)$ approaches the singularity -1 for $t \rightarrow -\infty$. Due to the stronger nonanalyticity in the single-scalar case, the numerically computed flow ceases to exist earlier.

methods prevents the flow to erroneously jump over the singularity of the propagator for a long time. Figure 5.3 shows how the flow approaches the singular point. Due to the reasons given above, for $N = 4$, we get closer to $u'(0) = -1$ in comparison to $N = 1$.

We have shown that pseudo-spectral methods can also be applied to numerically challenging problems, such as convexity. The convergence of the expansion coefficients is strongly connected to the properties of the solution. Therefore, it is not surprising that the numerical effort increases the closer the singularity is approached. We emphasize that there are other approaches, e.g., [127, 136], which are adjusted to tackle convexity issues. Pseudo-spectral methods have the striking advantage that the error is controllable by the convergence pattern of the expansion coefficients, which was especially demonstrated in the previous section. Here, we have used domains, whose boundaries were fixed during the flow. If one is generally interested in convexity mechanisms, less domains and coefficients are needed, when the boundaries are adapted to the flow of the singularity. On the other hand, if only IR quantities are of interest, e.g., the VEV, they can be inferred from the flow before convexity becomes challenging. We obtain $\bar{\kappa} = 0.183$ for $N = 1$ and $\bar{\kappa} = 0.130$ for $N = 4$ and the radial mass $\bar{m}^2 = 2\bar{\kappa}U''_{\text{eff}}(\bar{\kappa}) = 0.168$ for $N = 1$. It is worth mentioning that the VEV for $N = 4$ deviates by 2% from the VEV derived from the analytical large N solution. That indicates that the large N limit already is a proper approximation for the $N = 4$ case.

5.1.3. Flow between two critical regimes for $N = 1$

In the previous section, we have investigated flows far from criticality. As discussed in Sec. 4.1, for $d < 4$ nontrivial fixed points occur. The first one is the well known Wilson-Fisher fixed point. Lowering the dimension further, multicritical fixed points emerge. Now, we take a closer look at the first two nontrivial fixed points, the Wilson-Fisher fixed point among them, in $d = 2.4$. We are interested in a trajectory connecting both. Therefore, we start at the tricritical fixed point with a small deviation constructed from a linear combination of its relevant eigenperturbations. For our calculations, we employ Eq. (2.35) and a scale

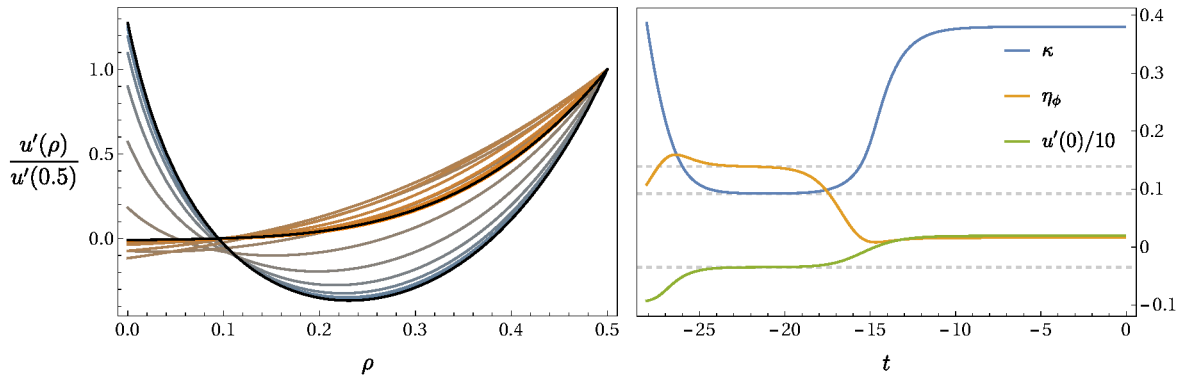


Fig. 5.4.: Flow between two criticalities. Left panel: Flow from the tricritical fixed-point potential (blue) to the Wilson-Fisher potential (orange), $t \in [0, -25]$. The fixed-point potential computed from the fixed-point equation are depicted as well (black). Right panel: Flow of the anomalous dimension η_ϕ , the VEV and $u'(0)$. The gray dashed lines denote the values of the Wilson-Fisher fixed-point solution obtained from solving the fixed-point equation.

dependent wave function renormalization, Eq. (2.36). As initial conditions we use the results of Sec. 4.1 [137, 138].

For approaching the Wilson-Fisher fixed point during the flow, we have to fine-tune the linear combination of both relevant directions of the tricritical fixed point. The perturbation is mainly along the second relevant (subleading) direction. The flow strongly depends on the numerical parameters. This is not surprising since small perturbations in the relevant direction may lead to large deviations during the flow as already seen for the large N case. Figure 5.4 shows the deformation of the potential $u'(\rho)$ from the tricritical fixed point to the Wilson-Fisher fixed point during the flow. The inner minimum of the tricritical fixed-point potential disappears. In the right panel the anomalous dimension, the VEV and $u'(0)$ are plotted over the logarithmic scale. While all quantities and the potential itself stay at the tricritical fixed point for many orders of magnitude, they finally approach the Wilson-Fisher fixed point. This can be seen from the plateaus at $-17 \gtrsim t \gtrsim -25$. The relevant direction becomes irrelevant at the Wilson-Fisher fixed point. Finally, the flow carries the critical behavior of the Wilson-Fisher fixed point although we have started at the tricritical fixed point. We emphasize that for such flows a very stable numerical method is indispensable for which pseudo-spectral methods are well suited.

5.2. Quantum Mechanics with a bounded potential

In this section, we consider \mathbb{Z}_2 symmetric flows in quantum mechanics which correspond to the Ising model in $d = 1$. RG flows in quantum mechanics have been of great interest in the context of, e.g., tunneling phenomena [235]. Note that in quantum mechanics, the potentials are functions of the space coordinate x instead of the field ϕ and the action is an

integral with respect to the Euclidean time. As exact solutions can be obtained by employing the Schrödinger equation, studies in quantum mechanics provide an excellent test case for probing the quality of FRG calculations. Furthermore, they may give an indication for the quantum field theory case. Here, we are not interested in tunneling phenomena, but in the evolution of microscopic potentials of a special shape. The UV potentials which we consider have the property that they are bounded from below and above, i.e., they are flat for large $|x|$. Due to its boundedness from above, it is to be expected that fluctuations for arbitrary large $|x|$ contribute significantly to the flow in contrast to the examples above. Here, a case study of such flows shall be given by means of three microscopic potentials as representatives. Furthermore, flat potentials are interesting in the context of dark energy and Higgs inflation [236–241]. The slow roll provides a mechanism to implement the idea of inflation and to solve problems of cosmology such as the horizon problem. It commonly requires a flat part of the potential in field direction. For details on Higgs inflation in the framework of the exact renormalization group, see [120, 242–244].

From the effective potentials, we extract the energies of the ground state and first excited state and compare them to the numerically exact results from the Schrödinger equation. In the case of bounded potentials, it is not clear to which accuracy the first excited state can really be estimated from the flow due to convexity mechanisms. To put the results into perspective, we also give the values obtained from various analytical approximations.

From a technical point of view, these considerations provide a further example to demonstrate the power of pseudo-spectral methods as a global resolution of the field range is required.

5.2.1. Models

Each of the following three microscopic potentials gives rise to a particularly interesting aspect. The first microscopic potential is given by

$$U_{\text{cl}}(x) = \frac{2}{\pi} \arctan(x^2). \quad (5.4)$$

If an infinite number of space coordinates is taken into account which formally corresponds to the large N limit, the flow for this potential can be solved explicitly. In Sec. 5.2.6, we exploit this fact to clarify our results. Second, we choose a modified version of the well-known Pöschl-Teller potential,

$$U_{\text{cl}}(x) = \frac{\lambda(1+\lambda)}{2} \left(1 - \frac{1}{\cosh^2(\lambda x)} \right). \quad (5.5)$$

For this potential, the Schrödinger equation can be solved analytically, such that all bound states and their corresponding energies are known [245]. Here, we will specify to the case

$\lambda = 1$. Lastly, we investigate the potential

$$U_{\text{cl}}(x) = e^{-1/x^2}, \quad (5.6)$$

which has a nonanalyticity at $x = 0$. Due to this nonanalyticity, it is not possible to extract physical information of the system from a simple Taylor series around its minimum. It is worthwhile to investigate how the nonanalyticity behaves during the flow and influences the convergence of the pseudo-spectral methods. All potentials are normalized such that $U_{\text{cl}}(0) = 0$ and $U_{\text{cl}}(|x| \rightarrow \infty) = 1$.

5.2.2. Exact results

At first, we present the exact solutions for the energies of the ground state and the first excited state, if they exist, for all potentials by solving the Schrödinger equation,

$$-\frac{1}{2} \frac{\partial^2}{\partial x^2} \Psi(x) + U_{\text{cl}}(x) \Psi(x) = E \Psi(x), \quad (5.7)$$

where Ψ denotes the quantum mechanical wave function. If no analytical solution exists, we again apply pseudo-spectral techniques, as done for the eigenvalue problem (2.23) in the context of fixed-point equations, to solve Eq. (5.7) “numerically exactly”. All energies and their corresponding wave functions were determined with an accuracy of at least 10^{-20} .

For the potential (5.4), the ground state energy E_0 , and the energy gap $\Delta E = E_1 - E_0$, are

$$E_0 = 0.448004, \quad \Delta E = 0.509453. \quad (5.8)$$

For the Pöschl-Teller potential (5.5) (with $\lambda = 1$), there is only one bound state, which can be stated explicitly,

$$\Psi_0(x) = \frac{1}{\cosh(x)}, \quad E_0 = 1/2. \quad (5.9)$$

On the other hand, for the nonanalytical potential (5.6), we obtain

$$E_0 = 0.356644, \quad \Delta E = 0.542040. \quad (5.10)$$

In order to assess the numerical results employing the FRG, we first compute E_0 and E_1 within the WKB and the one-loop approximation.

5.2.3. WKB approximation

The formula for the approximated energy levels within the WKB approximation reads,

$$\int_{-x_0}^{x_0} \sqrt{2(E_n - U_{\text{cl}}(x))} = \left(n + \frac{1}{2}\right) \pi, \quad (5.11)$$

where x_0 is the classical turning point, $U_{\text{cl}}(x_0) = U_{\text{cl}}(-x_0) = E_n$. The index n counts the energy level. Evaluating Eq. (5.11) for each model, we obtain for the potential (5.4),

$$E_0 \approx 0.520, \quad E_1 \approx 0.955, \quad \Delta E \approx 0.435. \quad (5.12)$$

For the Pöschl-Teller potential (5.5), the ground state energy is

$$E_0 \approx 0.582. \quad (5.13)$$

Finally for the last potential (5.6), we have

$$E_0 \approx 0.405, \quad E_1 \approx 0.905, \quad \Delta E \approx 0.500. \quad (5.14)$$

It is remarkable that E_1 deviates less than 1% from the exact value, whereas E_0 is off by 13% – 16%. This is to be expected, since the WKB approximation works well in the semiclassical limit $\lambda \ll 2x_0$, where $\lambda/2$ is the distance between two knots of the wave function Ψ . This translates into the condition $n \gg 1$.

5.2.4. One-loop approximation

As a further step to put subsequent results into perspective, we perform a one-loop calculation. The one-loop effective potential reads

$$U_{\text{eff}}^{1\text{-loop}}(x) = U_{\text{cl}}(x) + \frac{1}{2} \sqrt{\partial_x^2 U_{\text{cl}}(x)}, \quad (5.15)$$

which can be inferred from Eq. (2.16), see App. D for details. Note that for the trace no regularization is needed in the quantum mechanical case. Clearly, the one-loop effective potential is only a meaningful approximation for $\partial_x^2 U_{\text{cl}} > 0$. The ground state energy is given by the value of the effective potential at its minimum, which is in all our cases at $x = 0$, thus

$$E_0 = U_{\text{eff}}(x = 0), \quad (5.16)$$

whereas the energy gap is the square root of the curvature of it, also evaluated at the minimum,

$$\Delta E = \sqrt{\partial_x^2 U_{\text{eff}}(x)}|_{x=0}. \quad (5.17)$$

We obtain

$$E_0 = \frac{1}{\sqrt{\pi}} \approx 0.564, \quad \Delta E = \frac{2}{\sqrt{\pi}} \approx 1.128, \quad (5.18)$$

for the potential (5.4). For such a “rough” approximation, the value of the ground state energy is admissible. However, the one-loop result predicts that there are no further bound states, as the energy gap is too large. For the Pöschl-Teller potential (5.5), the one-loop

computation yields

$$E_0 = \frac{1}{\sqrt{2}} \approx 0.707, \quad \Delta E = \sqrt{2(1 - \sqrt{2})} \approx 0.910i. \quad (5.19)$$

The ground state energy is off by about 40% whereas the energy gap takes on an imaginary and therefore nonphysical value. This comes along with the fact that the convexity of the effective potential is not covered by a one-loop calculation. That phenomenon is well-known to be an artifact of the loop expansion, and extensively discussed in, e.g., [246, 247]. Finally, for the potential (5.6), no meaningful one-loop calculation can be provided. Due to the nonanalyticity, any order in perturbation theory fails to produce a nonzero result for the energy levels.

5.2.5. Flow of the effective potential

We study the full FRG flow of the given microscopic potentials starting from Λ and integrating down to an effective mass scale at which we encounter convexity mechanisms. In particular, we send $\Lambda \rightarrow \infty$ as UV divergences are absent. Note that the flow hardly depends on the UV modes [235]. We use the effective action (2.33). As we deal with the quantum mechanical case, the integration variable is the time coordinate and the field $\bar{\phi}$ is replaced by the space coordinate x . We compare the flows employing two different regulator functions, the linear optimized regulator (2.14) and the Callan-Symanzik regulator,

$$R_k(p^2) = k^2. \quad (5.20)$$

For the linear optimized regulator, the flow is given by Eq. (2.35) (setting $d = 1$ and $N = 1$). We deal with the dimensional version of it. Using the regulator (5.20), the flow equation reads

$$\partial_k U'_k = -\frac{1}{4}k \frac{3U''_k + 2\bar{\rho}U'''_k}{(k^2 + U'_k + 2\bar{\rho}U''_k)^{3/2}}, \quad (5.21)$$

where $\bar{\rho} = x^2/2$. For the ground state energy, we need the flow of the cosmological constant which is not incorporated in the flow of U'_k . Therefore, the flow of the potential at $\bar{\rho} = 0$ has to be solved in addition. As soon as the flow of its first derivative is known, this corresponds to a simple numerical integration of the flow equation of the potential. Note that this flow equation has to be normalized such that the flow of a vanishing potential also vanishes. We restrict our investigations to LPA ($Z_{\phi,k} = 1$). Both the scale k and the invariant $\bar{\rho}$ are compactified in the same way using Eq. (3.17) with $L = 1$.

We first point out some expectations on the outcome of the flow before discussing the actual results. If we start with a classical, bounded potential, the effective potential at $k = 0$ is bounded as well. One can prove this by considering the following definition of the

effective potential [248],

$$U_{\text{eff}}(\hat{x}) = \inf_{\Psi: \langle x \rangle = \hat{x}} \langle H \rangle_{\Psi}. \quad (5.22)$$

It states that the effective potential at a point \hat{x} is given by the infimum of the expectation value of the Hamiltonian over all states with position expectation value \hat{x} . Exhaustive discussions of the effective potential in quantum field theory can be found in, e.g., [248–251]. We assume that the classical potential is bounded from above by $C \in \mathbb{R}_+$ and from below by zero without loss of generality. Therefore, expression (5.22) must be greater than or equal to zero as a lower bound. For the upper bound, let us consider a normalized Gaussian function,

$$\Psi(x) = \left(\frac{e\lambda}{\pi}\right)^{1/4} e^{-\lambda(x-\hat{x})^2}, \quad (5.23)$$

as a possible state with the position expectation value \hat{x} . Employing Eq. (5.22), one easily derives

$$U_{\text{eff}}(\hat{x}) \leq \langle P^2/2 \rangle_{\Psi} + \langle U_{\text{cl}} \rangle_{\Psi} \leq \frac{\lambda}{2} + C, \quad (5.24)$$

which was to show. From the definition of the effective action (2.2), it is clear that the effective potential is convex at $k = 0$. However, any bounded function which is not constant cannot be convex. Consequently, if we could integrate the flow equations down to $k = 0$, we would end up with a constant potential, and the constant is exactly the ground state energy. Our naive expectation for the flow is therefore that we can hope to find the ground state energy, but probably not the energy of the first excited state. Surprisingly, it turns out that one can extract some estimate for the energy of the excited state from the flow.

As an exemplary case, we display the numerically computed flow for the nonanalytical potential (5.6). The other two potentials show the same qualitative behavior. In Tab. 5.1,

$U_{\text{cl}}(x) = 2/\pi \arctan(x^2)$			
	exact	CS	opt
E_0	0.448004	0.445	0.447
ΔE	0.509453	0.477	0.558
$U_{\text{cl}}(x) = 1 - 1/\cosh^2(x)$			
	exact	CS	opt
E_0	1/2	0.496	0.499
ΔE	-	0.464	0.585
$U_{\text{cl}}(x) = \exp(-1/x^2)$			
	exact	CS	opt
E_0	0.356644	0.355	0.356
ΔE	0.542040	0.515	0.570

Tab. 5.1.: Overview of exact results from solving the Schrödinger equation and results obtained from the flow of the potential for all three classical potentials. CS and opt indicate that the Callan-Symanzik and the optimized regulator were used, respectively.

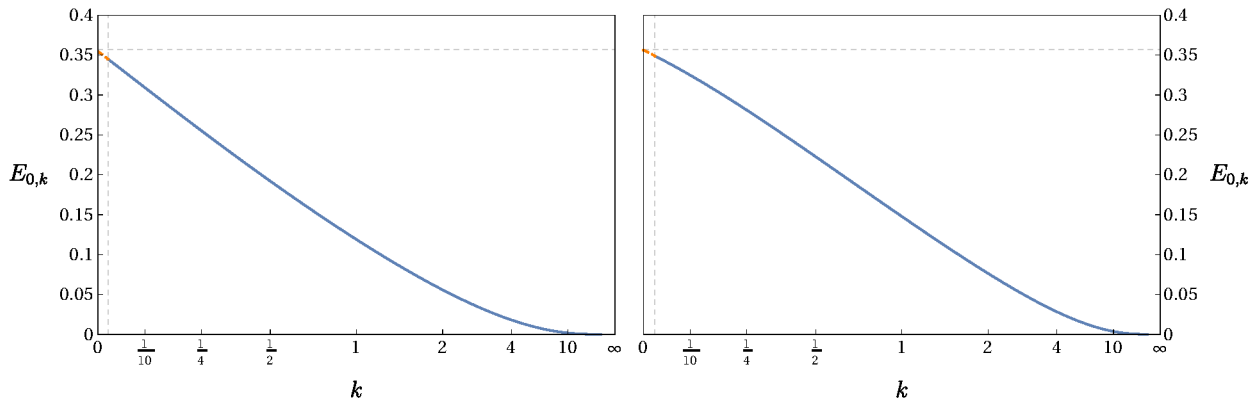


Fig. 5.5.: Flow of the potential (5.6) at vanishing position, which gives the ground state energy at scale k , $E_{0,k}$, for both Callan-Symanzik (left panel) and optimized (right panel) regulator. The horizontal dashed line indicates the exact value of the ground state energy, whereas the vertical line indicates the value up to which the numerical integration could be done. The orange dashed line is the extrapolation of our numerical values, given in blue.

E_0 and ΔE can be seen for the three potentials and the two regulators. Figure 5.5 depicts the potential at $x = 0$ as a function of the scale k for both the Callan-Symanzik and the optimized regulator. It corresponds to the ground state energy at scale k . For technical reasons, we cannot integrate down to $k = 0$, but only to a finite value k_{IR} , indicated by the vertical dashed line. From thereon, we extrapolate linearly to get an estimate of the true ground state energy. For both regulators, we get very precise estimates for the ground state energy. Generically, the optimized regulator gives slightly superior results for E_0 .

Next, we shall discuss the results on the energy gap. As argued above, in principle we should not expect to get any meaningful estimate from the effective potential. There is however a loophole in the above argument: It is based on the effective potential at scale $k = 0$, when all fluctuations are integrated out. However, when we consider the flow of the potential, we can extract additional information. The scale k can be interpreted to be the inverse length scale of a finite box where our physical system lives in. In this sense, we can indeed extract information on the energy gap, roughly when the scale is large enough to resolve the wave function of the first excited state, but small enough not to be too much influenced by the next-higher states. Bearing this in mind, we discuss the curvature of the flowing potential at vanishing position, which gives the energy gap at scale k , see Fig. 5.6. Remarkably, for both regulators, we get a quite good estimate of the true energy gap, however the finer details are more complicated. For the Callan-Symanzik regulator, we can already see the influence of convexity, as the derivative of the effective potential bends towards zero. This is not the case for the optimized regulator yet. Correspondingly, the optimized regulator overestimates the energy gap, whereas the estimate from the Callan-Symanzik regulator is below the true value. This behavior is also observed for the other potentials, and influences the prediction of the number of bound states. In this respect, the optimized regulator erroneously predicts only one bound state for the potential (5.4). On the other hand, the Callan-Symanzik regulator

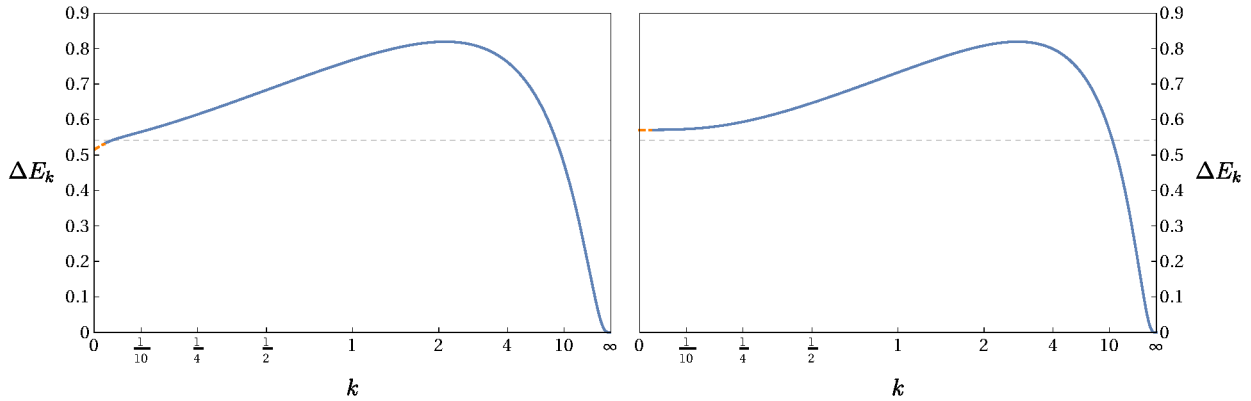


Fig. 5.6.: Flow of the second derivative of the potential (5.6) at vanishing position, which gives the energy gap ΔE_k at scale k , for both Callan-Symanzik (left panel) and optimized (right panel) regulator. The horizontal dashed line indicates the exact value of the energy gap, whereas the vertical line indicates the value up to which the numerical integration could be done. The orange dashed line is the extrapolation of our numerical values, given in blue.

predicts a second bound state for the Pöschl-Teller potential (5.5). We emphasize, that the extrapolation introduces further errors. Presumably one should read off the energy gap at some finite value of the scale k , as discussed above. However we found no a priori argument how to set this scale. Apart from convexity arguments, we expect that especially the energy of the first excited state improves if a nontrivial wave function renormalization is taken into account.

In Fig. 5.7, we depict the actual flow of the derivative of the potential, obtained with the Callan-Symanzik regulator. The nonanalyticity of the classical potential clearly affects the convergence of the expansion coefficients at $k = \infty$. Note that the other two potentials also give rise to nonanalyticities but in the complex plane. In comparison, the classical potential (5.4) shows the best convergence. However, one can see that the nonanalyticity of the classical potential is smoothed out quickly and does not affect the flow significantly for $k < \infty$. For small scales k , one can also see the tendency of the derivative of the potential to flow to zero, as it must due to convexity. In contrast to unbounded potentials, where convexity is numerically challenging near the origin, the numerical problems here arise for large values of $\bar{\rho}$. Hence, it gets increasingly difficult to resolve the flow.

5.2.6. Large N approximation

We have studied convexity of two different kinds of potentials: On the one hand, in Sec. 5.1, we dealt with an unbounded potential and observed the “usual” onset of convexity. Here, we consider bounded potentials where convexity appears to operate in a different way.

As the large N limit of $O(N)$ models can be solved analytically, we try to uncover more details on these mechanisms for this class of potentials. As already mentioned, the large N limit corresponds to the limit of infinitely many dimensions in quantum mechanics. For the

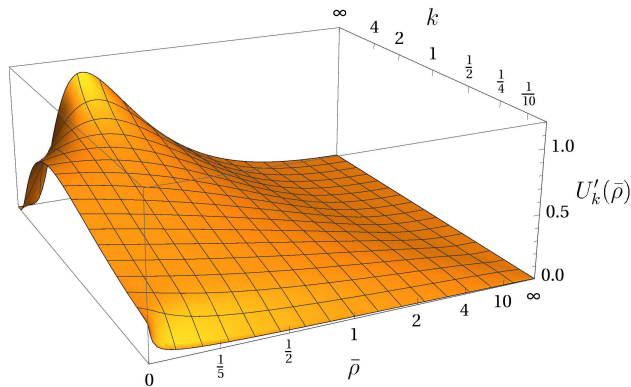


Fig. 5.7.: Flow of the derivative of the potential for the Callan-Symanzik regulator. One can see that the nonanalyticity of the classical potential smoothens out quickly. Convexity at small scales arises for large values of $\bar{\rho}$ in contrast to conventional unbounded potentials.

potential (5.4), the flow can be solved explicitly. The effective potential at $k = 0$ reads

$$U_{\text{eff}}(x) = \frac{-\pi x^2 + \sqrt{16\pi(1+x^4) - \pi^2}}{8\pi(1+x^4)} + \frac{2}{\pi} \left(\arctan(x^2) + \arctan\left(\sqrt{\frac{\pi}{16(1+x^4) - \pi}}\right) \right). \quad (5.25)$$

A plot of both the classical and the effective potential is given in Fig. 5.8. Notably, the large N effective potential is *not* convex. This seeming paradox has the following reason: Convexity is tied to the condition that the propagator avoids a singularity for negative $U'_k(\bar{\rho})$ and $U''_k(\bar{\rho})$ which appears in the equivalent of the radial mode propagator. In the large N approximation, however, only the equivalent of the Goldstone mode propagator survives. To be finite, it is enough that $U'_k(\bar{\rho})$ is nonnegative. This is indeed the case for the solution given above.

Not only in quantum mechanics and for bounded potentials, but in a much more general context, the large N limit does not necessarily give rise to a convex effective potential.

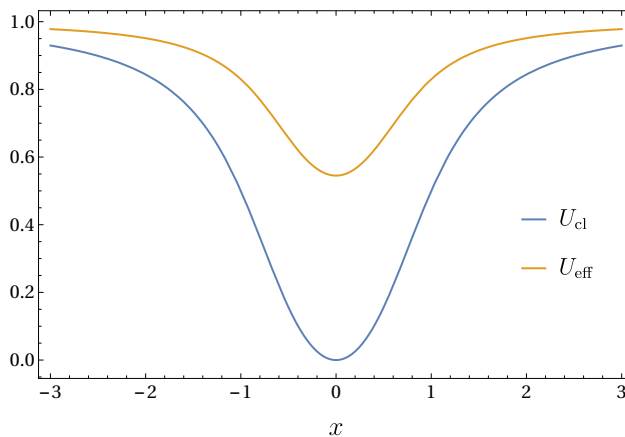


Fig. 5.8.: Comparison of the classical potential (5.4) and the corresponding effective potential (5.25) in the large N limit. In contrast to finite N , we do not observe convexity of the effective potential, but only that the derivative with respect to $\bar{\rho}$ is nonnegative.

It is easy to show for the $O(N)$ model in $d > 1$ that nonconvexities remain in the IR if $U_k''(\bar{\rho}) < 0$ for some $\bar{\rho}$. For a completely convex potential the presence of the radial mode propagator turns out to be indispensable as argued above. The Goldstone mode propagation only implements a “weak” convexity condition which applies for potentials with $U_k''(\bar{\rho}) \geq 0$.

Interestingly, there is no smooth interpolation between the large N limit and finite N at least for this type of effective potentials. Therefore, no conclusion for the finite N case can be drawn.

5.3. Flows of the Higgs potential in a Yukawa model

The discovery of the Higgs boson at the LHC [51, 52] completed the search for the building blocks of the standard model of particle physics. Although the mass of the Higgs boson cannot be predicted exactly by the standard model, it is not necessarily an arbitrary parameter. For instance, assuming that the description of fundamental physics in terms of standard-model degrees of freedom is valid at a high energy scale Λ and that the theory is sufficiently weakly coupled, the Higgs boson mass is restricted to a finite range, the so-called IR window [252–258]. The measured, comparatively small mass $\bar{m}_H \simeq 125\text{GeV}$ raises new questions concerning the Higgs-mass bounds and the stability of the electroweak vacuum.

Actually, the edges of the IR window [256, 259–285], i.e., the upper and lower admissible values, for the Higgs mass are not sharply defined, but depend on a number of additional assumptions. For the upper “triviality bound”, as the Higgs sector becomes strongly coupled at high scales for large values of the Higgs mass, perturbative estimates of this bound for example depend on an ad hoc choice of coupling values up to which perturbation theory is trusted. By contrast, nonperturbative methods have shown that this upper bound relaxes considerably if one allows the system to start microscopically with a strong Higgs self-coupling [53, 58].

In the following work, we concentrate on the lower edge of the IR window. There, a similar fuzziness arises due to the assumptions imposed on the precise form of the microscopic theory at the high scale Λ within a perturbative treatment. Taking only perturbatively renormalizable operators into account corresponds to fixing infinitely many couplings of higher-order operators. Otherwise, if the standard model is defined in terms of its symmetries, field content and measured IR parameters, the microscopic action remains largely unspecified as long as the underlying theory is not known. Electroweak collider data suggests that the explored region of theory space is close to the Gaussian fixed point. Here, power-counting can be applied. Whereas IR observables constrain relevant and marginal couplings, irrelevant couplings are left undetermined.

It has recently been shown that these unconstrained higher-dimensional operators in fact can relax the lower edge of the IR window, i.e., can decrease the lower (stability) bound on the Higgs mass without introducing metastability [53, 58, 59]. Comparatively simple modifications of the bare action, e.g., in terms of a dimension-six operator at the Planck scale can lower the lower mass bound by $\sim 1\text{GeV}$, while preserving absolute stability on all scales [59].

While controlled quantitative results have been obtained for a small class of operators represented by simple low-order polynomials of the field, a possible metastable regime with competing vacua has not been explored so far. For this purpose, a full functional renormalization of the effective Higgs potential as a function of the field and the RG scale is required.

The simple Yukawa model has proven to be useful for addressing the qualitative properties of the IR window. At the beginning of this section, we discuss which degrees of freedom of the standard model are incorporated in this model. We summarize recent results gained within perturbation theory to put our study into perspective. An extensive mean-field study in terms of Eq. (2.16), taking only fermionic fluctuations into account, follows. We explore the full RG flow of the potential by means of pseudo-spectral methods and compare it with both mean-field and polynomial results. Furthermore, we confirm the lowering of the Higgs-mass bounds to a high accuracy in the fully stable regimes. As a new result, we discuss the fate of the potential flows in the metastable regime. Finally, we consider the impact of convexity mechanisms on estimates of the tunnel rate from static quantities and the phase diagram as a function of the parameters of the microscopic action.

5.3.1. Higgs-Yukawa model with discrete symmetry

As mentioned above, the simple Yukawa model contains all degrees of freedom which are relevant for our study. The simplest ansatz for the classical Euclidean action S is given by Eq. (2.37), setting $d = 4$, $k = \Lambda$, $Z_{\phi,\Lambda} = 1$ and $Z_{\psi,\Lambda} = 1$. It corresponds to a reduction of the standard model to one fermion flavor ($N_f = 1$), the top quark ψ with the largest Yukawa coupling, and a real scalar Higgs field $\bar{\phi}$. The discrete chiral \mathbb{Z}_2 symmetry (2.38) mimics the electroweak symmetry group, and protects the fermions against acquiring a mass term. No massless Goldstone bosons appear after spontaneous symmetry breaking as the symmetry is discrete. Hence, the particle spectrum is gapped in the broken phase as in the standard model. This toy model was intensively discussed in the context of stability of the effective potential in the literature, e.g., [53, 173, 174, 286, 287].

In order to make semi-quantitative contact with the standard model, we impose Coleman-Weinberg renormalization conditions [247] on the effective potential obtained after integrating out all fluctuations down to the IR,

$$U'_{\text{eff}}(\bar{\phi}_0) = 0, \quad \bar{m}_H^2 = U''_{\text{eff}}(\bar{\phi}_0), \quad \bar{m}_t^2 = \bar{\phi}_0^2 \bar{h}_{\text{eff}}^2, \quad (5.26)$$

where primes denote the derivative of the potential with respect to the argument and \bar{m}_H and \bar{m}_t are the renormalized Higgs and top mass, respectively. All couplings are considered to be renormalized at a suitable renormalization point μ , e.g., $\mu = \bar{\phi}_0$. Note that if we take the scale dependence of $Z_{\phi,k}$ and $Z_{\psi,k}$ into account, we have to consider quantities renormalized by the wave function renormalizations as we do in the second part of this section. As the zero energy is irrelevant here, the zero point is chosen such that either $U(0) = 0$ or $U(\bar{\phi}_0) = 0$ depending on numerical convenience. For the observable parameters, we choose $\bar{m}_t = 173\text{GeV}$ for the top mass, and $\bar{\phi}_0 \equiv v = 246\text{GeV}$ for the electroweak VEV. The Higgs mass \bar{m}_H then is treated as a function of the cutoff and a functional of the bare action, $\bar{m}_H = \bar{m}_H[S_\Lambda; \Lambda]$.

Despite this apparent physical fixing, the simplified model, of course, deviates quantitatively from the standard model in essential aspects. For instance, whereas the center of the IR window for the Higgs mass is near $\sim 150\text{GeV}$ for a Planck scale cutoff in the standard model [283], it is near $\sim 215\text{GeV}$ for the present simple model at high energy scales [288] mainly due to the absence of the gauge sectors.

5.3.2. Perturbative effective single-scale potential

In order to make contact with the conventional perturbative treatment, we briefly sketch the standard line of argument to obtain an estimate of the effective potential. For simplicity, we consider only the one-loop level. Perturbatively, only the renormalizable operators of the bare potential are considered,

$$U_\Lambda = \frac{\bar{m}_\Lambda^2}{2}\bar{\phi}^2 + \frac{\bar{\lambda}_{2,\Lambda}}{8}\bar{\phi}^4, \quad (5.27)$$

featuring the bare mass parameter \bar{m}_Λ^2 and bare $\bar{\phi}^4$ coupling $\bar{\lambda}_{2,\Lambda}$. The estimate for the effective potential is based on the β function for the renormalized running coupling $\bar{\lambda}_{2,k}$,

$$\partial_t \bar{\lambda}_{2,k} = \frac{1}{16\pi^2}(9\bar{\lambda}_{2,k}^2 + 8\bar{h}^2\bar{\lambda}_{2,k} - 16\bar{h}_k^4), \quad (5.28)$$

depending as well on the renormalized running Yukawa coupling \bar{h}_k . For the present line of argument, it suffices to ignore the running of $\bar{h}_k = \bar{h}$ which will be fully included in our detailed studies later. The discussion can even be simplified further by noting that the $\bar{\lambda}_{2,k}$ -terms in (5.28) are small compared to the \bar{h}^4 term for small Higgs masses and large top masses. In this limit, which corresponds to ignoring scalar fluctuations, the integration of the β function yields

$$\partial_t \bar{\lambda}_{2,k} = -\frac{\bar{h}^4}{\pi^2} \quad \Rightarrow \quad \bar{\lambda}_{2,k} = \bar{\lambda}_{2,\mu} - \frac{\bar{h}^4}{2\pi^2} \ln \frac{k^2}{\mu^2}, \quad (5.29)$$

with μ denoting the renormalization point for $\bar{\lambda}_{2,k}$.

The conventional perturbative estimate of the effective potential is then inspired by the Coleman-Weinberg form of the effective potential [247]. One assumes that the effective potential is well approximated by identifying the dependence of the integrated scalar self-coupling on the RG scale k with the scalar field itself, $\bar{\lambda}_{2,k=\bar{\phi}}$. We emphasize, that the identification $k = \bar{\phi}$ mixes momentum scale information k with the field amplitude. In general, the full effective action in field theory would provide separate information about the two scales which need not be the same. By this identification, we obtain a *single-scale* potential which in our

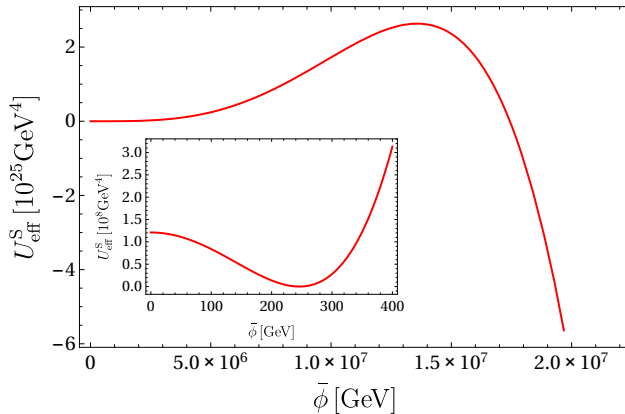


Fig. 5.9.: Conventional effective single-scale potential $U_{\text{eff}}^{\text{S}}$ as a function of the field amplitude $\bar{\phi}$. While the potential looks stable around the electroweak minimum, it develops an instability at large field values within our toy model. This instability seems to be driven by top fluctuations which turn the scalar self-coupling negative at large scales, cf. Eq. (5.29).

simple approximation reads

$$\begin{aligned} U_{\text{eff}}^{\text{S}}(\bar{\phi}) &= \frac{1}{2} \bar{m}_{\mu}^2 \bar{\phi}^2 + \frac{\bar{\lambda}_{2,k=\bar{\phi}}}{8} \bar{\phi}^4 \\ &= \frac{1}{2} \bar{m}_{\mu}^2 \bar{\phi}^2 + \frac{\bar{\lambda}_{2,\mu}}{8} \bar{\phi}^4 - \frac{\bar{h}^4 \bar{\phi}^4}{16\pi^2} \ln \frac{\bar{\phi}^2}{\mu^2}. \end{aligned} \quad (5.30)$$

One can show that the direct computation of the effective action via Eq. (2.16) leads to the same result, cf. App. E. Imposing the renormalization conditions (5.26) together with the choice $\mu = \bar{\phi}_0 = v$, we can write the single-scale potential as

$$U_{\text{eff}}^{\text{S}}(\bar{\phi}) = -\frac{1}{4} \left[\bar{m}_{\text{H}}^2 + \frac{\bar{m}_{\text{t}}^4}{2\pi^2 v^2} \right] \bar{\phi}^2 + \frac{1}{8} \left[\frac{\bar{m}_{\text{H}}^2}{v^2} + \frac{3\bar{m}_{\text{t}}^4}{4\pi^2 v^4} \right] \bar{\phi}^4 - \frac{\bar{m}_{\text{t}}^4 \bar{\phi}^4}{16\pi^2 v^4} \ln \frac{\bar{\phi}^2}{v^2}. \quad (5.31)$$

Note also, that the bare potential (5.27) remains completely unspecified in this derivation. The implicit use of only renormalizable operators together with the limit $\Lambda \rightarrow \infty$ permitted by perturbative renormalizability seems to suggest that the details of the bare potential are irrelevant.

Clearly, this single-scale potential develops an instability for large Yukawa couplings, i.e., large \bar{m}_{t} . For the present choice of parameters, the instability occurs at a scale of $\sim 10^7 \text{ GeV}$ in our toy model, see Fig. 5.9. This instability is related to the running of $\bar{\lambda}_{2,k}$, which turns negative at sufficiently large k , cf. Eq. (5.29).

In the full standard model, the corresponding instability scale is of order $\sim 10^{10} \text{ GeV}$. Current state-of-the-art calculations [280, 283, 285] determine the single-scale potential to NNLO precision, including two-loop threshold corrections, and self-consistent resummations [289, 290]. However, the present rather cartoon-like presentation in a toy model still captures the essence of the origin of the instability occurring in the perturbative estimate of the single-scale potential.

A qualitative difference arises in the standard model from the electroweak gauge fluctuations, which render the $\bar{\phi}^4$ coupling positive again at even higher scales. The single-scale potential becomes bounded from below and a second minimum arises beyond the Planck scale which turns out to be the global one. Therefore, the absolute instability of the single-scale potential is a particularity of our model. Below, this will actually be useful to make one of our main points more transparent.

5.3.3. Mean-field effective potential and stability

In the following, we use mean-field methods, cf. Eq. (2.16), to study the effective potential. We stick to the same simplifications as before, ignoring bosonic fluctuations and the running of the Yukawa coupling, but keep track of all scales involved, the momentum scale of fluctuations k , the field amplitude $\bar{\phi}$ and the UV cutoff scale Λ . Therefore, we are left with the evaluation of the determinant in Eq. (2.16) containing only fermionic contributions. Parts of this discussion follows [53, 58], where also more technical details can be found. Here, we focus on the new aspects arising for un-/metastable scenarios, cf. [141].

Mean-field potential

With these prerequisites, the mean-field potential is directly related to the fermion determinant. More precisely, working with an explicit UV cutoff Λ and an IR regulator scale k , the mean-field potential reads,

$$U_k^{\text{MF}}(\bar{\phi}) = U_\Lambda - \frac{1}{\Omega} \ln \det_{\Lambda, k} (i\not{\partial} + i\bar{h}\bar{\phi}), \quad (5.32)$$

where Ω denotes the spacetime volume, and irrelevant field independent constants are ignored. If we would introduce N_f fermion flavors, the mean-field approximation would become exact in the limit $N_f \rightarrow \infty$. The notation $\det_{\Lambda, k}$ indicates that the determinant is regularized and includes momentum modes p in the range $k^2 \leq p^2 \leq \Lambda^2$. The result is regularization dependent. As long as we do not send $\Lambda \rightarrow \infty$, this dependence is physical and can be viewed as a model for the details of the embedding into a more fundamental underlying UV complete theory. For a close contact with later sections, we use the linear optimized regulator (2.15). We emphasize that all conclusions remain the same also for a sharp momentum cutoff, proper-time or zeta-function regularization, see [58]. Evaluating the fermion determinant which is done in App. F, we obtain,

$$U_k^{\text{MF}}(\bar{\phi}) = U_\Lambda - \frac{\bar{h}^2(\Lambda^2 - k^2)\bar{\phi}^2}{16\pi^2} + \frac{\bar{h}^4\bar{\phi}^4}{16\pi^2} \ln \frac{\Lambda^2 + \bar{h}^2\bar{\phi}^2}{k^2 + \bar{h}^2\bar{\phi}^2}, \quad (5.33)$$

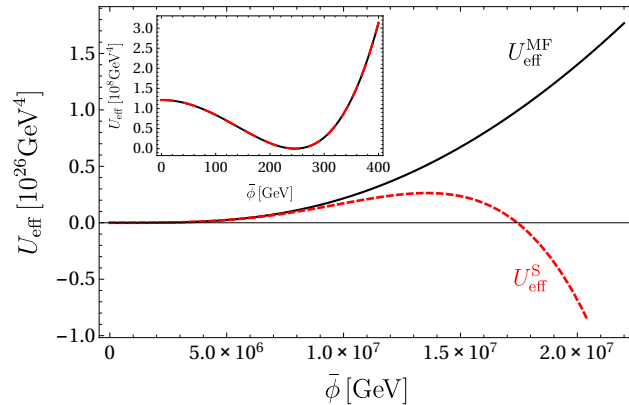


Fig. 5.10.: Comparison between the effective potential where the cutoff is kept finite (black solid line, $\Lambda = \Lambda_{\text{cr}} = 1.22 \cdot 10^7 \text{ GeV}$) and the single-scale potential (red dashed line). Both approaches describe the same low energy physics around the Fermi scale as they should, while at high energies a seeming instability appears for $U_{\text{eff}}^{\text{S}}$.

which makes all scale dependencies explicit. By varying the RG scale k from $k = \Lambda$ to $k \rightarrow 0$, we can observe how the mean-field effective potential as a function of the field amplitude $\bar{\phi}$,

$$U_{\text{eff}}^{\text{MF}}(\bar{\phi}) = U_{k=0}^{\text{MF}}(\bar{\phi}) = \frac{1}{2} \left(\bar{m}_{\Lambda}^2 - \frac{\bar{h}^2 \Lambda^2}{8\pi^2} \right) \bar{\phi}^2 + \frac{\bar{\lambda}_{2,\Lambda}}{8} \bar{\phi}^4 + \frac{\bar{h}^4 \bar{\phi}^4}{16\pi^2} \ln \left(1 + \frac{\Lambda^2}{\bar{h}^2 \bar{\phi}^2} \right), \quad (5.34)$$

is built up from fermionic fluctuations renormalizing the bare potential U_{Λ} .

Apart from the induced mass term $\sim \bar{h}^2 \Lambda^2 \bar{\phi}^2$, the whole interaction part of the determinant $\sim \bar{h}^4 \bar{\phi}^4 \ln(\dots)$ is positive. The bare mass term \bar{m}_{Λ}^2 can now be fixed by the renormalization condition (5.26), which sets the Fermi scale,

$$\bar{m}_{\Lambda}^2 = \frac{\bar{h}^2 \Lambda^2}{8\pi^2} - \frac{\bar{h}^4 v^2}{8\pi^2} \left[2 \ln \left(1 + \frac{\Lambda^2}{\bar{h}^2 v^2} \right) - \frac{\Lambda^2}{\Lambda^2 + \bar{h}^2 v^2} \right] - \frac{1}{2} \bar{\lambda}_{2,\Lambda} v^2. \quad (5.35)$$

Inserting Eq. (5.35) into Eq. (5.34) yields a globally stable effective potential for any value of the UV cutoff Λ and any admissible nonnegative value of the bare $\bar{\phi}^4$ coupling $\bar{\lambda}_{2,\Lambda} \geq 0$, cf. solid black line in Fig. 5.10. It is important to stress that a bare potential of quartic type, Eq. (5.27), with negative $\bar{\lambda}_{2,\Lambda}$ would be inconsistent right from the beginning, as the functional integral over the scalar field would be ill-defined.

For completeness of the presentation, we recall that the Higgs mass now becomes a function of the cutoff and $\bar{\lambda}_{2,\Lambda}$, cf. [53, 58],

$$\begin{aligned} \bar{m}_{\text{H}}^2 &= U_{\text{eff}}^{\text{MF}''}(v) \\ &= \frac{\bar{m}_{\text{t}}^4}{4\pi^2 v^2} \left[2 \ln \left(1 + \frac{\Lambda^2}{\bar{m}_{\text{t}}^2} \right) - \frac{3\Lambda^4 + 2\bar{m}_{\text{t}}^2 \Lambda^2}{(\Lambda^2 + \bar{m}_{\text{t}}^2)^2} \right] + v^2 \bar{\lambda}_{2,\Lambda}. \end{aligned} \quad (5.36)$$

This demonstrates that a lower bound for the Higgs mass is obtained by the physical restriction that the bare potential of $\bar{\phi}^4$ -type at a given UV cutoff Λ must be bounded from

below, i.e., $\bar{\lambda}_{2,\Lambda} \geq 0$. Thus, the lower bound (lower edge of the IR window) is given by $\bar{\lambda}_{2,\Lambda} = 0$ for this class of bare potentials. This way of determining the lower bound has been suggested in [286, 287], and has been used in full nonperturbative lattice simulations [291–294]. Generically, one observes a strong quantitative agreement with mean-field theory for this lower bound.

For the purpose of the present work, we reverse the line of argument: for a given Higgs mass of, say $\bar{m}_H = 125\text{GeV}$, this implies that a maximal scale of UV extension Λ is obtained. Choosing the minimal admissible value $\bar{\lambda}_{2,\Lambda} = 0$ a cutoff of $\Lambda_{\text{cr}} = 1.22 \cdot 10^7\text{GeV}$ is obtained by writing $\Lambda = \Lambda(\bar{m}_H^2, \bar{\lambda}_{2,\Lambda})$. For larger values of the UV cutoff, $\Lambda > \Lambda_{\text{cr}}$ no physical (mean-field) RG trajectory can be found that connects an admissible bounded bare potential to an IR Higgs mass of 125GeV. As long as $\Lambda \leq \Lambda_{\text{cr}}$, the bare potential as well as the effective potential do not exhibit an instability. Figure 5.10 shows a comparison between the mean-field potential (solid/black line) where the cutoff is kept finite and the single-scale potential (red/dashed line) where the cutoff has implicitly been sent to infinity. The single-scale potential approximation starts to break down for field amplitudes, where $\bar{h}\bar{\phi}/\Lambda \gtrsim \mathcal{O}(1)$, i.e., where terms which are dropped in the implicit $\Lambda \rightarrow \infty$ limit are actually sizable.

It is, of course, possible to reduce the multi-scale mean-field potential to the single-scale potential. First, we blindly enforce all renormalization conditions. In particular the first condition in (5.26) for large cutoffs compared to the electroweak scale implies

$$\bar{\lambda}_{2,\Lambda} = \frac{\bar{m}_H^2}{v^2} - \frac{\bar{h}^4}{2\pi^2} \left[\ln \frac{\Lambda^2}{\bar{m}_t^2} - \frac{3}{2} \right] + \mathcal{O}\left(\frac{1}{\Lambda^2}\right). \quad (5.37)$$

Inserting Eqs. (5.37) and (5.35) into the mean-field effective potential finally leads to a potential with the requested minimum at v and Higgs mass of \bar{m}_H by construction. The cutoff remains still a free parameter. In the naive large cutoff limit, we obtain

$$\begin{aligned} U_{\text{eff}}^{\text{MF}} \xrightarrow{\Lambda \rightarrow \infty} & -\frac{1}{4} \left[\bar{m}_H^2 + \frac{\bar{m}_t^4}{2\pi^2 v^2} \right] \bar{\phi}^2 + \left[\frac{\bar{m}_H^2}{v^2} + \frac{3\bar{m}_t^4}{4\pi^2 v^4} \right] \frac{1}{8} \bar{\phi}^4 \\ & - \frac{\bar{m}_t^4 \bar{\phi}^4}{16\pi^2 v^4} \ln \left(\frac{\Lambda^2}{\Lambda^2 + h^2 \bar{\phi}^2 v^2} \right) + \mathcal{O}\left(\frac{1}{\Lambda^2}\right). \end{aligned} \quad (5.38)$$

For a cutoff larger than the critical value Λ_{cr} , the potential develops an instability and rapidly approaches the single-scale potential, see Fig. 5.11. For $\Lambda > 10^8\text{GeV}$, the difference between the mean-field effective potential with a finite cutoff and the single-scale potential with implicit limit $\Lambda \rightarrow \infty$ becomes very small. Taking the naive limit $\Lambda \rightarrow \infty$, the single-scale potential (5.31) is obtained as expected.

We emphasize that the consistency condition that the bare potential should be bounded from below for a well-defined generating functional is no longer fulfilled for all $\Lambda > \Lambda_{\text{cr}}$. This can be directly read off from expression (5.37): $\bar{\lambda}_{2,\Lambda}$ has to be chosen negative for $\Lambda > \Lambda_{\text{cr}}$, and thus already the bare potential is unstable. At this point, we conclude that the apparent

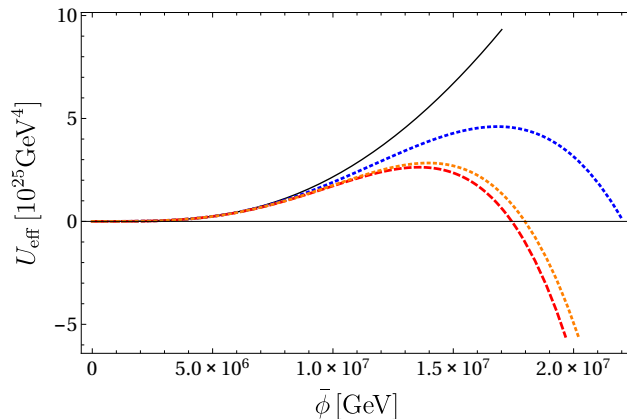


Fig. 5.11.: Approach of the mean-field potential to the single-scale potential if we blindly allow for cutoffs Λ larger than the critical value of $\Lambda_{\text{cr}} = 1.22 \cdot 10^7 \text{ GeV}$ (black solid) with IR physics kept fixed; $\Lambda = 2 \cdot 10^7 \text{ GeV}$ (blue dotted line), and $\Lambda = 5 \cdot 10^7 \text{ GeV}$ (orange dotted line). For $\Lambda > 10^8 \text{ GeV}$, there is no visible difference between the mean-field potential and the single-scale potential (red dashed line) in this plot.

instability of the single-scale potential appears due to an inconsistent UV boundary condition for the theory. As long as the consistency condition $\bar{\lambda}_{2,\Lambda} \geq 0$ is fulfilled, no instability can be found within the class of quartic bare potentials.

Generalized bare potentials

As already emphasized in [53, 58, 59], these observations do not imply that in- or metastabilities are completely excluded. Whether or not an in-/metastability occurs is not a matter of the fermionic fluctuations but has to be seeded by the microscopic underlying theory. A specific example from string phenomenology is given in [295].

From the perspective of the standard model as an effective field theory, the embedding into a UV complete theory is parametrized by the bare action at the cutoff Λ . Of course, the bare action is expected to host all operators compatible with the symmetry with couplings of order $\mathcal{O}(1)$ in units of the cutoff Λ .

In the following, we consider the simplest extension of the bare potential by including a higher-dimensional $\bar{\phi}^6$ operator as an example,

$$U_\Lambda = \frac{\bar{m}_\Lambda^2}{2} \bar{\phi}^2 + \frac{\bar{\lambda}_{2,\Lambda}}{8} \bar{\phi}^4 + \frac{\bar{\lambda}_{3,\Lambda}}{48\Lambda^2} \bar{\phi}^6. \quad (5.39)$$

Within the same mean-field approximation as used before, we can straightforwardly compute the mass of the Higgs boson in our model as a function of Λ and the parameters $\bar{\lambda}_{2,\Lambda}$ and $\bar{\lambda}_{3,\Lambda}$, cf. Eq. (5.36),

$$\bar{m}_H^2 = \frac{\bar{m}_t^4}{4\pi^2 v^2} \left[2 \ln \left(1 + \frac{\Lambda^2}{\bar{m}_t^2} \right) - \frac{3\Lambda^4 + 2\bar{m}_t^2 \Lambda^2}{(\Lambda^2 + \bar{m}_t^2)^2} \right] + v^2 \bar{\lambda}_{2,\Lambda} + \frac{v^4}{2\Lambda^2} \bar{\lambda}_{3,\Lambda}. \quad (5.40)$$

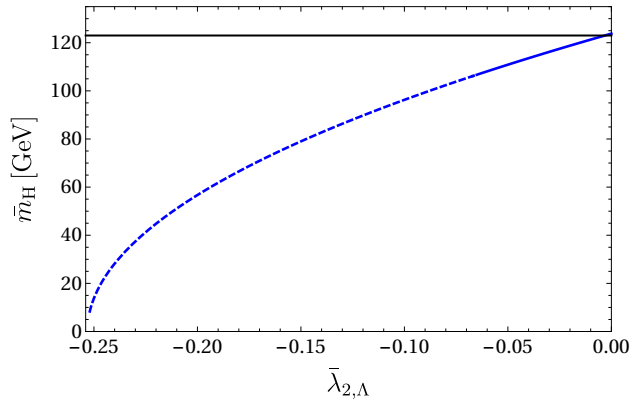


Fig. 5.12.: Higgs masses for the class of generalized bare potentials for $\Lambda = 10^7 \text{ GeV}$. The bare potential is stabilized by $\bar{\lambda}_{3,\Lambda} = 3$. The horizontal black solid line marks the lower Higgs mass consistency bound within quartic bare potentials. The blue solid line indicates values for $\bar{\lambda}_{2,\Lambda}$ where the IR potential is stable while for the blue dashed line a metastability occurs, $\bar{\lambda}_{2,\Lambda} \lesssim -0.067$.

It is obvious that the previous lower bound of (5.36) can be relaxed by a negative value for $\bar{\lambda}_{2,\Lambda}$, while a positive $\bar{\lambda}_{3,\Lambda}$ can stabilize the bare potential. For small negative $\bar{\lambda}_{2,\Lambda}$ and sufficiently large $\bar{\lambda}_{3,\Lambda}$ the effective potential as well as the potential at intermediate scales k are globally stable and have a unique minimum. In this regime, it is easily possible to obtain Higgs masses below the perturbative lower bound, i.e., decrease the edge of the IR window.

For even smaller $\bar{\lambda}_{2,\Lambda}$, i.e., larger absolute values of a negative $\bar{\lambda}_{2,\Lambda}$, the effective potential U_k^{MF} starts to develop a second minimum towards lower RG scales k and becomes metastable, while the bare potential U_Λ is still stable. For even smaller values of $\bar{\lambda}_{2,\Lambda}$, also the bare potential can become metastable.

For an illustration, let us assume a fixed cutoff $\Lambda = 10^7 \text{ GeV}$. Within the class of quartic bare potentials (5.27), the lowest Higgs mass according to (5.36) is given by $\bar{m}_H = 123.8 \text{ GeV}$ for $\bar{\lambda}_{2,\Lambda} = 0$. Stabilizing the more general class of bare potentials (5.39) with a fixed value of $\bar{\lambda}_{3,\Lambda} = 3$, we can choose negative values of $\bar{\lambda}_{2,\Lambda}$, yielding also smaller values of the Higgs mass, see Fig. 5.12. The resulting mean-field potentials are stable with a unique (electroweak) minimum on all scales (blue solid line) until we reach a value for the bare quartic coupling of $\bar{\lambda}_{2,\Lambda} = -0.065$. For even smaller values of $\bar{\lambda}_{2,\Lambda}$, a second minimum arises in the course of the mean-field flow, while the bare potential still has a unique minimum. This second minimum is a local minimum only for a small range of $\bar{\lambda}_{2,\Lambda}$ values, $-0.0671 < \bar{\lambda}_{2,\Lambda} < -0.065$. For $\bar{\lambda}_{2,\Lambda} < -0.0671$, the second minimum becomes the global one (blue dashed line), which renders the electroweak minimum in the effective potential metastable. Within this regime of metastability, the Higgs mass can be made arbitrarily small by a suitable choice of parameters even without any metastability in the bare potential.

It is important to emphasize that the metastability observed here in this model is a consequence of the shape of the bare potential encoded in both renormalizable and non-renormalizable operators. In the present model, this metastability remains invisible in the

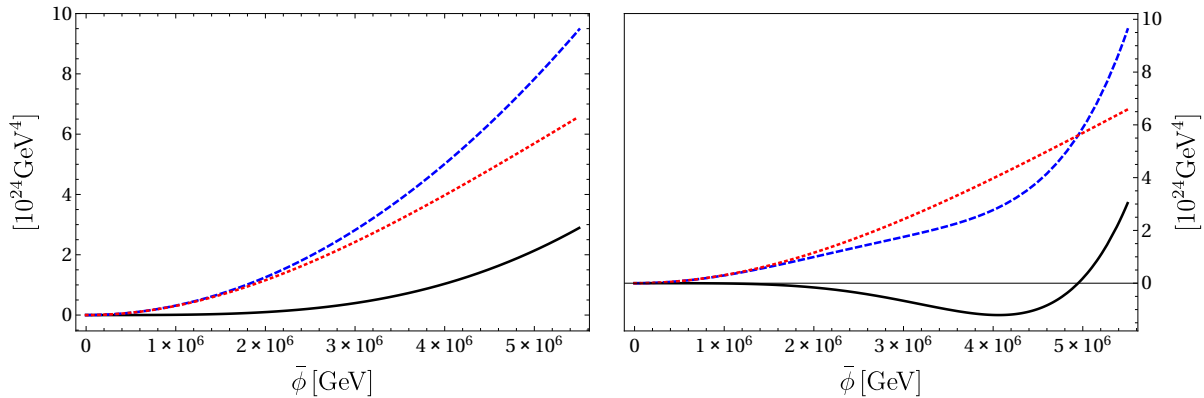


Fig. 5.13.: Mean-field potential (black solid) as the difference between the bare potential (blue dashed) and the absolute value of the fermion determinant (red dotted). The Fermi minimum at $\bar{\phi} = 246\text{GeV}$ is hardly visible on the scale of the plot. Left panel: the quartic bare potential always exceeds the contributions from the fermion loop for field values above the Fermi scale ($\Lambda = 10^7\text{GeV}$, $\bar{\lambda}_{2,\Lambda} = 0$, $\bar{\lambda}_{3,\Lambda} = 0$). Right panel: a metastability seeded by the bare potential develops in the course of the RG flow ($\Lambda = 10^7\text{GeV}$, $\bar{\lambda}_{2,\Lambda} = -0.15$, $\bar{\lambda}_{3,\Lambda} = 3$).

perturbatively estimated single-scale potential which would predict complete instability. We conclude that metastability properties of the model can only be reliably calculated if the bare potential at an UV scale is known. The single-scale potential is not sufficient as a matter of principle.

In the considered model, this conclusion becomes obvious as the single-scale potential does not even exhibit a metastable region. This is different from the standard model, where the single-scale potential itself predicts metastability for light Higgs masses, as the single-scale potential is stabilized by electroweak fluctuations again at high field amplitudes. Still, the same conclusion about the reliability of the metastability estimate of the single-scale potential holds as for the simple model.

The fact that the metastability in the effective potential is seeded in the bare potential is illustrated in Fig. 5.13. Here, the effective mean-field potential (black solid line) is shown as the difference between the bare potential (blue dashed line) and the absolute value of the fermion determinant (red dotted line). The left panel depicts the case with stable bare as well as effective potential (initial parameters: $\Lambda = 10^7\text{GeV}$, $\bar{\lambda}_{2,\Lambda} = 0$, $\bar{\lambda}_{3,\Lambda} = 0$). By contrast, the right panel shows the case where a second minimum arises in the effective potential (initial parameters: $\Lambda = 10^7\text{GeV}$, $\bar{\lambda}_{2,\Lambda} = -0.15$, $\bar{\lambda}_{3,\Lambda} = 3$). One clearly sees how the modified structure of the generalized bare potential with a negative $\bar{\lambda}_{2,\Lambda}$ is responsible for the second minimum at large scales besides the electroweak one (the latter at $\bar{\phi} = 246\text{GeV}$ is hardly visible on the scales of the plot). We emphasize again that there is no possibility for the mean-field potential to develop a second minimum for the general case of quartic bare potentials. As it can be seen in Fig. 5.13 for the smallest possible value $\bar{\lambda}_{2,\Lambda} = 0$, the bare potential always exceeds the fermion determinant, especially for larger UV values of $\bar{\lambda}_{2,\Lambda}$.

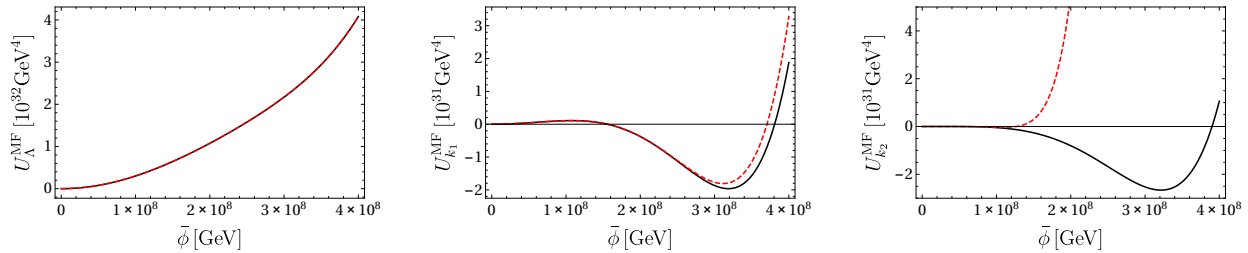


Fig. 5.14.: Full mean-field potential (black solid line) and the potential approximated by a Taylor expansion (red dashed line) around the origin up to ϕ^8 for different values of the RG scale k . The left panel shows the bare potential for $\Lambda = 10^9 \text{GeV}$ ($\bar{\lambda}_{3,\Lambda} = 3$, and $\bar{\lambda}_{2,\Lambda}$ is chosen such that $\bar{m}_H = 125 \text{GeV}$), where the Taylor approximation fits the full potential as it should. The middle plot shows the scalar potential slightly below the UV cutoff, $k_1 = 2.5 \cdot 10^8 \text{GeV} < \Lambda$, where the second minimum is built up. Towards the IR, $k_2 = 5 \cdot 10^7 \text{GeV}$, the second minimum settles while it disappears within the Taylor expansion (right plot).

Break down of the Taylor expansion at a mean-field example

With the mean-field effective potential, we can investigate the convergence of the Taylor expansion in the case of a metastability. In [59], a *pseudo-stable phase* was observed within a polynomial expansion. There, polynomial RG flows were observed that start at $k = \Lambda$ with a globally stable bare potential, then run through a metastable regime with two minima and finally end up in the IR $k = 0$ with one stable minimum at the Fermi scale. We now expand the mean-field effective average potential (5.33) around the minimum at the origin and follow its flow in comparison with the flow of the full mean-field effective potential. This is depicted in Fig. 5.14. Indeed, the potential approximated by a polynomial expansion shows the same pseudo-stable behavior as observed in [59]. A second minimum appears but disappears again after a short RG time. The polynomial expansion thus looks stable again in the IR. This is in contrast to the full mean-field potential where the second minimum survives the RG flow towards the IR. Thus, the global effective mean-field potential exhibits a metastability. We conclude that the pseudo-stable phase is an artifact of the finite convergence radius of the polynomial expansion.

This example shows that a simple Taylor expansion is not appropriate to correctly resolve the metastability of the effective potential which develops during the flow. That also holds for the beyond-mean-field case. Therefore, we are now interested in full flows of the potential as a function of the field and the RG scale.

5.3.4. Nonperturbative flow of the scalar potential

While the mean-field approximation is highly convenient for first analytically controllable estimates, we have to go beyond for quantitative accuracy, for which the FRG provides a perfect tool. Doing so, all fermionic and bosonic fluctuations are integrated out. Equation (2.37) serves as an ansatz for the effective average action. The flow of the effective potential

is given by Eq. (2.40). Again, it is convenient to consider the stable flow of its first derivative (2.41) and to compute the effective potential by integration. Now, we take the scaling of the wave function renormalizations in terms of the anomalous dimensions, Eq. (2.43) and Eq. (2.44), and the Yukawa coupling (2.42) into account. After the dimensionless electroweak VEV shows dimensional scaling, we switch to the dimensional flow. Note that we now consider dimensional quantities which are renormalized by the corresponding wave function renormalizations ($\bar{m}_H = \bar{m}_{H,R}$ and $\bar{m}_t = \bar{m}_{t,R}$).

For the flow of potentials exhibiting a single minimum, a polynomial expansion [53, 58, 296, 297] around the minimum has proven to be appropriate. However, the example of the seeming pseudo-stable phase above has shown that a proper description of metastability doubtlessly requires the resolution of the full potential as a function of both k and $\bar{\rho}$. In order to run the RG flow over many orders of magnitude in presence of a relevant operator $\bar{\phi}^2$ of canonical dimension 2, the PDE solver additionally needs to be of high precision. The following results show that pseudo-spectral methods are a well suited tool for these requirements. This enables us to choose high UV cutoffs. The choice is solely restricted by the number of digits needed for tuning the IR quantities. Due to the canonical scaling of the mass operator, we need to tune approximately twice as many digits as the number of orders of magnitude between the UV scale and the Fermi scale. All full potential computations have been done with `long double`. Thus, we restricted ourselves to a maximal UV cutoff of 10^{10}GeV for the full potential calculation. In principle, higher values for Λ are straightforwardly accessible by using a higher accuracy for the floating-point arithmetics.

Higgs-mass bounds

As a benchmark, we perform a comparison to local polynomial solutions of the flow equation. For this purpose, we compute Higgs masses for different initial values over a large range of cutoff values. In Fig. 5.15, we depict the resulting IR Higgs mass as a function of the UV cutoff Λ . The solid lines mark the Higgs masses computed within the polynomial truncation, whereas the filled circles correspond to those resulting from the pseudo-spectral full potential computation. For the restricted class of $\bar{\phi}^4$ bare potentials, the black data shows the resulting lowest possible Higgs mass, i.e., the conventional lower bound for $\bar{\lambda}_{2,\Lambda} = 0$. Examples within the class of generalized bare potentials that lead to a relaxation of the lower bound are shown in red ($\bar{\lambda}_{2,\Lambda} = -0.1$, $\bar{\lambda}_{3,\Lambda} = 3$) and orange ($\bar{\lambda}_{2,\Lambda} = -0.15$, $\bar{\lambda}_{3,\Lambda} = 3$). The black and red line agree with the results of [53]. For all cases, the pseudo-spectral data lies perfectly on top of the polynomial results. The orange data corresponds to a potential that develops a metastability, i.e., it seems pseudo-stable in the polynomial expansion. The full numerical PDE solution thus provides a strong confirmation that the polynomial expansion is suitable for extracting local information such as the Higgs mass (\sim curvature of the potential at $\bar{\phi}_{0,R} = v$), although the outer structure may not be displayed correctly.

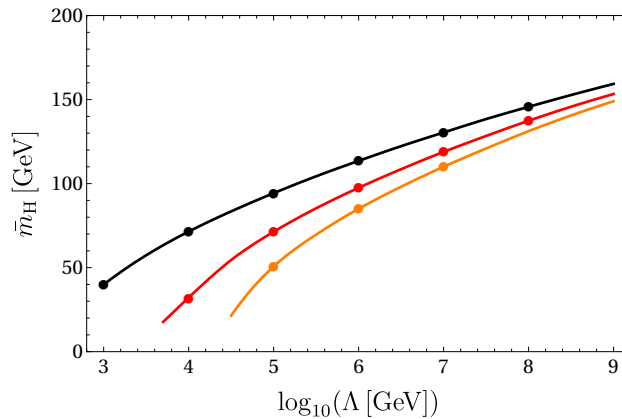


Fig. 5.15.: Higgs-boson mass as a function of the UV cutoff for various bare potentials. The filled circles are obtained by solving the full PDE system. These match perfectly with the Higgs masses computed within the polynomial expansion (2.22) of the scalar potential for the class of $\bar{\phi}^4$ -type bare potentials (black, conventional “lower bound” $\bar{\lambda}_{2,\Lambda} = 0$) as well as generalized bare potentials for the case where the effective potential is stable for $\Lambda \gtrsim 10^4 \text{GeV}$ (red, $\bar{\lambda}_{2,\Lambda} = -0.1$, $\bar{\lambda}_{3,\Lambda} = 3$) or develops a metastability (orange, $\bar{\lambda}_{2,\Lambda} = -0.15$, $\bar{\lambda}_{3,\Lambda} = 3$).

Full potential flows

Let us start with a closer look at the behavior of the full flow for the class of the $\bar{\phi}^4$ bare potentials. Obviously, the polynomial truncation lacks in describing the asymptotic behavior of the potential which can be seen in Fig. 5.16. This is not surprising since the flow equations suggest the asymptotic behavior to be that of the UV potential $\sim \bar{\phi}^4$ because fluctuations for large field amplitudes are suppressed. By contrast, the asymptotic behavior of the polynomial expansion is fixed by construction to the highest power of the field which is taken into account in the truncation, $\sim \bar{\phi}^{2N_p}$. These higher order couplings are generated during the RG flow, even if the bare potential is of $\bar{\phi}^4$ type. Therefore, considering only terms up to $\bar{\phi}^4$, (accidentally) displays the asymptotic behavior best.

Naively, the polynomial truncation up to sixth order in $\bar{\phi}$ seems to suggest an instability; however, the inflection point is beyond the radius of convergence of the polynomial expansion around the Fermi scale. This radius of convergence is approximately of the order of the curvature around the electroweak minimum [53]. For large field values the polynomial expansion behaves like an asymptotic series with alternating signs between the coefficients. Incidentally, an alternating series is also obtained from the polynomial expansion of the mean-field effective potential. As long as the $\bar{\phi}^4$ class of bare potentials is considered, no hint for an in-/metastability can be found within the radius of convergence of the polynomial expansion. This is confirmed by the fully stable potential obtained from the global pseudo-spectral flow.

We observe that the mean-field potential agrees quite well with the results for the full potential, for small as well as for larger field values, see green dashed curve in Fig. 5.16. The fluctuations of the bosons appear to play a minor role in this parameter regime near

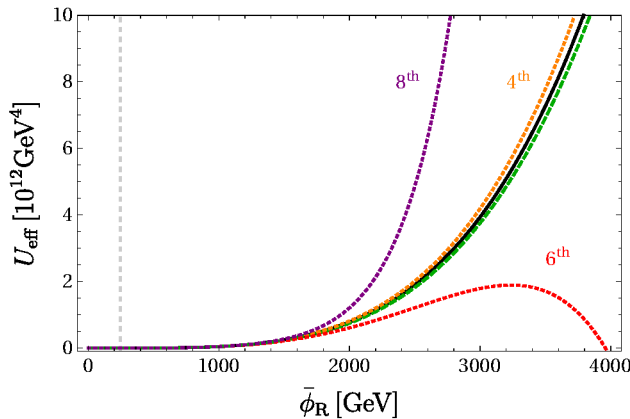


Fig. 5.16.: Comparison between the effective potential of the full calculation (black, $k_{\text{IR}} = 113.9\text{GeV}$), the mean-field result (green dashed) and polynomial truncated potentials (dotted) up to fourth order (orange), sixth order (red) and eighth order (purple) for the stable case. The cutoff is chosen to be $\Lambda = 10^9\text{GeV}$ and bare couplings are tuned such that the Higgs mass is 159.4GeV in all cases for reasons of comparison. The vertical gray-dashed line indicates the position of the Fermi minimum at $\phi_{\text{R}} = 246\text{GeV}$.

the lower edge of the IR window, where the fermionic contributions dominate. Moreover, neglecting the anomalous dimensions and the flow of the Yukawa coupling does not have a significant effect. Thus, the simple mean-field effective potential is an effective tool to get first insights into the global behavior of the scalar potential, justifying the seemingly severe approximations of Sec. 5.3.3.

The qualitative picture remains the same for full flows also in the class of generalized bare potentials. For those cases where no second minimum emerges during the polynomial truncated flow, we observe that also the full flow does not develop an outer minimum for field values larger than the Fermi scale. Our new results hence confirm the existence of a class of stable bare potentials giving rise to Higgs masses below the conventional lower bound as, for instance, depicted by the red curve in Fig. 5.15 for $\Lambda \gtrsim 10^4\text{GeV}$. Therefore, the mechanism of lowering the lower bound for completely stable potentials remains active beyond the polynomial expansion and the mean-field analysis. Thus, higher-order operators can diminish the lower Higgs-mass bound of the standard model.

Let us take a closer look at the inner workings of the equations. For large field amplitudes in the asymptotic regime of the potential, all fluctuations are suppressed as the threshold functions approach zero. In this regime, the flow is dominated by dimensional scaling, i.e., the first two terms in Eq. (2.40). This holds for the $\bar{\phi}^4$ as well as for the generalized class of bare potentials irrespectively of the stability properties.

Deviations from the mean-field limit require relevant bosonic fluctuations. In the small coupling (i.e., small Higgs mass) regime, this can indeed occur in the full flow due to threshold effects of the following type: If a second minimum emerges seeded by a suitable bare potential, the curvature near the top of the barrier between the minima is negative, such that the bosonic threshold function $l_0^{(\text{B})d}(u' + 2\rho u''; \eta_\phi)$ is enhanced. This type of bosonic

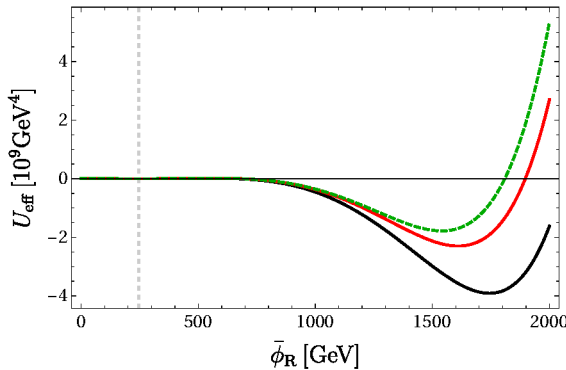


Fig. 5.17.: Comparison between the effective potential for a metastable case obtained by the full pseudo-spectral calculation where the anomalous dimensions are computed at the electroweak VEV (black/lower solid line, $k_{\text{IR}} = 105.5\text{GeV}$), at the outer minimum (red/upper solid line, $k_{\text{IR}} = 93.3\text{GeV}$) and the mean-field result (green dashed line). Setting the anomalous dimensions by hand to zero would yield a rather good agreement with the mean-field potential. The Higgs mass is tuned to $\bar{m}_{\text{H}} = 25\text{GeV}$ with the UV cutoff $\Lambda = 5\text{TeV}$ and $\bar{\lambda}_{3,\Lambda} = 1$.

enhancement is only visible in a full potential flow. To find out if these fluctuations really give rise to a significant deviation to the mean-field potential, we compare the flows ending up in the metastable regime as depicted in Fig. 5.17. For a meaningful comparison between mean-field and full flow, we tune the bare potential such that the IR physics including the Higgs mass is kept fixed. For illustrative purposes, we choose a UV cutoff of only 5TeV, a Higgs mass of 25GeV and $\bar{\lambda}_{3,\Lambda} = 1$. The mean-field potential (dashed line) differs from the full solutions (solid lines) integrated down to an IR value of $k_{\text{IR}} \sim 100\text{GeV}$, where the IR quantities have settled and convexity sets in. The full solutions correspond to defining the anomalous dimensions at the local Fermi minimum (black) or at the second global minimum (red). Both curves differ as fields and couplings are renormalized differently within the two schemes. The black curve corresponds to a renormalization choice better resolving the Fermi minimum whereas the red curve is better suited for the second minimum. In other words, the axes for the different solid lines have a different meaning due to the different field rescaling during the flow. Interestingly, the deviation between the mean-field and the full effective potential is mainly due to this different rescaling. If the anomalous dimensions were artificially set to zero, mean-field and full potential results would still match rather well.

5.3.5. Convexity of the effective potential

As argued in the first part of this chapter, we expect the effective potential to be a convex function of the field. For bosonic models, we have already seen that the Wetterich equation has this convexity property in the limit $k \rightarrow 0$. At finite k , the regulator term $\sim R_k$ sources a nonconvex contribution which vanishes in the limit $k \rightarrow 0$. By contrast, this convexity property cannot be seen neither in the perturbative construction of the single-scale potential nor in the mean-field approximation.

For potentials with a single minimum, we have seen in Sec. 5.1 that convexity of the running potential sets in rather late in RG time, i.e., convexity is driven by the very deep IR modes which are often no longer relevant for the IR observables. For instance in the examples above, we have stopped the flow at scales $k_{\text{IR}} \sim 10 \dots 100 \text{ GeV}$, where the IR Fermi scale observables have already settled to their physical values. Still, for these values of k , the approach to convexity has not fully set in yet. Whereas this demonstrates that convexity is not important for the static observables, it is an interesting question as to whether the approach to convexity can be important for estimates of the tunneling rate between two different minima. The relevance of this question becomes obvious from the fact that any tunneling barrier in a convex potential is (naively) exactly zero by construction.

With only one minimum at the Fermi scale, the onset of convexity follows along the lines of Sec. 5.1. However, in comparison to purely bosonic models, fermionic fluctuations delay convexity since they enter the flow equation with an opposite sign, cf. the last term in Eq. (2.40). Thus, bosonic fluctuations have to exceed the fermionic fluctuations first. As convexity also introduces nonanalyticities, its onset becomes numerically first visible in higher derivatives. Therefore, we consider the first derivative of the potential u' in the following. In the case of a single minimum, the balancing between bosons and fermions also implies that the onset of convexity becomes more pronounced if the boson coupling $\bar{\lambda}_{2,k}$ is enhanced relative to the fermion coupling \bar{h}_k . In terms of physical parameters, this implies that convexity should become more prominent for larger Higgs-to-top mass ratios. In Fig. 5.18, we plot u' for three different ratios $\bar{m}_{\text{H}}/\bar{m}_{\text{t}}$. The flow has been stopped at a

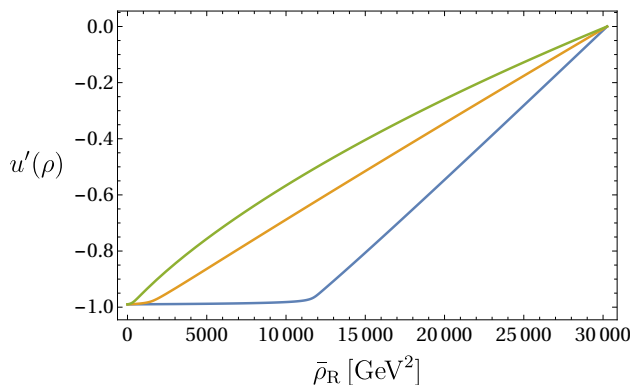


Fig. 5.18.: The approach to convexity of the potential is faster if the ratio between bosonic and fermionic coupling $\bar{m}_{\text{H}}/\bar{m}_{\text{t}}$ increases (from green/top to blue/bottom: $\bar{m}_{\text{H}}/\bar{m}_{\text{t}} = 0.23, 0.66, 1.12$). Here, the first derivative of the potential as a function of the renormalized dimensionful field invariant is depicted. All potentials exhibit a minimum (i.e., $u' = 0$) at $\bar{\phi}_{\text{R}} = 246 \text{ GeV}$ ($\bar{\rho}_{\text{R}} = 30258 \text{ GeV}^2$). The approach to convexity becomes manifest by a characteristic flattening of the inner region and u' approaching $u' \rightarrow -1$. We have chosen $\Lambda = 10^3 \text{ GeV}$ and $\bar{m}_{\text{H}} = 39.7 \text{ GeV}$ for the green/top curve stopping the flow at $k_{\text{IR}} = 33.4 \text{ GeV}$, and $\Lambda = 10^6 \text{ GeV}$ and $\bar{m}_{\text{H}} = 113.6 \text{ GeV}$ for the orange/middle curve stopping at $k_{\text{IR}} = 80 \text{ GeV}$. The blue curve is added for illustration; here $\Lambda = 6.5 \cdot 10^4 \text{ GeV}$, $v = 246 \text{ GeV}$, $\bar{m}_{\text{t}} = 426.3 \text{ GeV}$, $\bar{m}_{\text{H}} = 476.6 \text{ GeV}$, and $k_{\text{IR}} = 264.5 \text{ GeV}$, such that the curve is not tuned to the physical top mass in terms of the renormalization conditions (5.26).

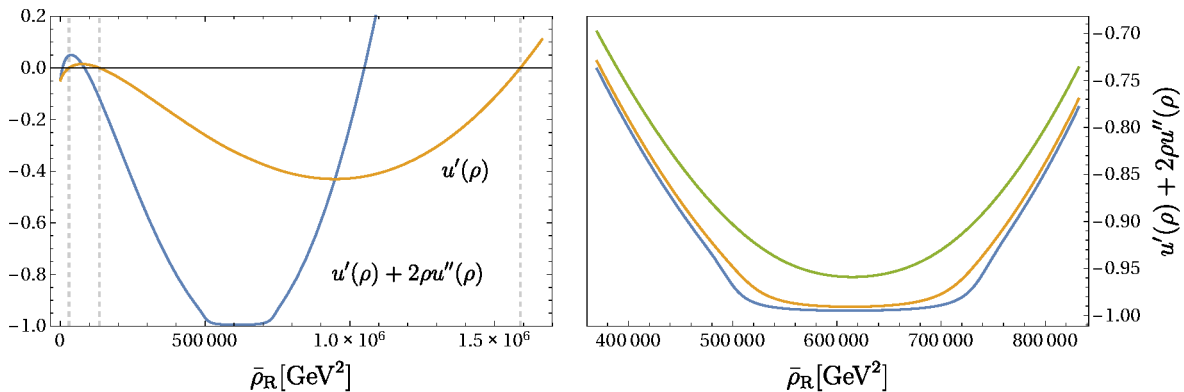


Fig. 5.19.: Onset of convexity at a scale $k \sim 100\text{GeV}$ for the case of two minima. Whereas the small-field region is still dominated by fermionic fluctuations, the bosons control the flow for larger field amplitudes, especially in the region of the minimum of the field-dependent mass term $u' + 2\rho u''$. Left panel: mass term and the first derivative of the potential u' over a wide field range. The vertical dashed lines mark the location of both minima and the maximum of the tunnel barrier of the potential in between. The minimum of the mass term approaches the singularity $u' + 2\rho u'' \rightarrow -1$, triggering the approach to convexity. This is shown in the right panel in detail for decreasing scale $k \in \{112.5, 110, 109.5\}\text{GeV}$ from top (green) to bottom (blue). For this example flow, we have used $\bar{m}_H = 24.1\text{GeV}$, $\lambda_{3,\Lambda} = 1$ and $\Lambda = 5\text{TeV}$.

scale k_{IR} such that the potentials have the same distance from the singularity of the bosonic propagator $1 - |u'(0)| = 0.01$. The faster approach to convexity then is directly visible in terms of the position of nonanalyticity $\rho_{\text{kin}}k$ which we observe to move towards larger field amplitudes if $\bar{m}_H/\bar{m}_t \sim \bar{\lambda}_{2,\text{eff}}/\bar{h}_{\text{eff}}$ for $k = k_{\text{IR}}$ increases. By contrast, if \bar{m}_H/\bar{m}_t is small, the characteristic flat region of u' is hardly visible at this particular scale k_{IR} and would increase only towards even smaller scales.

Let us now turn to the more interesting case of two minima which is numerically more challenging since the field-dependent “mass term” becomes negative, $u' + 2\rho u'' < 0$, not only for small fields but also for a second region at larger fields. As an illustrative example, we choose a similar flow as above. We plot this mass term in the region of both minima of the tunnel barrier, cf. Fig. 5.19 (left panel). For comparison we show $u'(\rho)$ as well. The dashed vertical lines indicate the position of both minima and the maximum in between. Convexity becomes first visible for larger fields at the minimum of the mass term which tends to $u' + 2\rho u'' \rightarrow -1$ after k has dropped below the scale of the top quark, cf. Fig. 5.19 (right panel). For the current example, this minimum of the mass term is located in between the maximum and the outer minimum of the potential, but this relative position may vary depending on the scale and the precise choice of parameters. As the maximum of the potential is situated within the region where $u' + 2\rho u'' < 0$ for larger fields, the flat region eventually extends beyond the maximum, significantly affecting the tunnel barrier for small scales $k \lesssim 100\text{GeV}$. For small fields, the fermions still control the flow at $k \sim 100\text{GeV}$.

However, for decreasing scale k the bosonic fluctuations win out over the fermionic ones and convexity sets in as well, similar to Fig. 5.18. We emphasize that the approach to convexity appears to set in at different scales for small and large field amplitudes.

In the present example, convexity affects the tunnel barrier at scales k which are more than an order of magnitude smaller than the field amplitude of the barrier and the outer minimum. A calculation of the tunnel rate which is dominated by the latter scales hence is expected to be only weakly influenced by the approach to convexity. As a general rule, we conclude that the standard recipes for calculations of the tunnel rate [298, 299] remain unaffected as long as the fermion fluctuations dominate the renormalization of the potential. Whether or not this is the case at the relevant scales of interest will in general depend on the details of the scale-dependent potential and thus also on the details of the bare potential. As soon as the bosonic fluctuations become important, the approach to convexity has also to be accounted for in estimates of the tunneling rate.

In the FRG context, a proposal for this has been worked out for scalar models in [300]. A formalism that can also systematically deal with further radiative effects in the resulting inhomogeneous instanton background on top of a radiatively generated potential has recently been developed with the help of a self-consistent functional scheme based on the 2PI effective action [301, 302].

We would like to emphasize the necessity of a simultaneous consistent treatment of the renormalization flow of the potential together with the fluctuation contributions in a tunnel-rate calculation – even if the bare potential was known exactly. Of course, unknown higher dimensional operators then further add to the indeterminacy of the vacuum decay rate [59, 303–306]. For instance, the influence of gravity-induced higher dimensional operators has been studied in [307–310].

5.3.6. Quantum phase diagram of the Higgs-Yukawa model

Can the outer global minimum be used to define the electroweak vacuum? If the occurrence of metastability is rather generic in presence of higher-dimensional operators, could it be possible to fix physical parameters with respect to the global minimum as the Fermi scale? In order to address these questions, we now reconsider the model from a more general viewpoint.

So far, we have fixed the model with the help of the renormalization conditions (5.26) applied to the first or innermost minimum. Instead, let us now start from a fixed UV cutoff Λ with some bare potential bounded from below and read off the IR phases from the effective potential at some IR scale k where all modes have decoupled (apart from the approach to convexity). We are most interested in this quantum phase diagram as a function of the (super-)renormalizable operators $\sim \bar{m}_\Lambda^2 \bar{\phi}^2$ and $\sim \bar{\lambda}_{2,\Lambda} \bar{\phi}^4$, as the electroweak precision data tells us that the standard model is sufficiently close to the Gaussian fixed

point, where perturbation theory based on these operators works very well. In other words, higher-dimensional operators do not take a momentarily measurable influence on collider data.

In the language of critical phenomena, the standard model appears to be close to a second-order quantum phase transition that effectively allows to push the UV cutoff to large values (compared to collider scales). The natural candidate in the standard model is the electroweak (quantum) phase transition represented by the order-disorder phase transition of discrete chiral symmetry in our simple model. It is, in fact, straightforward to verify by means of perturbation theory, mean-field theory or the functional RG that this phase transition is of second order for $\bar{\phi}^4$ type bare potentials in the stable regime. The “control parameter” for the quantum phase transition is the bare mass term \bar{m}_Λ^2 .

In the following, we perform this investigation for the class of generalized bare potentials. For this, we fix $\bar{\lambda}_{3,\Lambda} = 1$ as a representative of a higher-dimensional operator that induces absolute stability. We expect the following results to hold also for other polynomial operators that ensure absolute stability for large field amplitudes. For technical simplicity, we keep the Yukawa coupling $\bar{h}_k^2 \sim \mathcal{O}(1)$ fixed and also neglect the anomalous dimensions, as both do not induce qualitative differences. Still, we keep the full bosonic fluctuation contribution to the flow of the potential.

Choosing $\bar{\lambda}_{2,\Lambda}$ negative but with a small absolute value, the potential will still show only one minimum and the phase transition as a function of \bar{m}_Λ^2 still is of second order as for the $\bar{\phi}^4$ -class, cf. left-hand side of Fig. 5.20. Increasing the absolute value of a negative $\bar{\lambda}_{2,\Lambda}$ a bit, and starting with a large value of \bar{m}_Λ^2 , the sufficiently negative $\bar{\lambda}_{2,\Lambda}$ may seed a local higher minimum at large field amplitudes. Nevertheless, the system is in the symmetric phase with the global minimum at $\bar{\phi}_0 = 0$ (upper left part of Fig. 5.20). On the left-hand side of this figure, we do not further distinguish between the existence or nonexistence of a further local outer minimum; potentials with a local outer minimum shown here only represent possible examples.

Decreasing \bar{m}_Λ^2 , we indeed observe a second-order phase transition to a broken phase driven by fermion fluctuations where the order parameter $\bar{\phi}_0 = v$ is switched on continuously, cf. white region in Fig. 5.20. A local higher minimum at larger field amplitudes may arise by decreasing \bar{m}_Λ^2 or persists if it already existed. It is this second-order phase transition which can serve to define a “continuum limit” essentially establishing cutoff independence.

Decreasing \bar{m}_Λ^2 further, first leads to a lowering of the outer minimum such that the inner minimum becomes metastable (dotted region). The phase transition between the two cases is of first order (dashed lines). For even smaller mass parameters \bar{m}_Λ^2 , the inner minimum vanishes discontinuously while the outer remains (gray-shaded region in Fig. 5.20). We also classify this discontinuous change of the system as a first-order transition, even though it would not correspond to a thermal phase transition. On both sides of the lower dashed line, the system is dominated by the global minimum in the thermodynamic limit.

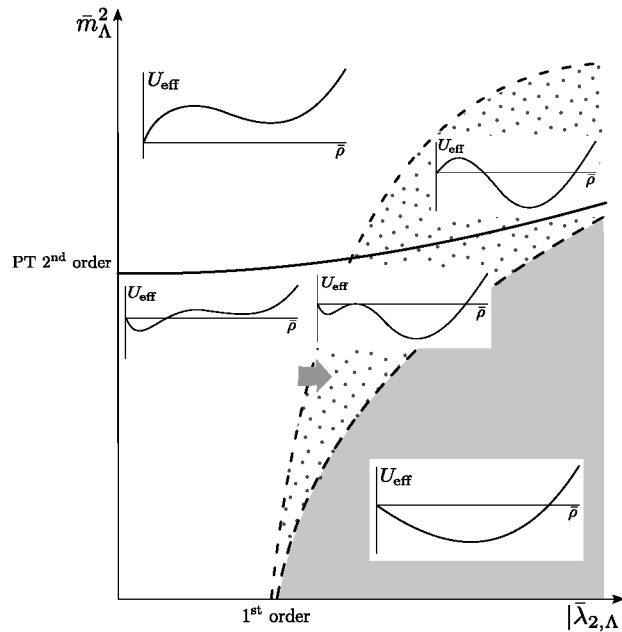


Fig. 5.20.: Quantum phase diagram of the IR effective potentials with possible metastabilities seeded from the bare action. As an example, the large amplitude $\bar{\rho} \sim \bar{\phi}^2$ region is stabilized by a $\bar{\phi}^6$ operator in the UV. The phase diagram is sketched for various initial values for a negative bare $\bar{\lambda}_{2,\Lambda}$ and suitable mass parameters \bar{m}_Λ^2 near the critical regions. In the dotted region the effective potential is metastable, while it is stable in the white and gray-shaded region. In the gray-shaded region only the outer minimum induced by a first order phase transition exists.

This analysis demonstrates that only the transition between the symmetric and symmetry-broken phase, which is driven by fermion fluctuations, is of second order. Therefore, only this transition can be used to separate the cutoff scale from the IR physics in this model. This forces us to associate the Fermi scale with the innermost minimum driven by fermion fluctuations. The outer one seeded by the bare action cannot be used for a definition of the Fermi scale as it is highly unlikely to match with the perturbative description of electroweak precision data. In our flows, this mismatch becomes visible in the practical difficulty to push the cutoff beyond $\sim 1\text{TeV}$ while satisfying all renormalization conditions with v corresponding to the outer minimum.

For negative $\bar{\lambda}_{2,\Lambda}$ with an even larger absolute value (right-hand side of Fig. 5.20), the phase portraits are similar in the sense that only the transition driven by the fermionic fluctuations in the inner region of the potential is a second-order transition. The difference is that this transition occurs only after the outer minimum seeded by the bare action has become the global one. As a consequence, both the symmetric phase for larger \bar{m}_Λ^2 as well as the fermion driven broken phase (inner minimum) are metastable (dotted region) on both sides of the transition. In this regime of bare potentials, the separation of IR physics from the UV scale hence goes along with a metastability.

We can also compare the phase portraits for fixed \bar{m}_Λ^2 and use $\bar{\lambda}_{2,\Lambda}$ as control parameter.

For instance, the transition marked by the gray thick arrow is a first-order broken-to-broken transition. This is likely to correspond to an equivalent transition first observed in lattice simulations of a similar chiral model [55].

We emphasize that the phase portraits determined here correspond to quantum phase transitions with control parameters corresponding to parameters of the bare action. This is a priori unrelated to the nature of finite temperature phase transitions in the same model, even though a relation might be established dynamically because of a thermal decoupling of the fermions. For recent lattice studies, see [57, 311].

5.4. Conclusions

We have shown that pseudo-spectral methods are not only a powerful tool for solving fixed-point equations but also flow equations of bosonic as well as fermionic models. We first discussed flows of the $O(N)$ model in three dimensions, for $N = 1, 4$ and in the large N limit. In all cases, we could achieve a highly stable and precise flow. We showed that our method can accomplish the time integration to machine precision, and always stays very close to the analytical solution exactly known in the large N limit. The error in this case is dominated by the condition of the differential equation. Even for numerically challenging tasks, as resolving the convexity of the effective potential in the IR, the flow was traceable for 5 orders of magnitude for $N = 4$, and about 2 orders of magnitude for $N = 1$. Between the first multicritical fixed point and the Wilson-Fisher fixed point in $d = 2.4$, we have found a separatrix. For the flow along the separatrix, we have integrated out almost 13 orders of magnitude at high precision. It would be interesting to investigate if there exists a separatrix connecting more than two (multi-)critical fixed points.

As a second model, we treated a set of \mathbb{Z}_2 -symmetric bounded potentials in quantum mechanics. Whereas it was sufficient to consider the flows on a finite field range for the unbounded potentials from above, bounded potentials need to be resolved globally for a numerically stable flow. This is more challenging but technically interesting to probe the capabilities of pseudo-spectral methods. For the three potentials that we discussed, we extracted the energies of the ground state and first excited state in the LPA truncation to satisfying accuracy, even though one might have expected from analytical arguments that the determination of the first excited state energy was not possible from the effective potential alone. It is worth mentioning that the nonanalyticity of the nonanalytical potential poses no problem to our method, in contrast to expansions in powers of the field.

In the second part of this chapter, we have investigated the RG flow of the Higgs potential in a Yukawa model. Within the mean-field calculation and the RG flow of the full potential, we have resolved both scales, k and $\bar{\phi}$, of the potential. This allows us to overcome the limitations of conventional approximation schemes, relying on identifications such as $k = \bar{\phi}$, or implicit perturbative limits $\Lambda \rightarrow \infty$. In case of metastabilities, we demonstrated that the

distinction of both scales is necessary for a clear analysis. Metastabilities are not primarily induced by fermion fluctuations, but have to be seeded by suitable properties of the bare potential. In particular, instabilities cannot occur if a well-defined bare action is restricted to contain only renormalizable operators. Upon the inclusion of suitable higher-dimensional operators, metastabilities generically occur for small Higgs masses and large cutoffs – at least within the class of simple polynomial bare potentials studied here.

The pseudo-spectral methods facilitate to resolve both the flow of one minimum and two competing minima taking all fermionic as well as bosonic fluctuations within LPA' into account. We have confirmed earlier results from local flows around the Fermi minimum to high accuracy, such as, for instance, the relaxation of the perturbative lower bound on the Higgs mass. On the other hand, the pseudo-spectral flow also reveals the limitations of the local flow in metastable regimes as competing minima turn out to be beyond the radius of convergence of local flows. In the small-Higgs-mass regime, the full functional flow demonstrated the usefulness of the mean-field approximation. However, mean field is not a suitable approximation to resolve the approach to convexity. For estimates of the tunnel rate, the influence of convexity is an intriguing question. As convexity is driven by the bosonic fluctuations of the deep IR modes, it clearly affects the tunnel rate in purely bosonic models. Employing pseudo-spectral methods, we have shown that convexity, by contrast, does not play a role for these estimates in our example since fermions still control the renormalization of the potential at the characteristic scales. Finally, we have investigated the quantum phase diagram of the model as a function of microscopic couplings of the perturbatively renormalizable operators. We have identified and characterized the “phase transitions”, and argued that the Fermi VEV is necessarily the one driven by fermionic fluctuations and cannot be the outermost one seeded by the bare potential. We have found a broken-to-broken transition which likely was already observed in lattice simulations.

To conclude, we emphasize that a full determination of consistency bounds for the IR observables of the standard model as a function of the cutoff Λ as the scale of maximum UV extension has not yet been completed. On the one hand, for a quantitatively precise picture, all interactions of the standard model have to be taken into account. For an approach in this direction in the framework of the FRG, see [58, 59]. On the other hand, there is no reason to restrict only to polynomial ansätze for the bare action. The mapping of a wide range of bare actions to the IR observables would have to be computed within the RG, technically corresponding to an extremization problem in an infinite-dimensional space. The capability of handling global flows and extending the current studies to nonpolynomial interactions is a necessary prerequisite for this.

6. Conclusions

This work has addressed questions relevant for various physical systems. New results were provided for the critical behavior of $O(N)$ models and Yukawa models, condensed matter systems featuring multicritical behavior, flows in multicritical $O(N)$ symmetric systems and of bounded potentials in quantum mechanics, the vacuum (meta-)stability in particle physics, and tunneling phenomena in fermionic systems. Technically, our studies rely on the powerful combination of the functional renormalization group (FRG) and the expansion of the effective potential by pseudo-spectral methods. The topics of this work are only a few examples of a big class of problems that cannot be considered by perturbative means or local expansions of the potential.

It was shown that pseudo-spectral methods are well-suited for solving functional fixed-point equations and flows since they are very flexible, have superior convergence properties and provide highly accurate results. In Chap. 4, we have applied these methods to fixed-point equations. In the first part, we have computed global scale invariant solutions for the $O(N)$ model in $d = 3$ and below and for the simple Yukawa model in $d = 3$ to high precision. As the nonlinear equations usually give rise to a bundle of local solutions, information about the global existence is of particular interest. Also in cases where polynomial expansions cannot be trusted, e.g., for the multicritical potentials which arise for fractional dimensions in the $O(N)$ model or the small N_f regime of the simple Yukawa model, we obtained fixed-point solutions. We emphasize, although expansions in Chebyshev polynomials seem to be nothing more than a reordering of terms of a Taylor series at first sight, there is a significant difference: To compute the expansion coefficients, only the information at one point is relevant for a Taylor expansion, whereas nonlocal information at a special set of collocation points is needed for a pseudo-spectral expansion.

The second part of Chap. 4 was dedicated to a detailed study of the phase diagram of the $O(N) \oplus O(M)$ model as a function of the dimension d . Little was known before about the stability trading between the fixed points, especially for the case $2 < d \leq 3$ with $N = M$. Employing pseudo-spectral methods, we gained access to the low dimensional case where Taylor-expansion results get unreliable and other techniques highly inefficient. Besides the isotropic fixed point (IFP) with symmetry enhancement, the decoupled fixed point (DFP) and the biconical fixed point (BFP), two additional fixed points take part in the stability trading mechanism for $d < 3$. These fixed points can be derived from an accidental symmetry at $N = M = 1$ in the local potential approximation, which is however slightly broken if the

anomalous dimensions are taken into account. Still, whether fulfilled or slightly broken, it has direct consequences for the stability trading close to $N = M = 1$. Depending on the dimension, several mechanisms occur. Whereas for $d \approx 3$, stability between the DFP and IFP is traded via one fixed point, the BFP, we found that different fixed points interact with the IFP and DFP separately for smaller d . Whether this symmetry is retained in a higher derivative expansion is crucial in order to understand how the overall picture changes quantitatively. This is left for future work.

Furthermore, we have found regions in the parameter space $N = M$ and d with two simultaneously stable multicritical fixed points. In every case, each was found in a separate region $\Delta < 0$, $\Delta > 0$ and $\Delta = 0$. We have conjectured that the sign of Δ at the extremum or saddle point (at nontrivial $(\kappa_\phi, \kappa_\chi)$) decides about what universality class is realized in the low-energy physics. However, in order to prove this and to understand if there is an appropriate macroscopic quantity corresponding to Δ , functional flows have to be considered. This would be possible with a generalization of our computations done in Chap. 5 to more than one order parameter.

To our knowledge, this is the first bosonic model in which coexisting stable fixed points were found. To clarify the situation for the case $N = M = 1$ in $d = 2$, the quantitative reliability needs to be investigated in further studies by increasing the order of the derivative expansion. It would be interesting if the coexisting stability region of the IFP and DFP remained. In this case, the system is supposed to show tetracritical or Berezinskii-Kosterlitz-Thouless type behavior. It would be fascinating to see how such situations show up within experiments.

With our numerical method, we are now able to study the case of the anisotropic anti-ferromagnet ($N = 1$ and $M = 2$) in detail. Furthermore, it would be interesting to know if there exist two-field generalizations of multicritical fixed points in the sense of Sec. 4.1 like the BFP which cannot be inferred from the single-field model. This could be also addressed with our method in the future.

In Chap. 5, we have considered functional flows of the FRG. In our examples, we have seen that a resolution on a finite domain is sufficient if quantum fluctuations are suppressed for large field values. However, the cases of the bounded potentials in quantum mechanics showed that the computation of global flows is also possible with pseudo-spectral methods and essential if fluctuations occur on the entire domain of definition. The high accuracy of our numerical method was discussed using examples of the large N flow and the flow between two criticalities over a wide range of scales in the $O(N)$ model.

For both, bounded and unbounded potentials, convexity sets in in the deep infrared but in different ways. Although challenging, with means of pseudo-spectral methods, we have observed the approach to convexity over many orders of magnitude, which was particularly demonstrated for unbounded potentials. In the case of bounded potentials in quantum mechanics, it seems at first sight to be impossible to read off the energy of the first excited

state due to convexity arguments. However, we have obtained reliable estimates from the flow on intermediate scales.

The last section was devoted to a detailed study of the Higgs-Yukawa model. First, we have discussed the origin of the appearing metastability in the standard model using perturbative techniques which shows up as an instability in the simplified model. Resolving both scales, the energy scale and the scalar field, the in-/metastability can be traced back to an ill-defined microscopic theory which occurs if the scale of the maximal ultraviolet (UV) extension is sent to infinity while the infrared (IR) behavior is kept fixed to the physical masses within our toy model. Thus, metastabilities cannot be induced by fermionic fluctuations and are seeded by the bare potential which was discussed using the example of taking a higher field operator into account. For the considered class of microscopic potentials, the full functional flows showed good agreement with the mean-field results, in particular for the case of stable potentials. For metastable potentials, minor differences occurred originating from the scale dependent wave function renormalizations. We have confirmed the relaxation of the perturbative lower Higgs-mass bound which was already seen by means of polynomial expansions. Still, open questions remain. Any UV boundary condition could be taken as a microscopic theory, as the underlying theory is unknown. It would be therefore interesting to also consider other shapes of the UV potential beyond polynomial ansätze and to investigate their impact on the Higgs-mass bounds. From these considerations, conclusions for the maximal UV extension of the standard model could be drawn.

Furthermore, we have studied the phase diagram in dependence on the perturbatively renormalizable operators taking higher dimensional field operators into account. We argued that the Fermi scale corresponds to the innermost nontrivial minimum driven by fermionic fluctuations and cannot be identified with the outer (global) minimum. We have found a first-order broken-to-broken transition which is likely to correspond to a transition observed in lattice simulations.

Tunneling phenomena are a difficult problem in theoretical physics. Quantum field theory in nonequilibrium is very intricate. Hence, estimates for the tunneling rate are derived from static quantities. However, as the approach to convexity can be hardly disentangled from the tunneling modes, especially in bosonic models, a semiclassical approach is employed. In the Higgs-Yukawa model, we have seen that convexity does not have any effect for these estimates, in contrast to bosonic models, as the fermionic fluctuations exceed the bosonic modes over a wide range of scales.

In this work, we have put forward a numerical method which has already been successfully applied to various topics in physics, but is only little used in the context of quantum field theory, especially within the FRG. Our studies of several physical systems have revealed that pseudo-spectral methods definitely add to the assortment of methods commonly used in the FRG.

Appendix A.

Threshold functions

The regulator functions can be rewritten in terms of dimensionless shape functions,

$$R_{\phi,k}(p) = Z_{\phi,k} p^2 r_{\phi,k}(p^2) \quad \text{and} \quad R_{\psi,k}(p) = -Z_{\psi,k} p r_{\psi,k}(p^2), \quad (\text{A.1})$$

for the bosonic and fermionic modes, respectively. For the linear optimized regulator, the shape functions are

$$r_{\phi,k}^{\text{opt}} = \left(\frac{k^2}{p^2} - 1 \right) \Theta(k^2 - p^2) \quad \text{and} \quad r_{\psi,k}^{\text{opt}} = \left(\sqrt{\frac{k^2}{p^2}} - 1 \right) \Theta(k^2 - p^2). \quad (\text{A.2})$$

The specific choice of the regulator only takes part in the threshold functions. These are single momentum integrals which have to be computed for the flow originating from the one-loop structure of the Wetterich equation (2.13). They read

$$l_0^{(\text{B/F})d}(\omega; \eta_{\phi/\psi}) = \frac{1}{4v_d} k^{-d} \int \frac{d^d p}{(2\pi)^d} \tilde{\partial}_t \log (P_{\phi/\psi} + \omega k^2), \quad (\text{A.3})$$

$$l_n^{(\text{B/F})d}(\omega; \eta_{\phi/\psi}) = -\frac{1}{4v_d} k^{2n-d} \int \frac{d^d p}{(2\pi)^d} \tilde{\partial}_t (P_{\phi/\psi} + \omega k^2)^{-n}, \quad (\text{A.4})$$

$$l_{n_1, n_2}^{(\text{FB})d}(\omega_\psi, \omega_\phi; \eta_\psi, \eta_\phi) = -\frac{1}{4v_d} k^{2(n_1+n_2)-d} \int \frac{d^d p}{(2\pi)^d} \tilde{\partial}_t (P_\psi + \omega_\psi k^2)^{-n_1} (P_\phi + \omega_\phi k^2)^{-n_2}, \quad (\text{A.5})$$

$$l_{\text{R},0}^{(\text{B})d}(\omega_\phi, \omega_\chi, \omega_{\phi\chi}; \eta_\phi, \eta_\chi) = \frac{1}{4v_d} k^{-d} \int \frac{d^d p}{(2\pi)^d} \tilde{\partial}_t \log [(P_\phi + \omega_\phi k^2) (P_\chi + \omega_\chi k^2) - \omega_{\phi\chi} k^4], \quad (\text{A.6})$$

$$m_2^{(\text{B})d}(\omega; \eta_\phi) = -\frac{1}{4v_d} k^{6-d} \int \frac{d^d p}{(2\pi)^d} p^2 \tilde{\partial}_t \frac{(\partial_{p^2} P_\phi)^2}{P_\phi^2} (P_\phi + \omega k^2)^{-2}, \quad (\text{A.7})$$

$$m_4^{(\text{B})d}(\omega; \eta_\phi) = -\frac{1}{4v_d} k^{6-d} \int \frac{d^d p}{(2\pi)^d} p^2 \tilde{\partial}_t (\partial_{p^2} P_\phi)^2 (P_\phi + \omega k^2)^{-4}, \quad (\text{A.8})$$

$$m_2^{(\text{F})d}(\omega; \eta_\psi) = -\frac{1}{4v_d} k^{6-d} \int \frac{d^d p}{(2\pi)^d} p^2 \tilde{\partial}_t (\partial_{p^2} P_\psi)^2 (P_\psi + \omega k^2)^{-4}, \quad (\text{A.9})$$

$$m_4^{(\text{F})d}(\omega; \eta_\psi) = -\frac{1}{4v_d} k^{4-d} \int \frac{d^d p}{(2\pi)^d} p^4 \tilde{\partial}_t \left[\partial_{p^2} \frac{1 + r_{\psi,k}}{(P_\psi + \omega k^2)} \right]^2, \quad (\text{A.10})$$

$$m_{1,2}^{(\text{FB})d}(\omega_\psi, \omega_\phi; \eta_\psi, \eta_\phi) = -\frac{1}{4v_d} k^{4-d} \int \frac{d^d p}{(2\pi)^d} p^2 \tilde{\partial}_t \left[\frac{1 + r_{\psi,k}}{P_\psi + \omega_\psi k^2} \frac{\partial_{p^2} P_\phi}{(P_\phi + \omega_\phi k^2)^2} \right]. \quad (\text{A.11})$$

We have used the definitions $v_d^{-1} := 2^{d+1} \pi^{d/2} \Gamma(d/2)$, and

$$P_\phi := p^2(1 + r_{\phi,k}), \quad P_\psi := p^2(1 + r_{\psi,k})^2. \quad (\text{A.12})$$

The derivative operator $\tilde{\partial}_t$ only acts on the scale dependency of the regulator,

$$\tilde{\partial}_t := \sum_{\Phi=\phi,\chi,\psi} \int d(q^2) \frac{\partial_t (Z_{\Phi,k} r_{\Phi,k}(q^2))}{Z_{\Phi,k}} \frac{\delta}{\delta r_{\Phi,k}(q^2)}. \quad (\text{A.13})$$

In order to perform the momentum integration, the substitution $p^2 \mapsto x$, where

$$\int \frac{d^d p}{(2\pi)^d} = 2v_d \int dx x^{d/2-1}, \quad (\text{A.14})$$

is employed. Inserting the linear optimized regulator (A.2), the loop integrals yield

$$l_0^{(\text{B})d}(\omega; \eta_\phi) = \frac{2}{d} \left(1 - \frac{\eta_\phi}{d+2} \right) \frac{1}{1+\omega}, \quad (\text{A.15})$$

$$l_n^{(\text{B})d}(\omega; \eta_\phi) = \frac{2}{d} \left(1 - \frac{\eta_\phi}{d+2} \right) \frac{n}{(1+\omega)^{n+1}}, \quad (\text{A.16})$$

$$l_0^{(\text{F})d}(\omega; \eta_\psi) = \frac{2}{d} \left(1 - \frac{\eta_\psi}{d+1} \right) \frac{1}{1+\omega}, \quad (\text{A.17})$$

$$l_n^{(\text{F})d}(\omega; \eta_\psi) = \frac{2}{d} \left(1 - \frac{\eta_\psi}{d+1} \right) \frac{n}{(1+\omega)^{n+1}}, \quad (\text{A.18})$$

$$l_{n_1, n_2}^{(\text{FB})d}(\omega_\psi, \omega_\phi; \eta_\psi, \eta_\phi) = \frac{2}{d} \left[\left(1 - \frac{\eta_\psi}{d+1} \right) \frac{n_1}{1+\omega_\psi} + \left(1 - \frac{\eta_\phi}{d+2} \right) \frac{n_2}{1+\omega_\phi} \right] \times \frac{1}{(1+\omega_\psi)^{n_1} (1+\omega_\phi)^{n_2}}, \quad (\text{A.19})$$

$$l_{\text{R},0}^{(\text{B})d}(\omega_\phi, \omega_\psi, \omega_{\phi\psi}; \eta_\phi, \eta_\chi) = \frac{2}{d} \frac{\left(1 - \frac{\eta_\chi}{d+2} \right) (1+\omega_\phi) + \left(1 - \frac{\eta_\phi}{d+2} \right) (1+\omega_\chi)}{(1+\omega_\phi)(1+\omega_\chi) - \omega_{\phi\chi}}, \quad (\text{A.20})$$

$$m_2^{(\text{B})d}(\omega; \eta_\phi) = \frac{1}{(1+\omega)^2}, \quad (\text{A.21})$$

$$m_4^{(\text{B})d}(\omega; \eta_\phi) = \frac{1}{(1+\omega)^4}, \quad (\text{A.22})$$

$$m_2^{(\text{F})d}(\omega; \eta_\psi) = \frac{1}{(1+\omega)^4}, \quad (\text{A.23})$$

$$m_4^{(\text{F})d}(\omega; \eta_\psi) = \frac{1}{(1+\omega_\psi)^4} + \frac{1-\eta_\psi}{d-2} \frac{1}{(1+\omega)^3} - \left(\frac{1-\eta_\psi}{2d-4} + \frac{1}{4} \right) \frac{1}{(1+\omega)^2}, \quad (\text{A.24})$$

$$m_{1,2}^{(\text{FB})d}(\omega_\psi, \omega_\phi; \eta_\psi, \eta_\phi) = \left(1 - \frac{\eta_\phi}{d+1} \right) \frac{1}{(1+\omega_\psi)(1+\omega_\phi)^2}. \quad (\text{A.25})$$

Appendix B.

Expansions via rational Chebyshev functions

In Sec. 3.3, we give a possible way, Eq. (3.17), to compactify the effective average potential. However, we actually use a slightly different approach in Sec. 4.1. Instead of applying the field compactification on the compactified first derivative of the potential, u'/ρ^α , in the outermost domain, we employ the rational Chebyshev functions,

$$R_n(x) = T_n \left(\frac{x-L}{x+L} \right), \quad (\text{B.1})$$

as a suitable orthogonal function set. Note that the compactification of the argument,

$$x_{\text{comp}} = \frac{x-L}{x+L}, \quad (\text{B.2})$$

which maps $\mathcal{M}_{\text{comp}} : [0, \infty) \rightarrow [-1, 1]$, is similar to the field compactification of Eq. (3.17) where the mapping to the domain of definition of the Chebyshev polynomials, $\mathcal{M}_{\text{lin}} : [0, 1] \rightarrow [-1, 1]$, is understood implicitly. Both approaches, (3.17) and the expansion via rational Chebyshev functions, differ only in the considered argument, x_{comp} for the former and x for the latter. Hence, most of the expansion properties using the basis set $\{R_n(x)\}_{n=0}^{N_p}$ can be derived from those employing Chebyshev polynomials. In particular, the convergence on the whole domain $[0, \infty)$ is ensured by the convergence of Chebyshev expansions on $[-1, 1]$.

The orthogonality condition reads

$$\int_0^\infty R_n(x)R_m(x) \frac{dx}{(x+1)\sqrt{x}} = \begin{cases} 0, & n \neq m \\ \pi, & n = m = 0 \\ \pi/2, & n = m \neq 0. \end{cases} \quad (\text{B.3})$$

Suitable sets of collocation points can be derived from the application of $\mathcal{M}_{\text{comp}}^{-1}$ on the grid points Eqs. (3.6)-(3.8). The Clenshaw algorithm can be applied also for this basis set inserting x_{comp} instead of x . Similar to the Chebyshev polynomials, the derivative of the

potential can be computed via a recursive algorithm for the coefficients,

$$\begin{aligned}
 a'_{N_p+1} &= \frac{N_p}{4} a_{N_p}, \\
 a'_{N_p} &= \frac{N_p - 1}{4} a_{N_p-1} - N_p a_{N_p}, \\
 a'_{N_p-1} &= \frac{N_p - 2}{4} a_{N_p-2} - (N_p - 1) a_{N_p-1} + \frac{7N_p}{4} a_{N_p}, \\
 a'_i &= \frac{i - 1}{4} a_{i-1} - \frac{3i}{4} a_i + \frac{3(i + 1)}{4} a_{i+1} - \frac{i + 2}{4} a_{i+2} - a'_{i+1}, \\
 a'_0 &= \frac{1}{4} (a_1 - a_2) - \frac{1}{2} a'_1,
 \end{aligned} \tag{B.4}$$

and dividing all coefficients a'_i by L . N_p denotes the order of the expansion of the potential. Employing Chebyshev polynomials, the derivative is a sum over $N_p - 1$ coefficients since the order of the polynomials is reduced by one. By contrast, $N_p + 1$ coefficients are generated in the case of rational Chebyshev functions as the inner derivative $\partial_x(x - L)/(x + L)$ has to be regarded within the expansion as well. For practical applications, it turned out to be numerically more stable to drop the last two coefficients.

Appendix C.

Rotated solutions with two order parameters

This chapter deals with the $\pi/4$ rotational symmetry of the flow equation (2.48) of the $O(N) \oplus O(M)$ model. More details on the occurrence of the two rotated counterparts of the decoupled fixed point (DFP) and biconical fixed point (BFP) in Sec. 4.2 and their corresponding critical exponents are given.

For $N = M$, the system gives rise to an exchange symmetry under $\phi \leftrightarrow \chi$. We find solutions exhibiting this symmetry as well as solutions which do not, e.g., the decoupled Gaussian fixed points (DGFPs). Such solutions emerge in pairs which transform into each other under $\phi \leftrightarrow \chi$. Thus, the complete spectrum of solutions is invariant under the exchange symmetry.

Let us set $\eta_\phi, \eta_\chi = 0$ and specialize to $N = M = 1$. We assume that $u_*(\rho_\phi, \rho_\chi)$ is a solution of Eq. (2.48). Inserting the $\pi/4$ -rotation (4.16) of $u_*(\rho_\phi, \rho_\chi)$,

$$\tilde{u}_*(\rho_\phi, \rho_\chi) = u_* \left(\frac{\rho_\phi + \rho_\chi - 2\sqrt{\rho_\phi \rho_\chi}}{2}, \frac{\rho_\phi + \rho_\chi + 2\sqrt{\rho_\phi \rho_\chi}}{2} \right), \quad (\text{C.1})$$

into Eq. (2.48), it becomes clear that $\tilde{u}_*(\rho_\phi, \rho_\chi)$ also satisfies the fixed-point equation. As the isotropic fixed point (IFP) is invariant under such a transformation, it is rotated into itself. For the BFP and the DFP, the transformation (4.16) turns a tetracritical fixed point with $\Delta > 0$ into a bicritical one $\Delta < 0$ resulting in two distinct solutions.

Let us take a closer look at those solutions which do not respect the exchange symmetry, i.e., $u_*(\rho_\phi, \rho_\chi) \neq u_*(\rho_\chi, \rho_\phi)$. Here, $\tilde{u}_*(\rho_\phi, \rho_\chi)$ denotes the formal rotation of $u_*(\rho_\phi, \rho_\chi)$. For any solution of Eq. (2.48), the first derivatives $\partial_\phi u_*(\rho_\phi, \rho_\chi)$ and $\partial_\chi u_*(\rho_\phi, \rho_\chi)$ have to vanish at the boundaries $\phi = 0$ and $\chi = 0$, respectively. This is required by the \mathbb{Z}_2 reflection symmetry in ϕ and χ . For any smooth solution which is symmetric under a reflection in ϕ/χ , the derivative must vanish at $\phi/\chi = 0$. Rotations of solutions which do not respect the $\phi \leftrightarrow \chi$ exchange symmetry violate that boundary condition: For the rotated function \tilde{u} , the

boundary condition, using (C.1), becomes

$$\begin{aligned} \partial_\phi \tilde{u}(\rho_\phi, \rho_\chi)|_{\rho_\phi=0} &= \sqrt{\frac{\rho_\chi}{2}} [\partial_y u(x, y) - \partial_x u(x, y)]|_{x=\rho_\chi/2, y=\rho_\chi/2} \\ &\stackrel{!}{=} 0. \end{aligned} \quad (\text{C.2})$$

The exchange symmetry of $u_*(\rho_\phi, \rho_\chi)$ would imply that

$$\partial_{\rho_\phi} u_*(\rho_\phi, \rho_\chi)|_{\rho_\phi=\rho_\chi} = \partial_{\rho_\chi} u_*(\rho_\phi, \rho_\chi)|_{\rho_\phi=\rho_\chi}. \quad (\text{C.3})$$

Using this condition in (C.2) allows us to conclude that

$$\partial_\phi \tilde{u}(\rho_\phi, \rho_\chi) = 0, \quad (\text{C.4})$$

if and only if u preserves the exchange symmetry. Thus, $\tilde{u}_*(\rho_\phi, \rho_\chi)$ cannot be a solution of (2.48), unless the original solution $u(\rho_\phi, \rho_\chi)$ satisfies the exchange symmetry. By contrast, rotating the linear combination $u_*(\rho_\phi, \rho_\chi) + u_*(\rho_\chi, \rho_\phi)$ gives a solution.

Now, let us assume that $u_*(\rho_\phi, \rho_\chi)$ is invariant under $\phi \leftrightarrow \chi$. From the considerations above, one can infer that the eigenvalue spectra of $u_*(\rho_\phi, \rho_\chi)$ and its rotated counterpart $\tilde{u}_*(\rho_\phi, \rho_\chi)$ are related to each other. The linearized equation describing small perturbations around the fixed point reads

$$-\theta \delta u = \sum_{i,j=0} \left. \frac{\partial(\partial_t u)}{\partial u^{(i,j)}} \right|_{u=u_*} \delta u^{(i,j)}, \quad (\text{C.5})$$

where δu is the eigenperturbation and θ the critical exponent, cf. Eq. (2.23). As Eq. (2.48) preserves the $\pi/4$ rotational symmetry and Eq. (C.5) is linear in δu , it preserves that symmetry as well. According to the line of argument for the fixed-point solutions, only those eigenperturbations δu that preserve the $\phi \leftrightarrow \chi$ symmetry are also eigenperturbations of the rotated solution \tilde{u} , cf. Tab. 4.2. The rotation of an eigenperturbation not exhibiting $\phi \leftrightarrow \chi$ exchange symmetry are not a solution of (C.5).

We emphasize that the decoupled fixed points are an exceptional case. For the decoupled solutions, some of the eigenvalues are degenerate. The corresponding eigenperturbations separately break the exchange symmetry. However, the linear combination of both eigendirections results in a $\phi \leftrightarrow \chi$ invariant perturbation. Thus, the corresponding critical exponent is also contained in the spectra of the rotated fixed points, cf. Tab. 4.2.

Let us now take the anomalous dimensions (2.52) and (2.53) into account. They are evaluated at the global minimum for tetracritical fixed-point potentials. For bicritical fixed points, η_ϕ is evaluated at the minimum in field direction ρ_ϕ and η_χ in field direction ρ_χ . Thus, we evaluate η_ϕ at the point ($\kappa_\phi \neq 0, \kappa_\chi = 0$), and analogously, η_χ at the point ($\kappa_\phi = 0, \kappa_\chi \neq 0$). Tab. 4.3 shows that the anomalous dimensions are not invariant under the rotation (4.16).

In fact, the difference between the anomalous dimensions of $u_*(\rho_\phi, \rho_\chi)$ and $\tilde{u}_*(\rho_\phi, \rho_\chi)$ may be large. Thus, the $\pi/4$ rotational symmetry is broken in LPA'. Note that this could change in a more extensive truncation, where a field-dependent wave function renormalization is taken into account. However, that does not affect the existence of $\tilde{u}_*(\rho_\phi, \rho_\chi)$. Moreover, those critical exponents that are exactly equal for the solution u and its rotation \tilde{u} in LPA, are still close to each other in LPA', cf. Tab. 4.3.

Now, we consider general values of $N = M$. Besides the radial mode, the Goldstone modes additionally contribute to the flow (2.48). It can be easily seen that they violate the $\pi/4$ rotational symmetry

$$\frac{1}{1 + \tilde{u}_*^{(1,0)}} + \frac{1}{1 + \tilde{u}_*^{(0,1)}} \rightarrow \frac{2\rho'_\phi \left(1 + u_*^{(1,0)}\right) - 2\rho'_\chi \left(1 + u_*^{(0,1)}\right)}{\rho'_\phi \left(1 + u_*^{(1,0)}\right)^2 - \rho'_\chi \left(1 + u_*^{(0,1)}\right)^2}, \quad (\text{C.6})$$

where $\rho'_\phi = (\rho_\phi + \rho_\chi - 2\sqrt{\rho_\phi\rho_\chi})/2$ and $\rho'_\chi = (\rho_\phi + \rho_\chi + 2\sqrt{\rho_\phi\rho_\chi})/2$. This is already clear since the radial part contains derivatives with respect to both fields whereas the Goldstone terms are fully decoupled. The transformation (4.16) generally couples both sectors. Similar to the LPA' case, for small deviations from $N = M = 1$, the symmetry is only broken slightly. Hence, we observe that $\tilde{u}_*(\rho_\phi, \rho_\chi)$ may still exist for larger and smaller $N = M$. Moreover, for $N = M$ far away from $N = M = 1$, $\tilde{u}_*(\rho_\phi, \rho_\chi)$ may become fully independent from $u_*(\rho_\phi, \rho_\chi)$.

Appendix D.

One-loop effective action in quantum mechanics

In Sec. 5.2.4, we consider the one-loop approximation for the effective potential. In what follows, some details on its derivation shall be given. For this purpose, we stick to the quantum mechanical case which corresponds to one dimensional quantum field theory. From (2.16), we know

$$U_{\text{eff}}^{1\text{-loop}} = U_{\text{cl}} + \frac{1}{2} \text{Tr} \ln \left(\frac{-\partial^2 + \partial_x^2 U_{\text{cl}}}{-\partial^2} \right), \quad (\text{D.1})$$

taking a proper normalization of the potential into account. For the presentation of the logarithm, we use Frullani's formula with the proper time parameter T and obtain

$$U_{\text{eff}}^{1\text{-loop}} = U_{\text{cl}} - \frac{1}{2\Omega} \int_0^\infty \frac{dT}{T} \left(e^{-T\partial_x^2 U_{\text{cl}}} - 1 \right) \text{Tr} e^{T\partial^2}, \quad (\text{D.2})$$

where Ω is the volume of the space. In momentum space, the trace can be easily evaluated. Thus, we are left with

$$U_{\text{eff}}^{1\text{-loop}} = U_{\text{cl}} - \frac{1}{4\sqrt{\pi}} \int_0^\infty \frac{dT}{T^{3/2}} \left(e^{-T\partial_x^2 U_{\text{cl}}} - 1 \right). \quad (\text{D.3})$$

The second term is convergent and reveals the one-loop contribution $\sqrt{\partial_x^2 U_{\text{cl}}}/2$ to the classical potential. Note that for the evaluation of the integral, $\partial_x^2 U_{\text{cl}} > 0$ was required. Therefore, the one-loop effective action only provides meaningful results for small x in the case of the bounded potentials (5.4) - (5.6).

Appendix E.

Computation of the single-scale potential

In Sec. 5.3.2, we argue that the single-scale potential can be obtained from the beta function of the $\bar{\phi}^4$ coupling. Here, we sketch its computation in terms of Eq. (2.16) and show that both derivations lead to the same result. The bare potential is given by Eq. (5.27). As in Sec. 5.3.2 only fermionic fluctuations are taken into account, we are solely concerned with the computation of the fermion determinant in

$$U_{\text{eff}}^{1\text{-loop}} = U_{\Lambda} - \frac{1}{\Omega} \ln \det (i\not{\partial} + i\bar{h}\bar{\phi}), \quad (\text{E.1})$$

where Ω is the spacetime volume. For this purpose, we also drop the scale dependence of the Yukawa coupling \bar{h} . Note that $i\not{\partial} + i\bar{h}\bar{\phi}$ is isospectral to $-i\not{\partial} + i\bar{h}\bar{\phi}$, hence

$$U_{\text{eff}}^{1\text{-loop}} = U_{\Lambda} - \frac{1}{2\Omega} \ln \left(\frac{\det (-\partial^2 + \bar{h}^2\bar{\phi}^2)}{\det (-\partial^2)} \right), \quad (\text{E.2})$$

with a proper normalization of the potential. The trace over momentum space and all Dirac indices yields

$$U_{\text{eff}}^{1\text{-loop}} = U_{\Lambda} - 2 \int_{\Lambda} \frac{d^4p}{(2\pi)^4} \ln \left(1 + \frac{\bar{h}^2\bar{\phi}^2}{p^2} \right), \quad (\text{E.3})$$

where only the momenta $p^2 < \Lambda^2$ are integrated out. The solution can be given analytically,

$$U_{\text{eff}}^{1\text{-loop}} = U_{\Lambda} - \frac{\Lambda^2\bar{h}^2\bar{\phi}^2}{16\pi^2} + \frac{1}{16\pi^2} \left[\bar{h}^4\bar{\phi}^4 \ln \left(1 + \frac{\Lambda^2}{\bar{h}^2\bar{\phi}^2} \right) - \Lambda^4 \ln \left(1 + \frac{\bar{h}^2\bar{\phi}^2}{\Lambda^2} \right) \right]. \quad (\text{E.4})$$

For large UV cutoffs Λ , we obtain

$$U_{\text{eff}}^{1\text{-loop}} \approx \left(\frac{\bar{m}_{\Lambda}^2}{2} - \frac{\Lambda^2\bar{h}^2}{8\pi^2} \right) \bar{\phi}^2 + \left(\frac{\bar{\lambda}_{\Lambda}}{8} + \frac{\bar{h}^4}{2} + \frac{\bar{h}^4}{16\pi^2} \ln \left(\frac{\Lambda^2}{\bar{h}^2\bar{\phi}^2} \right) \right) \bar{\phi}^4. \quad (\text{E.5})$$

The Λ divergences are swallowed by proper renormalization conditions for the $\bar{\phi}^2$ term,

$$\bar{m}_{\mu}^2 = \frac{\bar{m}_{\Lambda}^2}{2} - \frac{\Lambda^2\bar{h}^2}{8\pi^2}, \quad (\text{E.6})$$

for the $\bar{\phi}^4$ term at the scale $\bar{\phi} = \mu$,

$$\bar{\lambda}_\mu = \frac{\bar{\lambda}_\Lambda}{8} + \frac{\bar{h}^4}{2} + \frac{\bar{h}^4}{16\pi^2} \ln \left(\frac{\Lambda^2}{\bar{h}^2 \mu^2} \right). \quad (\text{E.7})$$

Inserting these into (E.5), provides the single-scale potential as it is given by (5.30).

Appendix F.

Computation of the scale dependent fermion determinant

Sec. 5.3.3 deals with the mean-field Higgs-Yukawa potential. For its computation, the fermion determinant has to be evaluated. Our starting point is formula (2.16), where we have implicitly sent $\Lambda \rightarrow \infty$. However, this limit is not necessarily well-defined. Hence, a proper regularization scheme must be employed for evaluating the (super-)trace. We use the linear optimized regulator. In order to keep both scales Λ and k , we re-derive the one-loop effective average action by integrating its flow from Λ to k ,

$$\Gamma_k^{1\text{-loop}} = S - \frac{1}{2} \text{STr} \ln \left(\frac{S^{(2)} + R_\Lambda}{S^{(2)} + R_k} \right). \quad (\text{F.1})$$

The super trace provides an additional minus sign for the fermionic fluctuations. From this, the mean-field potential can be determined to be

$$U_k^{\text{MF}} = U_\Lambda + \frac{1}{\Omega} \ln \left(\frac{\det(\mathbf{i}\not{\partial} + R_{\psi,\Lambda} + \mathbf{i}\bar{h}\bar{\phi})}{\det(\mathbf{i}\not{\partial} + R_{\psi,k} + \mathbf{i}\bar{h}\bar{\phi})} \right), \quad (\text{F.2})$$

where Ω is the spacetime volume and the scale dependence of the Yukawa coupling is neglected. As $\det(\mathbf{i}\not{\partial} + R_{\psi,k/\Lambda} + \mathbf{i}\bar{h}\bar{\phi}) = \det(-\mathbf{i}\not{\partial} + R_{\psi,k/\Lambda} + \mathbf{i}\bar{h}\bar{\phi})$, the mean-field potential can be rewritten

$$U_k^{\text{MF}} = U_\Lambda + \frac{1}{2\Omega} \ln \left(\frac{\det(p^2(1 + r_{\psi,\Lambda})^2 + \bar{h}^2\bar{\phi}^2)}{\det(p^2(1 + r_{\psi,k})^2 + \bar{h}^2\bar{\phi}^2)} \right) \quad (\text{F.3})$$

$$= U_\Lambda + \frac{1}{2\Omega} \text{Tr} \ln \left(\frac{p^2(1 + r_{\psi,\Lambda})^2 + \bar{h}^2\bar{\phi}^2}{p^2(1 + r_{\psi,k})^2 + \bar{h}^2\bar{\phi}^2} \right), \quad (\text{F.4})$$

where we have switched to the representation in momentum space. Note that the trace also runs over the four Dirac indices. Inserting the linear optimized regulator (2.15) and solving

the momentum integral,

$$U_k^{\text{MF}} = U_\Lambda + 2 \int \frac{d^4 p}{(2\pi)^4} \ln \left(\frac{p^2(1 + r_{\psi,\Lambda})^2 + \bar{h}^2 \bar{\phi}^2}{p^2(1 + r_{\psi,k})^2 + \bar{h}^2 \bar{\phi}^2} \right), \quad (\text{F.5})$$

which can be done analytically, leads to (5.34).

Bibliography

- [1] K. G. Wilson, *Renormalization group and critical phenomena. 1. Renormalization group and the Kadanoff scaling picture*, Phys. Rev. **B4** (1971), 3174–3183, DOI: [10.1103/PhysRevB.4.3174](https://doi.org/10.1103/PhysRevB.4.3174).
- [2] K. G. Wilson, *Renormalization group and critical phenomena. 2. Phase space cell analysis of critical behavior*, Phys. Rev. **B4** (1971), 3184–3205, DOI: [10.1103/PhysRevB.4.3184](https://doi.org/10.1103/PhysRevB.4.3184).
- [3] K. G. Wilson, *Renormalization Group and Strong Interactions*, Phys. Rev. D **3** (1971), 1818–1846, DOI: [10.1103/PhysRevD.3.1818](https://doi.org/10.1103/PhysRevD.3.1818).
- [4] J. Berges and C. Wetterich, *Equation of state and coarse grained free energy for matrix models*, Nucl. Phys. **B487** (1997), 675–720, DOI: [10.1016/S0550-3213\(96\)00670-0](https://doi.org/10.1016/S0550-3213(96)00670-0), arXiv:[hep-th/9609019](https://arxiv.org/abs/hep-th/9609019) [[hep-th](#)].
- [5] J. Braun, L. Fister, J. M. Pawłowski, and F. Rennecke, *From Quarks and Gluons to Hadrons: Chiral Symmetry Breaking in Dynamical QCD* (2014), arXiv:[1412.1045](https://arxiv.org/abs/1412.1045) [[hep-ph](#)].
- [6] C. S. Fischer, *Infrared properties of QCD from Dyson-Schwinger equations*, J. Phys. **G32** (2006), R253–R291, DOI: [10.1088/0954-3899/32/8/R02](https://doi.org/10.1088/0954-3899/32/8/R02), arXiv:[hep-ph/0605173](https://arxiv.org/abs/hep-ph/0605173) [[hep-ph](#)].
- [7] T. K. Herbst, J. M. Pawłowski, and B.-J. Schaefer, *Phase structure and thermodynamics of QCD*, Phys. Rev. **D88** (2013), 014007, DOI: [10.1103/PhysRevD.88.014007](https://doi.org/10.1103/PhysRevD.88.014007), arXiv:[1302.1426](https://arxiv.org/abs/1302.1426) [[hep-ph](#)].
- [8] H. Rohrer, *Properties of $GdAlO_3$ near the Spin-Flop Bicritical Point*, Phys. Rev. Lett. **34** (1975), 1638–1641, DOI: [10.1103/PhysRevLett.34.1638](https://doi.org/10.1103/PhysRevLett.34.1638).
- [9] N. F. Oliveira, A. P. Filho, S. R. Salinas, and C. C. Becerra, *Magnetic phase diagram of $NiCl_2 \cdot 6H_2O$: The low-temperature canted-paramagnetic boundary and the bicritical point*, Phys. Rev. B **18** (1978), 6165–6177, DOI: [10.1103/PhysRevB.18.6165](https://doi.org/10.1103/PhysRevB.18.6165).
- [10] A. Aharony, *Comment on Bicritical and Tetracritical Phenomena and Scaling Properties of the $SO(5)$ Theory*, Phys. Rev. Lett. **88** (2002), 059703, DOI: [10.1103/PhysRevLett.88.059703](https://doi.org/10.1103/PhysRevLett.88.059703).
- [11] X. Hu, *Bicritical and Tetracritical Phenomena and Scaling Properties of the $SO(5)$ Theory*, Phys. Rev. Lett. **87** (2001), 057004, DOI: [10.1103/PhysRevLett.87.057004](https://doi.org/10.1103/PhysRevLett.87.057004).
- [12] F. Gehring, H. Gies, and L. Janssen, *Fixed-point structure of low-dimensional relativistic fermion field theories: Universality classes and emergent symmetry*, Phys. Rev. **D92** (2015), 085046, DOI: [10.1103/PhysRevD.92.085046](https://doi.org/10.1103/PhysRevD.92.085046), arXiv:[1506.07570](https://arxiv.org/abs/1506.07570) [[hep-th](#)].
- [13] L. Classen, I. F. Herbut, L. Janssen, and M. M. Scherer, *Competition of density waves and quantum multicritical behavior in Dirac materials from functional renormalization*, Phys. Rev. **B93** (2016), 125119, DOI: [10.1103/PhysRevB.93.125119](https://doi.org/10.1103/PhysRevB.93.125119), arXiv:[1510.09003](https://arxiv.org/abs/1510.09003) [[cond-mat.str-el](#)].

- [14] P. W. Higgs, *Broken symmetries, massless particles and gauge fields*, Phys. Lett. **12** (1964), 132–133, DOI: [10.1016/0031-9163\(64\)91136-9](https://doi.org/10.1016/0031-9163(64)91136-9).
- [15] P. W. Higgs, *Broken Symmetries and the Masses of Gauge Bosons*, Phys. Rev. Lett. **13** (1964), 508–509, DOI: [10.1103/PhysRevLett.13.508](https://doi.org/10.1103/PhysRevLett.13.508).
- [16] A. Aharony, *Old and New Results on Multicritical Points*, Journal of Statistical Physics **110** (2003), 659–669, DOI: [10.1023/A:1022103717585](https://doi.org/10.1023/A:1022103717585).
- [17] A. Aharony, *Phase transitions and critical phenomena*, vol. 6, Academic Press, New York, 1976, p. 357.
- [18] A. Aharony, *Critical Behavior of Anisotropic Cubic Systems*, Phys. Rev. **B8** (1973), 4270–4273, DOI: [10.1103/PhysRevB.8.4270](https://doi.org/10.1103/PhysRevB.8.4270).
- [19] P. Calabrese, A. Pelissetto, and E. Vicari, *Multicritical phenomena in $O(n(1)) + O(n(2))$ symmetric theories*, Phys. Rev. **B67** (2003), 054505, DOI: [10.1103/PhysRevB.67.054505](https://doi.org/10.1103/PhysRevB.67.054505), arXiv:[cond-mat/0209580](https://arxiv.org/abs/cond-mat/0209580) [cond-mat].
- [20] E. Vicari, *Critical phenomena and renormalization-group flow of multi-parameter Φ^4 field theories*, PoS **LAT2007** (2007), 023, arXiv:[0709.1014](https://arxiv.org/abs/0709.1014) [hep-lat].
- [21] R. Folk, Y. Holovatch, and G. Moser, *Field theory of bicritical and tetracritical points. I. Statics*, Phys. Rev. E **78**, 041124 (2008), 041124, DOI: [10.1103/PhysRevE.78.041124](https://doi.org/10.1103/PhysRevE.78.041124), arXiv:[0808.0314](https://arxiv.org/abs/0808.0314) [cond-mat.stat-mech].
- [22] A. Eichhorn, D. Mesterházy, and M. M. Scherer, *Multicritical behavior in models with two competing order parameters*, Phys. Rev. **E88** (2013), 042141, DOI: [10.1103/PhysRevE.88.042141](https://doi.org/10.1103/PhysRevE.88.042141), arXiv:[1306.2952](https://arxiv.org/abs/1306.2952) [cond-mat.stat-mech].
- [23] A. Eichhorn, D. Mesterházy, and M. M. Scherer, *Stability of fixed points and generalized critical behavior in multifield models*, Phys. Rev. **E90** (2014), 052129, DOI: [10.1103/PhysRevE.90.052129](https://doi.org/10.1103/PhysRevE.90.052129), arXiv:[1407.7442](https://arxiv.org/abs/1407.7442) [cond-mat.stat-mech].
- [24] I. Boettcher, *Scaling relations and multicritical phenomena from Functional Renormalization*, Phys. Rev. **E91** (2015), 062112, DOI: [10.1103/PhysRevE.91.062112](https://doi.org/10.1103/PhysRevE.91.062112), arXiv:[1503.07817](https://arxiv.org/abs/1503.07817) [cond-mat.stat-mech].
- [25] A. Eichhorn, T. Helfer, D. Mesterházy, and M. M. Scherer, *Discovering and quantifying nontrivial fixed points in multi-field models*, Eur. Phys. J. **C76** (2016), 88, DOI: [10.1140/epjc/s10052-016-3921-3](https://doi.org/10.1140/epjc/s10052-016-3921-3), arXiv:[1510.04807](https://arxiv.org/abs/1510.04807) [cond-mat.stat-mech].
- [26] H. Rohrer and C. Gerber, *Bicritical and Tetracritical Behavior of $GdAlO_3$* , Phys. Rev. Lett. **38** (1977), 909–912, DOI: [10.1103/PhysRevLett.38.909](https://doi.org/10.1103/PhysRevLett.38.909).
- [27] A. R. King and H. Rohrer, *Spin-flop bicritical point in MnF_2* , Phys. Rev. B **19** (1979), 5864–5876, DOI: [10.1103/PhysRevB.19.5864](https://doi.org/10.1103/PhysRevB.19.5864).
- [28] R. A. Butera, L. M. Corliss, J. M. Hastings, R. Thomas, and D. Mukamel, *Neutron scattering investigation of the spin-flop transition in $MnCl_2 \cdot 4D_2O$* , Phys. Rev. B **24** (1981), 1244–1254, DOI: [10.1103/PhysRevB.24.1244](https://doi.org/10.1103/PhysRevB.24.1244).
- [29] K. Ohgushi and Y. Ueda, *Anomalous Magnetic Properties Near the Spin-Flop Bicritical Point in Mn_2AS_4 ($A = Si$ and Ge)*, Phys. Rev. Lett. **95** (2005), 217202, DOI: [10.1103/PhysRevLett.95.217202](https://doi.org/10.1103/PhysRevLett.95.217202).
- [30] C. C. Becerra, N. F. Oliveira, A. Paduan-Filho, W. Figueiredo, and M. V. P. Souza, *Magnetic phase diagram of $NiCl_2 \cdot 4H_2O$* , Phys. Rev. B **38** (1988), 6887–6893, DOI: [10.1103/PhysRevB.38.6887](https://doi.org/10.1103/PhysRevB.38.6887).

- [31] J. A. J. Basten, E. Frikkie, and W. J. M. de Jonge, *Neutron-scattering study of bicritical behavior in $\text{CsMnBr}_3 \cdot 2\text{D}_2\text{O}$* , Phys. Rev. B **22** (1980), 1429–1450, DOI: [10.1103/PhysRevB.22.1429](https://doi.org/10.1103/PhysRevB.22.1429).
- [32] A. Pelissetto and E. Vicari, *Multicritical behavior of two-dimensional anisotropic antiferromagnets in a magnetic field*, Phys. Rev. B **76**, 024436 (2007), 024436, DOI: [10.1103/PhysRevB.76.024436](https://doi.org/10.1103/PhysRevB.76.024436), eprint: [cond-mat/0702273](https://arxiv.org/abs/cond-mat/0702273).
- [33] M. Holschneider and W. Selke, *Biconical structures in two-dimensional anisotropic Heisenberg antiferromagnets*, Phys. Rev. B **76**, 220405 (2007), 220405, DOI: [10.1103/PhysRevB.76.220405](https://doi.org/10.1103/PhysRevB.76.220405), arXiv:[0710.1251](https://arxiv.org/abs/0710.1251) [[cond-mat.stat-mech](https://arxiv.org/abs/cond-mat.stat-mech)].
- [34] S.-C. Zhang, *A unified theory based on $SO(5)$ symmetry of superconductivity and antiferromagnetism*, Science **275** (1997), 1089, DOI: [10.1126/science.275.5303.1089](https://doi.org/10.1126/science.275.5303.1089).
- [35] S.-C. Zhang, J.-P. Hu, E. Arrigoni, W. Hanke, and A. Auerbach, *Projected $SO(5)$ models*, Phys. Rev. B **60** (1999), 13070–13084, DOI: [10.1103/PhysRevB.60.13070](https://doi.org/10.1103/PhysRevB.60.13070).
- [36] P. Calabrese, A. Pelissetto, and E. Vicari, *Comment on ‘Bicritical and tetracritical phenomena and scaling properties of the $SO(5)$ theory’ PBN Phys.Rev.Lett.87:057004,2001* (2002), arXiv:[cond-mat/0203533](https://arxiv.org/abs/cond-mat/0203533) [[cond-mat](https://arxiv.org/abs/cond-mat)].
- [37] B. Roy, *Multi-critical behavior of $Z_2 \times O(2)$ Gross-Neveu-Yukawa theory in graphene*, Phys. Rev. **B84** (2011), 113404, DOI: [10.1103/PhysRevB.84.113404](https://doi.org/10.1103/PhysRevB.84.113404), arXiv:[1106.1419](https://arxiv.org/abs/1106.1419) [[cond-mat.str-el](https://arxiv.org/abs/cond-mat.str-el)].
- [38] L. Classen, I. F. Herbut, L. Janssen, and M. M. Scherer, *Mott multicriticality of Dirac electrons in graphene*, Phys. Rev. **B92** (2015), 035429, DOI: [10.1103/PhysRevB.92.035429](https://doi.org/10.1103/PhysRevB.92.035429), arXiv:[1503.05002](https://arxiv.org/abs/1503.05002) [[cond-mat.str-el](https://arxiv.org/abs/cond-mat.str-el)].
- [39] J. M. Kosterlitz, D. R. Nelson, and M. E. Fisher, *Bicritical and tetracritical points in anisotropic antiferromagnetic systems*, Phys. Rev. **B13** (1976), 412–432, DOI: [10.1103/PhysRevB.13.412](https://doi.org/10.1103/PhysRevB.13.412).
- [40] D. R. Nelson, J. M. Kosterlitz, and M. E. Fisher, *Renormalization-Group Analysis of Bicritical and Tetracritical Points*, Phys. Rev. Lett. **33** (1974), 813–817, DOI: [10.1103/PhysRevLett.33.813](https://doi.org/10.1103/PhysRevLett.33.813).
- [41] W. Selke, *Evidence for a bicritical point in the XXZ Heisenberg antiferromagnet on a simple cubic lattice*, Phys. Rev. E **83** (2011), 042102, DOI: [10.1103/PhysRevE.83.042102](https://doi.org/10.1103/PhysRevE.83.042102).
- [42] V. V. Prudnikov, P. V. Prudnikov, and A. A. Fedorenko, *Field-theoretic description of the multicritical behavior of systems with two order parameters*, Journal of Experimental and Theoretical Physics Letters **68** (1998), 950–956, DOI: [10.1134/1.567959](https://doi.org/10.1134/1.567959).
- [43] P. Calabrese, A. Pelissetto, P. Rossi, and E. Vicari, *Field theory results for three-dimensional transitions with complex symmetries*, Int. J. Mod. Phys. **B17** (2003), 5829–5838, DOI: [10.1142/S0217979203023355](https://doi.org/10.1142/S0217979203023355), arXiv:[hep-th/0212161](https://arxiv.org/abs/hep-th/0212161) [[hep-th](https://arxiv.org/abs/hep-th)].
- [44] J. M. Pawłowski, M. M. Scherer, R. Schmidt, and S. J. Wetzel, *Physics and the choice of regulators in functional renormalisation group flows* (2015), arXiv:[1512.03598](https://arxiv.org/abs/1512.03598) [[hep-th](https://arxiv.org/abs/hep-th)].
- [45] F. Englert and R. Brout, *Broken Symmetry and the Mass of Gauge Vector Mesons*, Phys. Rev. Lett. **13** (1964), 321–323, DOI: [10.1103/PhysRevLett.13.321](https://doi.org/10.1103/PhysRevLett.13.321).

- [46] P. W. Higgs, *Spontaneous Symmetry Breakdown without Massless Bosons*, Phys. Rev. **145** (1966), 1156–1163, DOI: [10.1103/PhysRev.145.1156](https://doi.org/10.1103/PhysRev.145.1156).
- [47] G. S. Guralnik, C. R. Hagen, and T. W. B. Kibble, *Global Conservation Laws and Massless Particles*, Phys. Rev. Lett. **13** (1964), 585–587, DOI: [10.1103/PhysRevLett.13.585](https://doi.org/10.1103/PhysRevLett.13.585).
- [48] S. Weinberg, *A Model of Leptons*, Phys. Rev. Lett. **19** (1967), 1264–1266, DOI: [10.1103/PhysRevLett.19.1264](https://doi.org/10.1103/PhysRevLett.19.1264).
- [49] A. Salam, *Weak and Electromagnetic Interactions*, Conf. Proc. **C680519** (1968), 367–377.
- [50] S. L. Glashow, J. Iliopoulos, and L. Maiani, *Weak Interactions with Lepton-Hadron Symmetry*, Phys. Rev. **D2** (1970), 1285–1292, DOI: [10.1103/PhysRevD.2.1285](https://doi.org/10.1103/PhysRevD.2.1285).
- [51] G. Aad et al., *Observation of a new particle in the search for the Standard Model Higgs boson with the ATLAS detector at the LHC*, Phys. Lett. **B716** (2012), 1–29, DOI: [10.1016/j.physletb.2012.08.020](https://doi.org/10.1016/j.physletb.2012.08.020), arXiv:[1207.7214](https://arxiv.org/abs/1207.7214) [hep-ex].
- [52] S. Chatrchyan et al., *Observation of a new boson at a mass of 125 GeV with the CMS experiment at the LHC*, Phys. Lett. **B716** (2012), 30–61, DOI: [10.1016/j.physletb.2012.08.021](https://doi.org/10.1016/j.physletb.2012.08.021), arXiv:[1207.7235](https://arxiv.org/abs/1207.7235) [hep-ex].
- [53] H. Gies, C. Gneiting, and R. Sondenheimer, *Higgs Mass Bounds from Renormalization Flow for a simple Yukawa model*, Phys.Rev. **D89** (2014), 045012, DOI: [10.1103/PhysRevD.89.045012](https://doi.org/10.1103/PhysRevD.89.045012), arXiv:[1308.5075](https://arxiv.org/abs/1308.5075) [hep-ph].
- [54] P. Hegde, K. Jansen, C. J. D. Lin, and A. Nagy, *Stabilizing the electroweak vacuum by higher dimensional operators in a Higgs-Yukawa model*, PoS **LATTICE2013** (2014), 058, arXiv:[1310.6260](https://arxiv.org/abs/1310.6260) [hep-lat].
- [55] D. Y. J. Chu, K. Jansen, B. Knippschild, C. J. D. Lin, and A. Nagy, *A lattice study of a chirally invariant Higgs–Yukawa model including a higher dimensional Φ^6 -term*, Phys. Lett. **B744** (2015), 146–152, DOI: [10.1016/j.physletb.2015.03.050](https://doi.org/10.1016/j.physletb.2015.03.050), arXiv:[1501.05440](https://arxiv.org/abs/1501.05440) [hep-lat].
- [56] D. Y. J. Chu, K. Jansen, B. Knippschild, C. J. D. Lin, K.-I. Nagai, et al., *Phase structure and Higgs boson mass in a Higgs-Yukawa model with a dimension-6 operator*, PoS **LATTICE2014** (2014), 278, arXiv:[1501.00306](https://arxiv.org/abs/1501.00306) [hep-lat].
- [57] O. Akerlund and P. de Forcrand, *The Higgs-Yukawa model with higher dimension operators via EMFT* (2015), arXiv:[1508.07959](https://arxiv.org/abs/1508.07959) [hep-lat].
- [58] H. Gies and R. Sondenheimer, *Higgs Mass Bounds from Renormalization Flow for a Higgs-top-bottom model*, Eur.Phys.J. **C75** (2015), 68, DOI: [10.1140/epjc/s10052-015-3284-1](https://doi.org/10.1140/epjc/s10052-015-3284-1), arXiv:[1407.8124](https://arxiv.org/abs/1407.8124) [hep-ph].
- [59] A. Eichhorn, H. Gies, J. Jaeckel, T. Plehn, M. M. Scherer, et al., *The Higgs Mass and the Scale of New Physics*, JHEP **04** (2015), 022, DOI: [10.1007/JHEP04\(2015\)022](https://doi.org/10.1007/JHEP04(2015)022), arXiv:[1501.02812](https://arxiv.org/abs/1501.02812) [hep-ph].
- [60] N. Tetradis and C. Wetterich, *Critical exponents from effective average action*, Nucl.Phys. **B422** (1994), 541–592, DOI: [10.1016/0550-3213\(94\)90446-4](https://doi.org/10.1016/0550-3213(94)90446-4), arXiv:[hep-ph/9308214](https://arxiv.org/abs/hep-ph/9308214) [hep-ph].
- [61] J. Berges, N. Tetradis, and C. Wetterich, *Nonperturbative renormalization flow in quantum field theory and statistical physics*, Phys.Rept. **363** (2002), 223–386, DOI: [10.1016/S0370-1573\(01\)00098-9](https://doi.org/10.1016/S0370-1573(01)00098-9), arXiv:[hep-ph/0005122](https://arxiv.org/abs/hep-ph/0005122) [hep-ph].

-
- [62] B. Delamotte, *An Introduction to the nonperturbative renormalization group*, Lect.Notes Phys. **852** (2012), 49–132, DOI: [10.1007/978-3-642-27320-9_2](https://doi.org/10.1007/978-3-642-27320-9_2), arXiv:[cond-mat/0702365](https://arxiv.org/abs/cond-mat/0702365) [COND-MAT].
- [63] T. R. Morris and M. D. Turner, *Derivative expansion of the renormalization group in $O(N)$ scalar field theory*, Nucl.Phys. **B509** (1998), 637–661, DOI: [10.1016/S0550-3213\(97\)00640-8](https://doi.org/10.1016/S0550-3213(97)00640-8), arXiv:[hep-th/9704202](https://arxiv.org/abs/hep-th/9704202) [hep-th].
- [64] C. Bervillier, A. Juttner, and D. F. Litim, *High-accuracy scaling exponents in the local potential approximation*, Nucl.Phys. **B783** (2007), 213–226, DOI: [10.1016/j.nuclphysb.2007.03.036](https://doi.org/10.1016/j.nuclphysb.2007.03.036), arXiv:[hep-th/0701172](https://arxiv.org/abs/hep-th/0701172) [hep-th].
- [65] D. F. Litim and D. Zappala, *Ising exponents from the functional renormalisation group*, Phys. Rev. **D83** (2011), 085009, DOI: [10.1103/PhysRevD.83.085009](https://doi.org/10.1103/PhysRevD.83.085009), arXiv:[1009.1948](https://arxiv.org/abs/1009.1948) [hep-th].
- [66] F. Benitez, J.-P. Blaizot, H. Chate, B. Delamotte, R. Mendez-Galain, et al., *Non-perturbative renormalization group preserving full-momentum dependence: implementation and quantitative evaluation*, Phys.Rev. **E85** (2012), 026707, DOI: [10.1103/PhysRevE.85.026707](https://doi.org/10.1103/PhysRevE.85.026707), arXiv:[1110.2665](https://arxiv.org/abs/1110.2665) [cond-mat.stat-mech].
- [67] A. Codello and G. D’Odorico, *$O(N)$ -Universality Classes and the Mermin-Wagner Theorem*, Phys.Rev.Lett. **110** (2013), 141601, DOI: [10.1103/PhysRevLett.110.141601](https://doi.org/10.1103/PhysRevLett.110.141601), arXiv:[1210.4037](https://arxiv.org/abs/1210.4037) [hep-th].
- [68] R. Percacci and G. P. Vacca, *Are there scaling solutions in the $O(N)$ -models for large N in $d > 4$?* Phys.Rev. **D90** (2014), 107702, DOI: [10.1103/PhysRevD.90.107702](https://doi.org/10.1103/PhysRevD.90.107702), arXiv:[1405.6622](https://arxiv.org/abs/1405.6622) [hep-th].
- [69] A. Codello, N. Defenu, and G. D’Odorico, *Critical exponents of $O(N)$ models in fractional dimensions*, Phys. Rev. **D91** (2015), 105003, DOI: [10.1103/PhysRevD.91.105003](https://doi.org/10.1103/PhysRevD.91.105003), arXiv:[1410.3308](https://arxiv.org/abs/1410.3308) [hep-th].
- [70] W. Metzner, M. Salmhofer, C. Honerkamp, V. Meden, and K. Schonhammer, *Functional renormalization group approach to correlated fermion systems*, Rev. Mod. Phys. **84** (2012), 299, DOI: [10.1103/RevModPhys.84.299](https://doi.org/10.1103/RevModPhys.84.299), arXiv:[1105.5289](https://arxiv.org/abs/1105.5289) [cond-mat.str-el].
- [71] M. M. Scherer, S. Floerchinger, and H. Gies, *Functional renormalization for the BCS-BEC crossover*, Phil.Trans.Roy.Soc.Lond. **A369** (2011), 2779, arXiv:[1010.2890](https://arxiv.org/abs/1010.2890) [cond-mat.quant-gas].
- [72] H. Gies and L. Janssen, *UV fixed-point structure of the three-dimensional Thirring model*, Phys.Rev. **D82** (2010), 085018, DOI: [10.1103/PhysRevD.82.085018](https://doi.org/10.1103/PhysRevD.82.085018), arXiv:[1006.3747](https://arxiv.org/abs/1006.3747) [hep-th].
- [73] J. Braun, H. Gies, and D. D. Scherer, *Asymptotic safety: a simple example*, Phys.Rev. **D83** (2011), 085012, DOI: [10.1103/PhysRevD.83.085012](https://doi.org/10.1103/PhysRevD.83.085012), arXiv:[1011.1456](https://arxiv.org/abs/1011.1456) [hep-th].
- [74] J. Braun, *Fermion Interactions and Universal Behavior in Strongly Interacting Theories*, J.Phys. **G39** (2012), 033001, DOI: [10.1088/0954-3899/39/3/033001](https://doi.org/10.1088/0954-3899/39/3/033001), arXiv:[1108.4449](https://arxiv.org/abs/1108.4449) [hep-ph].
- [75] I. Boettcher, J. M. Pawłowski, and C. Wetterich, *Critical temperature and superfluid gap of the Unitary Fermi Gas from Functional Renormalization*, Phys.Rev. **A89** (2014), 053630, DOI: [10.1103/PhysRevA.89.053630](https://doi.org/10.1103/PhysRevA.89.053630), arXiv:[1312.0505](https://arxiv.org/abs/1312.0505) [cond-mat.quant-gas].

- [76] P. Kopietz, L. Bartosch, and F. Schutz, *Introduction to the functional renormalization group*, Lect.Notes Phys. **798** (2010), 1–380, DOI: [10.1007/978-3-642-05094-7](https://doi.org/10.1007/978-3-642-05094-7).
- [77] L. Janssen and H. Gies, *Critical behavior of the (2+1)-dimensional Thirring model*, Phys.Rev. **D86** (2012), 105007, DOI: [10.1103/PhysRevD.86.105007](https://doi.org/10.1103/PhysRevD.86.105007), arXiv:[1208.3327](https://arxiv.org/abs/1208.3327) [[hep-th](#)].
- [78] H. Gies, L. Janssen, S. Rechenberger, and M. M. Scherer, *Phase transition and critical behavior of $d=3$ chiral fermion models with left/right asymmetry*, Phys.Rev. **D81** (2010), 025009, DOI: [10.1103/PhysRevD.81.025009](https://doi.org/10.1103/PhysRevD.81.025009), arXiv:[0910.0764](https://arxiv.org/abs/0910.0764) [[hep-th](#)].
- [79] D. D. Scherer, J. Braun, and H. Gies, *Many-flavor Phase Diagram of the (2+1)d Gross-Neveu Model at Finite Temperature*, J.Phys. **A46** (2013), 285002, DOI: [10.1088/1751-8113/46/28/285002](https://doi.org/10.1088/1751-8113/46/28/285002), arXiv:[1212.4624](https://arxiv.org/abs/1212.4624) [[hep-ph](#)].
- [80] D. F. Litim, *Critical exponents from optimized renormalization group flows*, Nucl.Phys. **B631** (2002), 128–158, DOI: [10.1016/S0550-3213\(02\)00186-4](https://doi.org/10.1016/S0550-3213(02)00186-4), arXiv:[hep-th/0203006](https://arxiv.org/abs/hep-th/0203006) [[hep-th](#)].
- [81] F. Benitez, J.-P. Blaizot, H. Chate, B. Delamotte, R. Mendez-Galain, et al., *Solutions of renormalization group flow equations with full momentum dependence*, Phys.Rev. **E80** (2009), 030103, DOI: [10.1103/PhysRevE.80.030103](https://doi.org/10.1103/PhysRevE.80.030103), arXiv:[0901.0128](https://arxiv.org/abs/0901.0128) [[cond-mat.stat-mech](#)].
- [82] P. Jakubczyk, N. Dupuis, and B. Delamotte, *Reexamination of the nonperturbative renormalization-group approach to the Kosterlitz-Thouless transition*, Phys. Rev. **E90** (2014), 062105, DOI: [10.1103/PhysRevE.90.062105](https://doi.org/10.1103/PhysRevE.90.062105), arXiv:[1409.1374](https://arxiv.org/abs/1409.1374) [[cond-mat.stat-mech](#)].
- [83] M. Reuter and C. Wetterich, *Effective average action for gauge theories and exact evolution equations*, Nucl.Phys. **B417** (1994), 181–214, DOI: [10.1016/0550-3213\(94\)90543-6](https://doi.org/10.1016/0550-3213(94)90543-6).
- [84] H. Gies, *Introduction to the functional RG and applications to gauge theories*, Lect.Notes Phys. **852** (2012), 287–348, DOI: [10.1007/978-3-642-27320-9_6](https://doi.org/10.1007/978-3-642-27320-9_6), arXiv:[hep-ph/0611146](https://arxiv.org/abs/hep-ph/0611146) [[hep-ph](#)].
- [85] J. M. Pawłowski, *Aspects of the functional renormalisation group*, Annals Phys. **322** (2007), 2831–2915, DOI: [10.1016/j.aop.2007.01.007](https://doi.org/10.1016/j.aop.2007.01.007), arXiv:[hep-th/0512261](https://arxiv.org/abs/hep-th/0512261) [[hep-th](#)].
- [86] D. F. Litim and J. M. Pawłowski, *Flow equations for Yang-Mills theories in general axial gauges*, Phys.Lett. **B435** (1998), 181–188, DOI: [10.1016/S0370-2693\(98\)00761-8](https://doi.org/10.1016/S0370-2693(98)00761-8), arXiv:[hep-th/9802064](https://arxiv.org/abs/hep-th/9802064) [[hep-th](#)].
- [87] J. Braun, B. Klein, and B.-J. Schaefer, *On the Phase Structure of QCD in a Finite Volume*, Phys.Lett. **B713** (2012), 216–223, DOI: [10.1016/j.physletb.2012.05.053](https://doi.org/10.1016/j.physletb.2012.05.053), arXiv:[1110.0849](https://arxiv.org/abs/1110.0849) [[hep-ph](#)].
- [88] R.-A. Tripolt, J. Braun, B. Klein, and B.-J. Schaefer, *Effect of fluctuations on the QCD critical point in a finite volume*, Phys.Rev. **D90** (2014), 054012, DOI: [10.1103/PhysRevD.90.054012](https://doi.org/10.1103/PhysRevD.90.054012), arXiv:[1308.0164](https://arxiv.org/abs/1308.0164) [[hep-ph](#)].
- [89] J. Braun, *The QCD Phase Boundary from Quark-Gluon Dynamics*, Eur. Phys. J. **C64** (2009), 459–482, DOI: [10.1140/epjc/s10052-009-1136-6](https://doi.org/10.1140/epjc/s10052-009-1136-6), arXiv:[0810.1727](https://arxiv.org/abs/0810.1727) [[hep-ph](#)].

-
- [90] M. Mitter, J. M. Pawłowski, and N. Strodthoff, *Chiral symmetry breaking in continuum QCD* (2014), arXiv:[1411.7978 \[hep-ph\]](#).
- [91] M. Reuter, *Nonperturbative evolution equation for quantum gravity*, Phys. Rev. **D57** (1998), 971–985, DOI: [10.1103/PhysRevD.57.971](#), arXiv:[hep-th/9605030 \[hep-th\]](#).
- [92] M. Niedermaier and M. Reuter, *The Asymptotic Safety Scenario in Quantum Gravity*, Living Rev. Rel. **9** (2006), 5–173, DOI: [10.12942/lrr-2006-5](#).
- [93] R. Percacci, *Asymptotic Safety* (2007), arXiv:[0709.3851 \[hep-th\]](#).
- [94] E. Manrique and M. Reuter, *Bimetric Truncations for Quantum Einstein Gravity and Asymptotic Safety*, Annals Phys. **325** (2010), 785–815, DOI: [10.1016/j.aop.2009.11.009](#), arXiv:[0907.2617 \[gr-qc\]](#).
- [95] D. Benedetti, K. Groh, P. F. Machado, and F. Saueressig, *The Universal RG Machine*, JHEP **1106** (2011), 079, DOI: [10.1007/JHEP06\(2011\)079](#), arXiv:[1012.3081 \[hep-th\]](#).
- [96] D. Benedetti and F. Caravelli, *The Local potential approximation in quantum gravity*, JHEP **1206** (2012), 017, DOI: [10.1007/JHEP06\(2012\)017](#), [10.1007/JHEP10\(2012\)157](#), arXiv:[1204.3541 \[hep-th\]](#).
- [97] A. Eichhorn, *The Renormalization Group flow of unimodular $f(R)$ gravity* (2015), arXiv:[1501.05848 \[gr-qc\]](#).
- [98] M. Demmel, F. Saueressig, and O. Zanusso, *RG flows of Quantum Einstein Gravity in the linear-geometric approximation* (2014), arXiv:[1412.7207 \[hep-th\]](#).
- [99] N. Christiansen, D. F. Litim, J. M. Pawłowski, and A. Rodigast, *Fixed points and infrared completion of quantum gravity*, Phys.Lett. **B728** (2014), 114–117, DOI: [10.1016/j.physletb.2013.11.025](#), arXiv:[1209.4038 \[hep-th\]](#).
- [100] K. Falls, D. Litim, K. Nikolakopoulos, and C. Rahmede, *A bootstrap towards asymptotic safety* (2013), arXiv:[1301.4191 \[hep-th\]](#).
- [101] N. Christiansen, B. Knorr, J. M. Pawłowski, and A. Rodigast, *Global Flows in Quantum Gravity* (2014), arXiv:[1403.1232 \[hep-th\]](#).
- [102] S. Folkerts, D. F. Litim, and J. M. Pawłowski, *Asymptotic freedom of Yang-Mills theory with gravity*, Phys.Lett. **B709** (2012), 234–241, DOI: [10.1016/j.physletb.2012.02.002](#), arXiv:[1101.5552 \[hep-th\]](#).
- [103] A. Eichhorn and H. Gies, *Light fermions in quantum gravity*, New J.Phys. **13** (2011), 125012, DOI: [10.1088/1367-2630/13/12/125012](#), arXiv:[1104.5366 \[hep-th\]](#).
- [104] U. Harst and M. Reuter, *QED coupled to QEG*, JHEP **1105** (2011), 119, DOI: [10.1007/JHEP05\(2011\)119](#), arXiv:[1101.6007 \[hep-th\]](#).
- [105] P. Donà, A. Eichhorn, and R. Percacci, *Matter matters in asymptotically safe quantum gravity*, Phys. Rev. **D89** (2014), 084035, DOI: [10.1103/PhysRevD.89.084035](#), arXiv:[1311.2898 \[hep-th\]](#).
- [106] S. Weinberg, *Critical Phenomena for Field Theorists*, in: Erice Subnucl.Phys.1976:1, 1976, p. 1.
- [107] S. Weinberg, *Ultraviolet Divergences in Quantum Theories of Gravitation*, in: General Relativity: An Einstein Centenary Survey, 1980, pp. 790–831.
- [108] J. P. Boyd, *Chebyshev and Fourier Spectral Methods*, 2nd ed., Dover Publications, Inc., New York, 2000.

- [109] R. Robson and A. Prytz, *The discrete ordinate/pseudo-spectral method: review and application from a physicist's perspective*, Australian Journal of Physics **46** (1993), 465.
- [110] M. Ansorg, A. Kleinwachter, and R. Meinel, *Highly accurate calculation of rotating neutron stars: detailed description of the numerical methods*, Astron.Astrophys. **405** (2003), 711, DOI: [10.1051/0004-6361:20030618](https://doi.org/10.1051/0004-6361:20030618), arXiv:[astro-ph/0301173](https://arxiv.org/abs/astro-ph/0301173) [[astro-ph](#)].
- [111] R. P. Macedo and M. Ansorg, *Axisymmetric fully spectral code for hyperbolic equations*, J.Comput.Phys. **276** (2014), 357–379, DOI: [10.1016/j.jcp.2014.07.040](https://doi.org/10.1016/j.jcp.2014.07.040), arXiv:[1402.7343](https://arxiv.org/abs/1402.7343) [[physics.comp-ph](#)].
- [112] M. Kalisch and M. Ansorg, *Pseudo-spectral construction of non-uniform black string solutions in five and six spacetime dimensions* (2016), arXiv:[1607.03099](https://arxiv.org/abs/1607.03099) [[gr-qc](#)].
- [113] C. Canuto, M. Y. Hussaini, A. Quateroni, and T. A. Zang Jr., *Spectral Methods in Fluid Dynamics*, Springer Series in Computational Physics, 1988.
- [114] D. Haidvogel, M. Iskandarani, and J. Boyd, *A staggered spectral element model for the shallow water equations*, International Journal for Numerical Methods in Fluids (1995).
- [115] D. B. Haidvogel and T. Zang, *The accurate solution of poisson's equation by expansion in chebyshev polynomials*, Journal of Computational Physics **30** (1979), 167–180, DOI: [http://dx.doi.org/10.1016/0021-9991\(79\)90097-4](http://dx.doi.org/10.1016/0021-9991(79)90097-4).
- [116] D. F. Litim and L. Vergara, *Subleading critical exponents from the renormalization group*, Phys.Lett. **B581** (2004), 263–269, DOI: [10.1016/j.physletb.2003.11.047](https://doi.org/10.1016/j.physletb.2003.11.047), arXiv:[hep-th/0310101](https://arxiv.org/abs/hep-th/0310101) [[hep-th](#)].
- [117] C. S. Fischer and H. Gies, *Renormalization flow of Yang-Mills propagators*, JHEP **0410** (2004), 048, DOI: [10.1088/1126-6708/2004/10/048](https://doi.org/10.1088/1126-6708/2004/10/048), arXiv:[hep-ph/0408089](https://arxiv.org/abs/hep-ph/0408089) [[hep-ph](#)].
- [118] C. Gneiting, “Higgs mass bounds from renormalization flow,” diploma thesis, Heidelberg, 2005.
- [119] D. Zappala, *Enhancement of field renormalization in scalar theories via functional renormalization group*, Phys. Rev. **D86** (2012), 125003, DOI: [10.1103/PhysRevD.86.125003](https://doi.org/10.1103/PhysRevD.86.125003), arXiv:[1206.2480](https://arxiv.org/abs/1206.2480) [[hep-th](#)].
- [120] S. Grozdanov, D. Kraljić, and E. E. Svanes, *Inflationary potentials from the exact renormalisation group*, Nuclear Physics B **909** (2016), 657–676, DOI: [10.1016/j.nuclphysb.2016.06.001](https://doi.org/10.1016/j.nuclphysb.2016.06.001), arXiv:[1508.01484](https://arxiv.org/abs/1508.01484) [[hep-th](#)].
- [121] M. Heilmann, T. Hellwig, B. Knorr, M. Ansorg, and A. Wipf, *Convergence of Derivative Expansion in Supersymmetric Functional RG Flows*, JHEP **02** (2015), 109, DOI: [10.1007/JHEP02\(2015\)109](https://doi.org/10.1007/JHEP02(2015)109), arXiv:[1409.5650](https://arxiv.org/abs/1409.5650) [[hep-th](#)].
- [122] J. Berges, N. Tetradis, and C. Wetterich, *Nonperturbative renormalization flow in quantum field theory and statistical physics*, Phys. Rep. **363** (2002), 223, DOI: [10.1016/S0370-1573\(01\)00098-9](https://doi.org/10.1016/S0370-1573(01)00098-9), arXiv:[hep-ph/0005122](https://arxiv.org/abs/hep-ph/0005122) [[hep-ph](#)].
- [123] J. A. Adams, J. Berges, S. Bornholdt, F. Freire, N. Tetradis, et al., *Solving nonperturbative flow equations*, Mod. Phys. Lett. **A10** (1995), 2367–2380, DOI: [10.1142/S0217732395002520](https://doi.org/10.1142/S0217732395002520), arXiv:[hep-th/9507093](https://arxiv.org/abs/hep-th/9507093) [[hep-th](#)].

- [124] G. Papp, B. J. Schaefer, H. J. Pirner, and J. Wambach, *On the convergence of the expansion of renormalization group flow equation*, Phys. Rev. **D61** (2000), 096002, DOI: [10.1103/PhysRevD.61.096002](https://doi.org/10.1103/PhysRevD.61.096002), arXiv:[hep-ph/9909246](https://arxiv.org/abs/hep-ph/9909246) [hep-ph].
- [125] O. Bohr, B. J. Schaefer, and J. Wambach, *Renormalization group flow equations and the phase transition in $O(N)$ models*, Int. J. Mod. Phys. **A16** (2001), 3823–3852, DOI: [10.1142/S0217751X0100502X](https://doi.org/10.1142/S0217751X0100502X), arXiv:[hep-ph/0007098](https://arxiv.org/abs/hep-ph/0007098) [hep-ph].
- [126] B.-J. Schaefer and J. Wambach, *The Phase diagram of the quark meson model*, Nucl. Phys. **A757** (2005), 479–492, DOI: [10.1016/j.nuclphysa.2005.04.012](https://doi.org/10.1016/j.nuclphysa.2005.04.012), arXiv:[nucl-th/0403039](https://arxiv.org/abs/nucl-th/0403039) [nucl-th].
- [127] A. Bonanno and G. Lacagnina, *Spontaneous symmetry breaking and proper time flow equations*, Nucl. Phys. **B693** (2004), 36–50, DOI: [10.1016/j.nuclphysb.2004.06.003](https://doi.org/10.1016/j.nuclphysb.2004.06.003), arXiv:[hep-th/0403176](https://arxiv.org/abs/hep-th/0403176) [hep-th].
- [128] J.-M. Caillol, *The non-perturbative renormalization group in the ordered phase*, Nucl. Phys. **B855** (2012), 854–884, DOI: [10.1016/j.nuclphysb.2011.10.026](https://doi.org/10.1016/j.nuclphysb.2011.10.026).
- [129] D. Roscher, J. Braun, and J. E. Drut, *Phase structure of mass- and spin-imbanced unitary Fermi gases*, Phys. Rev. **A91** (2015), 053611, DOI: [10.1103/PhysRevA.91.053611](https://doi.org/10.1103/PhysRevA.91.053611), arXiv:[1501.05544](https://arxiv.org/abs/1501.05544) [cond-mat.quant-gas].
- [130] I. Boettcher, J. Braun, T. K. Herbst, J. M. Pawłowski, D. Roscher, et al., *Phase structure of spin-imbanced unitary Fermi gases*, Phys. Rev. **A91** (2015), 013610, DOI: [10.1103/PhysRevA.91.013610](https://doi.org/10.1103/PhysRevA.91.013610), arXiv:[1409.5070](https://arxiv.org/abs/1409.5070) [cond-mat.quant-gas].
- [131] T. Fischbacher and F. Synatschke-Czerwonka, *FlowPy: A Numerical solver for functional renormalization group equations*, Comput. Phys. Commun. **184** (2013), 1931–1945, DOI: [10.1016/j.cpc.2013.03.002](https://doi.org/10.1016/j.cpc.2013.03.002), arXiv:[1202.5984](https://arxiv.org/abs/1202.5984) [physics.comp-ph].
- [132] F. Synatschke-Czerwonka, T. Fischbacher, and G. Bergner, *The two dimensional $N = (2,2)$ Wess-Zumino Model in the Functional Renormalization Group Approach*, Phys. Rev. **D82** (2010), 085003, DOI: [10.1103/PhysRevD.82.085003](https://doi.org/10.1103/PhysRevD.82.085003), arXiv:[1006.1823](https://arxiv.org/abs/1006.1823) [hep-th].
- [133] M. Mitter and B.-J. Schaefer, *Fluctuations and the axial anomaly with three quark flavors*, Phys. Rev. **D89** (2014), 054027, DOI: [10.1103/PhysRevD.89.054027](https://doi.org/10.1103/PhysRevD.89.054027), arXiv:[1308.3176](https://arxiv.org/abs/1308.3176) [hep-ph].
- [134] N. Strodthoff, B.-J. Schaefer, and L. von Smekal, *Quark-meson-diquark model for two-color QCD*, Phys. Rev. **D85** (2012), 074007, DOI: [10.1103/PhysRevD.85.074007](https://doi.org/10.1103/PhysRevD.85.074007), arXiv:[1112.5401](https://arxiv.org/abs/1112.5401) [hep-ph].
- [135] T. K. Herbst, M. Mitter, J. M. Pawłowski, B.-J. Schaefer, and R. Stiele, *Thermodynamics of QCD at vanishing density*, Phys. Lett. **B731** (2014), 248–256, DOI: [10.1016/j.physletb.2014.02.045](https://doi.org/10.1016/j.physletb.2014.02.045), arXiv:[1308.3621](https://arxiv.org/abs/1308.3621) [hep-ph].
- [136] M. Peláez and N. Wschebor, *The ordered phase of $O(N)$ model within the Non-Perturbative Renormalization Group* (2015), arXiv:[1510.05709](https://arxiv.org/abs/1510.05709) [cond-mat.stat-mech].
- [137] J. Borchardt and B. Knorr, *Global solutions of functional fixed point equations via pseudospectral methods*, Phys. Rev. **D91** (2015), 105011, DOI: [10.1103/PhysRevD.91.105011](https://doi.org/10.1103/PhysRevD.91.105011), arXiv:[1502.07511](https://arxiv.org/abs/1502.07511) [hep-th].

- [138] J. Borchardt and B. Knorr, *Erratum: Global solutions of functional fixed point equations via pseudospectral methods [Phys. Rev. D **91**, 105011 (2015)]*, Phys. Rev. D **93** (2016), 089904, DOI: [10.1103/PhysRevD.93.089904](https://doi.org/10.1103/PhysRevD.93.089904).
- [139] J. Borchardt and A. Eichhorn, *Universal behavior of coupled order parameters below three dimensions*, Phys. Rev. **E94** (2016), 042105, DOI: [10.1103/PhysRevE.94.042105](https://doi.org/10.1103/PhysRevE.94.042105), arXiv:[1606.07449](https://arxiv.org/abs/1606.07449) [[cond-mat.stat-mech](#)].
- [140] J. Borchardt and B. Knorr, *Solving functional flow equations with pseudospectral methods*, Phys. Rev. D **94** (2016), 025027, DOI: [10.1103/PhysRevD.94.025027](https://doi.org/10.1103/PhysRevD.94.025027).
- [141] J. Borchardt, H. Gies, and R. Sondenheimer, *Global flow of the Higgs potential in a Yukawa model*, Eur. Phys. J. **C76** (2016), 472, DOI: [10.1140/epjc/s10052-016-4300-9](https://doi.org/10.1140/epjc/s10052-016-4300-9), arXiv:[1603.05861](https://arxiv.org/abs/1603.05861) [[hep-ph](#)].
- [142] E. S. Swanson, *A Primer on Functional Methods and the Schwinger-Dyson Equations*, AIP Conf. Proc. **1296** (2010), 75–121, DOI: [10.1063/1.3523221](https://doi.org/10.1063/1.3523221), arXiv:[1008.4337](https://arxiv.org/abs/1008.4337) [[hep-ph](#)].
- [143] C. Wetterich, *Exact evolution equation for the effective potential*, Phys. Lett. **B301** (1993), 90–94, DOI: [10.1016/0370-2693\(93\)90726-X](https://doi.org/10.1016/0370-2693(93)90726-X).
- [144] D. F. Litim, *Optimization of the exact renormalization group*, Phys. Lett. **B486** (2000), 92–99, DOI: [10.1016/S0370-2693\(00\)00748-6](https://doi.org/10.1016/S0370-2693(00)00748-6), arXiv:[hep-th/0005245](https://arxiv.org/abs/hep-th/0005245) [[hep-th](#)].
- [145] D. F. Litim, *Optimized renormalization group flows*, Phys. Rev. **D64** (2001), 105007, DOI: [10.1103/PhysRevD.64.105007](https://doi.org/10.1103/PhysRevD.64.105007), arXiv:[hep-th/0103195](https://arxiv.org/abs/hep-th/0103195) [[hep-th](#)].
- [146] D. F. Litim, *Mind the gap*, Int. J. Mod. Phys. **A16** (2001), 2081–2088, DOI: [10.1142/S0217751X01004748](https://doi.org/10.1142/S0217751X01004748), arXiv:[hep-th/0104221](https://arxiv.org/abs/hep-th/0104221) [[hep-th](#)].
- [147] Y. Nambu, *Quasiparticles and Gauge Invariance in the Theory of Superconductivity*, Phys. Rev. **117** (1960), 648–663, DOI: [10.1103/PhysRev.117.648](https://doi.org/10.1103/PhysRev.117.648).
- [148] J. Goldstone, *Field Theories with Superconductor Solutions*, Nuovo Cim. **19** (1961), 154–164, DOI: [10.1007/BF02812722](https://doi.org/10.1007/BF02812722).
- [149] J. Goldstone, A. Salam, and S. Weinberg, *Broken Symmetries*, Phys. Rev. **127** (1962), 965–970, DOI: [10.1103/PhysRev.127.965](https://doi.org/10.1103/PhysRev.127.965).
- [150] Brézin, J. C. Le Guillou, and J. Zinn-Justin, *Phase Transitions and Critical Phenomena*, ed. by c. Domb and M. Green, vol. 6, Academic Press, 1976, p. 125.
- [151] J. Berges, N. Tetradis, and C. Wetterich, *Critical equation of state from the average action*, Phys. Rev. Lett. **77** (1996), 873–876, DOI: [10.1103/PhysRevLett.77.873](https://doi.org/10.1103/PhysRevLett.77.873), arXiv:[hep-th/9507159](https://arxiv.org/abs/hep-th/9507159) [[hep-th](#)].
- [152] B. Widom, *Equation of State in the Neighborhood of the Critical Point*, The Journal of Chemical Physics **43** (1965), 3898–3905, DOI: <http://dx.doi.org/10.1063/1.1696618>.
- [153] M. E. Fisher and R. J. Burford, *Theory of Critical-Point Scattering and Correlations. I. The Ising Model*, Phys. Rev. **156** (1967), 583–622, DOI: [10.1103/PhysRev.156.583](https://doi.org/10.1103/PhysRev.156.583).
- [154] D. S. Ritchie and M. E. Fisher, *Theory of Critical-Point Scattering and Correlations. II. Heisenberg Models*, Phys. Rev. B **5** (1972), 2668–2692, DOI: [10.1103/PhysRevB.5.2668](https://doi.org/10.1103/PhysRevB.5.2668).

- [155] H. B. Tarko and M. E. Fisher, *Theory of critical point scattering and correlations. III. The Ising model below T_c and in a field*, Phys. Rev. B **11** (1975), 1217–1253, DOI: [10.1103/PhysRevB.11.1217](https://doi.org/10.1103/PhysRevB.11.1217).
- [156] J. M. Kosterlitz and D. J. Thouless, *Ordering, metastability and phase transitions in two-dimensional systems*, J. Phys. **C6** (1973), 1181–1203.
- [157] V. L. Berezinskii, *Destruction of long-range order in one-dimensional and two-dimensional systems possessing a continuous symmetry group. II. Quantum systems*, Sov. Phys. JETP **34** (1972), 610–616.
- [158] M. Grater and C. Wetterich, *Kosterlitz-Thouless phase transition in the two-dimensional linear sigma model*, Phys. Rev. Lett. **75** (1995), 378–381, DOI: [10.1103/PhysRevLett.75.378](https://doi.org/10.1103/PhysRevLett.75.378), arXiv:[hep-ph/9409459](https://arxiv.org/abs/hep-ph/9409459) [[hep-ph](#)].
- [159] G. Von Gersdorff and C. Wetterich, *Nonperturbative renormalization flow and essential scaling for the Kosterlitz-Thouless transition*, Phys. Rev. **B64** (2001), 054513, DOI: [10.1103/PhysRevB.64.054513](https://doi.org/10.1103/PhysRevB.64.054513), arXiv:[hep-th/0008114](https://arxiv.org/abs/hep-th/0008114) [[hep-th](#)].
- [160] P. Jakubczyk and A. Eberlein, *Thermodynamics of the two-dimensional XY model from functional renormalization*, Phys. Rev. **E93** (2016), 062145, DOI: [10.1103/PhysRevE.93.062145](https://doi.org/10.1103/PhysRevE.93.062145), arXiv:[1604.06470](https://arxiv.org/abs/1604.06470) [[cond-mat.stat-mech](#)].
- [161] D. J. Bishop and J. D. Reppy, *Study of the Superfluid Transition in Two-Dimensional He-4 Films*, Phys. Rev. Lett. **40** (1978), 1727–1730, DOI: [10.1103/PhysRevLett.40.1727](https://doi.org/10.1103/PhysRevLett.40.1727).
- [162] J. Maps and R. B. Hallock, *Onset of Superfluid Flow in ^4He Films Adsorbed on Mylar*, Phys. Rev. Lett. **47** (1981), 1533–1536, DOI: [10.1103/PhysRevLett.47.1533](https://doi.org/10.1103/PhysRevLett.47.1533).
- [163] Z. Hadzibabic, P. Kruger, M. Cheneau, B. Battelier, and J. Dalibard, *Berezinskii-Kosterlitz-Thouless crossover in a trapped atomic gas*, Nature **441** (2006), 1118–1121, DOI: [10.1038/nature04851](https://doi.org/10.1038/nature04851).
- [164] S. Tung, G. Lamporesi, D. Lobser, L. Xia, and E. A. Cornell, *Observation of the Presuperfluid Regime in a Two-Dimensional Bose Gas*, Phys. Rev. Lett. **105** (2010), 230408, DOI: [10.1103/PhysRevLett.105.230408](https://doi.org/10.1103/PhysRevLett.105.230408).
- [165] R. Desbuquois, L. Chomaz, T. Yefsah, J. Léonard, J. Beugnon, et al., *Superfluid behaviour of a two-dimensional Bose gas*, Nature Physics **8** (2012), 645–648, DOI: [10.1038/nphys2378](https://doi.org/10.1038/nphys2378), arXiv:[1205.4536](https://arxiv.org/abs/1205.4536) [[cond-mat.quant-gas](#)].
- [166] P. A. Murthy, I. Boettcher, L. Bayha, M. Holzmann, D. Kedar, et al., *Observation of the Berezinskii-Kosterlitz-Thouless Phase Transition in an Ultracold Fermi Gas*, Phys. Rev. Lett. **115** (2015), 010401, DOI: [10.1103/PhysRevLett.115.010401](https://doi.org/10.1103/PhysRevLett.115.010401).
- [167] A. Codello, *Scaling Solutions in Continuous Dimension*, J.Phys. **A45** (2012), 465006, DOI: [10.1088/1751-8113/45/46/465006](https://doi.org/10.1088/1751-8113/45/46/465006), arXiv:[1204.3877](https://arxiv.org/abs/1204.3877) [[hep-th](#)].
- [168] G. P. Vacca and L. Zambelli, *Multimeson Yukawa interactions at criticality*, Phys. Rev. **D91** (2015), 125003, DOI: [10.1103/PhysRevD.91.125003](https://doi.org/10.1103/PhysRevD.91.125003), arXiv:[1503.09136](https://arxiv.org/abs/1503.09136) [[hep-th](#)].
- [169] J. Zinn-Justin, *Quantum field theory and critical phenomena*, Int. Ser. Monogr. Phys. **77** (1989), 1–914.
- [170] A Cortijo, F Guinea, and M. A. H. Vozmediano, *Geometrical and topological aspects of graphene and related materials*, Journal of Physics A: Mathematical and Theoretical **45** (2012), 383001.

- [171] S. Hands and C. Strouthos, *Quantum critical behavior in a graphenelike model*, Phys. Rev. B **78** (2008), 165423, DOI: [10.1103/PhysRevB.78.165423](https://doi.org/10.1103/PhysRevB.78.165423).
- [172] L. Janssen and I. F. Herbut, *Antiferromagnetic critical point on graphene's honeycomb lattice: A functional renormalization group approach*, Phys. Rev. B **89** (2014), 205403, DOI: [10.1103/PhysRevB.89.205403](https://doi.org/10.1103/PhysRevB.89.205403).
- [173] V. Branchina and H. Faivre, *Effective potential (in)stability and lower bounds on the scalar (Higgs) mass*, Phys. Rev. **D72** (2005), 065017, DOI: [10.1103/PhysRevD.72.065017](https://doi.org/10.1103/PhysRevD.72.065017), arXiv:[hep-th/0503188](https://arxiv.org/abs/hep-th/0503188) [[hep-th](#)].
- [174] T. Krajewski and Z. Lalak, *Fine-tuning and vacuum stability in the Wilsonian effective action*, Phys. Rev. **D92** (2015), 075009, DOI: [10.1103/PhysRevD.92.075009](https://doi.org/10.1103/PhysRevD.92.075009), arXiv:[1411.6435](https://arxiv.org/abs/1411.6435) [[hep-ph](#)].
- [175] N. Tetradis and D. F. Litim, *Analytical solutions of exact renormalization group equations*, Nucl. Phys. **B464** (1996), 492–511, DOI: [10.1016/0550-3213\(95\)00642-7](https://doi.org/10.1016/0550-3213(95)00642-7), arXiv:[hep-th/9512073](https://arxiv.org/abs/hep-th/9512073) [[hep-th](#)].
- [176] E. Ising, *Beitrag zur Theorie des Ferromagnetismus*, Zeitschrift für Physik **31** (1925), 253–258, DOI: [10.1007/BF02980577](https://doi.org/10.1007/BF02980577).
- [177] L. Onsager, *Crystal Statistics. I. A Two-Dimensional Model with an Order-Disorder Transition*, Phys. Rev. **65** (1944), 117–149, DOI: [10.1103/PhysRev.65.117](https://doi.org/10.1103/PhysRev.65.117).
- [178] B. Knorr, *Ising and Gross-Neveu model in next-to-leading order* (2016), arXiv:[1609.03824](https://arxiv.org/abs/1609.03824) [[cond-mat.str-el](#)].
- [179] S. Wetzels, “Phase Transitions in Models with Two Order Parameters,” master thesis, Heidelberg, 2013.
- [180] D. Funaro, *Polynomial Approximations of Differential Equations*, Springer, 1992.
- [181] B. Guo, *Spectral Methods and Their Applications*, World Scientific, 1998.
- [182] J. C. Mason and D. C. Handscomb, *Chebyshev Polynomials*, CRC Press, 2003.
- [183] D. Funaro and O. Kavianian, *Approximation of Some Diffusion Evolution Equations in Unbounded Domains by Hermite Functions*, Mathematics of Computation **57** (1991), 597–619.
- [184] B. Guo, *Error estimation of Hermite spectral method for nonlinear partial differential equations*, Math. Comp. **68** (1999), 1067–1078.
- [185] B. Guo and J. Shen, *Laguerre-Garlekin method for nonlinear partial differential equations on a semi-infinite interval*, J. Numer. Math. **86** (2000), 635–654, DOI: [10.1007/PL00005413](https://doi.org/10.1007/PL00005413).
- [186] J. Shen, *Stable and efficient spectral methods in unbounded domains by using Laguerre functions*, SIAM J. Numer. Anal. **38** (2000), 1113–1133.
- [187] B. Guo and L. He, *The Fully Discrete Legendre Spectral Approximation of Two-Dimensional Unsteady Incompressible Fluid Flow in Stream Function Form*, SIAM J. Numer. Anal. **35** (2006), 146–176.
- [188] H. Wang and S. Xiang, *On the convergence rates of Legendre approximation*, Mathematics of Computation **81** (2011), 861–877, DOI: [10.1090/s0025-5718-2011-02549-4](https://doi.org/10.1090/s0025-5718-2011-02549-4).

- [189] J. P. Boyd and R. Petschek, *The Relationships Between Chebyshev, Legendre and Jacobi Polynomials: The Generic Superiority of Chebyshev Polynomials and Three Important Exceptions*, Journal of Scientific Computing **59** (2014), 1–27, DOI: [10.1007/s10915-013-9751-7](https://doi.org/10.1007/s10915-013-9751-7).
- [190] W. Guo, G. Labrosse, and R. Narayanan, *The Application of the Chebyshev-Spectral Method in Transport Phenomena (Lecture Notes in Applied and Computational Mechanics)*, Springer, 2013.
- [191] C. W. Clenshaw, *A note on the summation of Chebyshev series*, Math. Comp. **9** (1955), 118–120, DOI: [10.1090/S0025-5718-1955-0071856-0](https://doi.org/10.1090/S0025-5718-1955-0071856-0).
- [192] J. Boyd, *Orthogonal rational functions on a semi-infinite interval*, J.Comp.Phys. **70** (1987), 63–88.
- [193] J. P. Boyd, *Spectral methods using rational basis functions on an infinite interval*, Journal of Computational Physics **69** (1987), 112–142, DOI: [10.1016/0021-9991\(87\)90158-6](https://doi.org/10.1016/0021-9991(87)90158-6).
- [194] B. Guo, J. Shen, and Z. Wang, *Chebyshev rational spectral and pseudospectral methods on a semi-infinite interval*, Int. J. Numer. Meth. Engng. **53** (2002), 65–84.
- [195] Z.-Q. Wang and B.-Y. Guo, *A rational approximation and its applications to nonlinear partial differential equations on the whole line*, Journal of Mathematical Analysis and Applications **274** (2002), 374–403, DOI: [http://dx.doi.org/10.1016/S0022-247X\(02\)00334-7](http://dx.doi.org/10.1016/S0022-247X(02)00334-7).
- [196] A. Hasenfratz and P. Hasenfratz, *Renormalization Group Study of Scalar Field Theories*, Nucl. Phys. **B270** (1986), 687–701, DOI: [10.1016/0550-3213\(86\)90573-0](https://doi.org/10.1016/0550-3213(86)90573-0).
- [197] *BOOST C++ Libraries 1.57.0*, <http://www.boost.org>, 2014.
- [198] Guennebaud, G. and Jacob, B. and others, *Eigen v3*, <http://eigen.tuxfamily.org>, 2010.
- [199] *The Blitz++ meta-template library*, <http://blitz.sourceforge.net/>, Accessed: 2015-01-27.
- [200] A. Pelissetto and E. Vicari, *Critical phenomena and renormalization group theory*, Phys.Rept. **368** (2002), 549–727, DOI: [10.1016/S0370-1573\(02\)00219-3](https://doi.org/10.1016/S0370-1573(02)00219-3), arXiv:[cond-mat/0012164](https://arxiv.org/abs/cond-mat/0012164) [[cond-mat](https://arxiv.org/abs/cond-mat)].
- [201] I. H. Bridle, J. A. Dietz, and T. R. Morris, *The local potential approximation in the background field formalism*, JHEP **1403** (2014), 093, DOI: [10.1007/JHEP03\(2014\)093](https://doi.org/10.1007/JHEP03(2014)093), arXiv:[1312.2846](https://arxiv.org/abs/1312.2846) [[hep-th](https://arxiv.org/abs/hep-th)].
- [202] T. R. Morris, *The Renormalization group and two-dimensional multicritical effective scalar field theory*, Phys. Lett. **B345** (1995), 139–148, DOI: [10.1016/0370-2693\(94\)01603-A](https://doi.org/10.1016/0370-2693(94)01603-A), arXiv:[hep-th/9410141](https://arxiv.org/abs/hep-th/9410141) [[hep-th](https://arxiv.org/abs/hep-th)].
- [203] N. D. Mermin and H. Wagner, *Absence of Ferromagnetism or Antiferromagnetism in One- or Two-Dimensional Isotropic Heisenberg Models*, Phys. Rev. Lett. **17** (1966), 1133–1136, DOI: [10.1103/PhysRevLett.17.1133](https://doi.org/10.1103/PhysRevLett.17.1133).
- [204] P. Hohenberg, *Existence of Long-Range Order in One and Two Dimensions*, Phys.Rev. **158** (1967), 383–386, DOI: [10.1103/PhysRev.158.383](https://doi.org/10.1103/PhysRev.158.383).
- [205] A. Gelfert and W. Nolting, *The absence of finite-temperature phase transitions in low-dimensional many-body models: a survey and new results*, Journal of Physics: Condensed Matter **13** (2001), R505.

- [206] S. R. Coleman, *There are no Goldstone bosons in two-dimensions*, Commun.Math.Phys. **31** (1973), 259–264, DOI: [10.1007/BF01646487](https://doi.org/10.1007/BF01646487).
- [207] J. Le Guillou and J. Zinn-Justin, *Accurate critical exponents for Ising like systems in noninteger dimensions* (1987).
- [208] S. El-Showk, M. Paulos, D. Poland, S. Rychkov, D. Simmons-Duffin, et al., *Conformal Field Theories in Fractional Dimensions*, Phys.Rev.Lett. **112** (2014), 141601, DOI: [10.1103/PhysRevLett.112.141601](https://doi.org/10.1103/PhysRevLett.112.141601), arXiv:[1309.5089](https://arxiv.org/abs/1309.5089) [hep-th].
- [209] G. Bhanot, D. Duke, and R. Salvador, *Fractals and Interpolating Dimensions*, Phys.Lett. **B165** (1985), 355, DOI: [10.1016/0370-2693\(85\)91245-6](https://doi.org/10.1016/0370-2693(85)91245-6).
- [210] F. Hofling, C. Nowak, and C. Wetterich, *Phase transition and critical behavior of the $D = 3$ Gross-Neveu model*, Phys.Rev. **B66** (2002), 205111, DOI: [10.1103/PhysRevB.66.205111](https://doi.org/10.1103/PhysRevB.66.205111), arXiv:[cond-mat/0203588](https://arxiv.org/abs/cond-mat/0203588) [cond-mat].
- [211] J. Gracey, *Computation of critical exponent η at $O(1/N^{**3})$ in the four Fermi model in arbitrary dimensions*, Int.J.Mod.Phys. **A9** (1994), 727–744, DOI: [10.1142/S0217751X94000340](https://doi.org/10.1142/S0217751X94000340), arXiv:[hep-th/9306107](https://arxiv.org/abs/hep-th/9306107) [hep-th].
- [212] A. Vasiliev, S. E. Derkachov, N. Kivel, and A. Stepanenko, *The $1/n$ expansion in the Gross-Neveu model: Conformal bootstrap calculation of the index η in order $1/n^{**3}$* , Theor.Math.Phys. **94** (1993), 127–136, DOI: [10.1007/BF01019324](https://doi.org/10.1007/BF01019324).
- [213] S. Hands, A. Kocic, and J. B. Kogut, *Four Fermi theories in fewer than four-dimensions*, Annals Phys. **224** (1993), 29–89, DOI: [10.1006/aphy.1993.1039](https://doi.org/10.1006/aphy.1993.1039), arXiv:[hep-lat/9208022](https://arxiv.org/abs/hep-lat/9208022) [hep-lat].
- [214] L. Karkkainen, R. Lacaze, P. Lacock, and B. Petersson, *Critical behavior of the 3-d Gross-Neveu and Higgs-Yukawa models*, Nucl.Phys. **B415** (1994), 781–796, DOI: [10.1016/0550-3213\(94\)90309-3](https://doi.org/10.1016/0550-3213(94)90309-3), arXiv:[hep-lat/9310020](https://arxiv.org/abs/hep-lat/9310020) [hep-lat].
- [215] M. E. Fisher and D. R. Nelson, *Spin Flop, Supersolids, and Bicritical and Tetracritical Points*, Phys. Rev. Lett. **32** (1974), 1350–1353, DOI: [10.1103/PhysRevLett.32.1350](https://doi.org/10.1103/PhysRevLett.32.1350).
- [216] K.-S. Liu and M. E. Fisher, *Quantum lattice gas and the existence of a supersolid*, Journal of Low Temperature Physics **10** (1973), 655–683, DOI: [10.1007/BF00655458](https://doi.org/10.1007/BF00655458).
- [217] E. V. Orlov and A. I. Sokolov, *Critical thermodynamics of two-dimensional systems in the five-loop renormalization-group approximation*, Physics of the Solid State **42** (2000), 2151–2158, DOI: [10.1134/1.1324056](https://doi.org/10.1134/1.1324056).
- [218] L. Canet, B. Delamotte, D. Mouhanna, and J. Vidal, *Nonperturbative renormalization group approach to the Ising model: A Derivative expansion at order partial**4*, Phys. Rev. **B68** (2003), 064421, DOI: [10.1103/PhysRevB.68.064421](https://doi.org/10.1103/PhysRevB.68.064421), arXiv:[hep-th/0302227](https://arxiv.org/abs/hep-th/0302227) [hep-th].
- [219] B. Delamotte, M. Tissier, and N. Wschebor, *Scale invariance implies conformal invariance for the three-dimensional Ising model*, Phys. Rev. **E93** (2016), 012144, DOI: [10.1103/PhysRevE.93.012144](https://doi.org/10.1103/PhysRevE.93.012144), arXiv:[1501.01776](https://arxiv.org/abs/1501.01776) [cond-mat.stat-mech].
- [220] J. K. Esbensen, T. A. Ryttov, and F. Sannino, *Quantum critical behavior of semisimple gauge theories*, Phys. Rev. **D93** (2016), 045009, DOI: [10.1103/PhysRevD.93.045009](https://doi.org/10.1103/PhysRevD.93.045009), arXiv:[1512.04402](https://arxiv.org/abs/1512.04402) [hep-th].
- [221] S. Bornholdt, N. Tetradis, and C. Wetterich, *Coleman-Weinberg phase transition in two scalar models*, Phys. Lett. **B348** (1995), 89–99, DOI: [10.1016/0370-2693\(95\)00045-M](https://doi.org/10.1016/0370-2693(95)00045-M), arXiv:[hep-th/9408132](https://arxiv.org/abs/hep-th/9408132) [hep-th].

- [222] S. Bornholdt, N. Tetradis, and C. Wetterich, *High temperature phase transition in two scalar theories*, Phys. Rev. **D53** (1996), 4552–4569, DOI: [10.1103/PhysRevD.53.4552](https://doi.org/10.1103/PhysRevD.53.4552), arXiv:[hep-ph/9503282](https://arxiv.org/abs/hep-ph/9503282) [hep-ph].
- [223] M. Tissier, D. Mouhanna, J. Vidal, and B. Delamotte, *Randomly dilute Ising model: [$\langle EM \text{ SPACE} \rangle$] A nonperturbative approach*, Phys. Rev. **B65** (2002), 140402, DOI: [10.1103/PhysRevB.65.140402](https://doi.org/10.1103/PhysRevB.65.140402).
- [224] H. Gies, J. Jaeckel, and C. Wetterich, *Towards a renormalizable standard model without fundamental Higgs scalar*, Phys. Rev. **D69** (2004), 105008, DOI: [10.1103/PhysRevD.69.105008](https://doi.org/10.1103/PhysRevD.69.105008), arXiv:[hep-ph/0312034](https://arxiv.org/abs/hep-ph/0312034) [hep-ph].
- [225] J. Braun, H. Gies, L. Janssen, and D. Roscher, *Phase structure of many-flavor QED₃*, Phys. Rev. **D90** (2014), 036002, DOI: [10.1103/PhysRevD.90.036002](https://doi.org/10.1103/PhysRevD.90.036002), arXiv:[1404.1362](https://arxiv.org/abs/1404.1362) [hep-ph].
- [226] T. R. Morris, *Elements of the continuous renormalization group*, Prog. Theor. Phys. Suppl. **131** (1998), 395–414, DOI: [10.1143/PTPS.131.395](https://doi.org/10.1143/PTPS.131.395), arXiv:[hep-th/9802039](https://arxiv.org/abs/hep-th/9802039) [hep-th].
- [227] L. J. de Jongh, L. P. Regnault, J. Rossat-Mignod, and J. Y. Henry, *Field dependent neutron scattering study of the quasi 2-D Heisenberg antiferromagnet K₂MnF₄*, Journal of Applied Physics **53** (1982), 7963–7965, DOI: [10.1063/1.330242](https://doi.org/10.1063/1.330242).
- [228] L. J. de Jongh and H. J. M. de Groot, *Phase diagrams of weakly anisotropic Heisenberg antiferromagnets: II. Quasi 2-dimensional systems*, Solid State Communications **53** (1985), 737–741, DOI: [10.1016/0038-1098\(85\)90210-8](https://doi.org/10.1016/0038-1098(85)90210-8).
- [229] H. J. M. De Groot and L. J. De Jongh, *Phase diagrams of weakly anisotropic Heisenberg antiferromagnets, nonlinear excitations (solitons) and random-field effects*, Physica B+C **141** (1986), 1–36, DOI: [10.1016/0378-4363\(86\)90346-3](https://doi.org/10.1016/0378-4363(86)90346-3).
- [230] H. Rauh, W. A. C. Erkelens, L. P. Regnault, J. Rossat-Mignod, W. Kullman, et al., *Magnetic phase diagram of Rb₂MnCl₄, a quasi-two-dimensional uniaxial antiferromagnet*, Journal of Physics C Solid State Physics **19** (1986), 4503–4510, DOI: [10.1088/0022-3719/19/23/013](https://doi.org/10.1088/0022-3719/19/23/013).
- [231] R. A. Cowley, A. Aharony, R. J. Birgeneau, R. A. Pelcovits, G. Shirane, et al., *The bicritical phase diagram of two-dimensional antiferromagnets with and without random fields*, Zeitschrift fur Physik B Condensed Matter **93** (1993), 5–19, DOI: [10.1007/BF01308802](https://doi.org/10.1007/BF01308802).
- [232] R. van de Kamp, M. Steiner, and H. Tietze-Jaensch, *Study of the phase diagram and the critical behaviour of the 2D Heisenberg antiferromagnet with small uniaxial anisotropy*, Physica B: Condensed Matter **241** (1997), 570–572, DOI: [10.1016/S0921-4526\(97\)00646-7](https://doi.org/10.1016/S0921-4526(97)00646-7).
- [233] R. J. Christianson, R. L. Leheny, R. J. Birgeneau, and R. W. Erwin, *Critical dynamics of a spin-5/2 two-dimensional isotropic antiferromagnet*, Phys. Rev. B **63**, 140401 (2001), 140401, DOI: [10.1103/PhysRevB.63.140401](https://doi.org/10.1103/PhysRevB.63.140401), eprint: [cond-mat/0101097](https://arxiv.org/abs/cond-mat/0101097).
- [234] D. F. Litim, J. M. Pawłowski, and L. Vergara, *Convexity of the effective action from functional flows* (2006), arXiv:[hep-th/0602140](https://arxiv.org/abs/hep-th/0602140) [hep-th].
- [235] A. S. Kapoyannis and N. Tetradis, *Quantum mechanical tunneling and the renormalization group*, Phys. Lett. **A276** (2000), 225–232, DOI: [10.1016/S0375-9601\(00\)00671-X](https://doi.org/10.1016/S0375-9601(00)00671-X), arXiv:[hep-th/0010180](https://arxiv.org/abs/hep-th/0010180) [hep-th].

- [236] F. Bezrukov and M. Shaposhnikov, *The Standard Model Higgs boson as the inflaton*, Physics Letters B **659** (2008), 703–706, DOI: <http://dx.doi.org/10.1016/j.physletb.2007.11.072>.
- [237] J. Rubio, *Higgs inflation and vacuum stability*, J. Phys. Conf. Ser. **631** (2015), 012032, DOI: [10.1088/1742-6596/631/1/012032](https://doi.org/10.1088/1742-6596/631/1/012032), arXiv:1502.07952 [hep-ph].
- [238] F. Bezrukov, M. Yu. Kalmykov, B. A. Kniehl, and M. Shaposhnikov, *Higgs Boson Mass and New Physics*, JHEP **10** (2012), 140, DOI: [10.1007/JHEP10\(2012\)140](https://doi.org/10.1007/JHEP10(2012)140), arXiv:1205.2893 [hep-ph].
- [239] J. Rubio and M. Shaposhnikov, *Higgs-Dilaton cosmology: Universality versus criticality*, Phys. Rev. **D90** (2014), 027307, DOI: [10.1103/PhysRevD.90.027307](https://doi.org/10.1103/PhysRevD.90.027307), arXiv:1406.5182 [hep-ph].
- [240] F. Bezrukov, G. K. Karananas, J. Rubio, and M. Shaposhnikov, *Higgs-Dilaton Cosmology: an effective field theory approach*, Phys. Rev. **D87** (2013), 096001, DOI: [10.1103/PhysRevD.87.096001](https://doi.org/10.1103/PhysRevD.87.096001), arXiv:1212.4148 [hep-ph].
- [241] A. Yu. Kamenshchik and C. F. Steinwachs, *Question of quantum equivalence between Jordan frame and Einstein frame*, Phys. Rev. **D91** (2015), 084033, DOI: [10.1103/PhysRevD.91.084033](https://doi.org/10.1103/PhysRevD.91.084033), arXiv:1408.5769 [gr-qc].
- [242] E. J. Copeland, C. Rahmede, and I. D. Saltas, *Asymptotically safe Starobinsky inflation*, Phys. Rev. D **91** (2015), 103530, DOI: [10.1103/PhysRevD.91.103530](https://doi.org/10.1103/PhysRevD.91.103530).
- [243] A. Kaya, *Exact renormalization group flow in an expanding Universe and screening of the cosmological constant*, Phys. Rev. D **87** (2013), 123501, DOI: [10.1103/PhysRevD.87.123501](https://doi.org/10.1103/PhysRevD.87.123501).
- [244] I. D. Saltas, *Higgs inflation and quantum gravity: an exact renormalisation group approach*, Journal of Cosmology and Astroparticle Physics **2016** (2016), 048, arXiv:1512.06134 [hep-th].
- [245] G. Pöschl and E. Teller, *Bemerkungen zur Quantenmechanik des anharmonischen Oszillators*, Zeitschrift für Physik **83** (1933), 143–151, DOI: [10.1007/bf01331132](https://doi.org/10.1007/bf01331132).
- [246] Y. Fujimoto, L. O’Raifeartaigh, and G. Parravicini, *Effective Potential for Nonconvex Potentials*, Nucl. Phys. **B212** (1983), 268, DOI: [10.1016/0550-3213\(83\)90305-X](https://doi.org/10.1016/0550-3213(83)90305-X).
- [247] S. R. Coleman and E. J. Weinberg, *Radiative Corrections as the Origin of Spontaneous Symmetry Breaking*, Phys. Rev. **D7** (1973), 1888–1910, DOI: [10.1103/PhysRevD.7.1888](https://doi.org/10.1103/PhysRevD.7.1888).
- [248] T. L. Curtright and C. B. Thorn, *The Effective Potential in Quantum Mechanics*, J. Math. Phys. **25** (1984), 541, DOI: [10.1063/1.526204](https://doi.org/10.1063/1.526204).
- [249] S. Coleman, *Aspects of Symmetry*, Cambridge Books Online, Cambridge University Press, 1985.
- [250] K. Symanzik, *Renormalizable models with simple symmetry breaking. 1. Symmetry breaking by a source term*, Commun. Math. Phys. **16** (1970), 48–80, DOI: [10.1007/BF01645494](https://doi.org/10.1007/BF01645494).
- [251] P. M. Stevenson, *The Gaussian Effective Potential. 1. Quantum Mechanics*, Phys. Rev. **D30** (1984), 1712, DOI: [10.1103/PhysRevD.30.1712](https://doi.org/10.1103/PhysRevD.30.1712).
- [252] L. Maiani, G. Parisi, and R. Petronzio, *Bounds on the Number and Masses of Quarks and Leptons*, Nucl. Phys. **B136** (1978), 115, DOI: [10.1016/0550-3213\(78\)90018-4](https://doi.org/10.1016/0550-3213(78)90018-4).

- [253] N. V. Krasnikov, *Restriction of the Fermion Mass in Gauge Theories of Weak and Electromagnetic Interactions*, *Yad. Fiz.* **28** (1978), 549–551.
- [254] M. Lindner, *Implications of Triviality for the Standard Model*, *Z. Phys.* **C31** (1986), 295, DOI: [10.1007/BF01479540](https://doi.org/10.1007/BF01479540).
- [255] C. Wetterich, *THE MASS OF THE HIGGS PARTICLE*, in: Search for Scalar Particles: Experimental and Theoretical Aspects Trieste, Italy, July 23-24, 1987.
- [256] G. Altarelli and G. Isidori, *Lower limit on the Higgs mass in the standard model: An Update*, *Phys. Lett.* **B337** (1994), 141–144, DOI: [10.1016/0370-2693\(94\)91458-3](https://doi.org/10.1016/0370-2693(94)91458-3).
- [257] B. Schrempp and M. Wimmer, *Top quark and Higgs boson masses: Interplay between infrared and ultraviolet physics*, *Prog. Part. Nucl. Phys.* **37** (1996), 1–90, DOI: [10.1016/0146-6410\(96\)00059-2](https://doi.org/10.1016/0146-6410(96)00059-2), arXiv:[hep-ph/9606386](https://arxiv.org/abs/hep-ph/9606386) [[hep-ph](#)].
- [258] T. Hambye and K. Riesselmann, *Matching conditions and Higgs mass upper bounds revisited*, *Phys. Rev.* **D55** (1997), 7255–7262, DOI: [10.1103/PhysRevD.55.7255](https://doi.org/10.1103/PhysRevD.55.7255), arXiv:[hep-ph/9610272](https://arxiv.org/abs/hep-ph/9610272) [[hep-ph](#)].
- [259] I. V. Krive and A. D. Linde, *On the Vacuum Stability Problem in Gauge Theories*, *Nucl. Phys.* **B117** (1976), 265, DOI: [10.1016/0550-3213\(76\)90573-3](https://doi.org/10.1016/0550-3213(76)90573-3).
- [260] P. Q. Hung, *Vacuum Instability and New Constraints on Fermion Masses*, *Phys. Rev. Lett.* **42** (1979), 873, DOI: [10.1103/PhysRevLett.42.873](https://doi.org/10.1103/PhysRevLett.42.873).
- [261] A. D. Linde, *Vacuum Instability, Cosmology and Constraints on Particle Masses in the Weinberg-Salam Model*, *Phys. Lett.* **B92** (1980), 119, DOI: [10.1016/0370-2693\(80\)90318-4](https://doi.org/10.1016/0370-2693(80)90318-4).
- [262] N. Cabibbo, L. Maiani, G. Parisi, and R. Petronzio, *Bounds on the Fermions and Higgs Boson Masses in Grand Unified Theories*, *Nucl. Phys.* **B158** (1979), 295–305, DOI: [10.1016/0550-3213\(79\)90167-6](https://doi.org/10.1016/0550-3213(79)90167-6).
- [263] H. D. Politzer and S. Wolfram, *Bounds on Particle Masses in the Weinberg-Salam Model*, *Phys. Lett.* **B82** (1979), [Erratum: *Phys. Lett.*83B,421(1979)], 242–246, DOI: [10.1016/0370-2693\(79\)90746-9](https://doi.org/10.1016/0370-2693(79)90746-9).
- [264] J. Kuti, L. Lin, and Y. Shen, *Upper Bound on the Higgs Mass in the Standard Model*, *Phys. Rev. Lett.* **61** (1988), 678, DOI: [10.1103/PhysRevLett.61.678](https://doi.org/10.1103/PhysRevLett.61.678).
- [265] M. Sher, *Electroweak Higgs Potentials and Vacuum Stability*, *Phys. Rept.* **179** (1989), 273–418, DOI: [10.1016/0370-1573\(89\)90061-6](https://doi.org/10.1016/0370-1573(89)90061-6).
- [266] A. Hasenfratz, K. Jansen, C. B. Lang, T. Neuhaus, and H. Yoneyama, *The Triviality Bound of the Four Component ϕ^{**4} Model*, *Phys. Lett.* **B199** (1987), 531, DOI: [10.1016/0370-2693\(87\)91622-4](https://doi.org/10.1016/0370-2693(87)91622-4).
- [267] M. Luscher and P. Weisz, *Scaling Laws and Triviality Bounds in the Lattice ϕ^{**4} Theory. 3. N Component Model*, *Nucl. Phys.* **B318** (1989), 705, DOI: [10.1016/0550-3213\(89\)90637-8](https://doi.org/10.1016/0550-3213(89)90637-8).
- [268] M. Lindner, M. Sher, and H. W. Zaglauer, *Probing Vacuum Stability Bounds at the Fermilab Collider*, *Phys. Lett.* **B228** (1989), 139, DOI: [10.1016/0370-2693\(89\)90540-6](https://doi.org/10.1016/0370-2693(89)90540-6).
- [269] C. Ford, D. R. T. Jones, P. W. Stephenson, and M. B. Einhorn, *The Effective potential and the renormalization group*, *Nucl. Phys.* **B395** (1993), 17–34, DOI: [10.1016/0550-3213\(93\)90206-5](https://doi.org/10.1016/0550-3213(93)90206-5), arXiv:[hep-lat/9210033](https://arxiv.org/abs/hep-lat/9210033) [[hep-lat](#)].

- [270] U. M. Heller, M. Klomfass, H. Neuberger, and P. M. Vranas, *Numerical analysis of the Higgs mass triviality bound*, Nucl. Phys. **B405** (1993), 555–573, DOI: [10.1016/0550-3213\(93\)90559-8](https://doi.org/10.1016/0550-3213(93)90559-8), arXiv:[hep-ph/9303215](https://arxiv.org/abs/hep-ph/9303215) [[hep-ph](#)].
- [271] P. B. Arnold, *Can the Electroweak Vacuum Be Unstable?* Phys. Rev. **D40** (1989), 613, DOI: [10.1103/PhysRevD.40.613](https://doi.org/10.1103/PhysRevD.40.613).
- [272] M. Sher, *Precise vacuum stability bound in the standard model*, Phys. Lett. **B317** (1993), [Addendum: Phys. Lett.B331,448(1994)], 159–163, DOI: [10.1016/0370-2693\(93\)91586-C](https://doi.org/10.1016/0370-2693(93)91586-C), arXiv:[hep-ph/9307342](https://arxiv.org/abs/hep-ph/9307342) [[hep-ph](#)].
- [273] J. A. Casas, J. R. Espinosa, and M. Quiros, *Improved Higgs mass stability bound in the standard model and implications for supersymmetry*, Phys. Lett. **B342** (1995), 171–179, DOI: [10.1016/0370-2693\(94\)01404-Z](https://doi.org/10.1016/0370-2693(94)01404-Z), arXiv:[hep-ph/9409458](https://arxiv.org/abs/hep-ph/9409458) [[hep-ph](#)].
- [274] J. R. Espinosa and M. Quiros, *Improved metastability bounds on the standard model Higgs mass*, Phys. Lett. **B353** (1995), 257–266, DOI: [10.1016/0370-2693\(95\)00572-3](https://doi.org/10.1016/0370-2693(95)00572-3), arXiv:[hep-ph/9504241](https://arxiv.org/abs/hep-ph/9504241) [[hep-ph](#)].
- [275] B. Bergerhoff, M. Lindner, and M. Weiser, *Dynamics of metastable vacua in the early universe*, Phys. Lett. **B469** (1999), 61–68, DOI: [10.1016/S0370-2693\(99\)01273-3](https://doi.org/10.1016/S0370-2693(99)01273-3), arXiv:[hep-ph/9909261](https://arxiv.org/abs/hep-ph/9909261) [[hep-ph](#)].
- [276] G. Isidori, G. Ridolfi, and A. Strumia, *On the metastability of the standard model vacuum*, Nucl. Phys. **B609** (2001), 387–409, DOI: [10.1016/S0550-3213\(01\)00302-9](https://doi.org/10.1016/S0550-3213(01)00302-9), arXiv:[hep-ph/0104016](https://arxiv.org/abs/hep-ph/0104016) [[hep-ph](#)].
- [277] J. Ellis, J. R. Espinosa, G. F. Giudice, A. Hoecker, and A. Riotto, *The Probable Fate of the Standard Model*, Phys. Lett. **B679** (2009), 369–375, DOI: [10.1016/j.physletb.2009.07.054](https://doi.org/10.1016/j.physletb.2009.07.054), arXiv:[0906.0954](https://arxiv.org/abs/0906.0954) [[hep-ph](#)].
- [278] M. Holthausen, K. S. Lim, and M. Lindner, *Planck scale Boundary Conditions and the Higgs Mass*, JHEP **02** (2012), 037, DOI: [10.1007/JHEP02\(2012\)037](https://doi.org/10.1007/JHEP02(2012)037), arXiv:[1112.2415](https://arxiv.org/abs/1112.2415) [[hep-ph](#)].
- [279] J. Elias-Miro, J. R. Espinosa, G. F. Giudice, G. Isidori, A. Riotto, et al., *Higgs mass implications on the stability of the electroweak vacuum*, Phys. Lett. **B709** (2012), 222–228, DOI: [10.1016/j.physletb.2012.02.013](https://doi.org/10.1016/j.physletb.2012.02.013), arXiv:[1112.3022](https://arxiv.org/abs/1112.3022) [[hep-ph](#)].
- [280] G. Degrassi, S. Di Vita, J. Elias-Miro, J. R. Espinosa, G. F. Giudice, et al., *Higgs mass and vacuum stability in the Standard Model at NNLO*, JHEP **08** (2012), 098, DOI: [10.1007/JHEP08\(2012\)098](https://doi.org/10.1007/JHEP08(2012)098), arXiv:[1205.6497](https://arxiv.org/abs/1205.6497) [[hep-ph](#)].
- [281] S. Alekhin, A. Djouadi, and S. Moch, *The top quark and Higgs boson masses and the stability of the electroweak vacuum*, Phys. Lett. **B716** (2012), 214–219, DOI: [10.1016/j.physletb.2012.08.024](https://doi.org/10.1016/j.physletb.2012.08.024), arXiv:[1207.0980](https://arxiv.org/abs/1207.0980) [[hep-ph](#)].
- [282] I. Masina, *Higgs boson and top quark masses as tests of electroweak vacuum stability*, Phys. Rev. **D87** (2013), 053001, DOI: [10.1103/PhysRevD.87.053001](https://doi.org/10.1103/PhysRevD.87.053001), arXiv:[1209.0393](https://arxiv.org/abs/1209.0393) [[hep-ph](#)].
- [283] D. Buttazzo, G. Degrassi, P. P. Giardino, G. F. Giudice, F. Sala, et al., *Investigating the near-criticality of the Higgs boson*, JHEP **12** (2013), 089, DOI: [10.1007/JHEP12\(2013\)089](https://doi.org/10.1007/JHEP12(2013)089), arXiv:[1307.3536](https://arxiv.org/abs/1307.3536) [[hep-ph](#)].

- [284] E. Gabrielli, M. Heikinheimo, K. Kannike, A. Racioppi, M. Raidal, et al., *Towards Completing the Standard Model: Vacuum Stability, EWSB and Dark Matter*, Phys. Rev. **D89** (2014), 015017, DOI: [10.1103/PhysRevD.89.015017](https://doi.org/10.1103/PhysRevD.89.015017), arXiv:[1309.6632](https://arxiv.org/abs/1309.6632) [hep-ph].
- [285] A. V. Bednyakov, B. A. Kniehl, A. F. Pikelner, and O. L. Veretin, *Stability of the Electroweak Vacuum: Gauge Independence and Advanced Precision*, Phys. Rev. Lett. **115** (2015), 201802, DOI: [10.1103/PhysRevLett.115.201802](https://doi.org/10.1103/PhysRevLett.115.201802), arXiv:[1507.08833](https://arxiv.org/abs/1507.08833) [hep-ph].
- [286] K. Holland and J. Kuti, *How light can the Higgs be?* Nucl. Phys. Proc. Suppl. **129** (2004), [765(2003)], 765–767, DOI: [10.1016/S0920-5632\(03\)02706-3](https://doi.org/10.1016/S0920-5632(03)02706-3), arXiv:[hep-lat/0308020](https://arxiv.org/abs/hep-lat/0308020) [hep-lat].
- [287] K. Holland, *Triviality and the Higgs mass lower bound*, Nucl. Phys. Proc. Suppl. **140** (2005), [155(2004)], 155–161, DOI: [10.1016/j.nuclphysbps.2004.11.293](https://doi.org/10.1016/j.nuclphysbps.2004.11.293), arXiv:[hep-lat/0409112](https://arxiv.org/abs/hep-lat/0409112) [hep-lat].
- [288] A. Eichhorn and M. M. Scherer, *Planck scale, Higgs mass, and scalar dark matter*, Phys. Rev. **D90** (2014), 025023, DOI: [10.1103/PhysRevD.90.025023](https://doi.org/10.1103/PhysRevD.90.025023), arXiv:[1404.5962](https://arxiv.org/abs/1404.5962) [hep-ph].
- [289] A. Andreassen, W. Frost, and M. D. Schwartz, *Consistent Use of the Standard Model Effective Potential*, Phys. Rev. Lett. **113** (2014), 241801, DOI: [10.1103/PhysRevLett.113.241801](https://doi.org/10.1103/PhysRevLett.113.241801), arXiv:[1408.0292](https://arxiv.org/abs/1408.0292) [hep-ph].
- [290] A. Andreassen, W. Frost, and M. D. Schwartz, *Consistent Use of Effective Potentials*, Phys. Rev. **D91** (2015), 016009, DOI: [10.1103/PhysRevD.91.016009](https://doi.org/10.1103/PhysRevD.91.016009), arXiv:[1408.0287](https://arxiv.org/abs/1408.0287) [hep-ph].
- [291] Z. Fodor, K. Holland, J. Kuti, D. Negradi, and C. Schroeder, *New Higgs physics from the lattice*, PoS **LAT2007** (2007), 056, arXiv:[0710.3151](https://arxiv.org/abs/0710.3151) [hep-lat].
- [292] P. Gerhold and K. Jansen, *The Phase structure of a chirally invariant lattice Higgs-Yukawa model for small and for large values of the Yukawa coupling constant*, JHEP **09** (2007), 041, DOI: [10.1088/1126-6708/2007/09/041](https://doi.org/10.1088/1126-6708/2007/09/041), arXiv:[0705.2539](https://arxiv.org/abs/0705.2539) [hep-lat].
- [293] P. Gerhold and K. Jansen, *The Phase structure of a chirally invariant lattice Higgs-Yukawa model - numerical simulations*, JHEP **10** (2007), 001, DOI: [10.1088/1126-6708/2007/10/001](https://doi.org/10.1088/1126-6708/2007/10/001), arXiv:[0707.3849](https://arxiv.org/abs/0707.3849) [hep-lat].
- [294] P. Gerhold and K. Jansen, *Lower Higgs boson mass bounds from a chirally invariant lattice Higgs-Yukawa model with overlap fermions*, JHEP **07** (2009), 025, DOI: [10.1088/1126-6708/2009/07/025](https://doi.org/10.1088/1126-6708/2009/07/025), arXiv:[0902.4135](https://arxiv.org/abs/0902.4135) [hep-lat].
- [295] A. Hebecker, A. K. Knochel, and T. Weigand, *The Higgs mass from a String-Theoretic Perspective*, Nucl. Phys. **B874** (2013), 1–35, DOI: [10.1016/j.nuclphysb.2013.05.004](https://doi.org/10.1016/j.nuclphysb.2013.05.004), arXiv:[1304.2767](https://arxiv.org/abs/1304.2767) [hep-th].
- [296] A. Jakovac, I. Kaposvari, and A. Patkos, *Scalar mass stability bound in a simple Yukawa-theory from renormalisation group equations* (2015), arXiv:[1508.06774](https://arxiv.org/abs/1508.06774) [hep-th].
- [297] A. Jakovac, I. Kaposvari, and A. Patkos, *Renormalisation Group Determination of Scalar Mass Bounds in a Simple Yukawa-Model* (2015), arXiv:[1510.05782](https://arxiv.org/abs/1510.05782) [hep-th].

- [298] S. R. Coleman, *The Fate of the False Vacuum. 1. Semiclassical Theory*, Phys. Rev. **D15** (1977), [Erratum: Phys. Rev.D16,1248(1977)], 2929–2936, DOI: [10.1103/PhysRevD.15.2929](https://doi.org/10.1103/PhysRevD.15.2929), [10.1103/PhysRevD.16.1248](https://doi.org/10.1103/PhysRevD.16.1248).
- [299] C. G. Callan Jr. and S. R. Coleman, *The Fate of the False Vacuum. 2. First Quantum Corrections*, Phys. Rev. **D16** (1977), 1762–1768, DOI: [10.1103/PhysRevD.16.1762](https://doi.org/10.1103/PhysRevD.16.1762).
- [300] A. Strumia, N. Tetradis, and C. Wetterich, *The Region of validity of homogeneous nucleation theory*, Phys. Lett. **B467** (1999), 279–288, DOI: [10.1016/S0370-2693\(99\)01158-2](https://doi.org/10.1016/S0370-2693(99)01158-2), arXiv:[hep-ph/9808263](https://arxiv.org/abs/hep-ph/9808263) [[hep-ph](#)].
- [301] B. Garbrecht and P. Millington, *Green’s function method for handling radiative effects on false vacuum decay*, Phys. Rev. **D91** (2015), 105021, DOI: [10.1103/PhysRevD.91.105021](https://doi.org/10.1103/PhysRevD.91.105021), arXiv:[1501.07466](https://arxiv.org/abs/1501.07466) [[hep-th](#)].
- [302] B. Garbrecht and P. Millington, *Self-consistent solitons for vacuum decay in radiatively generated potentials*, Phys. Rev. **D92** (2015), 125022, DOI: [10.1103/PhysRevD.92.125022](https://doi.org/10.1103/PhysRevD.92.125022), arXiv:[1509.08480](https://arxiv.org/abs/1509.08480) [[hep-ph](#)].
- [303] V. Branchina and E. Messina, *Stability, Higgs Boson Mass and New Physics*, Phys. Rev. Lett. **111** (2013), 241801, DOI: [10.1103/PhysRevLett.111.241801](https://doi.org/10.1103/PhysRevLett.111.241801), arXiv:[1307.5193](https://arxiv.org/abs/1307.5193) [[hep-ph](#)].
- [304] V. Branchina, E. Messina, and A. Platania, *Top mass determination, Higgs inflation, and vacuum stability*, JHEP **09** (2014), 182, DOI: [10.1007/JHEP09\(2014\)182](https://doi.org/10.1007/JHEP09(2014)182), arXiv:[1407.4112](https://arxiv.org/abs/1407.4112) [[hep-ph](#)].
- [305] V. Branchina, E. Messina, and M. Sher, *Lifetime of the electroweak vacuum and sensitivity to Planck scale physics*, Phys. Rev. **D91** (2015), 013003, DOI: [10.1103/PhysRevD.91.013003](https://doi.org/10.1103/PhysRevD.91.013003), arXiv:[1408.5302](https://arxiv.org/abs/1408.5302) [[hep-ph](#)].
- [306] Z. Lalak, M. Lewicki, and P. Olszewski, *Higher-order scalar interactions and SM vacuum stability*, JHEP **05** (2014), 119, DOI: [10.1007/JHEP05\(2014\)119](https://doi.org/10.1007/JHEP05(2014)119), arXiv:[1402.3826](https://arxiv.org/abs/1402.3826) [[hep-ph](#)].
- [307] F. Loebbert and J. Plefka, *Quantum Gravitational Contributions to the Standard Model Effective Potential and Vacuum Stability* (2015), arXiv:[1502.03093](https://arxiv.org/abs/1502.03093) [[hep-ph](#)].
- [308] S. Bhattacharjee and P. Majumdar, *Gravitational Coleman–Weinberg potential and its finite temperature counterpart*, Nucl. Phys. **B885** (2014), 481–492, DOI: [10.1016/j.nuclphysb.2014.05.031](https://doi.org/10.1016/j.nuclphysb.2014.05.031), arXiv:[1210.0497](https://arxiv.org/abs/1210.0497) [[hep-th](#)].
- [309] N. Haba, K. Kaneta, R. Takahashi, and Y. Yamaguchi, *Gravitational effects on vanishing Higgs potential at the Planck scale*, Phys. Rev. **D91** (2015), 016004, DOI: [10.1103/PhysRevD.91.016004](https://doi.org/10.1103/PhysRevD.91.016004), arXiv:[1408.5548](https://arxiv.org/abs/1408.5548) [[hep-ph](#)].
- [310] Y. Abe, M. Horikoshi, and T. Inami, *Gravity loop corrections to the standard model Higgs in Einstein gravity* (2016), arXiv:[1602.03792](https://arxiv.org/abs/1602.03792) [[hep-ph](#)].
- [311] O. Akerlund, P. de Forcrand, and J. Steinbauer, *Effects of higher dimension operators on the Standard Model Higgs sector*, in: Proceedings, 33rd International Symposium on Lattice Field Theory (Lattice 2015), 2015, arXiv:[1511.03867](https://arxiv.org/abs/1511.03867) [[hep-lat](#)].

Danksagung

Ich möchte meinen Dank an all diejenigen richten, die mich bei der Erstellung der Arbeit unterstützt haben.

Ein großer Dank gehört Prof. Holger Gies für dessen gute Betreuung, Anregungen und fruchtbare Zusammenarbeit. Auch über fachliche Inhalte hinaus fand er stets Zeit, um mir mit seinem Rat zur Seite zu stehen.

Weiterhin möchte ich mich bei Benjamin Knorr, René Sondenheimer und Astrid Eichhorn für die ertragreiche Zusammenarbeit bedanken. Sie haben wesentlich zu den Projekten, aus denen diese Arbeit entstanden ist, beigetragen. Ohne sie wäre die Arbeit in ihrer vorliegenden Form nicht möglich gewesen. Mein Dank gilt außerdem Alexander Blinne, Luca Zambelli, Gian Paolo Vacca, Alfio Bonanno, Javier Rubio, Laura Classen, Michael Scherer, Andreas Wipf, Omar Zanusso, Martin Ammon, Stefan Lippoldt, Daniel Schmidt und Tobias Hellwig für wertvolle Diskussionen über Themen der theoretische Physik im Allgemeinen und Anregungen und Ideen bezüglich meiner eigenen Projekte.

Insbesondere danke ich Benjamin Knorr, René Sondenheimer und Holger Gies für hilfreiche Kommentare zum Manuskript dieser Arbeit.

Genossen habe ich sehr die Gespräche in den Mittagsrunden mit Alexander Blinne, Christian Kohlfürst, Nico Seegert, Julian Leiber, Michael Kalisch, David Schinkel, Albrecht Werner, Riccardo Martini und Alessandro Ugolotti über physikalische als auch nicht-physikalische Themen.

Nicht zuletzt möchte ich mich bei meiner Mutter und Schwester bedanken, die stets ein offenes Ohr für meine Sorgen und Nöte während des Entstehungsprozesses dieser Arbeit hatten.

Die Erstellung dieser Arbeit wurde finanziell gefördert durch die DFG unter den Projektnummern GRK1523/2 und Gi328/7-1.

Ehrenwörtliche Erklärung

Ich erkläre hiermit ehrenwörtlich, dass ich die vorliegende Arbeit selbständig, ohne unzulässige Hilfe Dritter und ohne Benutzung anderer als der angegebenen Hilfsmittel und Literatur angefertigt habe. Die aus anderen Quellen direkt oder indirekt übernommenen Daten und Konzepte sind unter Angabe der Quelle gekennzeichnet. Ergebnisse, die in Zusammenarbeit mit Mitarbeitern des Theoretisch-Physikalischen Instituts in Jena und des Imperial College in London entstanden sind, sind in der Arbeit entsprechend benannt. Weitere Personen waren an der inhaltlich-materiellen Erstellung der vorliegenden Arbeit nicht beteiligt. Insbesondere habe ich hierfür nicht die entgeltliche Hilfe von Vermittlungs- bzw. Beratungsdiensten (Promotionsberater oder andere Personen) in Anspruch genommen. Niemand hat von mir unmittelbar oder mittelbar geldwerte Leistungen für Arbeiten erhalten, die im Zusammenhang mit dem Inhalt der vorgelegten Dissertation stehen.

Die Arbeit wurde bisher weder im In- noch im Ausland in gleicher oder ähnlicher Form einer anderen Prüfungsbehörde vorgelegt.

Die geltende Promotionsordnung der Physikalisch-Astronomischen Fakultät ist mir bekannt. Ich versichere ehrenwörtlich, dass ich nach bestem Wissen die reine Wahrheit gesagt und nichts verschwiegen habe.

Jena,

Julia Borhardt